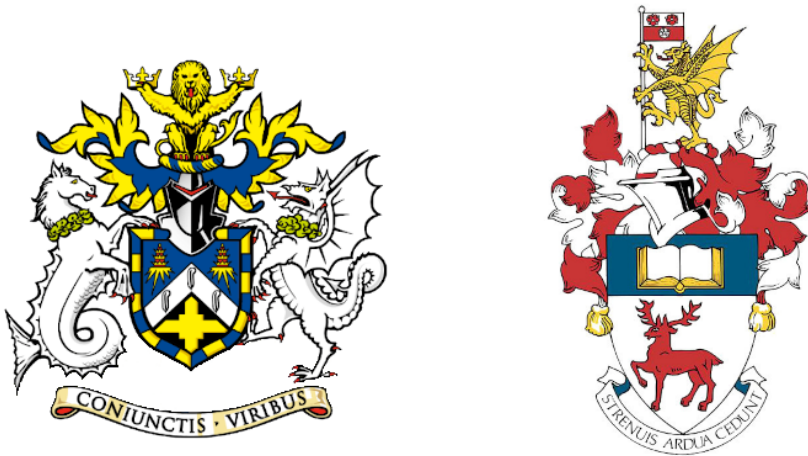


EXPANDING THE PHYSICS REACH OF DUNE IN THE NEAR AND FAR DETECTORS



Francisco Martínez López

*Submitted in partial fulfillment of the requirements
of the Degree of Doctor of Philosophy*

School of Physical and Chemical Sciences
Queen Mary University of London

School of Physics and Astronomy
University of Southampton

November 2024

Statement of originality

I, Francisco Martínez López, confirm that the research included within this thesis is my own work or that where it has been carried out in collaboration with, or supported by others, that this is duly acknowledged and my contribution indicated.

I attest that I have exercised reasonable care to ensure that the work is original, and does not to the best of my knowledge break any UK law, infringe any third party's copyright or other Intellectual Property Right, or contain any confidential material.

I accept that the University has the right to use plagiarism detection software to check the electronic version of the thesis.

I confirm that this thesis has not been previously submitted for the award of a degree by this or any other university.

The copyright of this thesis rests with the author and no quotation from it or information derived from it may be published without the prior written consent of the author.

Francisco Martínez López

November 8, 2024

Abstract

The Deep Underground Neutrino Experiment (DUNE) is a next-generation long-baseline neutrino oscillation experiment. Its primary goal is the determination of the neutrino mass hierarchy and the CP-violating phase. The DUNE physics programme also includes the detection of astrophysical neutrinos and the search for beyond the Standard Model (BSM) phenomena. DUNE will consist of a near detector (ND) complex placed at Fermilab, and a modular Liquid Argon Time Projection Chamber (LArTPC) far detector (FD) to be built in the Sanford Underground Research Facility (SURF), approximately 1300 km away from the neutrino production point.

This thesis describes three different projects within DUNE. First, a novel strategy to improve the triggering capabilities of the DUNE FD is proposed. It uses matched filters to enhance the production of online hits across all charge collection planes. Next, the possibility of detecting neutrinos coming from dark matter (DM) annihilations in the Sun with the FD is explored. The complementarity of DUNE to this kind of DM searches is shown. Finally, the simulation and reconstruction framework of ND-GAr, the gas argon ND proposed for Phase II of DUNE, is presented. A number of additions to this are described, particularly focused on the development of the particle identification (PID) capabilities of the detector. These are then used to perform the first event selection studies with an end-to-end simulation in ND-GAr, in particular the selection of pion exclusive samples in ν_μ CC interactions. All three of these projects share the common goal of enhancing the physics programme of DUNE.

¡Oh memoria, enemiga mortal de mi descanso!

El ingenioso hidalgo don Quijote de la Mancha

MIGUEL DE CERVANTES SAAVEDRA

Acknowledgements

First and foremost, I want to thank my supervisor Linda Cremonesi for her constant support throughout my PhD. Linda taught me many things, but most importantly how to be an independent researcher. Thank you for these four years full of great fun and great physics. This thesis is only possible thanks to her dedication.

Thank you to Stefano Moretti and Claire Shepherd-Themistocleous, my supervisors at Southampton and RAL. They have provided me with invaluable help during this adventure. I would also like to thank the other members of the QMUL neutrino group – Abbey Waldron, Alex Booth, Jon Hays, Nicola McConkey, Prabhjot Singh and Simranjit Singh Chhibra – for their guidance. Our Liquid Argon weekly meetings have always been the perfect space to discuss physics.

I came to the conclusion that the worth of a PhD increases exponentially with the number of friends you make along the way. That is why I thank my fellow students and postdocs in the QMUL particle physics group: Nathan, Aled, Kevin, Sid, Zahaab, Akeem, Callum, James, Talha, Christos, Elizabeth, Gitu, Rob, Albanik, Arnav, Jocelyn, Lottie, Mohammed, and Oscar. I could not imagine my life in this university without them. To more trips to The Cherry, karaoke parties and pub quizzes.

I also want to acknowledge the work of the DUNE DAQ Firmware Readout group. In particular, I would like to thank Alessandro Thea and Ivana Hristova for their help and the long chats about the DAQ. From my time on LTA at CERN, I also want to say thank you to Shyam Bhuller and Klaudia Wawrowska. All of them made going to the office in Prévessin really worth it.

For the last two years, ND-GAr has been main research focus. I want to thank the conveners of the group – Alysia Marino, Patrick Dunne and Tanaz Mohayai – for the

opportunity to contribute to their efforts. I also want to express my gratitude to Alan Bross, Leo Bellantoni, Tom Junk and Vivek Jain, for their insight and all the chats we have had, from physics to hardware and software. And of course, thank you to the other PhD students in the group: Callum Cox, Hank Hua, and Naseem Khan.

I am so grateful to be a part of the DUNE collaboration. During my PhD I have met many collaborators who are both excellent scientists and amazing people. Particularly, I want to thank Alex Wilkinson and Robert Kralik, with whom I share my excitement about neutrino physics either in conferences, collaboration meetings or in random pubs around London.

I want to thank everyone else who has been a part of my life while working on this thesis. Thank you to Bea for her unconditional support and for always believing in me. Thank you to Ana for her company in these last months of writing. Thank you to Giovanna for being there in the rough spots of this journey, especially at the beginning. Thank you to my friends in Spain for their patience and understanding. Finally, I would like to thank my parents and my siblings, who always supported and loved me. This thesis is also yours.

Contents

Statement of originality	3
Abstract	5
Acknowledgements	9
Contents	15
List of Figures	17
List of Tables	27
List of Abbreviations	29
1 Introduction	33
2 Neutrino physics	35
2.1 Neutrinos in the SM	35
2.2 Trouble in the neutrino sector	39
2.2.1 The solar neutrino problem	39
2.2.2 The atmospheric neutrino problem	41
2.3 Massive neutrinos	43
2.4 Neutrino oscillation formalism	46
2.4.1 Oscillations in vacuum	48
2.4.2 Oscillations in matter	50
2.4.3 Current status of neutrino oscillations	52
2.5 Open questions in the neutrino sector	54
2.6 Neutrino interactions	55

CONTENTS

3 The Deep Underground Neutrino Experiment	61
3.1 Overview	61
3.2 Physics goals of DUNE	63
3.3 LBNF beamline	66
3.4 Near Detector	66
3.4.1 ND-LAr	68
3.4.2 TMS/ND-GAr	69
3.4.3 PRISM	70
3.4.4 SAND	72
3.5 A More Capable Near Detector	72
3.5.1 Requirements	73
3.5.2 Reference design	73
3.5.3 R&D efforts	76
3.6 Far Detector	79
3.6.1 Horizontal Drift	80
3.6.2 Vertical Drift	82
3.6.3 FD Data Acquisition System	84
4 Matched Filter approach to Trigger Primitives	87
4.1 Motivation	87
4.2 Signal-to-noise ratio definition	90
4.3 Matched filters	92
4.4 Monte Carlo studies	95
4.4.1 Angular dependence	101
4.4.2 Hit sensitivity	102
4.5 VD ColdBox data taking	111
4.6 Summary	113
5 Dark Matter searches with neutrinos from the Sun	115
5.1 Gravitational capture of DM by the Sun	115

CONTENTS

5.2	Neutrino flux from DM annihilations	117
5.3	Computing limits from solar neutrino fluxes	118
5.4	High energy DM neutrino signals	121
5.4.1	DIS-like events	124
5.4.2	Single proton QE-like events	128
5.4.3	Results	132
5.5	Systematic uncertainties	134
5.5.1	Systematic uncertainties in the solar WIMP signal	135
5.5.2	Systematic uncertainties in the atmospheric background	136
5.5.3	Common systematic uncertainties	136
5.6	Summary	137
6	Particle identification in ND-GAr	139
6.1	GArSoft	140
6.1.1	Event generation	140
6.1.2	Detector simulation	141
6.1.3	Reconstruction	142
6.2	dE/dx measurement in the TPC	145
6.2.1	Truncated dE/dx mean	147
6.2.2	Mean dE/dx parametrisation	150
6.3	Muon and pion separation in the ECal and MuID	155
6.3.1	Track-ECal matching	158
6.3.2	Classification strategy	163
6.3.3	Feature selection and importance	166
6.3.4	Hyperparameter optimisation	178
6.3.5	Probability calibration	181
6.3.6	Performance	183
6.4	ECal time-of-flight	185
6.4.1	Arrival time estimations	187

CONTENTS

6.4.2	Proton and pion separation	189
6.5	Integration in GArSoft	191
6.6	Summary	194
7	Event selection in ND-GAr	195
7.1	Simulated data sample	196
7.2	ν_μ CC selection	198
7.2.1	Selection optimisation	200
7.2.2	Selection performance	204
7.2.3	Primary muon kinematics	208
7.3	Charged pion identification	212
7.3.1	Selection optimisation	214
7.3.2	ν_μ CC $1\pi^\pm$ selection	220
7.4	Neutral pion identification	223
7.5	Neutrino energy reconstruction	226
7.6	Systematic uncertainties	229
7.6.1	Flux uncertainties	229
7.6.2	Cross-section uncertainties	230
7.6.3	Detector uncertainties	233
7.7	Summary	236
8	Conclusion and outlook	239
A	Additional material on Matched Filter	241
A.1	Low-pass FIR filter design	241
A.2	Matched filter impulse-response function	244
A.3	Distortion and peak asymmetry	247
B	Additional material on Solar DM	251
B.1	Gravitational capture of DM by the Sun	251
B.2	Example: Kaluza-Klein Dark Matter	257

CONTENTS

B.3	Example: Leptophilic Dark Matter	261
C Additional material on ND-GAr PID		267
C.1	Energy calibration	267
C.2	Charged pion decay in flight	276
C.2.1	Track breakpoints	278
C.3	Neutral particle identification	284
C.3.1	ECal clustering	284
C.3.2	π^0 reconstruction	287
Bibliography		291

List of Figures

2.1	Solar neutrino fluxes for the solar model BS05(OP).	41
2.2	Zenith angle distributions for the selected ν_e and ν_μ events in the SK detector.	42
2.3	$K^0 \rightleftharpoons \bar{K}^0$ mixing through W^\pm exchange.	47
2.4	Feynman diagrams of the most relevant CC interactions to long-baseline neutrino oscillation experiments.	56
2.5	Total muon neutrino CC cross section per nucleon as a function of the neutrino energy.	57
2.6	Schematic representation of a ν_μ CCQE interaction with a neutron inside a nucleus.	58
3.1	Schematic diagram of the DUNE experiment and the LBNF beamline. .	62
3.2	Schematic longitudinal section of the LBNF beamline at Fermilab. . . .	65
3.3	Predicted neutrino fluxes at the FD in FHC mode and RHC mode. . . .	67
3.4	Representation of the ND hall in Phase II.	68
3.5	Schematic representation of the external components of ND-LAr , including the cryostat and the PRISM movable system.	69
3.6	Schematic view of the TMS detector, highlighting its main parts.	70
3.7	Cross section of the ND-GAr geometry, showing the HPgTPC , ECal and magnet.	71
3.8	Predicted beam muon neutrino flux at the ND location for different off-axis positions.	72

LIST OF FIGURES

3.9	Diagram of the ALICE TPC, showing the two drift chambers, inner and outer field cages and readout chambers.	74
3.10	View of the 12-sided ECal barrel and outer muon tagger geometries of ND-GAr.	75
3.11	Photographs of the TOAD pressure vessel at RHUL.	77
3.12	Electron microscope image and schematic diagram of a GEM electrode.	78
3.13	Schematic diagram showing the operating principle of a LArTPC with wire readout.	79
3.14	Proposed design for the FD-2 module following the HD principle.	80
3.15	Schematic representation of an APA frames showing the U, V, X and G wires.	81
3.16	A PDS module containing 24 X-ARAPUCAs and the location of the modules on the APA frames.	82
3.17	Proposed design for the FD-1 and FD-3 modules following the VD principle.	83
3.18	Schematic representation of the electrode strip configuration for a top and bottom CRU.	84
3.19	Detailed diagram of the DUNE FD DAQ system.	85
4.1	Schematic representation of the Trigger Primitive Generation chain in the DUNE FD.	88
4.2	Example unfiltered waveform from a ProtoDUNE-SP raw data capture.	89
4.3	Example filtered waveform from a ProtoDUNE-SP raw data capture.	91
4.4	Example matched filtered waveform from a ProtoDUNE-SP raw data capture.	92
4.5	Relative change in the S/N for the ProtoDUNE-SP raw data capture for different values of δ and σ from the matched filter parametrisation.	94
4.6	Distribution of the change in the S/N on the induction planes from the ProtoDUNE-SP raw data capture after the optimal matched filters are applied.	95

LIST OF FIGURES

4.7 Distributions of the particles track length in the liquid argon for the generated single particle monoenergetic samples.	96
4.8 Schematic representation of the two rotated reference frames used in the analysis of the MC filter performance.	98
4.9 Distributions of the mean S/N change per event for the different MC samples after applying the matched filters.	99
4.10 Angular dependence of the mean S/N and the S/N improvement for the monoenergetic muon sample.	100
4.11 Angular dependence of the mean S/N and the S/N improvement for the monoenergetic electron sample.	101
4.12 Raw event display for an electron event showing the true, standard, and matched filter hits produced.	103
4.13 Dependence of the precision, sensitivity, and F_1 scores on the threshold values used in the hit finder for the FIR and matched filters.	105
4.14 Dependence of the averaged hit sensitivity on the kinetic energy of the events for the matched filter and standard hits, for the case of the muon and electron samples.	107
4.15 Distributions of the hit sensitivity in the U and V planes versus the sensitivity in the X plane for the standard hits and the matched filter hits in the electron sample.	108
4.16 Standard residuals and quantile-quantile plots for the hit sensitivity of the X and U planes.	109
4.17 Schematic diagram of the vertical drift ColdBox setup at CERN.	110
4.18 Event display of the data taken with the matched filter and HMA trigger at the VD ColdBox.	111
4.19 Comparison between firmware-produced and simulated TP quantities for a matched filter run at the VD ColdBox.	112

LIST OF FIGURES

5.1	NuWro-computed $\nu_\mu - {}^{40}\text{Ar}$ charged-current scattering cross section as a function of the neutrino energy.	118
5.2	Expected atmospheric neutrino flux as a function of the neutrino energy E_ν at Homestake at solar minimum.	120
5.3	Computed spectra of muon neutrinos at the DUNE FD site from $\tau^+\tau^-$ and $b\bar{b}$ annihilations in the Sun for different DM masses.	122
5.4	Distribution of the muon neutrino energies from the $\tau^+\tau^-$ and $b\bar{b}$ annihilation channels.	123
5.5	Angular distributions for the $b\bar{b}$ DIS sample with $m_{\text{DM}} = 10$ GeV and the atmospheric background.	124
5.6	Signal efficiency and background rejection for the $b\bar{b}$ sample with $m_{\text{DM}} = 10$ GeV as a function of the angular cuts.	125
5.7	Signal efficiencies for the $\tau^+\tau^-$ and $b\bar{b}$ DIS samples as functions of the DM mass.	127
5.8	Angular distributions for the $\tau^+\tau^-$ QE sample with $m_{\text{DM}} = 5$ GeV and the atmospheric background.	128
5.9	Performance of the BDT classifier for the $\tau^+\tau^-$ QE signal with $m_{\text{DM}} = 5$ GeV.	130
5.10	Signal efficiencies for the $\tau^+\tau^-$ and $b\bar{b}$ single proton QE samples as functions of the DM mass.	131
5.11	Projected 90% confidence level upper limits for DUNE on the spin-dependent DM -nucleon scattering cross section as a function of m_{DM}	133
6.1	Schematic diagram showing the different modules involved in the ND-GAr neutrino event production.	144
6.2	Fractional residuals between the true and the reconstructed calibrated dE/dx means and the 60% truncated means.	148
6.3	Estimated values of the mean dE/dx bias and resolution for the stopping proton sample at different values of the truncation factor.	149

LIST OF FIGURES

6.4 Examples of the truncated mean dE/dx LanGauss fits for various $\beta\gamma$ bins, from a simulated FHC neutrino sample.	150
6.5 Resulting one and two dimensional projections of the posterior probability distributions of the ALEPH $\langle dE/dx \rangle$ parameters.	152
6.6 Truncated mean dE/dx as a function of the $\beta\gamma$ product, together with the best fit obtained using the ALEPH parametrisation.	153
6.7 Distribution of the 60% truncated mean dE/dx versus reconstructed momentum for the FHC neutrino sample.	154
6.8 Estimated values of the mean dE/dx bias and resolution obtained for the true protons in a FHC neutrino sample as a function of the momentum.	155
6.9 True momentum distributions for the primary muon and the post FSI charged pions in ν_μ CC $N\pi^\pm$ interactions inside ND-GAr	156
6.10 Distributions of energy deposits in the ECal for a muon and a charged pion with similar momenta.	157
6.11 Performance of the new track-cluster association algorithm for different values of the χ^2 cut.	159
6.12 Schematics of a method to deal with track- ECal associations in non-zero t_0 neutrino interaction events using the cluster time.	161
6.13 Performance of the new track-cluster association algorithm when applying the cluster t_0 correction for different values of the χ^2 cut.	162
6.14 Momentum distributions for the reconstructed muons and charged pions in a FHC sample, together with the fraction of them reaching the ECal and MuID	164
6.15 Predicted truncated $\langle dE/dx \rangle$ versus momentum, for electrons, muons, charged pions and protons, obtained using the ALEPH parametrisation .	165
6.16 Example ECal feature distributions for muons and charged pions in the five different momentum ranges considered.	168
6.17 Example MuID feature distributions for muons and charged pions in the three different momentum ranges considered.	169

LIST OF FIGURES

6.18 Results of the PCA , Shapley and Gini feature importance analyses for the momentum range $0.3 \leq p < 0.8 \text{ GeV}/c$	171
6.19 Results of the PCA , Shapley and Gini feature importance analyses for the momentum range $0.8 \leq p < 1.5 \text{ GeV}/c$	172
6.20 Evolution of the SHAP importance for the top six most important features across all five momentum ranges.	175
6.21 Permutation importances for the ten most important features in the different momentum ranges.	177
6.22 Values of the precision and sensitivity obtained for 10^4 BDT hyperparameter configurations, for the momentum regions I, III and V.	179
6.23 Reliability diagrams for the BDT classifier used in the momentum range $0.3 \leq p < 0.8 \text{ GeV}/c$	182
6.24 Uncalibrated and calibrated predicted probabilities assigned by the BDT classifier in the momentum range $0.3 \leq p < 0.8 \text{ GeV}/c$	183
6.25 Calibrated predicted probabilities assigned by the BDT classifiers for the true muons and charged pions in a FHC neutrino sample.	184
6.26 Efficiency and purity of the muon selection as a function of the reconstructed momentum for the FHC neutrino sample.	185
6.27 Schematic diagram of the hit selection used for the ECal ToF measurement.	186
6.28 Particle velocity versus momentum measured with different ECal arrival time estimations.	188
6.29 Mass spectra for p and π^\pm particles, using different ECal time resolution values and arrival time estimates.	190
6.30 Efficiency and purity for the proton selection as a function of the momentum, for $\Delta\tau = 0.10 \text{ ns}$	191
6.31 Distributions of the velocities measured by ToF with the inner ECal , for different momentum bins, in a FHC neutrino interaction sample. The Gaussian fits are performed around the maxima for each particle species.	192

LIST OF FIGURES

6.32 Distributions of proton dE/dx and ToF scores for a sample of 100000 FHC neutrino interactions in the HPgTPC.	193
7.1 Schematic diagram of the HPgTPC including the fiducial volume.	199
7.2 True positive, false positive, and false negative true neutrino energy distributions for a ν_μ CC selection.	200
7.3 Efficiency and purity for the ν_μ CC selection as a function of the different cuts.	202
7.4 Significance for the ν_μ CC selection as a function of the different cuts.	202
7.5 Cumulative efficiency and purity for the ν_μ CC selection.	203
7.6 True neutrino energy spectra for the ν_μ CC selection.	205
7.7 Efficiency and purity for the ν_μ CC selection as a function of the true neutrino energy.	206
7.8 True neutrino energy spectrum for the ν_μ CC selection with and without sign selection.	207
7.9 Efficiency 2D distributions for the ν_μ CC selection given the true position of the interaction vertex.	208
7.10 Distributions for the reconstructed versus truth primary muon momentum, longitudinal momentum, transverse momentum, and angle.	209
7.11 Efficiency and purity of the ν_μ CC selection as a function of the primary muon true momentum and beam angle.	210
7.12 Fractional residual distributions for the position of the primary vertex in the ν_μ CC selection.	211
7.13 Distribution of events based on their true and reconstructed π^\pm multiplicity, for a given selection.	212
7.14 Efficiency and purity for the ν_μ CC $0\pi^\pm$ selection as a function of the different cuts.	214
7.15 Efficiency and purity for the ν_μ CC $1\pi^\pm$ selection as a function of the different cuts.	216

LIST OF FIGURES

7.16 Row and column normalised distributions of events given their true and reconstructed π^\pm multiplicity.	217
7.17 Purity versus efficiency achieved for the different cut configurations explored separated by the various ν_μ CC $N\pi^\pm$ selections.	218
7.18 Efficiency of the ν_μ CC $N\pi^\pm$ selections as a function of the hadronic invariant mass.	219
7.19 Reconstructed kinematic distributions for the pion candidate in the ν_μ CC $1\pi^\pm$ selection.	221
7.20 Distributions for the reconstructed versus truth pion kinetic energy and angle between the pion and muon in the ν_μ CC $1\pi^\pm$ selection.	222
7.21 Efficiency of the ν_μ CC $1\pi^\pm$ selection as a function of the true pion kinetic energy and pion-muon angle.	223
7.22 Invariant mass distribution obtained for the unassociated ECal cluster pairs in the event.	225
7.23 Reconstructed neutrino energy spectra for the ν_μ CC selection obtained using the truth and reconstructed information	227
7.24 Neutrino energy residuals distributions for the ν_μ CC selection obtained using the truth and reconstructed information	228
7.25 Estimated dE/dx resolution as a function of the track length for true muons and protons in a ν_μ CC sample.	234
A.1 Power spectra for the current low-pass FIR filter and the optimal filter obtained using the Parks-McClellan algorithm.	242
A.2 Relative change in the S/N of the ProtoDUNE-SP raw data capture for different values of the cutoff frequency f_c and the transition width δf . .	243
A.3 Distribution of the relative change of the S/N on the different wire planes after the optimal FIR filter was applied.	244

LIST OF FIGURES

A.4 Waveforms for two muon events, one parallel to the APA and to the wires in the U plane and other normal to the APA plane and perpendicular to the U plane wires.	247
A.5 Distribution of the peak asymmetry for the monoenergetic muon sample and dependence of the S/N change on the mean peak asymmetry of the event.	248
B.1 Input solar parameters used in the capture rate computation as a function of the solar radius.	253
B.2 Capture rates as a function of the DM mass for the DM -electron interactions, SD DM -nucleons interactions, and SI DM -nucleons interactions.	254
B.3 Feynman diagrams for B^1B^1 annihilation into SM fermions.	257
B.4 Feynman diagrams for B^1B^1 annihilation into a Higgs boson pair.	258
B.5 Computed spectra of muon neutrinos at the DUNE FD site from B^1 annihilations in the Sun for various values of M_{LKP}	259
B.6 Projected 90% confidence level upper limit for DUNE on the spin-dependent B^1 -proton scattering cross section as a function of M_{LKP}	260
B.7 Projected 90% confidence level sensitivity of DUNE to the scale Λ of an EFT containing only leptophilic DM axial-axial interactions.	264
C.1 Distribution of the Geant4 -level energy deposits per unit length in the stopping proton sample.	268
C.2 Distribution of the reconstructed ionisation charge per unit length for different reclustering values.	269
C.3 Distribution of the Geant4 -simulated energy losses per unit length versus residual range for the stopping proton sample.	271
C.4 Fitted most probable dQ/dx values for each dE/dx bin, together with best fit to the logarithmic calibration function.	272
C.5 Fitted most probable dQ/dx values for each dE/dx bin for three different ADC bit limits.	273

LIST OF FIGURES

C.6 Area normalised dE/dx distributions for the true and the reconstructed energy deposits in the stopping proton sample.	275
C.7 Fraction of charged pions with $p = 500$ MeV/ c decaying in the HPgTPC and example event display.	277
C.8 Values of $\chi_k^{2(FB)}$, F_k , $D_k^{1/R}$, and D_k^ϕ versus position along the drift direction for a reconstructed track in a π^+ decay event.	279
C.9 Residual distributions of the true and reconstructed decay position along the drift coordinate, using the position of the maximum of $\chi_k^{2(FB)}$ and F_k as estimates of the decay position.	280
C.10 Distributions of the extrema of $\chi_k^{2(FB)}$, F_k , $D_k^{1/R}$, and D_k^ϕ for non-decaying and decaying reconstructed pion tracks.	282
C.11 Outputs of the BDT classifier for a test sample of decaying pion+muon tracks and non-decaying pion tracks.	283
C.12 Dependence of the decay position finding resolution and BDT performance on the true value of the decay angle.	283
C.13 Mean values of the F_1 -score marginal distributions for the different free parameters of the new clustering algorithm.	285
C.14 Number of cluster per photon and invariant mass distributions for photon pairs from single π^0 events using the standard and new ECal clustering algorithms.	287

List of Tables

2.1	Values of T_3 and $Y/2$ assigned to the first generation of fermions.	37
2.2	Neutral current couplings.	38
2.3	Summary of neutrino oscillation parameters determined in the Neutrino Global Fit of 2020.	54
3.1	Summary of the two-phased plan for DUNE	63
3.2	Exposure and time required to achieve the different physics milestones of the two phases.	64
5.1	Systematic uncertainties for the solar WIMP signal events.	135
5.2	Systematic uncertainties for the solar WIMP atmospheric background events.	136
6.1	Momentum ranges and description of the PID approach assumed for the muon and pion classification task.	166
6.2	Optimal values of the hyperparameters used by the BDT , for each momentum range.	180
6.3	Performance metrics of the BDT s with optimal hyperparameters, for the different momentum ranges.	181
7.1	Estimated event rates in ND-GAr	197
7.2	Step-by-step ν_μ CC selection cuts and cumulative passing rates.	204
7.3	Neutrino interaction systematic parameters implemented in GENIE used in the DUNE TDR LBL analysis.	231

LIST OF TABLES

7.4	Neutrino interaction systematic parameters used in the DUNE TDR LBL analysis not present in GENIE.	232
7.5	Expected performance for ND-GAr, both from simulation studies and extrapolated from ALICE and PEP-4.	236
A.1	Characteristic parameters of the two monoenergetic muon events selected for the peak asymmetry study.	249
C.1	Calibration parameters obtained from the fit of the ND-GAr simulated stopping proton sample to the calibration function.	274
C.2	Summary of parameters and sampled values used in the optimisation of the clustering algorithm.	286

List of Abbreviations

ADC	Analog to Digital Converter	CRU	Charge-Readout Unit
ALEPH	Apparatus for LEP PHysics	DAQ	Data AcQuisition
ALICE	A Large Ion Collider Experiment	DIS	Deep Inelastic Scattering
APA	Anode Plane Assembly	DM	Dark Matter
ASIC	Application-Specific Integrated Circuit	DP	Dual Phase
ATLAS	A Toroidal LHC ApparatuS	DUNE	Deep Underground Neutrino Experiment
BDT	Boosted Decision Tree	ECal	Electromagnetic Calorimeter
BE	Back-End	EFT	Effective Field Theory
BooNE	Booster Neutrino Experiment	EM	ElectroMagnetic
BSM	Beyond the Standard Model	FD	Far Detector
CAF	Common Analysis File	FHC	Forward Horn Current
CALICE	CAlorimeter for LInear Collider Experiment	FHiCL	Fermilab Hierarchical Configuration Language
CC	Charged Current	FIR	Finite Impulse Response
CDR	Conceptual Design Report	FPGA	Field Programmable Gate Array
CKM	Cabibbo-Kobayashi-Maskawa	FSI	Final State Interaction
CMS	Compact Muon Solenoid	FV	Fiducial Volume
COH	COHerent	GALLEX	GALLium EXperiment
CP	Charge Parity	GArc	Gaseous Argon
CPT	Charge Parity Time reversal	GAT0	Gaseous Argon T0
CRP	Charge-Readout Plane		

LIST OF ABBREVIATIONS

GEM	Gas Electron Multiplier	MACRO	Monopole, Astrophysics and
GOAT	Gas-argon Operation of ALICE		Cosmic Ray Observatory
	TPC	MC	Monte Carlo
GORG	GEM Over-pressurized with Reference Gases	MEC	Meson-Exchange Current
		MINERvA	Main Injector Experiment for ν -A
HD	Horizontal Drift	MINOS	Main Injector Neutrino
HK	Hyper-Kamiokande		Oscillation Search
HMA	Horizontal Muon Algorithm	MIP	Minimum Ionising Particle
HPgTPC	High Pressure gaseous Time Projection Chamber	MPV	Most Probable Value
ILD	International Large Detector	MSW	Mikheev-Smirnov-Wolfenstein
IMB	Irvine-Michigan-Brookhaven detector	MuID	Muon IDentification system
IO	Inverted Ordering	MWPC	Multi-Wire Proportional readout Chamber
IQR	InterQuartile range	NC	Neutral Current
IROC	Inner ReadOut Chamber	ND	Near Detector
K2K	KEK to Kamioka	ND-GAr	Near Detector Gaseous Argon
KamLAND	Kamioka Liquid Scintillator Antineutrino Detector	ND-LAr	Near Detector Liquid Argon
KK	Kaluza-Klein	NEXT	Neutrino Experiment with a Xenon Tpc
LAr	Liquid Argon	NN	Nearest Neighbours
LArTPC	Liquid Argon Time Projection Chamber	NO	Normal Ordering
LBL	Long BaseLine	NOMAD	Neutrino Oscillation MAgnetic Detector
LBNF	Long Baseline Neutrino Facility	NOvA	NuMI Off-Axis ν_e Appearance
LEP	Large Electron-Positron Collider	OROC	Outer ReadOut Chamber
LHC	Large Hadron Collider	PAI	Photo-Absorption Ionisation
LKP	Lightest Kaluza- Klein Particle	PC	Principal Component

LIST OF ABBREVIATIONS

PCA	Principal Component Analysis	SI	Spin-Independent
PCB	Printed Circuit Board	SiPM	Silicon PhotoMultiplier
PDF	Probability Density Function	SIS	Shallow Inelastic Scattering
PDG	Particle Data Group	SK	Super-Kamiokande
PDS	Photon Detection System	SM	Standard Model
PEP	Positron-Electron Project	SNB	Supernova Neutrino Burst
PID	Particle IDentification	SNO	Sudbury Neutrino Observatory
PMNS	Pontecorvo-Maki-Nakagawa-Sakata	SP	Single Phase
POT	Protons On Target	SPY	Solenoid with Partial Yoke
PPFX	Package to Predict the FluX	SRC	Short-Range Correlated
PRISM	Precision Reaction-Independent Spectrum Measurement	SuperNEMO	Super Neutrino Ettore Majorana Observatory
QE	QuasiElastic	SURF	Sandford Underground Research Facility
RENO	Reactor Experiment for Neutrino Oscillation	SVD	Singular Value Decomposition
RES	RESonant	T2K	Tokai to Kamioka
RHC	Reverse Horn Current	TDR	Technical Design Report
RMS	Root Mean Square	TMS	Temporary Muon Spectrometer
ROC	Receiver Operating Characteristic	TOAD	Test stand of an Overpressure Argon Detector
RPA	Random Phase Approximation	ToF	Time-of-Flight
S/N	Signal-to-Noise ratio	TP	Trigger Primitive
SAGE	Soviet-American Gallium Experiment	TPC	Time Projection Chamber
SAND	System for on-Axis Neutrino Detection	UED	Universal Extra Dimensions
SBND	Short-Baseline Near Detector	VD	Vertical Drift
SD	Spin-Dependent	VUV	Vacuum UltraViolet
		WIB	Warm Interface Board

LIST OF ABBREVIATIONS

WIMP Weakly Interacting Massive Particle

Introduction

The beginning is the most important part of any work.

– Plato, *The Republic*

The Standard Model (**SM**) of particle physics [1–3] has provided a deep understanding of the electromagnetic, weak and strong interactions, and over the past decades it has passed all kind of precision tests [4]. However, the **SM** by itself cannot explain certain observed phenomena, such as the baryon asymmetry of the universe [5], the existence of dark matter (**DM**) [6], or the origin of neutrino masses [7].

One of the biggest puzzles in physics nowadays is how the universe came to be matter-dominated. Following the Big Bang, matter and antimatter were created in equal amounts. A. D. Sakharov described what are the necessary conditions to generate a matter-antimatter asymmetry in the early universe [8]. One of them is the existence of interactions that violate the charge-parity (**CP**) symmetry. It has already been established that the amount of **CP** violation in the quark sector is not enough to generate the baryon asymmetry [9]. Leptons could contribute to the **CP** violation through the neutrino oscillation mechanism [10]. However, there is no experimental evidence for this so far.

Another yet to be solved mystery of modern physics concerns the nature of **DM**. From astrophysical observations (see Ref. [6] and references therein), we are aware of the existence of some unknown matter which only interacts gravitationally with other particles. Usually, extensions of the **SM** include feasible **DM** candidates. These are usually

CHAPTER 1. INTRODUCTION

very stable, heavy particles with small interactions (if any) with **SM** particles. These states are known as weakly interacting massive particles (**WIMPs**) [11, 12]. Experiments looking for **DM** have constrained the interaction cross section between **DM** and **SM** particles to be very small for **DM** masses below 1 TeV [13].

Among other next generation particle physics experiments, the Deep Underground Neutrino Experiment (**DUNE**) stands out. Conceived as a neutrino oscillation experiment, it will provide definitive answers to different open questions in the neutrino sector. Its main goals are the discovery of **CP** violation in the leptonic sector and the determination of the neutrino mass ordering [14]. It will also provide precision measurements of the oscillation parameters within the three-flavour picture.

The **DUNE** far detector (**FD**) will also search for baryon-number violation and neutrinos originated from supernova explosions. Moreover, its near detector (**ND**) complex will sit next to the most powerful neutrino beam to date, allowing for a rich neutrino cross section programme. This broad physics range requires a superb performance from the detectors, which can also be used to look for other **BSM** phenomena.

In this thesis, I explore three different aspects of **DUNE**. First, I propose a method to enhance the sensitivity of the online processing in the **FD** to low energy events. Then, I investigate the potential of detecting neutrino fluxes from **DM** annihilations inside the Sun with the **DUNE FD**. Next, I discuss my work on the reconstruction of **ND-GAr**, the gaseous argon component of the **DUNE ND**. Finally, I make use of those upgrades to perform the first event selection studies with fully reconstructed events in this detector.

This thesis opens with an overview of the status of neutrino physics in Chapter 2. Chapter 3 introduces **DUNE**, its physics programme and various components, including **ND-GAr**. In Chapter 4 I review the possibility of using matched filters to form online hits in the **FD**. The solar **DM** analysis is presented in Chapter 5. Chapter 6 describes the work on the **ND-GAr** reconstruction, focused on particle identification. The event selection studies in **ND-GAr** are covered in Chapter 7. Eventually, the thesis concludes with Chapter 8, where I discuss future plans for the different projects.

2

Neutrino physics

Little particles of inspiration sleet through the universe all the time traveling through the densest matter in the same way that a neutrino passes through a candyfloss haystack, and most of them miss.

– Terry Pratchett, *Sourcery*

Ever since they were postulated in 1930 by Wolfgang Pauli to explain the continuous β decay spectrum [15], and later found by F. Reines and C. Cowan at the Savannah River reactor in 1953 [16], neutrinos have had a special place among all other elementary particles. They provide a unique way to probe a wide range of physics, from nuclear physics to cosmology, from astrophysics to colliders. Moreover, there is compelling evidence to believe that the study of neutrinos may be the key to unveiling different aspects of BSM physics, difficult to test elsewhere [17].

In this Chapter, I review the basics of neutrino physics, from their role within the SM to the main open questions related to the neutrino sector, paying special attention to the phenomenology of neutrino oscillations.

2.1 Neutrinos in the SM

The SM of fundamental interactions was initially proposed in 1967 by S. Glashow, S. Weinberg and A. Salam[1–3]. This theoretical framework describes the dynamics of leptons and quarks, by introducing a collection of mediating gauge vector bosons and one scalar particle, known as the Higgs boson. It assumes that the local gauge

CHAPTER 2. NEUTRINO PHYSICS

symmetry $SU(3) \times SU(2)_L \times U(1)_Y$ is an internal symmetry of the system, with $SU(3)$ describing quantum chromodynamics, and $SU(2)_L \times U(1)_Y$ being the gauge groups of the electroweak sector. For a detailed overview of the [SM](#) of electroweak interactions, see Ref. [18].

In the [SM](#), neutrinos appear in three flavours, namely ν_e , ν_μ , and ν_τ . These are associated with the corresponding charged leptons, e , μ , and τ . Neutrinos exist only as left-handed particles, grouped in doublets with the charged leptons, while the latter come in both chirality states:

$$\begin{pmatrix} \nu_e \\ e_L^- \end{pmatrix}, \quad \begin{pmatrix} \nu_\mu \\ \mu_L^- \end{pmatrix}, \quad \begin{pmatrix} \nu_\tau \\ \tau_L^- \end{pmatrix}, \quad e_R^-, \quad \mu_R^-, \quad \tau_R^-. \quad (2.1)$$

Similarly, quarks also exist in both chirality states, and are grouped as:

$$\begin{pmatrix} u_L \\ d_L \end{pmatrix}, \quad \begin{pmatrix} s_L \\ c_L \end{pmatrix}, \quad \begin{pmatrix} t_L \\ b_L \end{pmatrix}, \quad u_R, \quad d_R, \quad s_R, \quad c_R, \quad t_R, \quad b_R. \quad (2.2)$$

The absence of right-handed neutrino fields implies that neutrinos are strictly massless within the [SM](#). This restriction follows from the experimental observation that all neutrinos produced via weak interactions are pure left-handed helicity states [19] (and similarly antineutrinos are pure right-handed states). The hypothetical existence of right-handed neutrinos could be indirectly inferred from the observation of non-zero neutrino masses. Nevertheless, the existence of neutrino masses is not a sufficient condition for the existence of such fields.

Left and right-handed fermions transform differently under $SU(2)_L \times U(1)_Y$ rotations, as the right-handed particles are singlets under $SU(2)_L$. Applying a local transformation, they change as:

$$\begin{aligned} \psi_L &\longrightarrow e^{-iY\beta(x)/2} e^{-iT_a\alpha_a(x)} \psi_L, \\ \psi_R &\longrightarrow e^{-iY\beta(x)/2} \psi_R, \end{aligned} \quad (2.3)$$

where $Y/2$ and T_a are the generators of $U(1)_Y$ and $SU(2)_L$, respectively, and $\beta(x)$ and

2.1. NEUTRINOS IN THE SM

Table 2.1: Values of T_3 and $Y/2$ assigned to the first generation of fermions.

	e_L	ν_e	e_R	u_L	d_L	u_R	d_R
T_3	-1/2	1/2	0	1/2	-1/2	0	0
$Y/2$	-1/2	-1/2	-1	1/6	1/6	2/3	-1/3

$\alpha_a(x)$ are the parameters of the rotation.

The values of the quantum numbers $Y/2$ and T_3 , the weak hypercharge and the third component of the weak isospin, have to be assigned to the different particles. The values of T_3 follow from the assigned SU(2) representations of the matter fields. After the spontaneous symmetry breaking $SU(2)_L \times U(1)_Y \rightarrow U(1)_{EM}$, one finds the relation which determines the electric charge:

$$Q = T_3 + \frac{Y}{2}. \quad (2.4)$$

Setting the electric charge to -1 for electrons, we can find the values of the weak hypercharge for the rest of the fermions. The resulting values for the first generation of leptons and quarks are shown in Tab. 2.1.

It is clear that the free Lagrangian of the theory is not invariant under the gauge transformations, as the kinetic terms contain derivatives. Therefore, to make it invariant one needs to introduce a set of gauge bosons. They appear in the so-called covariant derivative, which replaces the common derivative and transforms in the same way as the fermion fields under local rotations. This constraint fixes completely the transformations of the spin-1 fields. For left and right-handed particles, the covariant derivatives are given by:

$$\begin{aligned} D_\mu \psi_L &= \left(\partial_\mu + ig' \frac{Y}{2} B_\mu + ig T_a W_\mu^a \right) \psi_L, \\ D_\mu \psi_R &= \left(\partial_\mu + ig' \frac{Y}{2} B_\mu \right) \psi_R, \end{aligned} \quad (2.5)$$

where W_μ^i , $i = 1, 2, 3$ and B_μ are the gauge bosons for the $SU(2)_L$ and $U(1)_Y$ groups, respectively, and g and g' are the corresponding gauge couplings. It can be shown that

CHAPTER 2. NEUTRINO PHYSICS

Table 2.2: Neutral current couplings.

	u	d	ν_e	e
$2v_f$	$1 - \frac{8}{3}\sin^2\theta_W$	$-1 + \frac{4}{3}\sin^2\theta_W$	1	$-1 + 4\sin^2\theta_W$
$2a_f$	1	-1	1	-1

these fields transform in the adjoint representation of the gauge group.

So far, the theory only contains massless particles, as adding bare mass terms to the Lagrangian would spoil the gauge symmetry. Therefore, the mass terms need to be induced by a spontaneous breaking of the symmetries. In the [SM](#), this is achieved by the Higgs mechanism [20–22]. The Higgs doublet is coupled to the gauge bosons through the covariant derivative, and to the fermions through the Yukawa couplings [18]. Upon spontaneous symmetry breaking, the vacuum expectation value of the Higgs field generates the mass terms of the particles.

In order to obtain the physical intermediate vector boson states, we need to perform the following redefinitions:

$$\begin{aligned} A_\mu &= \sin \theta_W W_\mu^3 + \cos \theta_W B_\mu, \\ Z_\mu &= \cos \theta_W W_\mu^3 - \sin \theta_W B_\mu, \\ W_\mu^\pm &= \frac{1}{\sqrt{2}} (W_\mu^1 \mp i W_\mu^2), \end{aligned} \tag{2.6}$$

where A_μ is the photon field, and Z_μ and W_μ^\pm are the neutral and the charged weak boson fields, respectively. The Weinberg angle, θ_W , can be written in terms of the gauge couplings:

$$\begin{aligned} \cos \theta_W &= \frac{g}{\sqrt{g^2 + g'^2}}, \\ \sin \theta_W &= \frac{g'}{\sqrt{g^2 + g'^2}}. \end{aligned} \tag{2.7}$$

The gauge couplings and the Weinberg angle allow to express the electric charge as $e = g' \cos \theta_W = g \sin \theta_W$.

At this point, the interacting part of the electroweak Lagrangian can be re-written

2.2. TROUBLE IN THE NEUTRINO SECTOR

as the sum of three contributions: the electromagnetic (EM), charged-current (**CC**) and neutral-current (**NC**) components:

$$\begin{aligned}\mathcal{L}_{\text{EW}}^{\text{int}} &= \mathcal{L}_{\text{EM}} + \mathcal{L}_{\text{CC}} + \mathcal{L}_{\text{NC}} \\ &= -eA_\mu J_{\text{EM}}^\mu - \frac{g}{2\sqrt{2}} (W_\mu^+ J_{\text{CC}}^\mu + \text{h.c.}) - \frac{g}{2\cos\theta_W} Z_\mu J_{\text{NC}}^\mu,\end{aligned}\tag{2.8}$$

with $+\text{h.c.}$ being an abbreviation for adding the Hermitian conjugate of the preceding terms and the currents defined as:

$$\begin{aligned}J_{\text{EM}}^\mu &= \sum_f Q_f \bar{f} \gamma^\mu f, \\ J_{\text{CC}}^\mu &= \sum_\ell \bar{\nu}_\ell \gamma^\mu (1 - \gamma_5) \ell + \sum_f \bar{u}_f \gamma^\mu (1 - \gamma_5) d_f, \\ J_{\text{NC}}^\mu &= \sum_f \bar{f} \gamma^\mu (v_f - a_f \gamma_5) f,\end{aligned}\tag{2.9}$$

where f denotes any **SM** fermion, ℓ and ν_ℓ a charged lepton and a neutrino of any flavour, and u_f and d_f an up-like and a down-like quark of any flavour¹. For the **NC** case, the values of the v_f and a_f couplings are given in Tab. 2.2.

As seen in Eqs. (2.8) and (2.9), in the electroweak theory neutrinos are coupled to the Z boson in a flavour universal way. Therefore, by measuring the so-called invisible decay width of the Z boson we have an estimate of the number of light (i.e. lighter than the Z boson) neutrino flavours. This number was measured by **LEP** in a combined analysis of $e^+e^- \rightarrow \mu^+\mu^-$ and $e^+e^- \rightarrow \text{hadrons}$ to be $N_\nu = 2.9840 \pm 0.0082$ [23].

2.2 Trouble in the neutrino sector

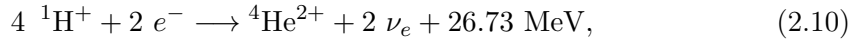
2.2.1 The solar neutrino problem

Neutrinos are produced everywhere in vast amounts. One of the most prominent sources of neutrinos in our vicinity is our Sun. The Sun is powered mainly by two nuclear fusion

¹Note that these fields are written in the flavour basis. Moving to the mass eigenstates one has to introduce the **CKM** matrix, which induces transitions between up- and down-like quarks from different generations.

CHAPTER 2. NEUTRINO PHYSICS

reactions, the p – p chain and the CNO cycle [24]. In both cases, the overall reaction is:



where hydrogen is converted to helium and part of the released energy is lost to the neutrinos. The electron neutrinos produced are often labelled after the processes that generate them. Figure 2.1 shows the solar neutrino flux as a function of the neutrino energy, broken down by the production process.

In the late 1960s, the Brookhaven Solar Neutrino Experiment, led by R. Davis, started data taking with the goal of measuring the solar neutrino flux [25]. The experiment used a tank containing 380 m³ of tetrachloroethene (C₂Cl₄), a liquid commonly used in dry-cleaning, located 1.5 km underground in the Homestake mine in Lead, South Dakota. The incoming neutrinos would get captured following the reaction:



allowing a measurement of the neutrino flux by counting the ³⁷Ar isotopes. The threshold for this reaction is 0.814 MeV, just below the 0.862 MeV line from the ⁷Be ground state transition.

The results of the experiment were compared to the theoretical predictions made by J. Bahcall [27]. During its operation from 1968 to 2002, the experiment observed a solar ν_e flux that was approximately a third of the total prediction [28].

In the early 1990s, the **SAGE** [29] and **GALLEX** [30] experiments started operations. The detection principle used for both experiments was similar to that of the Homestake experiment, but using ⁷¹Ga instead of C₂Cl₄. With a detection threshold of 0.233 MeV, the Gallium-based experiments were able to observe the *pp* neutrino flux. Both experiments measured a solar electron neutrino flux that was a factor of two lower than the predictions, demonstrating that this deficit was energy-dependent.

In the early 2000s, the **SNO** experiment put an end to the solar neutrino puzzle

2.2. TROUBLE IN THE NEUTRINO SECTOR

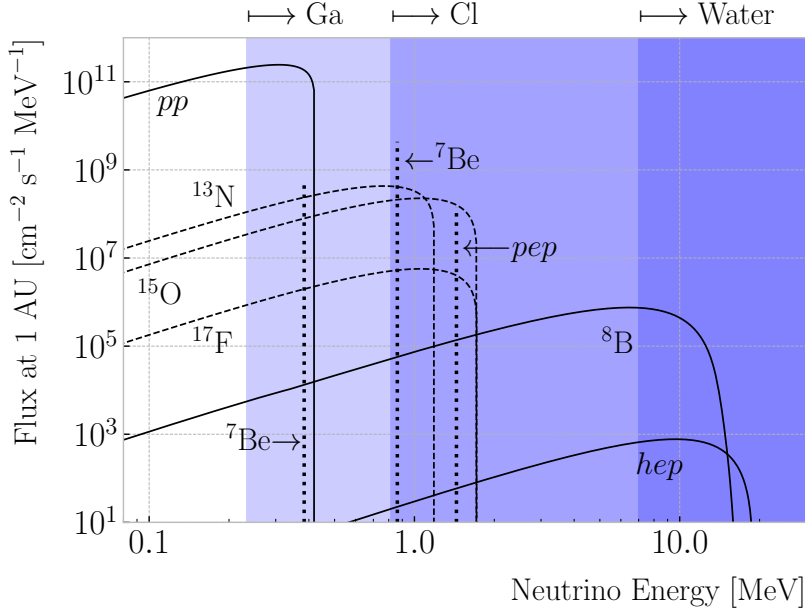


Figure 2.1: Solar neutrino fluxes for the solar model BS05(OP). The detection thresholds for Gallium, Chlorine and water-based experiments are also shown. Figure adapted from Ref. [26].

[31, 32]. Thanks to its directional capabilities, being a Cherenkov light detector, as well as to its heavy water target, SNO measured the total solar neutrino flux through the NC process:

$$\nu_\alpha + d \longrightarrow n + p + \nu_\alpha, \quad (2.12)$$

where d denotes the deuterium nucleus and $\alpha = e, \mu, \tau$. This measurement agreed with the solar model predictions. Then, measuring the CC reaction:

$$\nu_e + d \longrightarrow p + p + e^-, \quad (2.13)$$

they were able to establish that the ν_μ and ν_τ solar fluxes are in fact non-zero, revealing that electron neutrinos were transitioning into different flavours.

2.2.2 The atmospheric neutrino problem

When cosmic-rays interact with the atoms in the upper atmosphere, a plethora of hadrons, mainly π and K mesons, are produced. In particular, for the charged pions,

CHAPTER 2. NEUTRINO PHYSICS

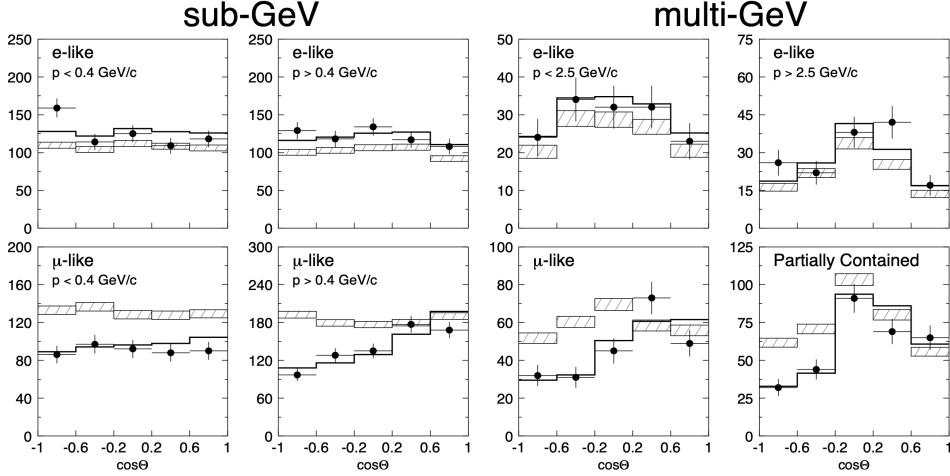


Figure 2.2: Zenith angle distributions for the selected ν_e (top row) and ν_μ (bottom row) events in the SK detector. The hatched region corresponds to the expectation in the case of no oscillations, whereas the solid line indicates the best-fit in the case of $\nu_\mu \rightarrow \nu_\tau$ oscillations. Figure taken from Ref. [38].

the following decay chain dominates:

$$\begin{aligned} \pi^+ &\longrightarrow \mu^+ + \nu_\mu, \\ \mu^+ &\longrightarrow e^+ + \bar{\nu}_\mu + \nu_e, \end{aligned} \tag{2.14}$$

and similar for the antiparticles, as the relevant matrix elements for the meson decays are proportional to the lepton mass. For neutrino energies < 1 GeV, the ratio:

$$\frac{N(\nu_\mu + \bar{\nu}_\mu)}{N(\nu_e + \bar{\nu}_e)}, \tag{2.15}$$

of produced neutrinos and antineutrinos is, to a good approximation, equal to two [33].

During the 1980s, several proton decay experiments, like Kamiokande [34], IMB [35], MACRO [36], and Soudan-2 [37], measured the flux of atmospheric neutrinos. This was an important part of their research programme, as the atmospheric neutrinos constitute their main background. All these experiments reported an atmospheric neutrino ratio lower than the predictions.

A few years before the SNO discovery, in 1998, the Super-Kamiokande collaboration (SK) measured the atmospheric ν_e and ν_μ spectra as a function of the zenith angle

2.3. MASSIVE NEUTRINOS

[38]. Upward-going particles have negative zenith angle, $\cos \Theta < 0$, indicating that they entered from the bottom of the detector. These upward-going neutrinos had to travel through the Earth in order to reach the detector, allowing **SK** to probe a broad range of baselines. Figure 2.2 shows the reported distributions (black dots), compared to the no oscillations prediction (hatched region). This measurement confirmed that muon neutrinos transition to other flavours, and that this phenomenon depends both on the energy and the path length of the neutrino.

The **SK** and **SNO** findings provided definitive evidence for the existence of neutrino oscillations, and therefore non-zero neutrino masses. This constitutes one of the groundbreaking discoveries of modern physics and has acted as driving force for **BSM** searches. The minimal extension of the **SM** we can make to address this phenomenon is introducing different masses for at least two of the neutrinos. This way, we are left with three neutrino mass eigenstates ν_1 , ν_2 , and ν_3 , with masses m_1 , m_2 , and m_3 respectively, which in general will not coincide with the flavour eigenstates, ν_e , ν_μ , and ν_τ .

2.3 Massive neutrinos

The existence of neutrino oscillations imply that neutrinos are massive particles. However, as we have seen before, within the **SM** neutrinos are massless, as they do not have a mass term in the Lagrangian. If one wants to give neutrinos a mass, the particle content of the **SM** needs to be expanded.

A way of generating massive neutrinos while maintaining gauge invariance is by introducing an arbitrary number of sterile neutrinos N_i , $i = 1, \dots, m$. These allow for two different types of neutrino mass terms [39]:

$$-\mathcal{L}_{M_\nu} = \sum_{i=1}^m \sum_{j=1}^3 M_D^{ij} \bar{N}_i \nu_{Lj} + \frac{1}{2} \sum_{i=1}^m \sum_{j=1}^m M_N^{ij} \bar{N}_i N_j^c + \text{h.c.}, \quad (2.16)$$

where M_D is a complex $m \times 3$ matrix and M_N a complex and symmetric $m \times m$ matrix. The first term, often referred to as the Dirac mass term, arises from the corresponding

CHAPTER 2. NEUTRINO PHYSICS

Yukawa interaction after the spontaneous electroweak symmetry breaking, similar to the other fermions. The second term, called the Majorana mass term, is allowed in the Lagrangian as it is a singlet of the gauge group. However, it violates lepton number conservation by two units.

If one imposes lepton number symmetry conservation, the Majorana term must vanish, $M_N = 0$. In this case, if $m = 3$ we can identify the sterile neutrinos as the right-handed component of the neutrino field. The Dirac mass matrix can be diagonalised using two unitary matrices, V_R^ν and V_L^ν , as:

$$M_D = V_R^\nu \text{ diag}(m_1, m_2, m_3) V_L^{\nu\dagger}, \quad (2.17)$$

where m_i , $i = 1, 2, 3$ are the masses of the three neutrino mass eigenstates.

The neutrino mass term can be written in terms of the resulting eigenstates as:

$$-\mathcal{L}_{M_\nu} = \sum_{i=1}^3 m_i \bar{\nu}_{Di} \nu_{Di}, \quad (2.18)$$

with:

$$\nu_{Di} = \left(V_L^{\nu\dagger} \nu_L \right)_i + \left(V_R^{\nu\dagger} N \right)_i. \quad (2.19)$$

In this scenario, both the low energy particle budget and the symmetries of the [SM](#) have to be modified. Moreover, the masses of the neutrinos are generated exclusively through the Higgs mechanism, which does not explain why they are much smaller than those of the charged leptons.

Going back to the general case, we can re-write Eq. (2.16) in matrix form as:

$$-\mathcal{L}_{M_\nu} = \frac{1}{2} (\bar{\nu}_L^c, \bar{N}) \begin{pmatrix} 0 & M_D^T \\ M_D & M_N \end{pmatrix} \begin{pmatrix} \nu_L \\ N^c \end{pmatrix} + \text{h.c.} = \bar{\nu}^c M_\nu \nu + \text{h.c.}, \quad (2.20)$$

with $\nu = (\nu_L, N^c)^T$ being a $(3+m)$ -dimensional vector grouping the active and the sterile neutrinos. The matrix M_ν , which is a complex $(3+m) \times (3+m)$ symmetric

2.3. MASSIVE NEUTRINOS

matrix, can be diagonalised by means of a unitary matrix V^ν , yielding:

$$M_\nu = V^\nu \operatorname{diag}(m_1, m_2, \dots, m_{3+m}) V^{\nu T}. \quad (2.21)$$

Using this eigendecomposition, the neutrino mass term can be expressed as:

$$-\mathcal{L}_{M_\nu} = \frac{1}{2} \sum_{i=1}^{3+m} m_i \bar{\nu}_{Mi} \nu_{Mi}, \quad (2.22)$$

where the states ν_{Mi} , commonly referred to as Majorana neutrinos, are defined as:

$$\nu_{Mi} = \left(V^{\nu \dagger} \nu \right)_i + \left(V^{\nu \dagger} \nu \right)_i^c, \quad (2.23)$$

in such a way that the Majorana condition, $\nu_M^c = \nu_M$, holds true.

As a consequence of the Majorana condition, the neutrino and the antineutrino states can be described in terms of a single field. As opposed to the charged leptons, which need to be represented by a four-component or Dirac spinor, the Majorana neutrino is described by a two-component or Weyl spinor.

If the eigenvalues of the Majorana mass matrix, M_N , are much larger than the electroweak symmetry breaking scale, the diagonalisation of M_ν leads to 3 light and m heavy neutrino states:

$$-\mathcal{L}_{M_\nu} = \frac{1}{2} \bar{\nu}_l M_l \nu_l + \frac{1}{2} \bar{\nu}_h M_h \nu_h, \quad (2.24)$$

where the two mass matrices are given by:

$$\begin{aligned} M_l &\simeq -V_l^T M_D^T M_N^{-1} M_D V_l, \\ M_h &\simeq V_h^T M_N V_h, \end{aligned} \quad (2.25)$$

with V_l and V_h two unitary matrices.

This scenario represents the so-called see-saw mechanism [40–44]. The name comes from the fact that the masses of the heavy states are proportional to M_N , whereas for the light states they are proportional to M_N^{-1} . While both the heavy and the light

CHAPTER 2. NEUTRINO PHYSICS

neutrinos are Majorana particles, it can be shown that the heavy states are mainly right-handed, whereas the light ones are mostly left-handed.

2.4 Neutrino oscillation formalism

Neutrino oscillations were first proposed in 1958 by B. Pontecorvo [45], inspired by the neutral kaon oscillation phenomenon [46]. Neutral kaons, K^0 and \bar{K}^0 , have opposite strangeness (± 1) and are produced in strong processes. It was observed that, when having a beam initially pure of neutral kaons of one type, these would transition into their antiparticles while propagating. Because the weak interaction does not conserve strangeness, neutral kaons can change their identity via the processes shown in Fig. 2.3.

The mixing considered initially by Pontecorvo was between the neutrino and the antineutrino states, as only one neutrino flavour was known at the time. After the discovery of the muon neutrino, the mixing between flavours was also explored [47].

In the general case, we have 3 active and m sterile neutrinos, resulting in $3 + m$ neutrino mass eigenstates. Working in the mass basis, the leptonic charged-current Lagrangian can be written as:

$$-\mathcal{L}_{\text{CC}}^{\text{lep}} = \frac{g}{\sqrt{2}} (\bar{e}_L, \bar{\mu}_L, \bar{\tau}_L) \gamma^\mu U \begin{pmatrix} \nu_1 \\ \nu_2 \\ \vdots \\ \nu_{3+m} \end{pmatrix} W_\mu^+ + \text{h.c.}, \quad (2.26)$$

where U is a $3 \times (3 + m)$ matrix which obeys $UU^\dagger = I_{3 \times 3}$, but in general will not be unitary, $U^\dagger U \neq I_{(3+m) \times (3+m)}$. This is due to the fact that U is a submatrix of the full unitary matrix V^ν that diagonalises the neutrino mass term.

The leptonic mixing matrix, U , establishes how the neutrino mass states couple to the charged leptons. In general, a complex $n \times n$ matrix can be fully specified by $2n^2$ real parameters. If the matrix is unitary, then the number of independent parameters reduces to n^2 , as one has to impose n normalisation and $n(n - 1)$ orthogonality constraints. In our case, we can further reduce the number of parameters by performing a phase

2.4. NEUTRINO OSCILLATION FORMALISM

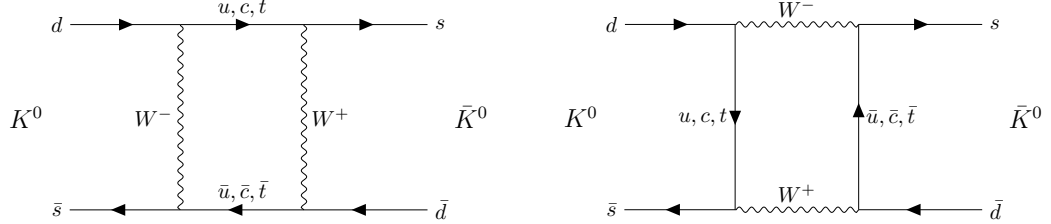


Figure 2.3: $K^0 \rightleftharpoons \bar{K}^0$ mixing through W^\pm exchange.

redefinition of the charged lepton fields, without affecting the physics. This is not true for the neutrinos. As they may be their own antiparticles, one is not allowed to remove any physically relevant phases. If we consider n generations of leptons, the total number of parameters in the mixing matrix is $n^2 - n$. Out of these, half of them are mixing angles, while the other half are complex phase factors.

Considering the extended SM without any additional sterile neutrino states, the resulting 3×3 mixing matrix is unitary. This matrix, often called the Pontecorvo-Maki-Nakagawa-Sakata (PMNS) matrix [48, 49], relates the set of active neutrinos and the three mass eigenstates as:

$$|\nu_\alpha\rangle = \sum_{i=1}^3 U_{\alpha i}^* |\nu_i\rangle, \quad (2.27)$$

where the Greek index α denotes the flavour $\{e, \mu, \tau\}$ and the Latin index i the mass state $\{1, 2, 3\}$. This leptonic mixing matrix may be parametrized in terms of 6 parameters, 3 of which are mixing angles θ_{12} , θ_{13} and θ_{23} , one CP-violating phase δ_{CP} , and 2 Majorana phases α and β :

$$U = \begin{pmatrix} 1 & 0 & 0 \\ 0 & c_{23} & s_{23} \\ 0 & -s_{23} & c_{23} \end{pmatrix} \begin{pmatrix} c_{13} & 0 & s_{13} e^{-i\delta_{CP}} \\ 0 & 1 & 0 \\ -s_{13} e^{i\delta_{CP}} & 0 & c_{13} \end{pmatrix} \begin{pmatrix} c_{12} & s_{12} & 0 \\ -s_{12} & c_{12} & 0 \\ 0 & 0 & 1 \end{pmatrix} \begin{pmatrix} 1 & 0 & 0 \\ 0 & e^{i\alpha} & 0 \\ 0 & 0 & e^{i\beta} \end{pmatrix}, \quad (2.28)$$

where $c_{ij} \equiv \cos \theta_{ij}$ and $s_{ij} \equiv \sin \theta_{ij}$. This matrix is analogous to the Cabibbo-Kobayashi-Maskawa (CKM) matrix in the quark sector. If neutrinos are Dirac fermions, we can drop the Majorana phases in the PMNS matrix, as in this case we can perform the phase redefinitions. In any case, these phases play no role in the neutrino oscillation phenomenology.

CHAPTER 2. NEUTRINO PHYSICS

In the case that additional sterile neutrinos states are present, the full leptonic mixing matrix would not be unitary in general. For instance, in the see-saw scenario, the 3×3 submatrix for the three light Majorana neutrinos is not unitary. However, the deviations from unitarity are of the order $\mathcal{O}(M_D/M_N)$, and therefore expected to be negligible.

2.4.1 Oscillations in vacuum

Consider the case where a neutrino of flavour α is produced at $t = 0$, and then it propagates through vacuum. Such a state will evolve in time according to the relation [50]:

$$|\nu_\alpha(\vec{x}, t)\rangle = \sum_{i=1}^3 U_{\alpha i}^* e^{-i(E_i t - \vec{p}_i \cdot \vec{x})} |\nu_i(\vec{x} = \vec{0}, t = 0)\rangle, \quad (2.29)$$

in the plane wave approximation, as the mass eigenstates are also eigenstates of the free Hamiltonian.

This way, the probability for the neutrino to transition from flavour α to flavour β will be given by:

$$\begin{aligned} P(\nu_\alpha \rightarrow \nu_\beta) &= |\langle \nu_\beta | \nu_\alpha(\vec{x}, t) \rangle|^2 = \left| \sum_{i=1}^3 \sum_{j=1}^3 U_{\alpha i}^* U_{\beta j} e^{-i(E_i t - \vec{p}_i \cdot \vec{x})} \langle \nu_j | \nu_i \rangle \right|^2 \\ &= \left| \sum_{i=1}^3 U_{\alpha i}^* U_{\beta i} e^{-i(E_i t - \vec{p}_i \cdot \vec{x})} \right|^2, \end{aligned} \quad (2.30)$$

where we have used the orthogonality relation $\langle \nu_i | \nu_j \rangle = \delta_{ij}$. A usual approximation to take at this point is to consider ultra-relativistic neutrinos, i.e. $p_i \simeq E$, so we can write the dispersion relations as:

$$E_i = \sqrt{p_i^2 + m_i^2} \approx E + \frac{m_i^2}{2E}. \quad (2.31)$$

In the end, assuming $t \propto L$ where L is the distance between the production and the

2.4. NEUTRINO OSCILLATION FORMALISM

detection points, the probability for the $\nu_\alpha \rightarrow \nu_\beta$ transition becomes:

$$\begin{aligned} P(\nu_\alpha \rightarrow \nu_\beta) &= \sum_{i,j} U_{\alpha i}^* U_{\beta i} U_{\alpha j} U_{\beta j}^* e^{-i \frac{\Delta m_{ij}^2}{2E} L} \\ &= \delta_{\alpha\beta} - 4 \sum_{i < j} \Re e [U_{\alpha i}^* U_{\beta i} U_{\alpha j} U_{\beta j}^*] \sin^2 \left(\frac{\Delta m_{ij}^2}{4E} L \right) \\ &\quad + 2 \sum_{i < j} \Im m [U_{\alpha i}^* U_{\beta i} U_{\alpha j} U_{\beta j}^*] \sin \left(\frac{\Delta m_{ij}^2}{2E} L \right), \end{aligned} \quad (2.32)$$

where Δm_{ij}^2 is the difference of the squared masses of the j th and i th neutrino mass eigenstates. A usual way to write the phase responsible for the oscillations is:

$$\Delta_{ij} \equiv \frac{\Delta m_{ij}^2}{4E} L \simeq 1.27 \frac{\Delta m_{ij}^2}{(\text{eV}^2)} \frac{L}{(\text{km})} \frac{(\text{GeV})}{E}. \quad (2.33)$$

Notice that, in the case of antineutrinos, the only difference would be the sign of the last term in the oscillation probability. As the process $\bar{\nu}_\alpha \rightarrow \bar{\nu}_\beta$ is the **CP**-mirror image of $\nu_\alpha \rightarrow \nu_\beta$, the differences between their oscillation probabilities would be a measure of **CP** symmetry violation:

$$\begin{aligned} A_{CP}^{\alpha\beta} &= P(\nu_\alpha \rightarrow \nu_\beta) - P(\bar{\nu}_\alpha \rightarrow \bar{\nu}_\beta) \\ &= 4 \sum_{i < j} \Im m [U_{\alpha i}^* U_{\beta i} U_{\alpha j} U_{\beta j}^*] \sin 2\Delta_{ij}. \end{aligned} \quad (2.34)$$

Assuming that **CPT** invariance holds, then the following relation must be true:

$$P(\nu_\alpha \rightarrow \nu_\beta) = P(\bar{\nu}_\beta \rightarrow \bar{\nu}_\alpha), \quad (2.35)$$

as these two process are related by the **CPT** symmetry. From the definition of probability, we also must have:

$$\sum_\beta P(\nu_\alpha \rightarrow \nu_\beta) = \sum_\beta P(\bar{\nu}_\alpha \rightarrow \bar{\nu}_\beta) = 1, \quad (2.36)$$

where the sum includes all flavours (also α). From these two constraints, one can prove

CHAPTER 2. NEUTRINO PHYSICS

that:

$$A_{CP}^{\alpha\beta} = -A_{CP}^{\beta\alpha}, \quad (2.37)$$

and in particular:

$$A_{CP}^{\alpha\alpha} = 0. \quad (2.38)$$

A direct consequence of this last relation is that there are no observable **CP**-violating effects in the so-called disappearance experiments. One needs to perform appearance experiments, where the flavour detected is different from the original flavour, in order to measure the **CP** asymmetry. Neutrino experiments often report the amount of **CP**-violation through the Jarlskog invariant [51]. In terms of the parametrisation typically used to write the **PMNS** matrix, it is given by:

$$J = \frac{1}{8} \cos \theta_{13} \sin 2\theta_{12} \sin 2\theta_{13} \sin 2\theta_{23} \sin \delta_{CP}. \quad (2.39)$$

The Jarlskog invariant can be used to compare the amount of **CP**-violation in the lepton and the quark sectors, where $J = 3.12_{-0.12}^{+0.13} \times 10^{-5}$ in the latter [52].

2.4.2 Oscillations in matter

When neutrinos propagate through matter, their oscillation can be affected mainly in two ways. First, neutrinos can inelastically scatter with nuclei, thus destroying the coherent propagation of their quantum state. Nevertheless, in most cases this effect is negligible (even in very dense mediums like the core of the Sun). Second, neutrinos can also experience coherent or forward scatterings, that can affect their oscillation but not lose the coherent propagation of the state.

The first model to account for neutrino oscillations in matter was proposed by S. Mikheev, A. Smirnov and L. Wolfenstein (**MSW**) [53, 54]. It relies on the fact that, as the only charged lepton present in ordinary matter is the electron, electron neutrinos can undergo both charged and neutral-current interactions with matter, whereas for muon and tau neutrinos just neutral current processes are possible.

2.4. NEUTRINO OSCILLATION FORMALISM

An illustrative way to introduce the **MSW** mechanism is by considering the two flavour case. It can be shown that the evolution of the two flavour eigenstates in vacuum is given by the following time-dependent Schrödinger equation:

$$i \frac{d}{dt} \begin{pmatrix} \nu_e \\ \nu_\mu \end{pmatrix} = H_V \begin{pmatrix} \nu_e \\ \nu_\mu \end{pmatrix}, \quad (2.40)$$

with a vacuum Hamiltonian given by:

$$H_V = \frac{\Delta m^2}{4E} \begin{pmatrix} -\cos 2\theta & \sin 2\theta \\ \sin 2\theta & \cos 2\theta \end{pmatrix}, \quad (2.41)$$

where Δm^2 is the mass splitting between the two neutrino states and θ the only mixing angle. For simplicity, I omit the terms of the Hamiltonian that are proportional to the identity, as they do not affect the oscillation phenomenology.

The **NC** contribution to the matter potential is identical for all the flavours, and has the form:

$$V_{\text{NC}} = -\frac{G_F}{\sqrt{2}} N_n(x), \quad (2.42)$$

where G_F is the Fermi constant and $N_n(x)$ the local neutron density. Because it is common to all flavours, I do not take it into account in the effective Hamiltonian, as it would appear as a term proportional to the identity. The **CC** component only affects the electron neutrino (and antineutrino). It can be written as:

$$V_{\text{CC}} = \pm \sqrt{2} G_F N_e(x), \quad (2.43)$$

with $N_e(x)$ being the local electron density in the material. In the end, the effective Hamiltonian which describes the propagation of the flavour eigenstates in matter only contains an extra $\nu_e - \nu_e$ element:

$$H_M = H_V + \begin{pmatrix} V_{\text{CC}} & 0 \\ 0 & 0 \end{pmatrix}. \quad (2.44)$$

The solution to the Schrödinger equation greatly simplifies if one considers the case

CHAPTER 2. NEUTRINO PHYSICS

of a constant matter density. In that case, the effective Hamiltonian can be diagonalised, obtaining the effective neutrino mass eigenstates in matter. It can be re-written in the same form as the vacuum Hamiltonian:

$$H_M = \frac{\Delta m_m^2}{4E} \begin{pmatrix} -\cos 2\theta_m & \sin 2\theta_m \\ \sin 2\theta_m & \cos 2\theta_m \end{pmatrix}, \quad (2.45)$$

where the effective mass splitting and the effective mixing angle are given by:

$$\begin{aligned} \Delta m_m^2 &= \lambda \Delta m^2, \\ \sin 2\theta_m &= \frac{\sin 2\theta}{\lambda}, \end{aligned} \quad (2.46)$$

with:

$$\begin{aligned} \lambda &= \sqrt{(\cos 2\theta - A)^2 + \sin^2 2\theta}, \\ A &= \pm \frac{2\sqrt{2}G_F N_e E}{\Delta m^2}. \end{aligned} \quad (2.47)$$

In terms of the effective matter oscillation parameters, the transition probability $\nu_e \rightarrow \nu_\mu$ (in the two flavour approximation) reads:

$$P(\nu_e \rightarrow \nu_\mu) = \sin^2 2\theta_m \sin^2 \left(\frac{\Delta m_m^2}{2E} L \right) \quad (2.48)$$

From this last equation one can see that, when $\cos 2\theta = A > 0$ the oscillations are greatly enhanced. This effect is known as the [MSW](#) resonance. For the neutrinos, this resonant condition is only satisfied if $\Delta m^2 > 0$ (the opposite is true for antineutrinos). This can be exploited by long-baseline experiments, which can gain sensitivity to the neutrino mass hierarchy through matter effects.

2.4.3 Current status of neutrino oscillations

A wide range of neutrino experiments provide experimental input to the neutrino oscillation framework, both using natural or human-made neutrino sources. The results

2.4. NEUTRINO OSCILLATION FORMALISM

from one of the neutrino global fit analyses, shown in Tab. 2.3², summarise well our current understanding of the different oscillation parameters.

Solar neutrino experiments detect neutrinos produced in thermonuclear reactions inside the Sun, mainly from the so-called p–p chain and the CNO cycle. These neutrinos have a typical energy in the range from 0.1 to 20 MeV. These experiments (Homestake [55], GALLEX [30], SAGE [29], Borexino [56], SK [57] and SNO [58]) provide the best sensitivities to θ_{12} and Δm_{21}^2 .

Atmospheric neutrino experiments detect the neutrino flux produced when cosmic rays scatter with particles in Earth’s atmosphere. These collisions generate particle showers that eventually produce electron and muon neutrinos (and antineutrinos). Their energies range from few MeV to about 10^9 GeV. Experiments like SK [59] and IceCube [60] use atmospheric neutrinos to measure oscillations, and are specially sensitive to θ_{23} and Δm_{32}^2 .

Reactor neutrino experiments look for the $\bar{\nu}_e$ spectrum produced by nuclear reactors, with energies in the MeV scale. Depending on the distance to the source, long-baseline experiments like KamLAND [61] are sensitive to the solar mass splitting Δm_{21}^2 , whereas much shorter baseline experiments such as RENO [62] or DayaBay [63] measure θ_{13} and Δm_{31}^2 .

Accelerator experiments measure neutrino interactions from beams generated by particle accelerators. Mesons are produced when the protons from the accelerator collide into a target. These are then focused into a beam, with some of them decaying into muon neutrinos while the rest are removed from the beam by an absorber. Depending on the configuration one can obtain a beam made of mostly neutrinos or antineutrinos. The typical energies of these neutrinos are in the GeV range. Experiments such as NOvA [64], T2K [65], MINOS [66], OPERA [67] and K2K [68] (and in the future DUNE [69]) are primarily sensitive to θ_{13} , θ_{23} and Δm_{32}^2 . Also, in the coming years DUNE [69] and Hyper-Kamiokande (HK) [70] will be sensitive to δ_{CP} .

²These are the updated results reported during M. Tórtola’s talk at Neutrino 2024 (see this [link](#)).

CHAPTER 2. NEUTRINO PHYSICS

Table 2.3: Summary of neutrino oscillation parameters determined in the Neutrino Global Fit of 2020 [71].

Parameter	Best fit $\pm 1\sigma$	3σ range
Δm_{21}^2 [eV $^2 \times 10^{-5}$]	$7.55^{+0.22}_{-0.20}$	6.98 – 8.19
$ \Delta m_{31}^2 $ [eV $^2 \times 10^{-3}$] (NO)	$2.51^{+0.02}_{-0.03}$	2.43 – 2.58
$ \Delta m_{31}^2 $ [eV $^2 \times 10^{-3}$] (IO)	$2.41^{+0.03}_{-0.02}$	2.34 – 2.49
$\sin^2 \theta_{12}/10^{-1}$	3.04 ± 0.16	2.57 – 3.55
$\sin^2 \theta_{23}/10^{-1}$ (NO)	$5.64^{+0.15}_{-0.21}$	4.23 – 6.04
$\sin^2 \theta_{23}/10^{-1}$ (IO)	$5.64^{+0.15}_{-0.18}$	4.27 – 6.03
$\sin^2 \theta_{13}/10^{-2}$ (NO)	$2.20^{+0.05}_{-0.06}$	2.03 – 2.38
$\sin^2 \theta_{13}/10^{-2}$ (IO)	$2.20^{+0.07}_{-0.04}$	2.04 – 2.38
δ_{CP}/π (NO)	$1.12^{+0.16}_{-0.12}$	0.76 – 2.00
δ_{CP}/π (IO)	$1.50^{+0.13}_{-0.14}$	1.11 – 1.87

2.5 Open questions in the neutrino sector

A crucial question that remains open these days, and is of vital importance for the oscillation phenomenology, is whether the mass eigenstate ν_3 is the heaviest (what we call normal ordering) or the lightest (referred to as inverted ordering) of the mass states. In other words, this means that we do not know the sign of Δm_{32}^2 , so we can either have $m_1 < m_2 < m_3$ (NO) or $m_3 < m_1 < m_2$ (IO).

Also relevant to the neutrino oscillations, there is the problem regarding the θ_{23} octant. Previous experimental results were compatible with its value being close to maximal, $\theta_{23} \sim 45^\circ$ [72, 73]. However, global data fits indicate a deviation from the maximal mixing, giving rise to two degenerate solutions, one in the lower octant $\theta_{23} < 45^\circ$ and another in the higher octant $\theta_{23} > 45^\circ$ (see e.g. Ref. [71]).

Another big puzzle is related to the value of δ_{CP} . Nowadays it is poorly constrained, with all values between π and 2π being consistent with data. A prospective measurement different from $\delta_{CP} = 0, \pm\pi$ will be a sign of CP-violation in the leptonic sector, and thus contribute along with that measured in the quark sector to the total amount of

2.6. NEUTRINO INTERACTIONS

CP-violation. The amount of **CP**-violation in the leptonic sector can be key to explain the matter anti-matter asymmetry in our universe, through the process referred to as leptogenesis [74].

These three questions, because of their nature, could be understood thanks to the next generation of oscillation experiments, like **DUNE**.

Notwithstanding, there are other mysteries that can not be unveiled just by conducting oscillation experiments, as certain quantities do not influence these phenomena. Among these there is the question of the absolute values of the neutrino masses. Depending on the value of the lightest of the neutrino masses we can have different mass spectra, from hierarchical $m_1 \ll m_2 < m_3$ (**NO**) or $m_3 \ll m_1 < m_2$ (**IO**) to quasi-degenerate $m_1 \simeq m_2 \simeq m_3$.

Other open question concerns the nature of the neutrinos themselves. If neutrinos are Dirac particles then their mass term can be generated through the usual Higgs mechanism by adding right-handed neutrino fields. However, if they are Majorana particles and therefore their own antiparticles, there is no need to add extra fields to have the mass term in the Lagrangian. Experiments like **SuperNEMO** [75], **SNO+** [76], and **NEXT** [77], which search for neutrino-less double beta decay, will be able to determine whether neutrinos are Dirac or Majorana particles.

2.6 Neutrino interactions

The study of neutrino-nucleus interactions is of great importance for long baseline neutrino oscillation experiments. The interaction model provides a mapping between the energy of the incoming neutrino and the final state particles after the interaction. Because in these kinds of experiments neutrinos are obtained as secondary decay products of mesons, typically charged pions and kaons, their energies are not known a priori. Not only that, but the kinematics of the interacting nuclei are also unknown. Therefore, we rely on the neutrino interaction models to provide this relation between the observables in the detector and the true kinematics of the neutrino. Limited understanding of the

CHAPTER 2. NEUTRINO PHYSICS

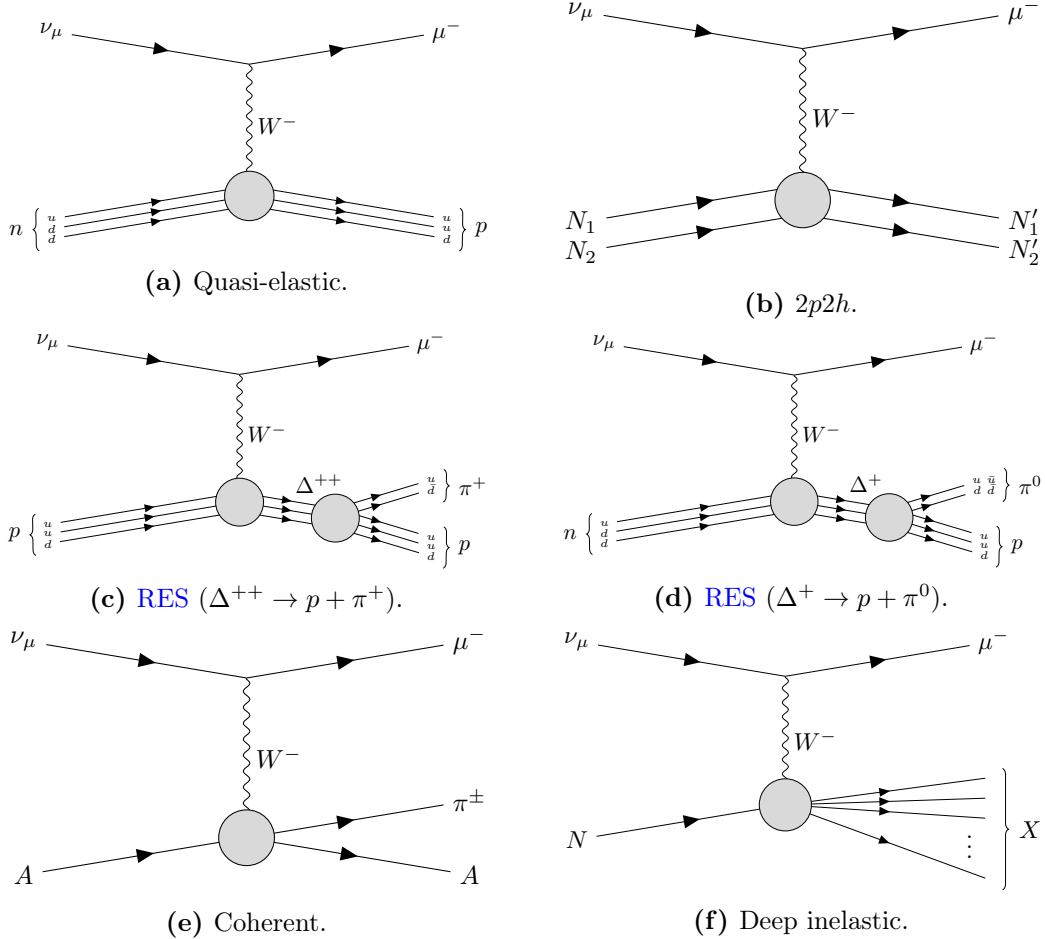


Figure 2.4: Feynman diagrams of the most relevant CC interactions to long-baseline neutrino oscillation experiments.

interaction modelling is expected to be the one of the leading sources of systematic uncertainties in the next generation of long-baseline experiments [78–80].

In long-baseline neutrino oscillation experiments, the energies relevant for the neutrino interactions with nuclei sit around the GeV-scale. Figure 2.4 shows examples of the most common neutrino CC interactions in this energy range. In these diagrams, A indicates that the interaction happened with the nucleus as a whole, whereas N denotes a single nucleon.

At low energies, below 1 GeV, quasi-elastic (QE) interactions dominate. In a CCQE interaction a neutrino (antineutrino) interacts with a neutron (proton), converting it into a proton (neutron) which is then ejected from the nucleus together with the resulting

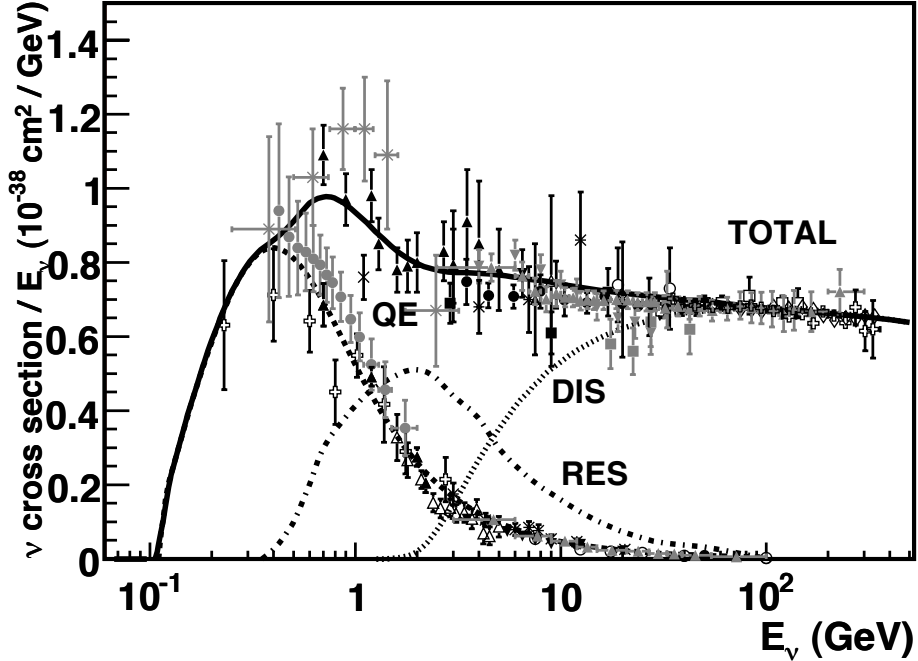


Figure 2.5: Total ν_μ CC cross section per nucleon as a function of the neutrino energy. The contributions from the different channels are shown. Figure taken from Ref. [81].

charged lepton. Neutrinos can also scatter off bound states of nucleons inside the nucleus. These interactions are typically denoted as $nphn$, as the neutrino interacts with a bound state of n nucleons and leave n holes in the nucleus. Particularly relevant are the $2p2h$ events, as distinguishing them from pure CCQE events is challenging. The $2p2h$ neutrino interactions are dominated by meson exchange current events (MEC), where the nucleons are bound by the exchange of a virtual meson.

At energies above 1 GeV the neutrino is able to excite the nucleons into a baryonic resonance, which promptly decays into a nucleon and a pion. These are the so-called resonant (RES) interactions. Neutrinos also interact with entire nuclei coherently, in the process known as coherent (COH) interaction. These kinds of reactions also produce a single pion in the final state. At high neutrino energies, above 5 GeV, deep inelastic scattering (DIS) takes place. In these processes, the neutrino interacts with a single quark within the nucleon, breaking the nucleon and producing a hadronic shower.

Figure 2.5 shows a compilation of measurements of the total ν_μ CC cross section

CHAPTER 2. NEUTRINO PHYSICS

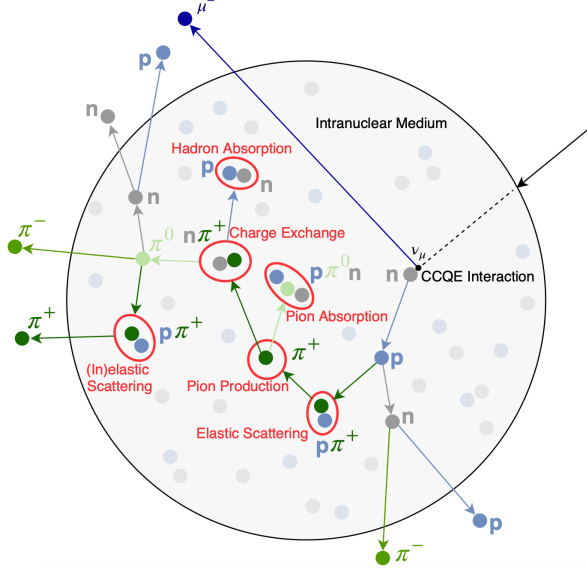


Figure 2.6: Schematic representation of a ν_μ CCQE interaction with a neutron inside a nucleus. The reaction produces a muon and a proton, which travel through the nuclear medium. The outgoing proton undergoes various kinds of hadronic FSI on its way out. Figure taken from Ref. [82].

(see Ref. [81] for the details of the different experimental results). Also shown are the contributions from the different interaction modes. The contribution of the CCCOH interaction is omitted, as it is negligible compared to the others. This shows how the interaction model needs to accurately predict the neutrino-nucleon cross section for the different interaction modes across a broad energy range, to obtain the correct relative contributions.

Nuclear effects alter the neutrino cross section, as well as the multiplicities of the final state particles. Therefore, the interaction models need to account for the effects introduced by the nuclei. There are several models available to describe the initial state of the nucleus, like the relativistic Fermi gas model [83], the local Fermi gas model [84], or spectral functions [85]. The other main effect that interaction models have to deal with are the so-called final state interactions (FSI). These are the interactions of the particles produced in the neutrino-nucleon scattering as they travel through the nuclear medium. Typically, the lepton exits the nucleus without interacting. However, hadrons tend to get scattered, absorbed or re-emitted. These effects are usually described by

2.6. NEUTRINO INTERACTIONS

means of intra-nuclear cascade models [86]. Figure 2.6 illustrates the effects of FSI on the observable particle content in the detector after a ν_μ CCQE interaction.

There exists a rich experimental programme dedicated to the measurement of neutrino cross sections. The list of such experiments in the recent years include MiniBooNE [87], MINERvA [88], MicroBooNE [89] and SBND [90]. Additionally, thanks to their near detectors, long-baseline experiments can perform cross section measurements. Some recent examples are NOvA [91] or T2K [92]. Future oscillation experiments will greatly benefit from these measurements, as the measurement of the oscillation parameters depends on the cross-section modelling. However, there are alternative data-driven approaches to extract the oscillation probabilities without relying on a neutrino interaction model, which are planned to be explored in the next generation of experiments [93, 94]. The importance of the near detector in long-baseline oscillation experiments, and in particular in the context of DUNE, will be discussed further in the next Chapters.

3

The Deep Underground Neutrino Experiment

Deep in the human unconscious is a pervasive need for a logical universe that makes sense. But the real universe is always one step beyond logic.

– Frank Herbert, *Dune*

The Deep Underground Neutrino Experiment ([DUNE](#)) is a next generation long-baseline neutrino oscillation experiment [[14](#)]. It will address several questions in neutrino physics, study neutrinos from astrophysical sources and search for beyond the standard model physics.

This Chapter reviews the main goals of [DUNE](#), the operating principle of the [LBNF](#) beamline, the role that the near detector plays in the oscillation measurement, and the design of the far detector modules and their data acquisition ([DAQ](#)) system.

3.1 Overview

The main physics goals of [DUNE](#) are:

- measure the neutrino mass hierarchy, the amount of [CP](#) violation in the leptonic sector and the θ_{23} octant,
- detect rare low energy neutrino events, like neutrinos from supernova bursts, and
- search for proton decay and other beyond the standard model phenomena.

CHAPTER 3. THE DEEP UNDERGROUND NEUTRINO EXPERIMENT

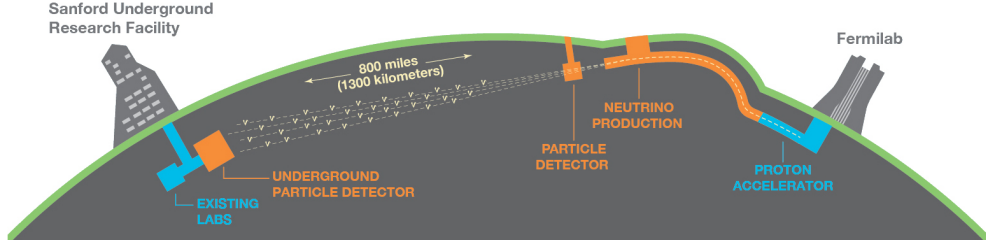


Figure 3.1: Schematic diagram of the [DUNE](#) experiment and the [LBNF](#) beamline [14].

The design of [DUNE](#) has been tailored with these goals in mind. It will consist of two neutrino detectors. A near detector ([ND](#)) complex will be placed at Fermilab, 574 m downstream of the neutrino production point, whereas a larger far detector ([FD](#)) will be built in the Sandford Underground Research Facility ([SURF](#)), South Dakota, approximately 1300 km away. Figure 3.1 shows a simplified diagram with the various components of [DUNE](#) (not to scale).

The beam neutrinos will be provided by the Long-Baseline Neutrino Facility ([LBNF](#)) beamline, the multi-megawatt wide-band neutrino beam planned for Fermilab. It will produce neutrinos travelling in the direction of [SURF](#), with the capability to switch between neutrino and antineutrino mode.

Before arriving to the [FD](#), the neutrino beam meets the [ND](#) complex, which serves as the experiment's control. The design of the [DUNE ND](#) is mainly driven by the needs of the oscillation physics programme, as its main role is to measure the unoscillated neutrino energy spectra. From these we can predict the unoscillated spectra at the [FD](#), which can be compared to the spectra measured at the [FD](#) to extract the oscillation parameters. Additionally, the [ND](#) has a physics programme of its own, including cross section measurements and [BSM](#) physics searches.

The technology chosen for the [FD](#) modules of [DUNE](#) is the liquid Argon time projection chamber ([LArTPC](#)). Its four modules will record neutrino interactions from the accelerator-produced beam arriving at predictable times. As it also aims to record rare and low energy events, like supernovae and solar neutrinos, the [FD](#) requires trigger

3.2. PHYSICS GOALS OF DUNE

Table 3.1: Summary of the two-phased plan for [DUNE](#). Adapted from Ref. [95].

Parameter	Phase I	Phase II	Benefit
FD mass	20 kt fiducial	40 kt fiducial	FD statistics
Beam power	up to 1.2 MW	2.4 MW	FD statistics
ND config.	ND-LAr, TMS, SAND	ND-LAr, ND-GAr, SAND	Systematic constraints

schemes which can deal with both kinds of physics, and also maximum uptime.

[DUNE](#) is planned to be built using a staged approach consisting of two phases, which are summarised in Tab. 3.1. Phase I consists of a [FD](#) with 50% of the total fiducial mass, a reduced version of the [ND](#) complex and a 1.2 MW proton beam. It will be sufficient to achieve some early physics goals, like the determination of the neutrino mass ordering. For its Phase II, [DUNE](#) will feature the full four [FD](#) modules, a more capable [ND](#) and a 2.4 MW proton beam. The physics milestones for the two phases are given in Tab. 3.2, in a staging scenario which assumes that Phase II is completed after six years of operation.

A summary of the [DUNE](#) science programme can be found in the [DUNE FD](#) Technical Design Report ([TDR](#)) Volume I [14]. For a detailed discussion on the two-phased approach the reader is referred to the [DUNE](#) Snowmass 2021 report [95].

3.2 Physics goals of DUNE

As noted in the literature (see for instance Ref. [71] for a review), the parameter space of the neutrino oscillation phenomena within the three-flavour picture is quite constrained by current experimental data. However, there are still crucial open questions, like the mass ordering, the value of δ_{CP} or the θ_{23} octant. One of the main goals of [DUNE](#) is to determine precisely the values of these parameters [96].

To address these questions [DUNE](#) can look to the subdominant oscillation channel $\nu_\mu \rightarrow \nu_e$ ($\bar{\nu}_\mu \rightarrow \bar{\nu}_e$) and study the energy dependence of the ν_e ($\bar{\nu}_e$) appearance probability. When we focus on the antineutrino channel $\bar{\nu}_\mu \rightarrow \bar{\nu}_e$ there is a change in the sign of δ_{CP} , thus introducing [CP](#)-violation. Moreover, due to the absence of positrons in the

CHAPTER 3. THE DEEP UNDERGROUND NEUTRINO EXPERIMENT

Table 3.2: Exposure and time required to achieve the different physics milestones of the two phases. The predictions assume a Phase II staging scenario where **FD** modules 3 and 4 are deployed in years 4 and 6 and both the beam and **ND** are upgraded after 6 years. Adapted from Ref. [95].

Stage	Physics milestone	Exposure (kt-MW-years)	Years (staged)
Phase I	5σ MO ($\delta_{CP} = -\pi/2$)	16	1-2
	5σ MO (100% of the δ_{CP} values)	66	3-5
	3σ CPV ($\delta_{CP} = -\pi/2$)	100	4-6
Phase II	5σ CPV ($\delta_{CP} = -\pi/2$)	334	7-8
	δ_{CP} resolution of 10 degrees ($\delta_{CP} = 0$)	400	8-9
	5σ CPV (50% of the δ_{CP} values)	646	11
	3σ CPV (75% of the δ_{CP} values)	936	14
	$\sin^2(2\theta_{13})$ resolution of 0.004	1079	16

composition of the Earth, there is a sign difference for the matter effect contribution when looking at the antineutrino channel. This asymmetry is proportional to the baseline length L and is sensitive to the sign of Δm_{31}^2 , and thus to the neutrino mass ordering.

Another of the main physics goals of **DUNE** is the search for baryon-number violating processes. Specifically, it will try to answer the question of whether protons are stable or not. There is no symmetry argument that forbids protons from decaying, but its apparent stability seems to suggest that baryon number is conserved [97]. However, proton decay is a usual feature of grand-unified theories, where electromagnetic, weak and strong interactions are unified above a certain energy scale [98].

As the energy deposition scale for these kinds of searches is nearly the same as that for long-baseline neutrino oscillations, **DUNE** will be able to look for them. It has several advantages over other experiments, such as excellent imaging and particle identification, which can be translated into lower backgrounds.

The last of the main objectives of **DUNE** is the detection of neutrinos originated in supernovae explosions, what is called a supernova neutrino burst (**SNB**). These neutrinos carry with them information about the core-collapse process, from the progenitor to the explosion and the remnant; but also may have information about new exotic physics. So far, the only neutrino events ever recorded from such a process were a few dozens of $\bar{\nu}_e$

3.2. PHYSICS GOALS OF DUNE

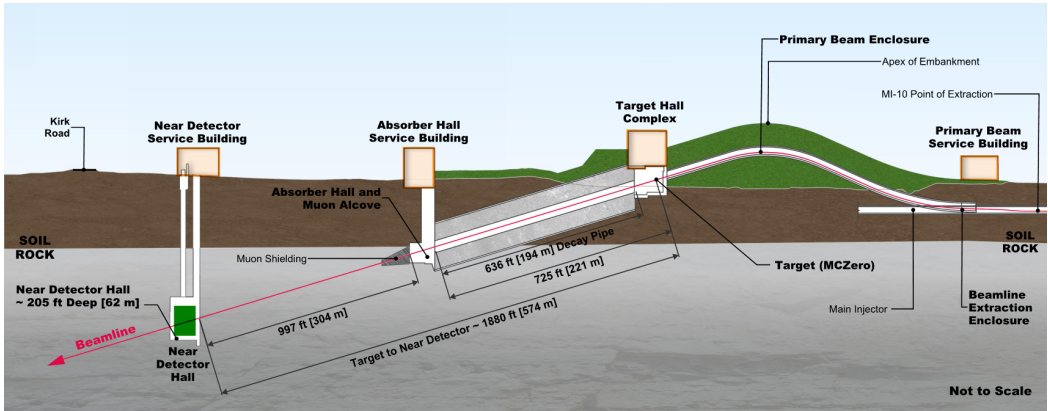


Figure 3.2: Schematic longitudinal section of the LBNF beamline at Fermilab (not to scale). Figure taken from Ref. [101].

events from the 1987A supernova located in the Magellanic Cloud, 50 kpc away from Earth [99, 100].

DUNE aims to collect SNB events. Although these are quite rare, as the expected supernovae explosion events are about one every few decades for our galaxy and Andromeda, the long lifetime of the experiment (around a couple of decades as well) makes it reasonable to expect some. Nowadays the main sensitivity to SNB of most experiments is via the $\bar{\nu}_e$ flux from inverse beta decay. One of the advantages of DUNE is its expected sensitivity to MeV-scale ν_e events, since the dominant channel will be ν_e CC scattering.

Moreover, due to the stringent requirements that the main physics goals set for DUNE, it will also enable searches for all kind of BSM physics. Among other things, DUNE will be able to look for: active-sterile neutrino mixing, non-unitarity of the PMNS matrix, non-standard interactions, Lorentz and CPT violations, neutrino trident production, light-mass DM, boosted DM, and heavy neutral leptons. The reader is referred to the DUNE FD TDR Volume II [96] for a full discussion of the physics scope of DUNE.

CHAPTER 3. THE DEEP UNDERGROUND NEUTRINO EXPERIMENT

3.3 LBNF beamline

The [LBNF](#) project is responsible for producing the neutrino beam for the [DUNE](#) detectors. A detailed discussion of the [LBNF](#) programme can be found in the [DUNE/LBNF CDR](#) Volume III [101].

A schematic diagram of the longitudinal section of the [LBNF](#) beamline is shown in Fig. 3.2. First, a beam of 60 – 120 GeV protons is extracted from the Fermilab Main Injector. This beam is aimed towards the target area, where it collides with a cylindrical graphite target to produce charged pions and kaons.

The diffuse, secondary beam of particles is focused by a pair of magnetic horns. These select the positively charged particles when operated in Forward Horn Current ([FHC](#)) mode, or the negatively charged ones when the current is reversed, also known as Reverse Horn Current ([RHC](#)) mode. The focused secondary beam then enters a 194 m decay pipe where the pions and kaons will predominantly produce $\mu^+\nu_\mu$ pairs when in [FHC](#) mode (or $\mu^-\bar{\nu}_\mu$ in [RHC](#) mode).

At the end of the decay pipe a hadron absorber removes the undecayed hadrons and muons from the beam, which reduces the ν_e ($\bar{\nu}_e$) and $\bar{\nu}_\mu$ (ν_μ) contamination coming from the μ^+ (μ^-) decays. The resulting neutrino flux at the [FD](#) is shown in Fig. 3.3, both for [FHC](#) (left) and [RHC](#) (right) modes. These predictions show the intrinsic $\bar{\nu}_e$ contamination and wrong sign component from wrong sign and neutral meson decays, as well as muons decaying before reaching the absorber.

3.4 Near Detector

To estimate the oscillation parameters we measure the neutrino energy spectra at the [FD](#). This reconstructed energy arises from a convolution of the neutrino flux, cross section, detector response and the oscillation probability. Using theoretical and empirical models to account for the other effects, one can extract the oscillation probability using the measurement. However, these models have associated a number of uncertainties that

3.4. NEAR DETECTOR

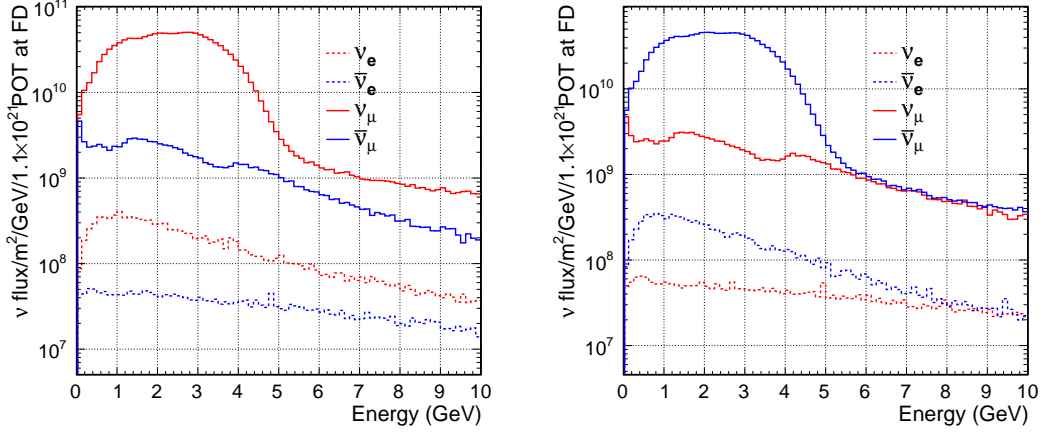


Figure 3.3: Predicted neutrino fluxes at the FD in FHC mode (left panel) and RHC mode (right panel). Figures taken from Ref. [96].

are then propagated to the oscillation parameters.

One of the main roles of the ND is to measure the neutrino interaction rates before the oscillation effects become relevant, i.e. close to the production point. By measuring the ν_μ and ν_e energy spectra, and that of their corresponding antineutrinos, at the ND we can constrain the model uncertainties. A complete cancellation of the uncertainties when taking the ratio between the FD and ND measurements is not possible, as that would require both detectors to have identical designs and the neutrino fluxes seen by them to be the same. Because of the distance, the flux probed by the FD will have a different energy and flavour composition than that at the ND, as neutrinos oscillate and the beam spreads. The differences in the flux also determine the design of the detectors, therefore the ND is limited in its capability to match the FD design.

Nevertheless, having a highly capable ND, DUNE can minimise the systematic uncertainties affecting the observed neutrino energy. The ND data can be used to tune the model parameters by comparison with the prediction. Then, one uses the tuned model to predict the unoscillated FD spectra. Comparing the prediction with the measured spectra it is possible to extract the oscillation parameters.

Additionally, the ND will have a physics programme of its own. In particular, it will measure neutrino cross sections that will then be used to constrain the model used in

CHAPTER 3. THE DEEP UNDERGROUND NEUTRINO EXPERIMENT

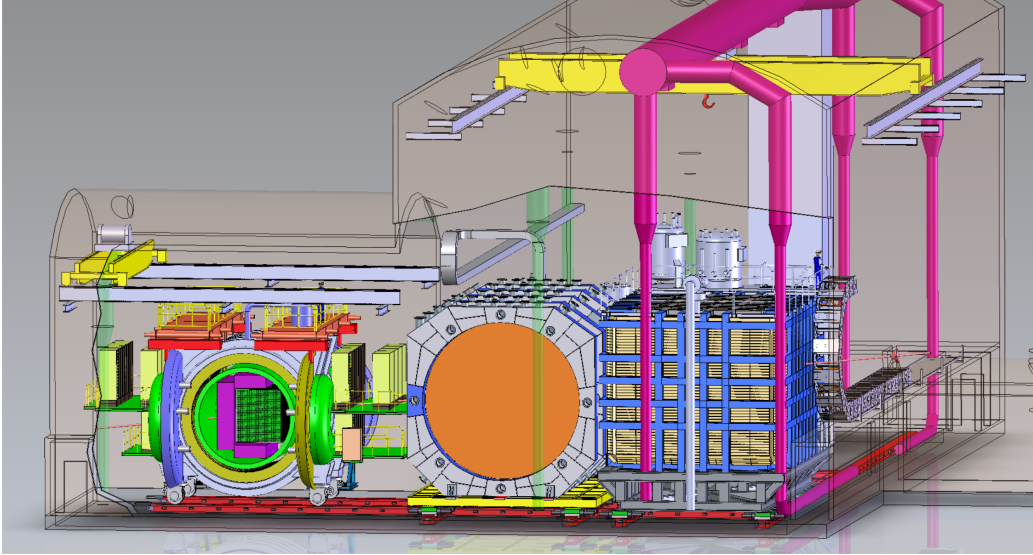


Figure 3.4: Representation of the [ND](#) hall in Phase II, showing the different subcomponents. From right to left, in the direction of the beam, we have [ND-LAr](#), [ND-GAr](#) and [SAND](#). Figure taken from Ref. [102].

the long-baseline oscillation analysis. It will also be used to search for [BSM](#) phenomena such as heavy neutral leptons, dark photons, millicharged particles, etc.

The [DUNE ND](#) can be divided in three main components, a [LArTPC](#) known as [ND-LAr](#), a magnetised muon spectrometer, which will be the Temporary Muon Spectrometer ([TMS](#)) in Phase I and [ND-GAr](#) in Phase II, and the System for on-Axis Neutrino Detection ([SAND](#)). The layout of the Phase II [DUNE ND](#) can be seen in Fig. 3.4. The first two components of the [ND](#) will be able to move off-axis, in what is called the Precision Reaction-Independent Spectrum Measurement ([PRISM](#)) concept. More details on the purpose and design of the [ND](#) can be found in the [DUNE ND](#) Conceptual Design Report ([CDR](#)) [102].

3.4.1 ND-LAr

[ND-LAr](#) is a [LArTPC](#), as the [ND](#) needs a [LAr](#) component to reduce cross section and detector systematic uncertainties in the oscillation analysis. However, its design differs significantly from those proposed for the [FD](#) modules. Because of the high event rates at the [ND](#), approximately 55 neutrino interaction events per 10 μs spill,

3.4. NEAR DETECTOR

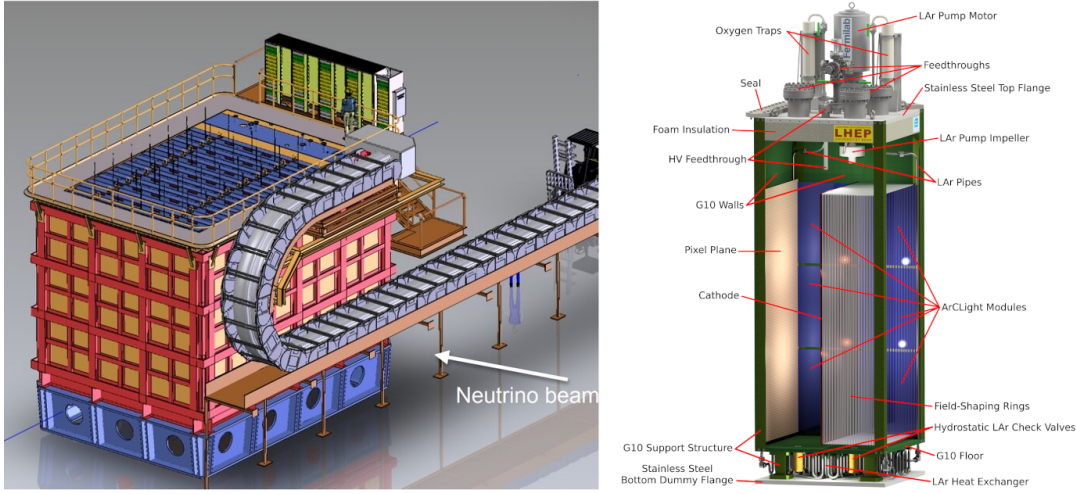


Figure 3.5: Schematic representation of the external components of [ND-LAr](#), including the cryostat and the [PRISM](#) movable system (left) and detailed drawing of one ArgonCube module (right). Figure adapted from Ref. [14].

[ND-LAr](#) will be built in a modular way. Each of the modules, based on the ArgonCube technology, is a fully instrumented, optically isolated [TPC](#) with a pixelated readout [104]. The pixelisation allows for full 3D reconstruction and the optical isolation reduces the problems due to overlapping interactions. Figure 3.5 shows a representation of the external parts of [ND-LAr](#) (left) and a detailed diagram of an ArgonCube module (right).

With a fiducial mass of 67 t and dimensions 7 m (w) \times 3 m (h) \times 5 m (l), [ND-LAr](#) will be able to manage high event rates and contain the hadronic systems from the beam neutrino interactions, but muons with a momentum higher than 0.7 GeV/c will exit the detector.

3.4.2 TMS/ND-GAr

To accurately estimate the neutrino energy, the momentum of the outgoing muons needs to be determined. That is the reason why a muon spectrometer is needed downstream of [ND-LAr](#).

In Phase I that role will be fulfilled by [TMS](#). It is a magnetised sampling calorimeter, with alternating steel and plastic scintillator layers. Figure 3.6 shows a schematic view of the [TMS](#) detector. The magnetic field allows a precise measurement of the sign of the

CHAPTER 3. THE DEEP UNDERGROUND NEUTRINO EXPERIMENT

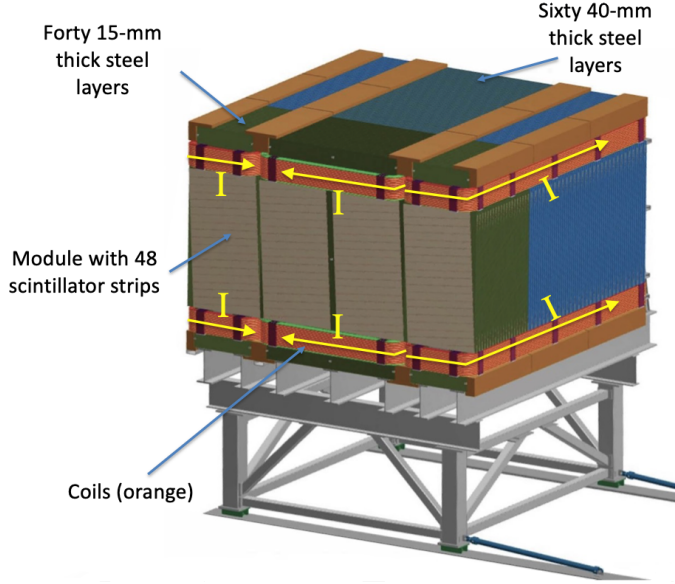


Figure 3.6: Schematic view of the [TMS](#) detector, highlighting its main parts. Figure adapted from Ref. [103].

muon, so one can distinguish between neutrino and antineutrino interactions.

After the Phase II upgrade, [TMS](#) will be replaced with a more capable near detector. The current technology considered is [ND-GAr](#). This detector is a magnetised, high-pressure gaseous argon ([GAr](#)) TPC (often denoted as [HPgTPC](#)) surrounded by an electromagnetic calorimeter ([ECal](#)) and a muon tagger. A cross section of its geometry can be seen in Fig. 3.7. [ND-GAr](#) will be able to measure the momenta of the outgoing muons while also detecting neutrino interactions inside the [GAr](#) volume. This allows [ND-GAr](#) to constrain the systematic uncertainties even further, as it will be able to accurately measure neutrino interactions at low energies thanks to the lower tracking thresholds of the [GAr](#).

3.4.3 PRISM

In general, the observed peak neutrino energy of a neutrino beam decreases as the observation angle with respect to the beam direction increases. This feature has been used in other long-baseline neutrino experiments, like [T2K](#) (2.5° off-axis) and [NOvA](#) (0.8° off-axis), to achieve narrower energy distributions. The [DUNE PRISM](#) concept

3.4. NEAR DETECTOR

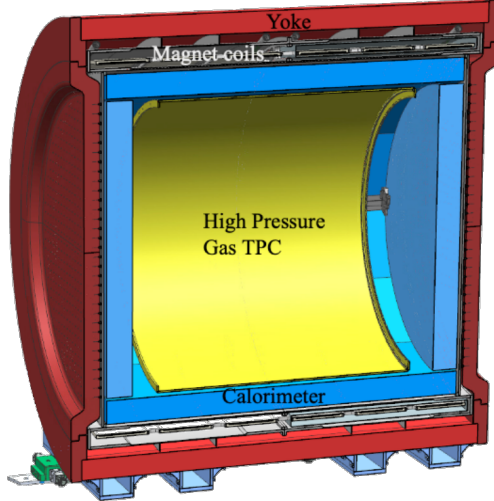


Figure 3.7: Cross section of the [ND-GAr](#) geometry, showing the [HPgTPC](#), [ECal](#) and magnet. Figure adapted from Ref. [105].

exploits this effect using a movable [ND](#). Within [PRISM](#) both [ND-LAr](#) and the muon spectrometer ([TMS](#) in Phase I and [ND-GAr](#) in Phase II) can be moved up to 3.2° off-axis, equivalent to moving the detectors 30.5 m laterally through the [ND](#) hall.

This will allow us to record additional data samples with different energy compositions. Figure 3.8 compares the on-axis muon neutrino flux at the [ND](#) with the fluxes at different off-axis positions. As the off-axis position increases the neutrino flux becomes closer to a monoenergetic beam with a lower peak energy. These samples can be used to perform a data-driven determination of the relation between true and reconstructed neutrino energy, to reduce the dependence on the interaction model. The off-axis samples are linearly combined to produce a narrow Gaussian energy distribution centered on the target true energy. From the combination coefficients one can build a sample of reconstructed neutrino events that will determine the energy mapping.

The [PRISM](#) samples will also be used to form a flux at the [ND](#) location similar in shape to the oscillated flux measured by the [FD](#). This method can be used to extract the oscillation parameters with minimal input from the neutrino interaction model [94].

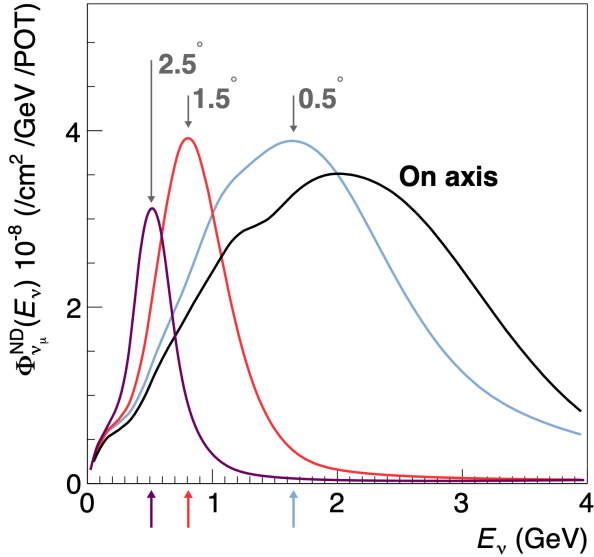


Figure 3.8: Predicted beam muon neutrino flux at the [ND](#) location for different off-axis positions. Figure taken from Ref. [102].

3.4.4 SAND

The role of [SAND](#) is to monitor the beam stability by measuring the on-axis neutrino energy spectra. As the [PRISM](#) programme requires that [ND-LAr](#) and its downstream muon spectrometer spend about half of the time in off-axis positions, it is not possible to monitor the stability of the beam with the movable detectors. Moreover, for the success of [PRISM](#) it is essential to have a stable beam configuration, or at least a quick assessment and modeling of the distortions.

The [SAND](#) detector is magnetised, and features an inner low density tracker, a [LAr](#) target with optical readout and a surrounding sampling calorimeter.

3.5 A More Capable Near Detector

In [DUNE](#) Phase II, a more capable near detector is needed to achieve the ultimate physics goals of the experiment. The current leading proposal for this detector is [ND-GAr](#). As mentioned previously, it will fulfill the role of [TMS](#), measuring the momentum and sign of the charged particles exiting [ND-LAr](#). Additionally, it will be able to measure

3.5. A MORE CAPABLE NEAR DETECTOR

neutrino interactions inside the [HPgTPC](#), achieving lower energy thresholds than those of the [ND](#) and [FD LArTPCs](#). It will also provide a uniform event acceptance, similar to the [FD](#), which could not be achieved by [ND-LAr + TMS](#). By doing so, [ND-GAr](#) will allow to constrain the relevant systematic uncertainties for the [LBL](#) analysis even further. A detailed discussion on the requirements, design, performance and physics of [ND-GAr](#) can be found in the [DUNE ND CDR](#) [102] and the [ND-GAr](#) white paper [106].

3.5.1 Requirements

The primary requirement for [ND-GAr](#) is to measure the momentum and charge of muons from ν_μ and $\bar{\nu}_\mu$ [CC](#) interactions in [ND-LAr](#), in order to measure their energy spectrum. To achieve the sensitivity to the neutrino oscillation parameters described in the [DUNE FD TDR Volume II](#) [96], [ND-GAr](#) should be able to constrain the muon energy within a 1% uncertainty or better.

Another requirement for [ND-GAr](#) is the precise measurement of neutrino interactions on argon for the energies relevant to the neutrino oscillation program. The goal is to constrain the cross section systematic uncertainties in the regions of phase space that are not accessible to [ND-LAr](#). This requires the kinematic acceptance for muons in [ND-GAr](#) to exceed that of [ND-LAr](#), being comparable to that observed in the [FD](#).

[ND-GAr](#) should also be able to help establish the relationship between true and reconstructed energy from neutrino interactions on argon, being sensitive to particles that are not observed or may be misidentified in [ND-LAr](#). In particular, [ND-GAr](#) needs to have low tracking thresholds in order to measure the spectrum of pions and protons produced in final-state interactions ([FSI](#)). It also must be able to accurately measure the pion multiplicity in 1, 2 and 3 pion final states, to inform the pion mass correction in the [LArTPCs](#).

3.5.2 Reference design

The final design of [ND-GAr](#) is still under preparation. However, a preliminary baseline design was in place at the time of the [ND CDR](#). This section summarises the main

CHAPTER 3. THE DEEP UNDERGROUND NEUTRINO EXPERIMENT

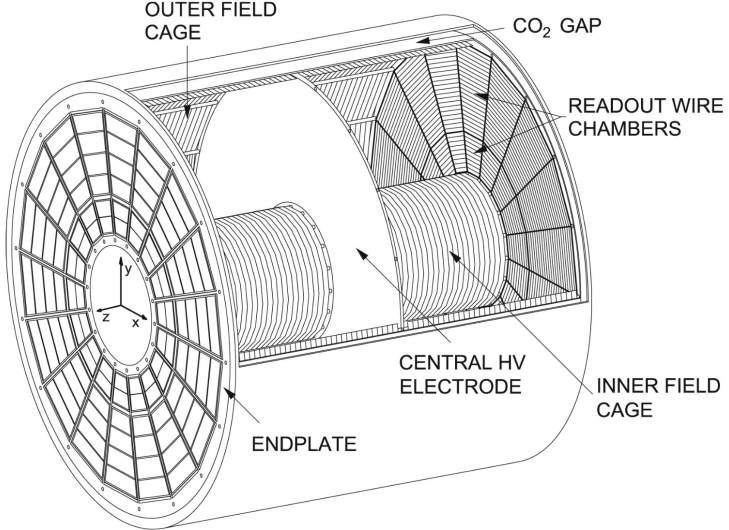


Figure 3.9: Diagram of the [ALICE TPC](#), showing the two drift chambers, inner and outer field cages and readout chambers. Figure taken from Ref. [102].

features of that design, as it is also the one used by default in our simulation. The different options under consideration for the [ND-GAr](#) design are further discussed in the [DUNE](#) Phase II white paper [105].

HPgTPC

The reference design for the [ND-GAr](#) HPgTPC follows closely that of the [ALICE TPC](#) [107]. It is a cylinder with a central high-voltage cathode, generating the electric field for the two drift volumes, with a maximum drift distance of 2.5 m each. The anodes will be instrumented with charge readout chambers. The original design repurposed the multi-wire proportional readout chambers (MWPCs) of [ALICE](#). However, some of the current R&D efforts focus on a gas electron multiplier (GEM) [108] option instead. Figure 3.9 shows a schematic diagram of the [ALICE TPC](#) design. The basic [ND-GAr](#) geometry will resemble this, except for the inner field cage.

[ND-GAr](#) will use a 90:10 molar fraction Ar:CH₄ mixture at 10 bar. With this baseline gas mixture light collection is not possible, as the quenching gas absorbs most of the VUV photons. Additional R&D efforts are underway, to understand if different mixtures allow for the light signal to be used to provide a t_0 while maintaining stable charge gain.

3.5. A MORE CAPABLE NEAR DETECTOR

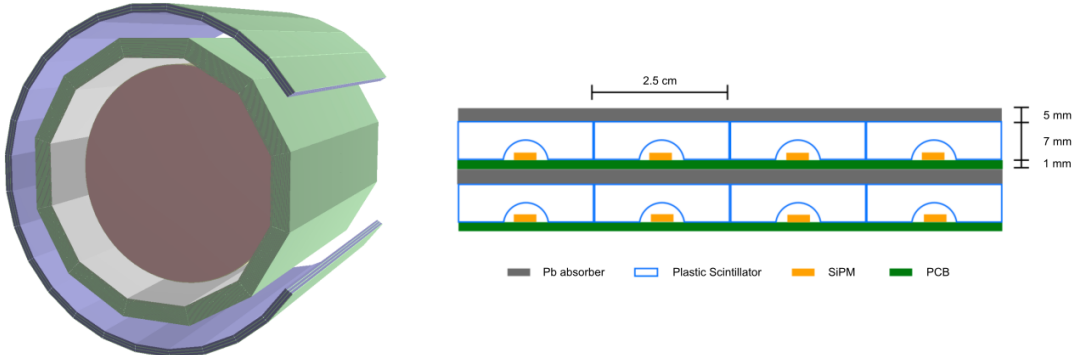


Figure 3.10: View of the 12-sided [ECal](#) barrel and outer muon tagger geometries (left) and layout of the [ECal](#) tile layers for the 5 mm Pb, 7 mm scintillator option (right). Figure adapted from Ref. [102].

ECal

The main role of the [ND-GAr ECal](#) is the calorimetric measurement of the electron energies and the reconstruction of photons, in particular those from neutral pion decays. Also, the [ECal](#) is able to provide a t_0 timestamp for neutrino interactions, by associating its activity to the tracks in the [HPgTPC](#). The [ECal](#) will also be able to perform neutron reconstruction using time-of-flight measurements, and reject external backgrounds thanks to its sub-nanosecond time resolution.

The [ECal](#) design features three independent subdetectors, two end caps at each side and a barrel surrounding the [HPgTPC](#). Each of the detectors is divided in modules, which combine alternating layers of plastic scintillator and absorber material read out by silicon photomultipliers ([SiPMs](#)). The inner scintillator layers consist of $2.5 \times 2.5 \text{ cm}^2$ high-granularity tiles, whereas the outer layers are made out of 4 cm wide cross-strips spanning the whole module length. The current barrel geometry consists of 8 tile layers and 34 strip layers, while the end caps feature 6 and 36 respectively. The scintillator (Pb absorber) layers are 7 mm (5 mm) thick. The 12-sided geometry of the [ECal](#) barrel (left) and the layout of the tile layers (left) can be seen in Fig. 3.10. This design was inspired by the [CALICE](#) analog hadron calorimeter prototype [109].

CHAPTER 3. THE DEEP UNDERGROUND NEUTRINO EXPERIMENT

Magnet

The [ND-GAr](#) magnet design, known as the Solenoid with Partial Yoke ([SPY](#)), consists of two coupled solenoids with an iron return yoke [110]. The idea behind the design is to have a solenoid as thin as possible, as well as a return yoke mass distribution that minimises the material budget between [ND-LAr](#) and [ND-GAr](#). The magnet needs to provide a 0.5 T field in the direction perpendicular to the beam, parallel to the drift electric field. It needs to host the pressure vessel and the surrounding [ECal](#), which points to an inner diameter of ~ 6.4 m.

The solenoid is a single layer coil, based on niobium titanium superconducting Rutherford cable. The total length of the coil is 7.5 m. The bobbin will be split in four segments, grouped in pairs with two identical cryostats connected in series. The iron yoke features an aperture in the upstream side, to minimise the energy loss of the muons coming from [ND-LAr](#). Still, its material will be enough to reduce the magnetic field reaching [SAND](#), and also stop the charged pions produced inside the [HPgTPC](#).

Muon system

The design of the [ND-GAr](#) muon system is still in a preliminary stage. Its role is to distinguish between muons and pions punching through the [ECal](#). This is especially important for wrong-sign determination, to separate the background $\bar{\nu}_\mu$ [CC](#) interactions from neutral current events.

In its current form, the muon system consists of three layers of longitudinal sampling structures. It alternates 10 cm Fe absorber slabs with 2 cm plastic scintillator strips. The transverse granularity required is still under study.

3.5.3 R&D efforts

There are several [ND-GAr](#)-related prototypes, mostly focused on the [TPC](#) charge readout and electronics. The priority is to test the full readout chain, in a high-pressure environment, using a gas mixture with high argon fraction. A detailed summary of these

3.5. A MORE CAPABLE NEAR DETECTOR

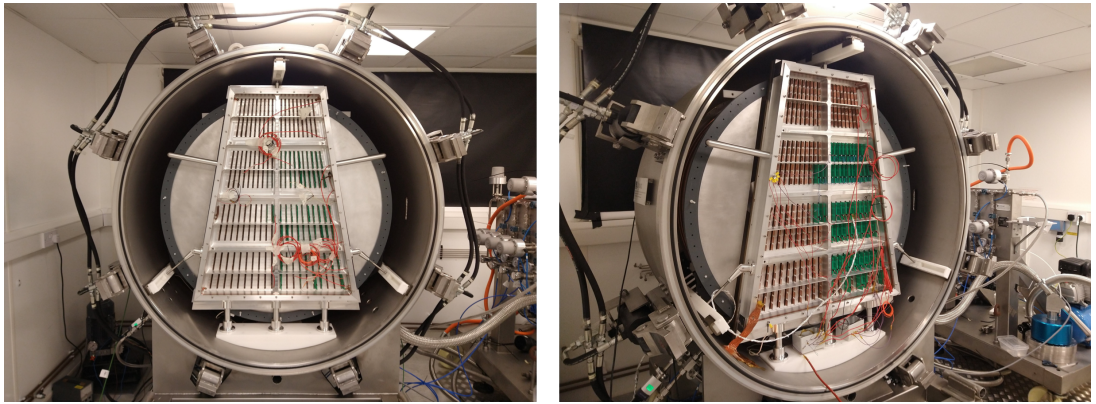


Figure 3.11: Photographs of the **TOAD** pressure vessel at RHUL. The **TPC** is mounted inside the vessel, and the **OROC** is supported by an aluminium frame. Figure taken from Ref. [111].

can be found in the [DUNE Phase II white paper](#) [105].

Multi-Wire Proportional Chambers

As mentioned before, the original **ND-GAr** design repurposes the **MWPCs** of the **ALICE TPC**, which became available after the recent upgrade [112]. These were operated using a 90:10:5 Ne:CO₂:N₂ gas mixture at 1 atm. Therefore, their performance needed to be studied in an argon gas environment at high pressure.

The Gas-argon Operation of **ALICE TPC (GOAT)** test stand tested the **ALICE** readout chambers at high pressure. In particular, it used one of the previously operated **ALICE** inner **MWPCs**, also known as inner readout chambers (**IROC**), in a pressure vessel rated to 10 atm. It measured the gas gain at various pressure points, voltages and gas mixtures.

The Test stand of an Overpressure Argon Detector (**TOAD**) tested an **ALICE** outer **MWPC**, also known as outer readout chamber (**OROC**), up to 5 atm. During its time at RHUL, it was used to study the achievable gas gain of the **OROC** [111]. At the moment, it is being commissioned at Fermilab for a full detector test of the readout electronics and the **DAQ**.

Figure 3.11 shows the interior of the **TOAD** pressure vessel. The **TPC** is mounted inside the vessel on three rails. The back of the **OROC**, supported by an aluminium

CHAPTER 3. THE DEEP UNDERGROUND NEUTRINO EXPERIMENT

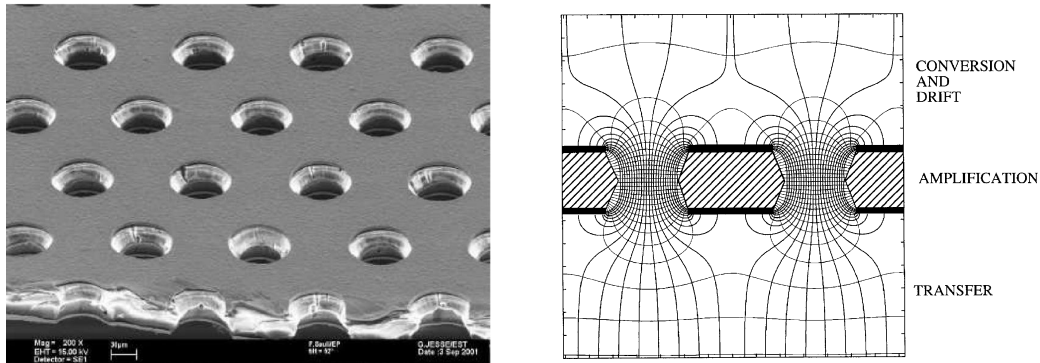


Figure 3.12: Left panel: electron microscope image of a $50\ \mu\text{m}$ thick **GEM** electrode, with hole pitch and diameter of 140 and $70\ \mu\text{m}$, respectively. Right panel: Schematics of a **GEM** electrode cross section, showing the electric field lines around the holes. Figures taken from Ref. [113].

frame, can be seen at the front.

Gas Electron Multiplier

An alternative to the **MWPC** option is the use of **GEMs**. These are a type of micro-pattern detector, where the ionisation electrons passing through the holes in the **GEM** layers are accelerated by a high-intensity electric field. The acceleration causes the electrons to ionise the medium, resulting in an avalanche which increases the signal exponentially [108]. **GEMs** are used in numerous experiments that need a high spatial resolution, like **ALICE** [114] and **CMS** [115] after their upgrades.

Figure 3.12 (left panel) shows an electron microscope picture of a $50\ \mu\text{m}$ thick **GEM** electrode, with a pitch between neighbouring holes of $140\ \mu\text{m}$ and a hole diameter of $70\ \mu\text{m}$. A schematic representation of the cross section of a **GEM** layer is shown in Fig. 3.12 (right panel).

The Gaseous Argon T0 (**GAT0**¹) prototype studies the use of thick **GEMs** made out of glass to achieve optical imaging of the primary ionisation. Using a 10 atm pressure vessel, the goal is to study different argon-based mixtures that allow for a precise t_0 determination.

¹Spanish for cat.

3.6. FAR DETECTOR

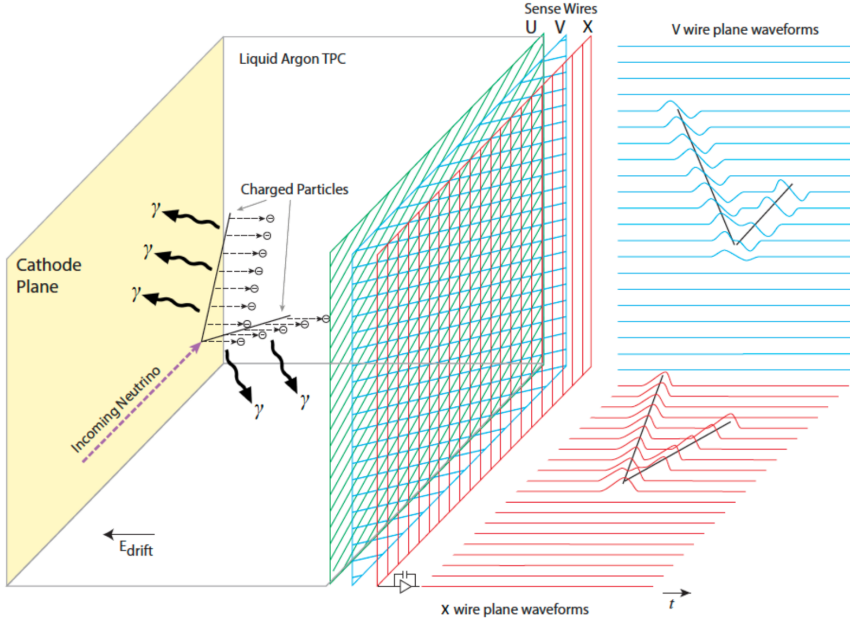


Figure 3.13: Schematic diagram showing the operating principle of a LArTPC with wire readout. Figure taken from Ref. [14].

The GEM Over-pressurized with Reference Gases (GORG²) test stand is currently testing a GEM-based charge readout, using a triple-GEM stack.

3.6 Far Detector

The DUNE FD complex will sit 1300 km away from the beam target and 1.5 km underground at SURF, South Dakota. Two caverns will host the four FD modules, two of them per cavern, each embedded in cryostats of dimensions 18.9 m (w) \times 17.8 m (h) \times 65.8 m (l). A central, smaller cavern will host the cryogenic system.

Three out of the four modules are confirmed to be LArTPC detectors, with a LAr fiducial mass of at least 10 kt each. The first and third FD modules, FD-1 and FD-3, will use a Vertical Drift (VD) technology, whereas the second module, FD-2, will have a Horizontal Drift (HD) direction. The technology for the fourth module is still to be decided. Detailed descriptions of the HD and VD designs can be found in the DUNE FD TDR Volume IV [116] and the DUNE FD VD TDR [117], respectively.

²Persian for wolf.

CHAPTER 3. THE DEEP UNDERGROUND NEUTRINO EXPERIMENT

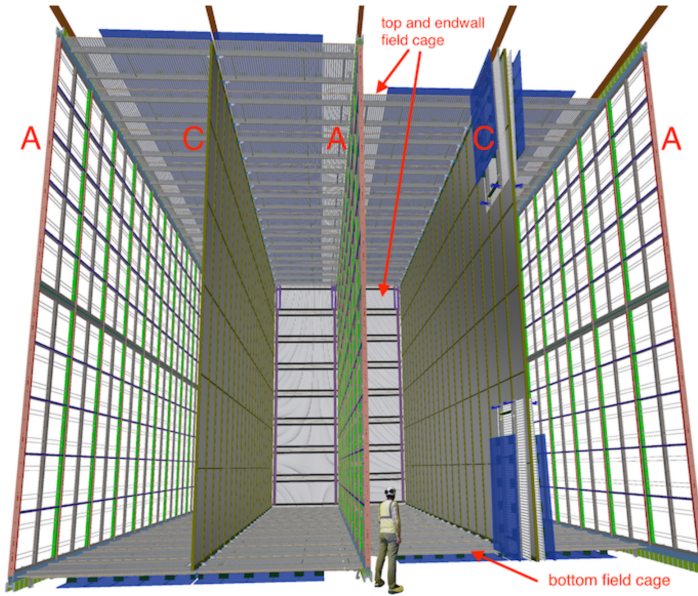


Figure 3.14: Proposed design for the FD-2 module following the HD principle. The labels A and C denote the anode and cathode walls, respectively. Figure taken from Ref. [14].

For each event, with energies ranging from a few MeV to several GeV, these detectors collect both the scintillation light and the ionisation electrons created when the charged particles produced in the neutrino-nucleus interactions ionise the argon nuclei. In both HD and VD designs the characteristic 128 nm scintillation light of argon is collected by a photon detection system (PDS). This light will indicate the time at which electrons start to drift, thus enabling reconstruction over the drift coordinate when compared to the time when the first ionisation electrons arrive to the anode. Reconstruction of the topology in the transverse direction is achieved using the charge readout. Fig. 3.13 illustrates the detection principle described, for the case of a HD detector with a wire readout.

3.6.1 Horizontal Drift

In the HD design the ionisation electrons produced as charged particles traverse the LAr drift horizontally towards the anode planes, due to the effect of an electric field. These anode planes are made out of three layers of wire readout. This design, previously

3.6. FAR DETECTOR

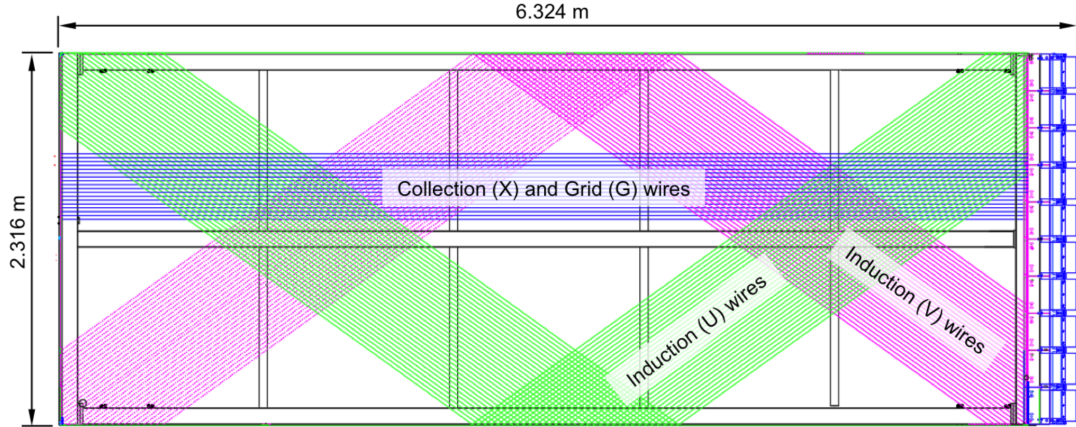


Figure 3.15: Schematic representation of an [APA](#). The black lines represent the [APA](#) steel frame. The green and magenta lines correspond to the direction of the U and V induction wires respectively. The blue lines indicate the direction of the X collection wires and the wire shielding G. Figure taken from Ref. [14].

known as single-phase ([SP](#)), was tested in the ProtoDUNE-[SP](#) detector at CERN. The prototype collected data from a hadron beam and cosmic rays, providing high-quality data sets for calibration and performance studies.

Each [FD HD](#) detector module is divided in four drift regions, with a maximum drift length of 3.5 m, by alternating anode and cathode walls. The surrounding field cage ensures the uniformity of the 500 V/cm horizontal electric field across the drift volumes. The three anode walls, which constitute the charge readout of the detector, are built by stacking anode plane assemblies ([APA](#)), 2 high times 25 wide. The design of the [HD](#) modules is shown in Fig. 3.14.

Each [APA](#) is made of 2560 active wires arranged in three layers, plus an extra grid layer, wrapped around a metal frame. The two induction wire planes, U and V, sit at $\pm 35.7^\circ$ to the vertical on each side of the [APA](#). The collection and shielding plane wires, X and G, run parallel to the vertical direction. The ionisation electrons drift past the induction planes, generating bipolar signals on those wires, and are collected by the collection plane, producing a monopolar positive signal. The spacing between the wires is ~ 5 mm, and it defines the spatial resolution of the [APA](#).

The front-end readout electronics, also called cold electronics as they are immersed

CHAPTER 3. THE DEEP UNDERGROUND NEUTRINO EXPERIMENT

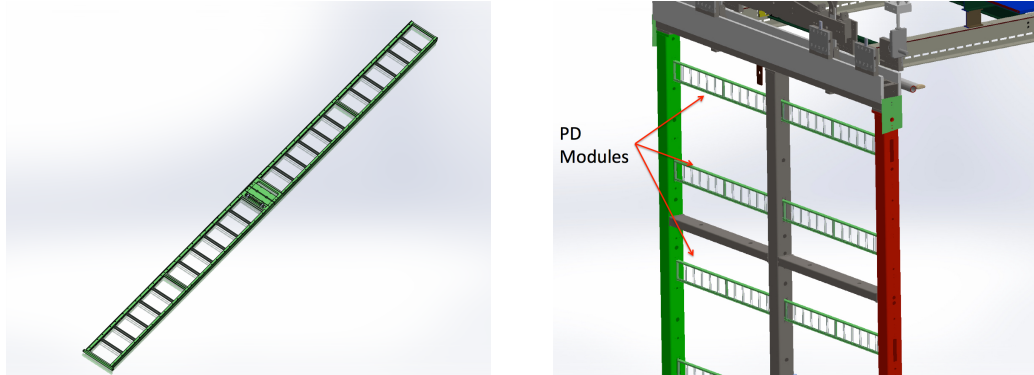


Figure 3.16: A [PDS](#) module containing 24 X-ARAPUCAs (left) and the location of the modules on the [APA](#) frames (right). Figure taken from Ref. [14].

in the [LAr](#), are attached to the top of the up [APAs](#) and the bottom of the down [APAs](#). Mounted on the front-end mother boards we have a series of [ASICs](#) that digitise the signals from the collection and induction planes. Each wire signal goes to a charge-sensitive amplifier, then to a pulse-shaping circuit, and finally to the analogue-to-digital converter. This part of the process happens inside the [LAr](#) to minimise the number of cables penetrating the cryostat. The digitised signals come out finally via a series of high-speed serial links to the warm interface boards ([WIBs](#)), from where the data is sent to the back-end [DAQ](#) through optical fibers.

The [PDS](#) uses modules of X-ARAPUCA devices, mounted on the [APA](#) frames between the wire planes. Each X-ARAPUCA consists of layers of dichroic filter and wavelength-shifter. They shift the [VUV](#) scintillation light into the visible spectrum, sending the visible photons to [SiPM](#) devices. The [PDS](#) modules are $209\text{ cm} \times 12\text{ cm} \times 2\text{ cm}$ bars, containing 24 X-ARAPUCAs. There are 10 of these [PDS](#) modules per [APA](#). Fig. 3.16 shows a [PDS](#) module (left) and the placement of the modules on the [APAs](#) (right).

3.6.2 Vertical Drift

In the [VD](#) case the ionisation electrons will drift vertically until they meet a printed circuit board-based ([PCB](#)) readout plane. It is based on the original dual-phase ([DP](#)) design deployed at CERN, in the detector known as ProtoDUNE-[DP](#), which used a vertical drift design with an additional amplification of the ionisation electrons using a

3.6. FAR DETECTOR

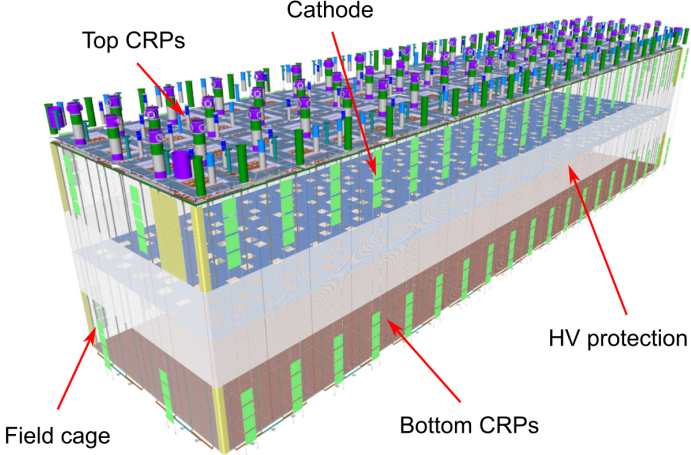


Figure 3.17: Proposed design for the FD-1 and FD-3 modules following the VD principle. Figure adapted from Ref. [117].

GAir layer above the liquid phase. The VD module incorporates the positive features of the DP design without the complications of having the LAr-GAir interface.

The current design of the FD VD module consists of two drift chambers with a maximum drift distance of 6.5 m. A cathode plane splits the detector volume perpendicular to the drift direction, while the two anode planes are connected to the bottom and top walls of the detector. The layout of a VD module is shown in Fig. 3.17. Compared with the HD design, the VD option offers a slightly larger instrumented volume and a more cost-effective solution for the charge readout.

As in the HD design, each drift volume features a 500 V/cm electric field and a field cage that ensures its uniformity. The anode planes are arrays of $3.4\text{ m} \times 3\text{ m}$ charge-readout planes (CRPs). These are formed by a pair of charge-readout units (CRUs), which are built from two double-sided perforated PCBs, with their perforations aligned. The perforations allow the drift electrons to pass between the layers.

The PCB face opposite to the cathode has a copper guard plane which acts as shielding, while its reverse face is etched with electrode strips forming the first induction plane. The outer PCB has electrode strips on both faces, the ones facing the inner PCB form the second induction plane, while the outermost ones form the collection plane. Fig.

CHAPTER 3. THE DEEP UNDERGROUND NEUTRINO EXPERIMENT

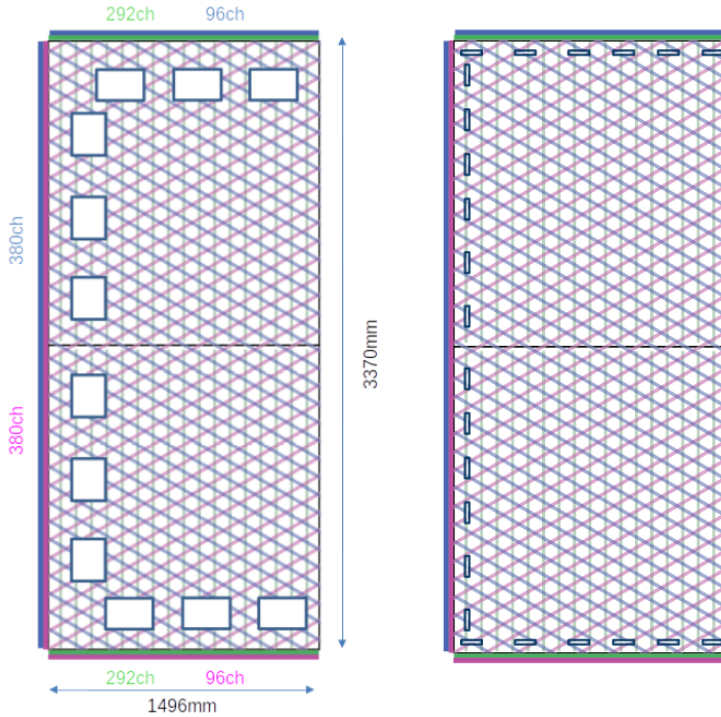


Figure 3.18: Schematic representation of the electrode strip configuration for a top (left) and bottom (right) CRU. Figure taken from Ref. [117].

3.18 shows the layout of the electrode strips for the top (left) and bottom (right) CRUs. The magenta and blue lines represent the first and second induction planes, respectively, and the green lines correspond to the collection plane.

The PDS in the VD module will use the same X-ARAPUCA technology developed for the HD design. The plan is to place the PDS modules on the cryostat walls and on the cathode, in order to maximise the photon yield.

3.6.3 FD Data Acquisition System

The data acquisition (DAQ) system receives, processes and stores data from the detector modules. In the case of DUNE, the DAQ architecture is designed to work for all FD modules interchangeably, except some aspects of the upstream part which may depend on the specific module technology.

The enormous sample rate and the number of channels in the TPC and PDS readouts will produce a very large volume of data. These pose really strong requirements and

3.6. FAR DETECTOR

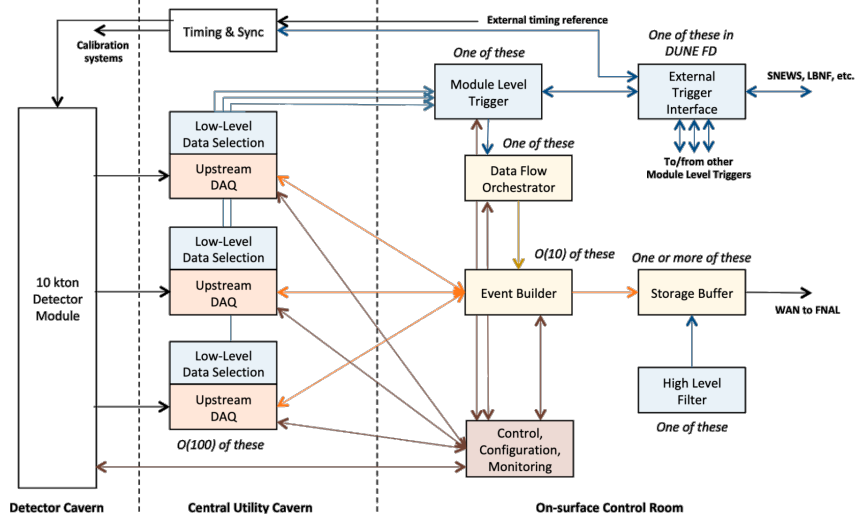


Figure 3.19: Detailed diagram of the [DUNE FD DAQ](#) system. Figure taken from Ref. [116].

challenges to the [DUNE FD DAQ](#) architecture. It will be required to read out data of the order of ten thousand or more channels at rates of a few MHz. To cope with the huge data volume, segmented readouts and compression algorithms are used to reduce the data rate to manageable levels.

The [DAQ](#) system of the [DUNE FD](#) is composed of five different subsystems. The first one is the upstream [DAQ](#), which receives the raw data from the detector, buffers it and performs some low-level pre-processing. The minimally processed data is then fed into a hierarchical data selection system, which then performs a module level trigger decision. In case of a positive decision, a trigger command is produced and executed by the data flow orchestrator, located in the back-end ([BE](#)) [DAQ](#) subsystem. Subsequently, the [DAQ BE](#) retrieves the relevant data from the buffers located in the upstream [DAQ](#), adds all the data into a cohesive record, and saves it to permanent storage. Watching over all the other subsystems we also have the control, configuration and monitoring subsystem and the time and synchronization subsystem. Figure 3.19 shows a schematic diagram of the [DAQ](#) system, showing the different subsystems and their relations.

A notorious challenge for the [DUNE DAQ](#) system comes from its broad physics goals. We must be prepared to process events spanning a wide range of time windows, from

CHAPTER 3. THE DEEP UNDERGROUND NEUTRINO EXPERIMENT

5 ms in the case of beam and cosmic neutrinos and nucleon decay events, to 100 s in the case of [SNBs](#). This requires a continuous readout of the detector modules. Moreover, because of the off-beam measurements, we need to ensure the capabilities of online data processing and self-triggering. Taking this into account, together with the technical constraints, the [DUNE FD DAQ](#) faces a series of challenges: it needs to be fault tolerant and redundant to reduce downtime, accommodate new components while it keeps serving the operational modules, have large upstream buffers to handle [SNB](#) physics, be able to support a wide range of readout windows, and reduce the throughput of data to permanent storage to be at most 30 PB/year.

4

Matched Filter approach to Trigger

Primitives

It is a capital mistake to theorize before one has data. Insensibly one begins to twist facts to suit theories, instead of theories to suit facts.

– Arthur Conan Doyle, *A scandal in Bohemia*

The **DAQ** system is responsible for the data that will be collected in the **DUNE FD**. Therefore, it has the capability of either expanding or limiting our physics reach, depending on its specifications. This is important for the low energy physics programme, as it requires more sensitive and reliable methods to pick up the relevant signals.

In this Chapter, I present a novel method to improve the sensitivity of the **DUNE FD** by enhancing the production of hits in the online processing. This is possible thanks to a more efficient filtering strategy, the matched filter, which benefits the induction channels of the detector.

4.1 Motivation

The lowest-level objects that are formed within the **DUNE FD DAQ** system are the so-called trigger primitives (**TPs**) [118]. These represent the hits on a channel, and are used as input to the rest of the **DAQ** trigger chain. The **TPs** are formed in the hit finder chain, shown in Fig. 4.1. This chain takes the raw **ADC** data from the detector, removes the constant pedestal of the signal using a dynamical median estimation method,

CHAPTER 4. MATCHED FILTER APPROACH TO TRIGGER PRIMITIVES

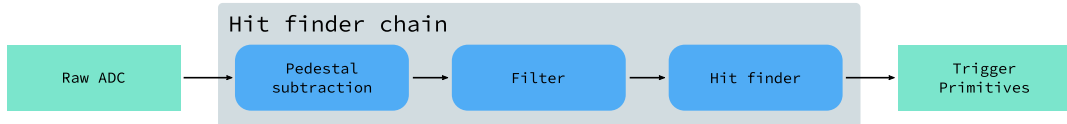


Figure 4.1: Schematic representation of the Trigger Primitive Generation chain in the DUNE FD.

applies a filter to the waveform, and tries to find peaks over a certain threshold. These peaks form the **TPs**, which contain information such as the start and end times over the threshold, the maximum **ADC** value, and the corresponding **ADC** integral. Currently, there are two implementations of the hit finder chain, one firmware-based and other software-based.

The filter implemented in the firmware of the upstream **DUNE FD DAQ** is a 32nd-order low-pass finite impulse response (**FIR**) filter. The output of such filter for a discrete system can be written as:

$$y[i] = \sum_{j=0}^N h[i]x[i-j], \quad (4.1)$$

where N is the order of the filter, y is the output sequence, x is the input sequence and h is the set of filter coefficients. The current implementation in the firmware uses a set of 16 non-zero integer coefficients. For the software case, only a 5th-order filter is used, as the filtering is the most CPU-expensive part of the software hit finder.

Filtering is a vital step in the hit finder chain. It helps suppress the noise and enhances the signal peaks with respect to the noiseless baseline. A good filtering strategy allows us to use lower thresholds when forming the **TPs**, thus increasing the sensitivity of our detector to low energy physics events. In such events, the hits produced by the ionisation electrons tend to have lower amplitudes than those of interest to the **LBL** physics programme of the **DUNE** experiment.

This is particularly important for the induction planes. In general, signal peaks in the induction channels have smaller amplitudes than the ones in the collection plane. This, together with the fact that the pulse shapes are bipolar, reduces our capacity to

4.1. MOTIVATION

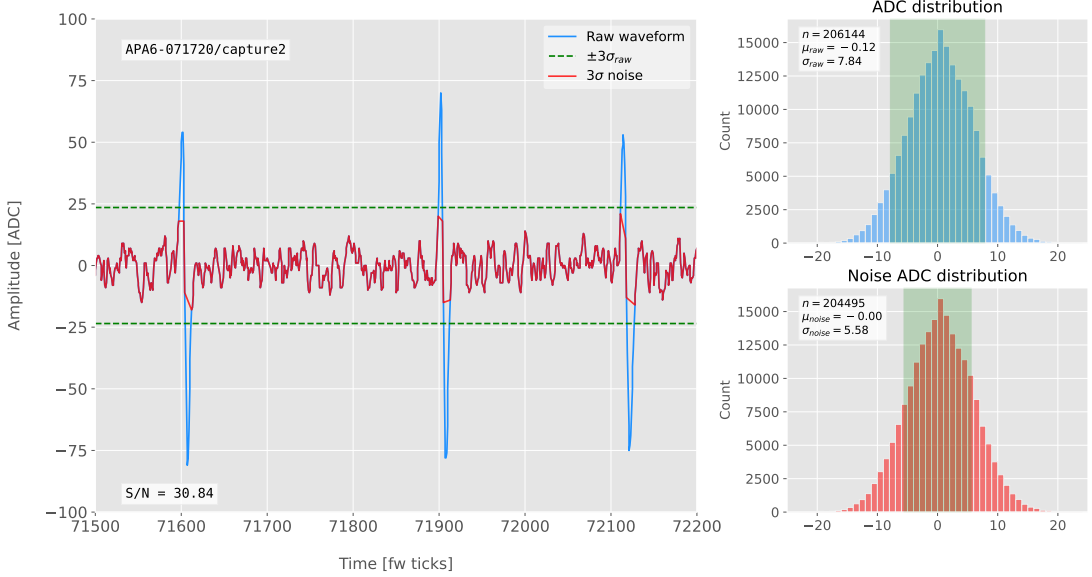


Figure 4.2: Left panel: Zoomed unfiltered waveform corresponding to channel 7840 from the ProtoDUNE-SP raw data capture `felix-2020-07-17-21:31:44` (blue line). The green dashed lines mark the region $\pm 3\sigma_{raw}$. The resulting noise waveform is also shown (red line). Top right panel: **ADC** distribution for channel 7840, where the green shaded region represents $\pm \sigma_{raw}$. Bottom right panel: noise **ADC** distribution for channel 7840, where the green shaded region represents $\pm \sigma_{noise}$.

detect the hits on these channels. The inefficiency of detecting **TPs** in the induction planes (denoted as U and V planes) leads trigger algorithms to focus mainly on the **TPs** from the collection plane (so-called X plane). As a result, the possibility of making trigger decisions based on the coincidence of **TPs** across the three readout planes remains nowadays unexploited in **DUNE**. This will be beneficial for low energy events, as it adds redundancy to the algorithms, as well as for other physics that requires online directionality information, like the supernova pointing.

A possible improvement of the current hit finder chain may require optimising the existing filter or choosing a new filter implementation. A filter strategy which benefits the induction signals may be able to enhance the detection efficiency of **TPs** from the induction planes, and ideally make it comparable to that of the collection plane.

The goal is to implement a better **FIR** filter and to evaluate its performance relative to the current one. To do so, I need to take into account the limitations of the firmware: the **FIR** filter shall have maximum 32 coefficients (so-called taps) whose values are 12-bit

CHAPTER 4. MATCHED FILTER APPROACH TO TRIGGER PRIMITIVES

unsigned integers. Although it is technically possible to include non-integer coefficients, it would be a technical challenge. For instance, in the **HD** design there are 40 **FIR** instances per **APA**, as there are 4 **FIR** blocks per optical link and 10 optical links per **APA**. Therefore, the impact of increasing the complexity of the filter will be amplified forty times in the **FPGA** load. With these restrictions, the task is to provide a set of 32 coefficients which yield an optimal filter performance for the induction channels. A solution compatible with the software hit finder implementation is not considered, due to its current limitations concerning the filtering stage.

4.2 Signal-to-noise ratio definition

In the following, I use the signal-to-noise ratio (**S/N**) as a measure of the **FIR** filter performance. The **S/N** metrics allow us to compare different filter implementations, and serve as a basis for more detailed studies presented later in this Chapter. Here, I demonstrate how to extract its value for a set of ProtoDUNE-**SP** data. Specifically, I use the **ADC** capture `felix-2020-07-17-21:31:44`, a raw data capture taken for firmware validation purposes. I define the **S/N** of a channel as the height of the signal peaks relative to the size of the noise. To quantify this, I first estimate the standard deviation of the **ADC** data for each channel, σ_{ADC} . Then, I define the corresponding noise waveform to be the **ADC** values in the range $\pm 3 \sigma_{\text{ADC}}$. From this new noise data I compute the mean and standard deviation, μ_{noise} and σ_{noise} , so I can write the **S/N** for any given channel as:

$$\text{S/N} = \frac{\max [\text{ADC}] - \mu_{\text{noise}}}{\sigma_{\text{noise}}}, \quad (4.2)$$

where $\max [\text{ADC}]$ is simply the maximum **ADC** value found in the corresponding channel.

As an example, I apply this definition of the **S/N** to a waveform from one of the channels of the data capture. Figure 4.2 shows a zoomed region of the waveform corresponding to channel 7840 (blue line), where one can clearly see three signal peaks

4.2. SIGNAL-TO-NOISE RATIO DEFINITION

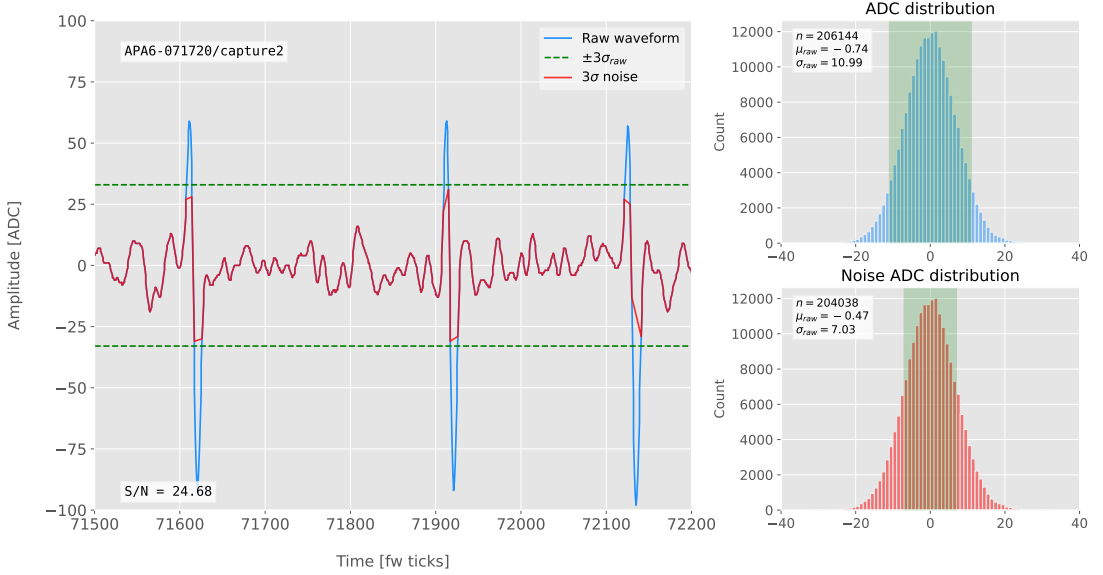


Figure 4.3: Left panel: Zoomed filtered waveform corresponding to channel 7840 from the ProtoDUNE-SP raw data capture `felix-2020-07-17-21:31:44` (blue line). The filter used was the current implementation of the low-pass FIR filter in the firmware. The green dashed lines mark the region $\pm 3\sigma_{raw}$. The resulting noise waveform is also shown (red line). Top right panel: ADC distribution for channel 7840 after filtering, where the green shaded region represents $\pm \sigma_{raw}$. Bottom right panel: noise ADC distribution for channel 7840 after filtering, where the green shaded region represents $\pm \sigma_{noise}$.

and continuous additive noise¹. I estimated the standard deviation of this raw waveform to be $\sigma_{raw} = 7.84$ ADC, and from this I am able to define the noise waveform (red line) as the ADC values in the range ± 23.52 ADC. This way, I obtain $\mu_{noise} = 0.01$ ADC and $\sigma_{noise} = 5.58$ ADC, which gives $S/N = 30.84$.

I repeat this calculation now for the corresponding filtered waveform, using the current firmware FIR filter. Figure 4.3 shows the same time window for the filtered waveform from channel 7840 (blue line). In this case, the standard deviation of the waveform is larger than before, giving $\sigma_{raw} = 10.99$ ADC. The noise waveform (red line) is formed by selecting the ADC values in the ± 32.91 ADC range, which gives $\mu_{noise} = -0.47$ ADC and $\sigma_{noise} = 7.03$ ADC. Finally, one obtains $S/N = 24.68$. Notice that the value of the S/N decreases after the filtering. Clearly, one can see that the noise baseline has increased by a factor of 1.35 when we applied the FIR filter, and at the

¹There are actually 6 peaks, 3 positive and 3 negative, but, because by design for induction channels the expected signal pulse shapes are bipolar, we treat them as a collection of 3 individual signals.

CHAPTER 4. MATCHED FILTER APPROACH TO TRIGGER PRIMITIVES

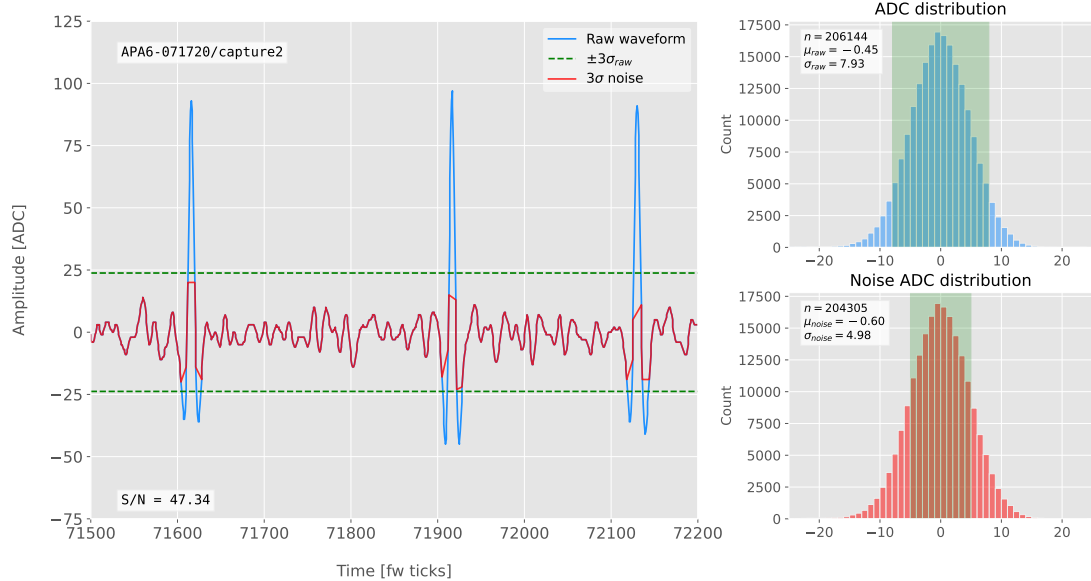


Figure 4.4: Left panel: Zoomed match filtered waveform corresponding to channel 7840 from the ProtoDUNE-SP raw data capture `felix-2020-07-17-21:31:44` (blue line). The filter used was directly extracted from the data, being the 32 values around the first peak in the original waveform. The green dashed lines mark the region $\pm 3\sigma_{raw}$. The resulting noise waveform is also shown (red line). Top right panel: ADC distribution for channel 7840 after match filtering, where the green shaded region represents $\pm \sigma_{raw}$. Bottom right panel: noise ADC distribution for channel 7840 after match filtering, where the green shaded region represents $\pm \sigma_{noise}$

same time the amplitude of the signal peaks has remained almost unchanged, leading to this poorer S/N value.

4.3 Matched filters

In the context of signal processing, a matched filter is the optimal linear filter for maximising the S/N in the presence of additive noise. It is obtained by convolving a conjugated time-reversed known template with an unknown signal to detect the presence of the template in the signal [119].

For a discrete signal, assuming that the additive noise is Gaussian, the impulse-response vector associated to the matched filter is given by:

$$h \propto s, \quad (4.3)$$

4.3. MATCHED FILTERS

where s is a reversed signal template sequence of length N equal to the order of the filter. A detailed discussion on the derivation of this formula can be found in App. A.2.

To test whether this choice of filter is appropriate one needs to choose a signal template. As an example of how a matched filter would affect our signal, I simply took the matched filter coefficients to be the 32 ADC values around a signal peak present in the data. In Fig. 4.4 (left panel) I plotted a zoomed region for channel 7840 in the raw data capture `felix-2020-07-17-21:31:44`, after applying the matched filter described before (blue line). When compared to the raw and FIR filtered case (see Figs. 4.2 and 4.3), after applying the matched filter the standard deviation of the noise waveform (red line) decreases and at the same time the signal peaks are enhanced. This leads to an improvement of the S/N by a factor of 1.92 when compared to the raw waveform.

To obtain the matched filter that is more suitable for our data, I explored different configurations of signal templates. I parametrise the signal using the bipolar function:

$$f(x) = -A(x + \delta) e^{-x^2/\sigma^2}, \quad (4.4)$$

where the parameter δ controls the asymmetry between the positive and negative peaks and σ controls their width. The amplitude parameter A is set such that it keeps the height of the biggest peak to be less than 200 ADC in absolute value.

As this parametrisation is only adequate for bipolar signals, I will focus exclusively on the induction channels. Also, to achieve the best possible performance, I optimise the coefficients for the U and V planes separately. However, as I will discuss, the differences are not very pronounced. In case it is not technically possible to separate channels in the firmware according to the plane they are coming from and use different sets of filter coefficients for them, we can just find a common set of coefficients. In such case, I do not expect the results to change drastically.

Figure 4.5 presents the results of the parameter scan, for channels in the induction planes U (left panel) and V (right panel). For each configuration of σ and δ the resulting matched filter was applied to all channels in the corresponding plane within the data

CHAPTER 4. MATCHED FILTER APPROACH TO TRIGGER PRIMITIVES

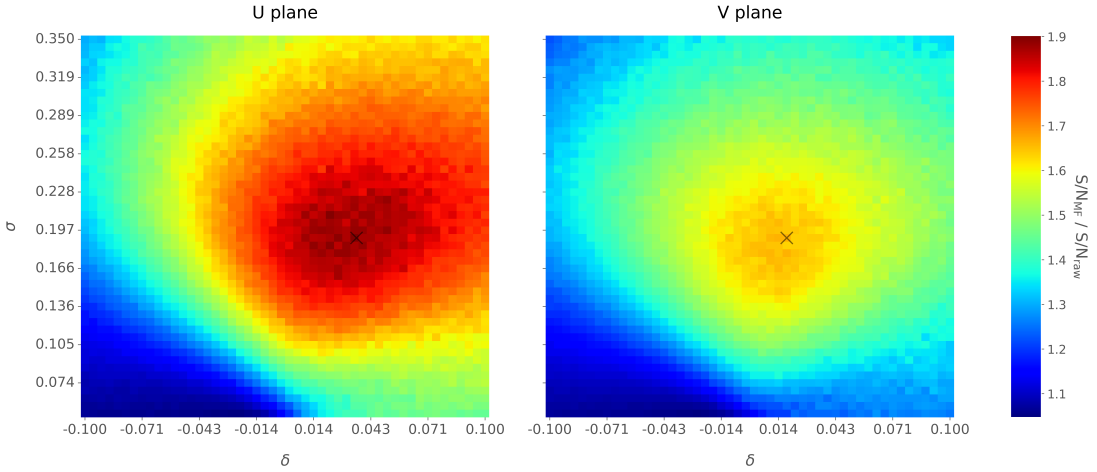


Figure 4.5: Relative change in the S/N for the ProtoDUNE-SP raw data capture `felix-2020-07-17-21:31:44` for different values of δ and σ from the matched filter parametrisation in Eq. (4.4). The black crosses in both panels denote the location of the maximum ratio value.

capture `felix-2020-07-17-21:31:44`. The change in S/N is computed with respect to the raw waveforms, and then the mean value for all channels is kept as a score for each filter. One can see that the improvements obtained for the U plane are in general higher than the ones for the V plane. However, these ratios are substantially higher than the ones obtained for the low-pass FIR filters studies shown in App. A.1. For the optimal configurations, I attained improvements up to a factor of 1.85 for the U plane and 1.65 for the V plane.

The sets of optimal matched filter coefficients were obtained for the parameters $\delta = 0.035$, $\sigma = 0.191$ for the U plane and $\delta = 0.018$, $\sigma = 0.191$ for the V plane. I show these two sets of coefficients in Fig. 4.6 (left panel). Figure 4.6 (right panel) shows the distribution of the relative S/N change after the optimal matched filters for the U and V were applied to the corresponding channels in the raw data capture `felix-2020-07-17-21:31:44`. As mentioned before, the mean improvement achieved for the U plane channels is slightly higher than the one for the V channels. Note, however, that the spread of the distribution for the V plane is smaller than the one for the U plane.

Overall, one can see that the improvements on the S/N are much more significant in

4.4. MONTE CARLO STUDIES

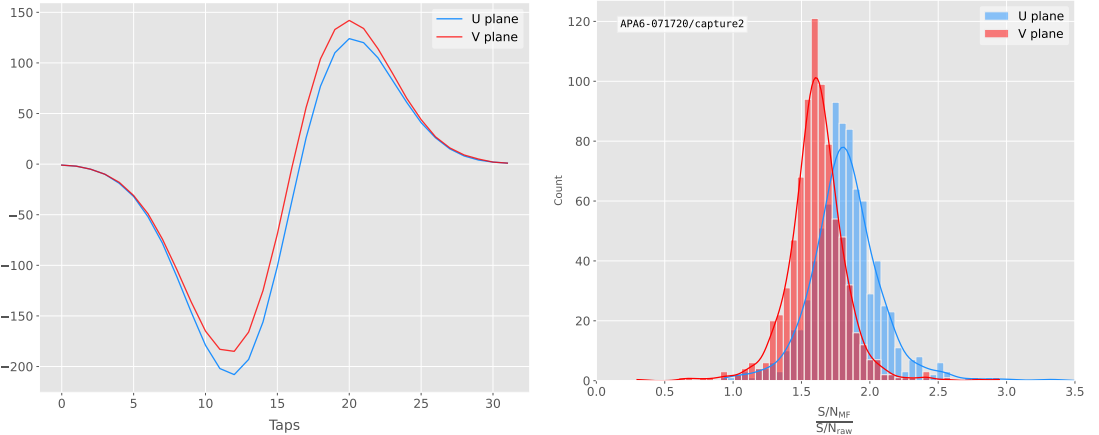


Figure 4.6: Left panel: Optimal matched filter coefficients for the U (blue line) and V (red line) planes. The filters were computed with the parametrisation in Eq. (4.4) for the parameter values $\delta = 0.035$, $\sigma = 0.191$ and $\delta = 0.018$, $\sigma = 0.191$, respectively. Right panel: Distribution of the relative change of the S/N on the two induction wire planes from the ProtoDUNE-SP raw data capture `felix-2020-07-17-21:31:44` after their respective optimal matched filters are applied.

the case of the matched filter than they were for the low-pass **FIR** filters, described in App. A.1. The analysis of the raw data captures from ProtoDUNE-SP suggests that matched filters increase the **S/N** of induction channels by a factor of 1.5 more than the optimal low-pass **FIR** filters.

Although these results are by themselves great points in favour of the matched filter, more studies are needed to completely assess the robustness of this approach. I proceeded then to test the matched filter with simulated data samples.

4.4 Monte Carlo studies

To further test the matched filter, the next step is to generate and process data samples using LArSoft [120], the simulation and reconstruction software of the **DUNE FD**. In this way, one can control the particle content of the samples, the orientation of the tracks and their energy, and therefore see how the matched filter behaves in various situations.

To begin with, I prepared different monoenergetic and isotropic samples containing a single particle per event. Each sample contains a different particle species, namely

CHAPTER 4. MATCHED FILTER APPROACH TO TRIGGER PRIMITIVES

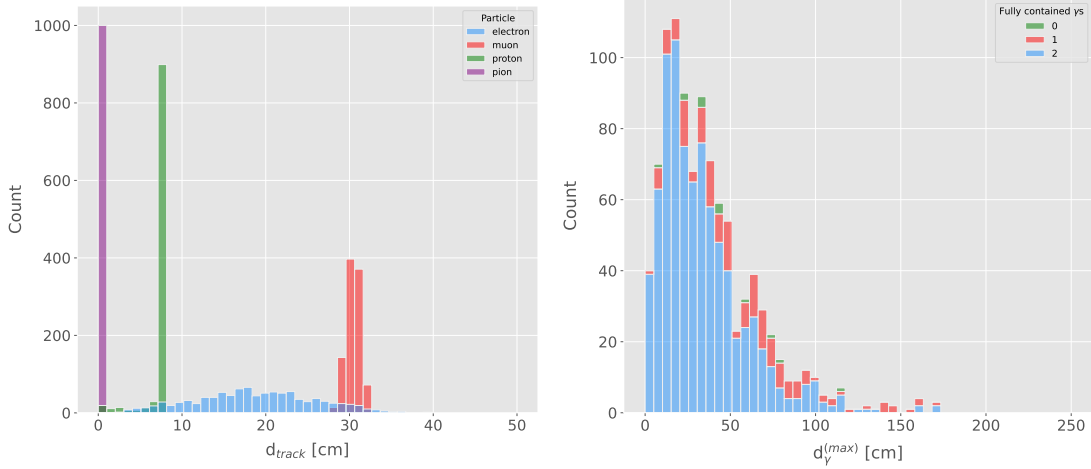


Figure 4.7: Left panel: distributions of the particles track length in the liquid argon for the generated $E_k = 100$ MeV monoenergetic samples, electrons (blue), muons (red), protons (green) and neutral pions (purple). Right panel: distribution of the length of the longest photon in the neutral pion sample after the decay process $\pi^0 \rightarrow \gamma\gamma$.

electrons, muons, protons and neutral pions, all with a kinetic energy of $E_k = 100$ MeV. I chose these because of the fairly different topologies they generate in the liquid argon, ranging from shower-like to track-like.

The events were generated with the single particle gun, and the [Geant4](#) [121–123] stage of the LArSoft simulation was run with the standard configuration for the [DUNE FD HD](#) design.

For simplicity, I restricted the particles to start drifting in a single [TPC](#) volume², so I focus exclusively on the signals coming from one [APA](#). The chosen kinetic energy for all the particles is $E_k = 100$ MeV, as this produce tracks which are typically contained in one [TPC](#) volume. Figure 4.7 (left panel) shows the distributions of the track lengths in the liquid argon of all generated particles with $E_k = 100$ MeV. One can see that, in the case of the track-like particles (i.e. muons and protons), their length distributions are quite sharp and centered at relatively low distances (30 and 8 cm, respectively). For electrons, the distribution is quite broad but it does not extend past ~ 30 cm. The case of the neutral pions can be misleading. As they decay promptly, the track length associated to the true [MC](#) particle is always < 1 cm. In Fig. 4.7 (right panel) I show

²A [TPC](#) volume is defined as the drift region between a single [APA](#) and the cathode.

4.4. MONTE CARLO STUDIES

the effective length distribution of the longest photon after the pion decays as $\pi^0 \rightarrow \gamma\gamma$, highlighting the number of fully contained photons in the **TPC** volume per event (either zero, one, or two). One can see that the vast majority of events have both photons contained in the **TPC** volume, whereas a negligible fraction of them have none. However, for the sake of caution, I keep only the pion events with both photons contained.

The next step is to process the sample through the detector simulation. To make adequate estimations of the noise levels, one needs to turn off the default zero-suppression of the waveforms produced by the simulation. At this stage I am only interested in the waveforms with noise added, so I keep the noise addition option as true in the configuration. However, for studies related to the hit finder performance one also needs to store the noiseless waveforms, to retrieve the truth information of the hits. I will discuss this approach next.

To reduce the amount of data to process, I use the information from the **Geant4** step of the simulation to select only the active channels, i.e. the channels where some ionisation electrons arrived. Moreover, I only extract the waveforms from one **APA** and exclusively those coming from induction channels. Finally, I also store the truth values for the orientation of the tracks and the energies of the particles to use them in the analysis.

Then, I apply the matched filter to the resulting waveforms. The coefficients used are those that I found using the ProtoDUNE-**SP** data samples. The **S/N** of both the raw and filtered signals is also computed.

The reported values of the **S/N** of each event are obtained taking the average of the **S/N** over all the active channels in the event. That is, if a certain event has N_{chan} active channels the two **S/N** values, both for the raw and filtered waveforms, are computed as:

$$(S/N_{fir})_{event} = \frac{\sum_{i=0}^{N_{chan}} (S/N_{fir})_i}{N_{chan}},$$

$$(S/N_{raw})_{event} = \frac{\sum_{i=0}^{N_{chan}} (S/N_{raw})_i}{N_{chan}}.$$
(4.5)

However, for the ratio of the raw and filtered **S/N** (what I call the relative **S/N** change)

CHAPTER 4. MATCHED FILTER APPROACH TO TRIGGER PRIMITIVES

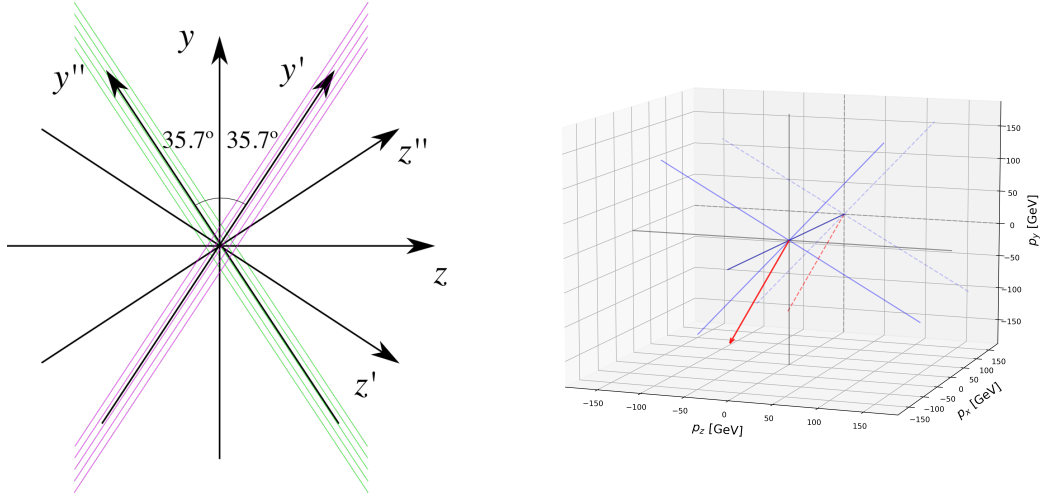


Figure 4.8: Left panel: schematic representation of the two new rotated reference frames used in this analysis (denoted as prime and double prime), viewed from the yz plane. The magenta stack of lines represent the wires in the U plane, whereas the green lines correspond to the wires in the V plane. Right panel: 3D representation of the momentum of one of the generated monoenergetic muons (red arrow) in the original reference frame (black lines), along with the new reference frame used for the U plane waveforms (blue lines). In the yz plane I added the projection of these three.

per event I do not take the ratio of the previous two quantities but compute the average of the individual ratios per channel in the event:

$$\left(\frac{S/N_{fir}}{S/N_{raw}} \right)_{event} = \frac{\sum_{i=0}^{N_{chan}} \left(\frac{S/N_{fir}}{S/N_{raw}} \right)_i}{N_{chan}}, \quad (4.6)$$

therefore:

$$\left(\frac{S/N_{fir}}{S/N_{raw}} \right)_{event} \neq \frac{(S/N_{fir})_{event}}{(S/N_{raw})_{event}}. \quad (4.7)$$

Additionally, for the analysis of the samples it was necessary to use two different reference frames, to study separately the signals coming from the U and V induction planes. Focussing on a single **APA**, the U and V channels have a different orientation in the yz plane. In the case of U channels, these are tilted \$35.7^\circ\$ clockwise from the vertical (\$y\$ direction), whereas the V channels are at the same angle but in the anticlockwise direction. Because of this, the best option is to deal with two new coordinate systems

4.4. MONTE CARLO STUDIES

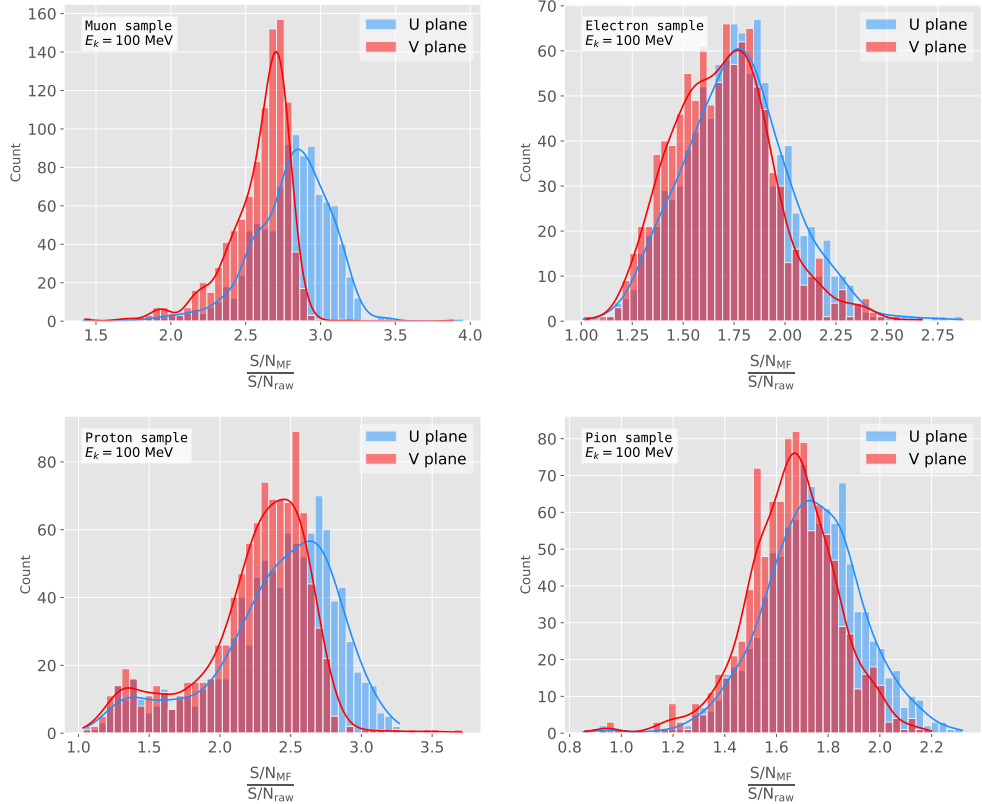


Figure 4.9: Distributions of the mean S/N change per event for the different MC samples after applying the matched filters. Here I separated the change in the U plane (blue) and the V plane (red) channels. From top left to bottom right: muon, electron, proton and neutral pion. All the events have a fixed kinetic energy of $E_k = 100 \text{ MeV}$.

rotated by $\pm 35.7^\circ$ along the x axis, so the new y' and y'' directions are aligned with the U and V induction channels, respectively.

Figure 4.8 (left panel) shows a schematic representation of the original reference frame together with the two rotated ones (denoted by primed and double primed). This way, one can easily understand how parallel was a track to the channels in the two induction planes. Figure 4.8 (right panel) shows a 3D representation of the momentum of a track (red arrow) in the original reference frame (black lines), along with the new reference frame for the U plane (blue lines). I added the projections onto the yz plane of these, to show the usefulness of the new reference frame to tell whether a track is parallel or perpendicular to the channels in a induction plane.

Figure 4.9 shows the distribution of the average S/N change per event when I apply

CHAPTER 4. MATCHED FILTER APPROACH TO TRIGGER PRIMITIVES

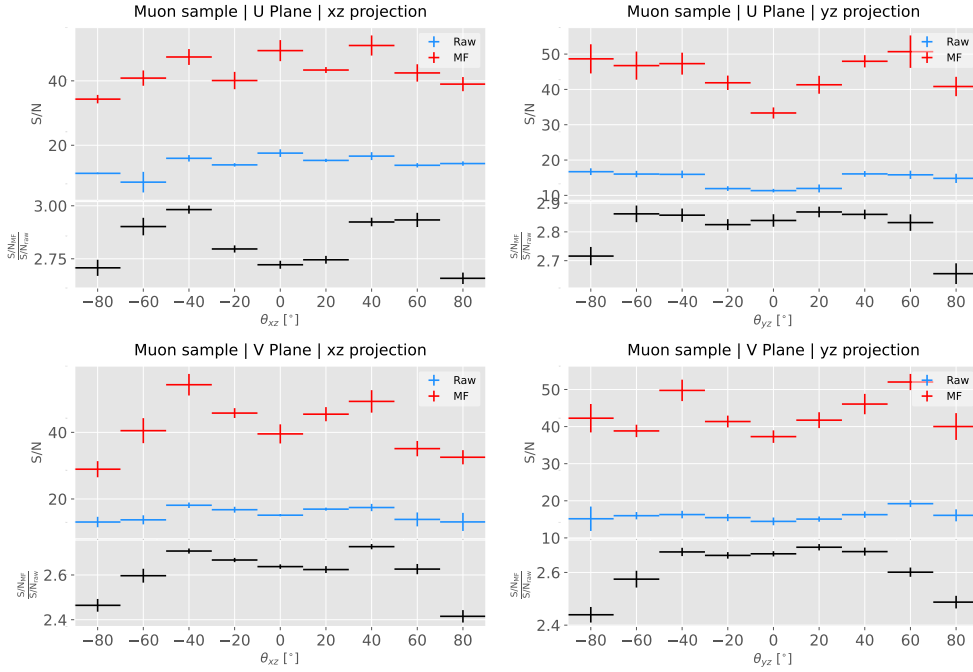


Figure 4.10: Angular dependence of the mean S/N and the S/N improvement for the monoenergetic muon sample. The top and bottom rows correspond to the U and V planes, respectively. The top subplots show the mean S/N for raw (blue) and filtered (red) waveforms whereas the bottom subplots depict the averaged S/N improvement (black).

the optimised matched filters. I produce separate distributions for the channels in the U (red) and V (blue) induction planes. Notice that the S/N distributions for the track-like particles, i.e. muons (top left panel) and protons (bottom left panel), have significantly larger mean values than the distributions of the shower like particles, i.e. electrons (top right panel) and neutral pions (bottom right panel). An important difference between these results and the ones obtained before for the ProtoDUNE-SP data is that the overall improvements that I get with simulated data are more significant. This could be due to an underestimation of the noise levels in the LArSoft simulation. Nonetheless, the concluding message is that the previously optimised matched filters give an overall significant improvement of the S/N for the different samples.

4.4. MONTE CARLO STUDIES

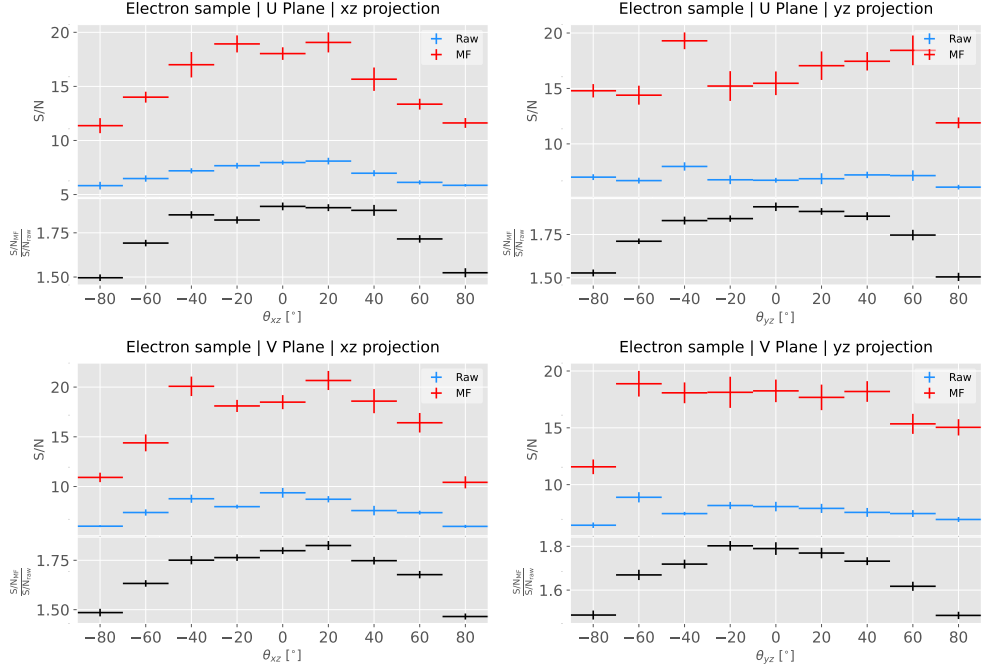


Figure 4.11: Angular dependence of the mean S/N and the S/N improvement for the monoenergetic electron sample. The top and bottom rows correspond to the U and V planes, respectively. The top subplots show the mean S/N for raw (blue) and filtered (red) waveforms whereas the bottom subplots depict the averaged S/N improvement (black).

4.4.1 Angular dependence

Having these monoenergetic samples, one can study the angular dependence of the matched filter performance. This is an important point, as it is well established that for certain track configurations the S/N is much lower than average, as the corresponding waveforms are severely distorted. Therefore, it is necessary to check how the matched filter behaves in different cases, and how the S/N change for those compares to the average.

Figure 4.10 shows the angular dependence of the S/N for the monoenergetic $E_k = 100$ MeV isotropic muons, for the different induction planes and projections. The angles for each event are given by the components of the initial value of the momentum of the particles, taking the angles of the projections on the xz and yz planes with respect to the z axis (more accurately, one needs to compute these angles twice for each event, a pair

CHAPTER 4. MATCHED FILTER APPROACH TO TRIGGER PRIMITIVES

for the $xy'z'$ coordinate system and the other for the $xy''z''$, as explained previously). The top row shows the dependence on the angles corresponding to the U plane, i.e. $\theta_{xz'}$ and $\theta_{y'z'}$, whereas the bottom row shows the angular dependence viewed from the V plane, $\theta_{xz''}$ and $\theta_{y''z''}$. In each panel, the top subplot represents the mean values of the S/N for the raw (blue) and matched filtered (red) signals, and the bottom subplot the averaged S/N change (black). The horizontal lines show the most probable value for the corresponding angular bin, obtained from a fit to a Landau distribution. The vertical lines represent the error in the parameter estimation.

Both for the raw and matched filtered samples, the S/N is lower for tracks that are normal to the APA ($\theta_{xz} \sim \pm 90^\circ$). Similarly, tracks parallel to the wires ($\theta_{yz} \sim \pm 90^\circ$) tend to have higher S/N than those perpendicular to these ($\theta_{yz} \sim 0$). The S/N improvement seems to follow similar trends for both projections in the two planes. In the xz plane there is a slight preference for tracks with $\theta_{xz} \sim \pm 45^\circ$ (particularly in the U plane), whereas in yz the S/N change plateaus around the central region.

Figure 4.11 shows the corresponding angular dependence results for the $E_k = 100$ MeV electrons sample. Although the S/N behaviour in this case is similar to what I observed for the muons, some differences are evident. A possible explanation can be that, because a significant fraction of the hits in these events are produced by the secondary particles generated in the EM shower, some of the S/N ratios do not correspond to the directional information of the primary electron. Even so, the S/N change distribution exhibits a consistent pattern and it is clear that the matched filter enhances the signal regardless of the electron direction.

4.4.2 Hit sensitivity

One of the advantages of the matched filter, directly related to increasing the S/N, is the capability of forming TPs that before fell below the threshold. For instance, Fig. 4.12 shows the raw ADC data from an example electron event with the produced true hits superimposed (black boxes), together with the hits produced by the standard hit finder chain (blue circles), i.e. using the current FIR filter, and the hits obtained using the

4.4. MONTE CARLO STUDIES

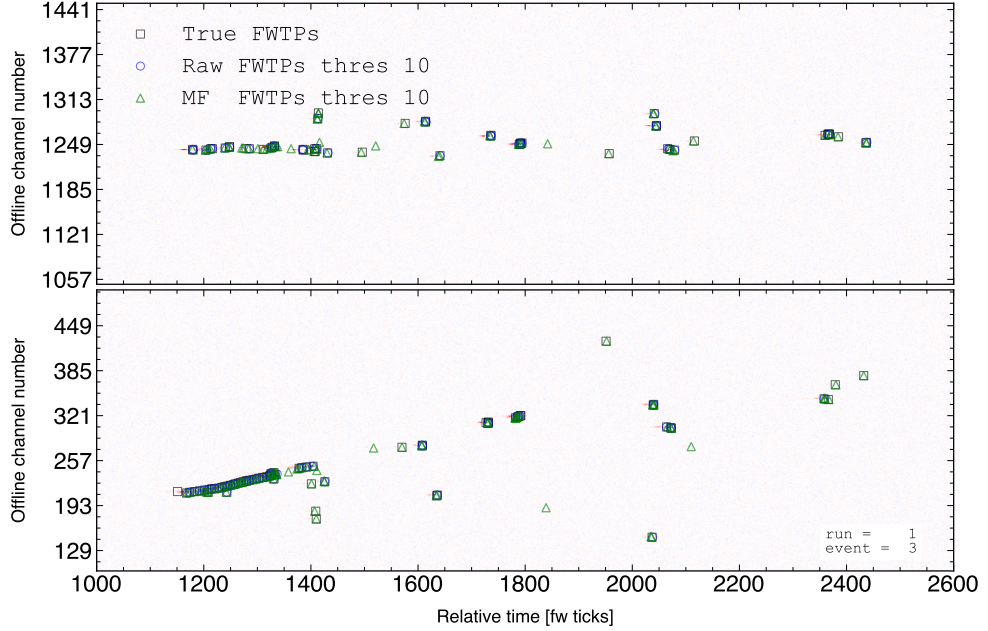


Figure 4.12: Raw event display showing the time (in firmware ticks) versus offline channel number for a $E_k = 100$ MeV electron event. The bottom and top panels correspond to the channels in the U and V planes, respectively. The true hits are superimposed (black boxes), as well as the hits from the standard (blue circles) and the matched filter (green triangles) hit finder chains.

matched filters (green triangles). Both the standard and the matched filter hit finders run with a threshold of 10 ADC. Notice that the standard hits match well the true ones in the initial part of the event, where we have a track-like object. However, it misses most of the hits produced by the EM shower at later times. On the other hand, the hits produced with the matched filter have a better agreement with the true hits even for the more diffuse shower activity.

Even though the matched filter produces more hits as a result of the enhancement of the signal peaks relative to the noise level, it is also true that it may pick up some spurious hits not related to any real activity if one lowers the thresholds too much. Therefore, some optimisation of the threshold is needed, as there is a trade-off between precision and sensitivity.

Having this in mind, I compare the produced hits from both the standard and the matched filter hit finders to the true hits. By running the hit finders on the samples

CHAPTER 4. MATCHED FILTER APPROACH TO TRIGGER PRIMITIVES

with different values of the threshold I can understand how low these can be pushed, and then evaluate the gains obtained from this.

To study how the hit formation depends on the energy, I prepared new isotropic samples with the same types of particles as previously (muons, electrons, protons and neutral pions) but with a flat kinetic energy distribution ranging from 5 to 100 MeV.

To estimate the hit sensitivity for a certain sample, one needs to recover the set of true hits to be able to compare these with the ones produced. To do so, I modify the procedure I use to extract the raw waveforms. For this kind of study, I run the detector simulation in two steps, first I produce the waveforms without noise and extract them in the same format I used for the raw data. Then, the noise is added and the noisy waveforms are similarly written to a file.

To have a better comparison between the true hits and the ones produced from the raw waveforms after applying the two filters, I apply the [FIR](#) filter and the matched filters to the noiseless waveforms as well. I run the hit finder with a minimal threshold (in this case I use 1 ADC) on the filtered noiseless waveforms, generating two sets of true hits. I will refer to these as the standard true hits (with the default [FIR](#) filter) and the matched filter true hits, respectively. This allows for a more precise matching between the different groups of hits produced, as it will account for any delays and distortions introduced by the filters.

In the case of the raw waveforms (with noise added), I run the hit finder on them with different values of the threshold, after applying either the [FIR](#) or the matched filters. I name theses simply standard and matched filter hits, respectively. Then, I match the generated hits to the true hits, the standard hits to the standard true hits and the matched filter hits to the matched filter true hits. The matching is performed by comparing the channel number and the timestamp of the hits. To count as a match, I require that all hits with the same channel number and timestamp have overlapping hit windows, i.e. the time windows between their hit end and hit start times need to overlap. If more than one hit in one of the groups have hit overlap with the same hit in the other group, I only count the match with the closest hit peak time value.

4.4. MONTE CARLO STUDIES

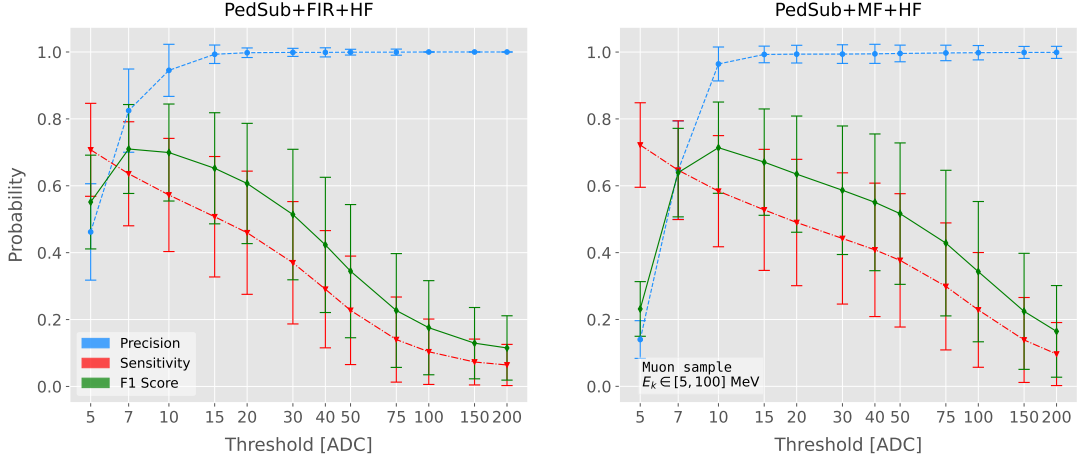


Figure 4.13: Dependence of the precision (blue), sensitivity (red), and F_1 (green) scores on the threshold values used in the hit finder, for the **FIR** (left panel) and matched filter (right panel) cases. The results were obtained after matching the hits to the true hits in the case of the isotropic muon sample with kinetic energy in the range 5 to 100 MeV, taking only into account the induction plane channels. The points represent the mean value while the error bars indicate one standard deviation around that mean value.

To quantify the performance of the two hit finder approaches, I use a classical method from statistical classification known as confusion matrix [124]. It divides the outputs in four categories: true positive (TP, both truth and predicted values are true), false negative (FN, truth value is true but predicted is false), false positive (FP, truth value is false but predicted is true) and true negative (TN, both truth and predicted values are false).

The contents of the confusion matrix allow us to compute other derived scores to assess the performance of our classification. In this study, I make use of three of these metrics, namely the precision or positive predictive value:

$$\text{PPV} = \frac{\text{TP}}{\text{TP} + \text{FP}}, \quad (4.8)$$

the sensitivity or true positive rate:

$$\text{TPR} = \frac{\text{TP}}{\text{TP} + \text{FN}}, \quad (4.9)$$

CHAPTER 4. MATCHED FILTER APPROACH TO TRIGGER PRIMITIVES

and the F_1 score [125]:

$$F_1 = \frac{2\text{TP}}{2\text{TP} + \text{FP} + \text{FN}}, \quad (4.10)$$

which is the harmonic mean of the precision and the sensitivity.

For this specific case I am not going to make use of the true negative category, as its definition in this context can be ambiguous because one does not have clear instances in the classification process. This way, I only count the number of true positives as the total amount of hits I can match between true and raw populations, the number of false negatives will be the number of missing true hits, and the false positives the number of hits which do not match any true hit.

In Fig. 4.13 I show the precision (blue), sensitivity (red) and F_1 -score (green) I obtain as a function of the threshold used in the hit finder for the muon sample. Because the matched filters are only applied to induction channels, I consider exclusively the hits coming from the U and V planes. The panel on the left corresponds to the results I get when running the hit finder on the [FIR](#) filtered waveforms, whereas the right panel contains the scores for the matched filter case. The points are centered at the threshold value used and represent the mean value obtained for each score using all the generated events, while the error bars indicate one standard deviation around the mean value.

One can see that the precision for the matched filter case is lower when the thresholds are very low, as the noise baseline is slightly amplified, but then rises to high values quicker than for the [FIR](#) case. The other difference one can spot is that the sensitivity in the [FIR](#) case starts dropping faster at around the same threshold values where the precision stabilises around 1, while in contrast for the matched filter this rapid decrease starts at higher threshold values. A similar scan for the same thresholds was performed for the electron sample in the same energy range, yielding similar results.

In Fig. 4.14 I show the average hit sensitivity versus the kinetic energy of the events, both for the matched filter hits (blue) and the standard hits (red). The left panel corresponds to the muon sample, whereas the one on the right corresponds to the electron sample, both with kinetic energies between 5 and 100 MeV. In each panel, the

4.4. MONTE CARLO STUDIES

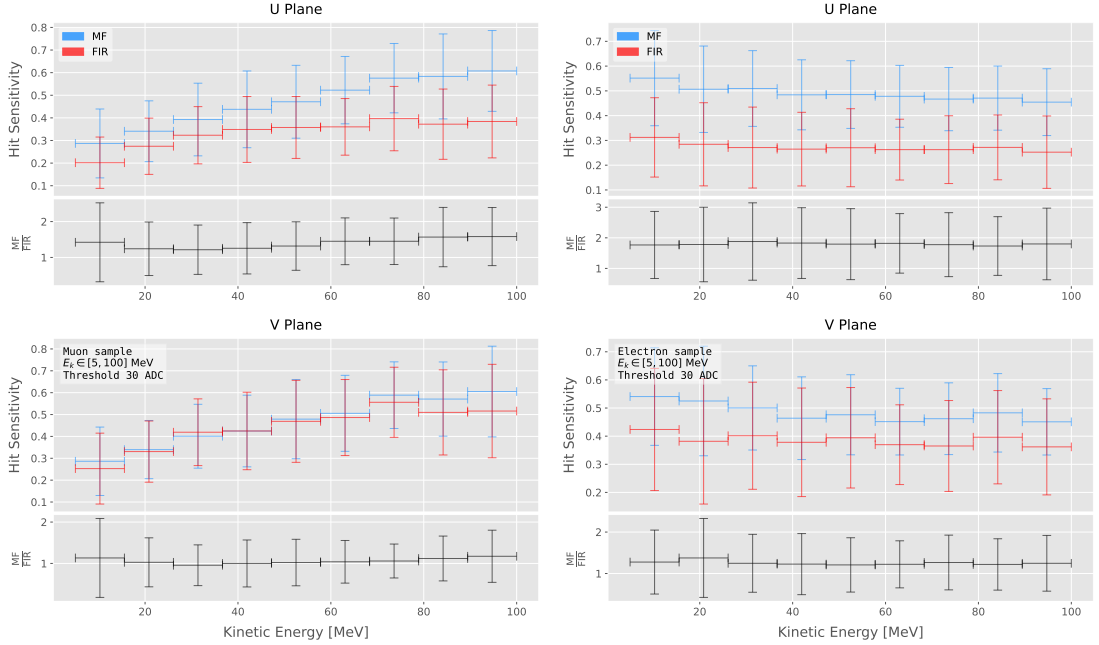


Figure 4.14: Dependence of the averaged hit sensitivity on the kinetic energy of the events for the matched filter (blue) and standard (red) hits, for the case of the muon (left panel) and electron (right panel) samples, separated between U (top plots) and V (bottom plots) induction wire planes. The top subplots contain the hit sensitivities for the two hit finder alternatives, while the bottom subplots show the ratio between the two. The horizontal lines sit at the mean value and represent the size of the energy bins, while the vertical error bars indicate one standard deviation around that mean value.

top plot corresponds to hits in the U plane, while the bottom plot contains the same information for the V plane. Each plot contains two subplots, the one on the top shows the hit sensitivity values for the matched filter and standard hits separate, while the bottom subplot depicts the ratio between the matched filter and standard sensitivities. The horizontal lines are placed at the mean value obtained in the fit and represent the width of the E_k bins used, while the vertical error bars indicate one standard deviation around that mean. In both cases, the threshold used was 30 ADC, as I require the precision to be higher than 0.99 for both matched filter and standard cases.

In general, the improvements are better for the U than for the V plane. While for the U channels I achieve a mean improvement of 50% and 80% for muons and electrons, respectively, the improvement in the V plane is stalled at 10% and 25%. Nevertheless, looking at the sensitivities for the matched filter hits in both planes, one can see these

CHAPTER 4. MATCHED FILTER APPROACH TO TRIGGER PRIMITIVES

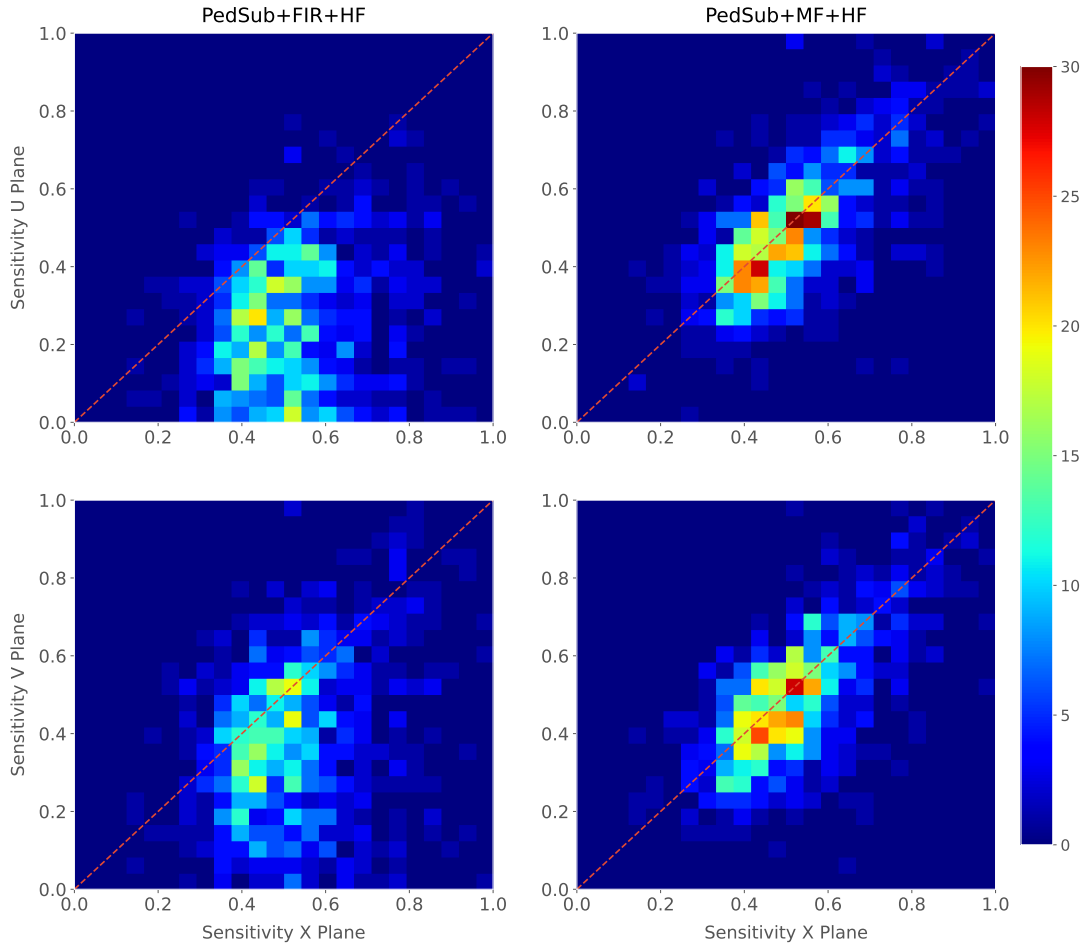


Figure 4.15: Distributions of the hit sensitivity in the U (top panels) and V (bottom panels) planes versus the hit sensitivity in the X plane, both for the standard hits (left panels) and the matched filter hits (right panels), in the case of the electron sample and a threshold of 30 ADC.

have similar mean values for each energy bin. On the other hand, for the standard hits the sensitivity remains higher for the V plane. This way, it looks there is a less significant gain because the hit sensitivity was already high.

Another interesting observation is the different behaviors for muons and electrons. While hit sensitivity for muons grows significantly with energy, in the case of electrons it decreases slightly with the kinetic energy. However, when it comes to the improvement on the sensitivities, this remains almost constant in all cases.

Furthermore, we can look at how the concurrence of hits between the different wire planes has changed. For any given event, I expect to have a similar number of hits in

4.4. MONTE CARLO STUDIES

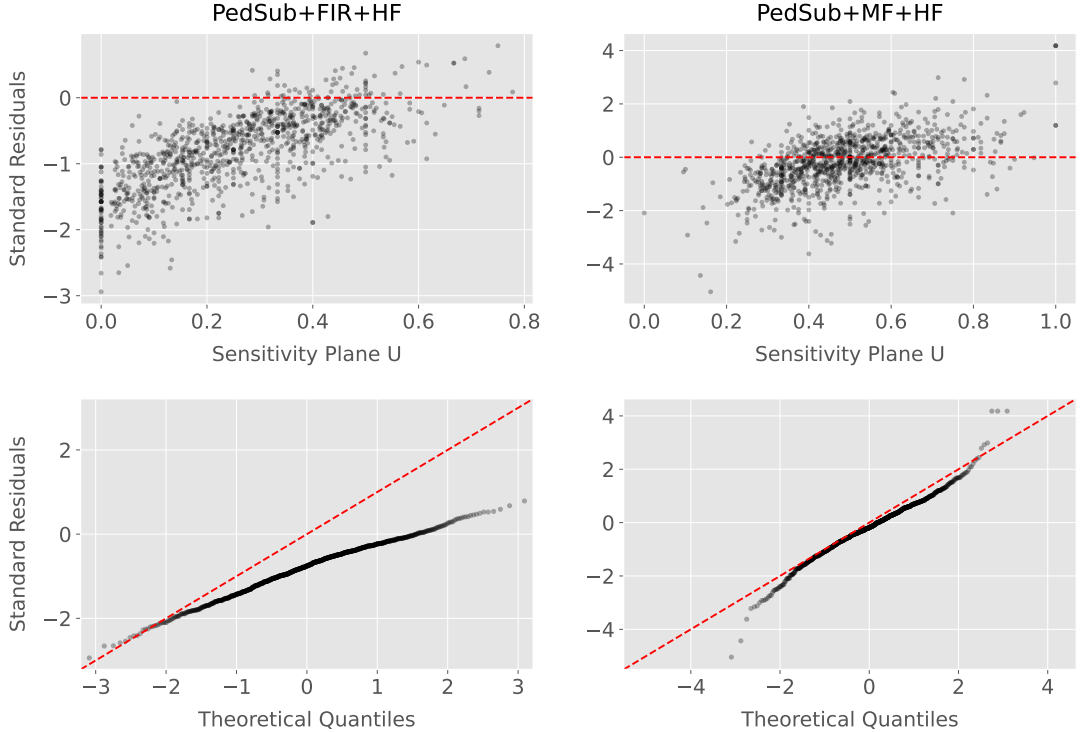


Figure 4.16: Top panels: standard residual plots of the hit sensitivities between the X and U planes. Bottom panels: quantile-quantile plots of the hit sensitivity standard residuals between the X and U planes. In all cases, the left panel corresponds to the standard hits while the right panel represents the matched filter case, all from the electron sample with a 30 ADC threshold.

the three planes. As the ionisation electrons need to cross the U and V planes prior to reaching the collection plane X, they will induce current in those wire planes. A way to check the concurrence of hits across planes is by comparing the hit sensitivities in the different planes for each individual event. Although the sensitivities will not be exactly equal across planes, ideally they should be normally distributed around the diagonal.

Figure 4.15 shows the hit sensitivity in the U (top panels) and V (bottom panels) planes versus the hit sensitivity in the X plane, for the case of the standard hits (left panels) and the matched filter hits (right panels). All plots were generated for the electron sample and a threshold of 30 ADC. From these, one can see a clear trend. The standard hit finder chain produces hit sensitivities in the induction planes that are systematically lower than the sensitivity in the X plane, i.e. most of the points sit below the diagonal (red dashed line). In contrast, when the matched filters are applied, the

CHAPTER 4. MATCHED FILTER APPROACH TO TRIGGER PRIMITIVES

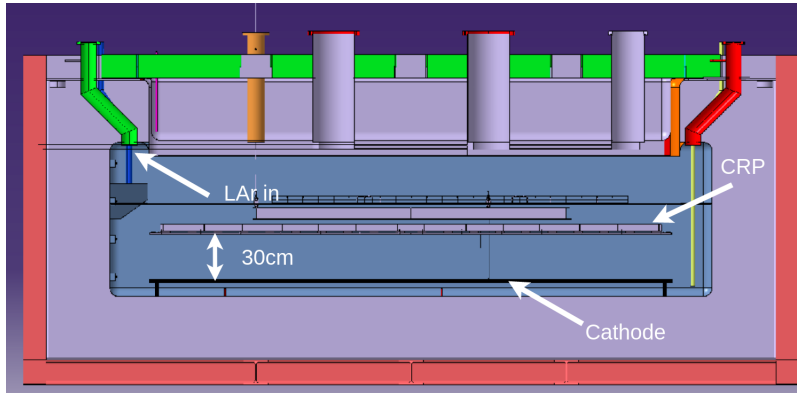


Figure 4.17: Schematic diagram of the vertical drift ColdBox setup at CERN.

majority of the events are distributed around the diagonal. This points out that the concurrence of hits across planes has improved.

To exemplify the improvement I obtain, I take the residuals of the hit sensitivities for the X and U planes. Assuming the diagonal hypothesis, i.e. given a dataset of the form (x, y) for any x I take the predicted y value to be equal to the value of x , I can compute the standard residuals for the hit sensitivities in U given the sensitivities for X. In Fig. 4.16 (top panels) I show these standard residuals against the corresponding values of the hit sensitivity in the U plane, for the electron sample with kinetic energy between 5 and 100 MeV. Comparing the scatter points in the case of the standard hits (left panel) and the matched filter hits (right panel), it can be seen that the residuals for the standard hit finder follow a certain pattern and their mean deviates from 0.

To see clearly if the residuals are normally distributed, in Fig. 4.16 (bottom panels) I plot the corresponding quantile-quantile plot for both the standard (left panel) and matched filter (right panel) residuals. One can clearly see that the points for the standard hit finder case follow a strongly non-linear pattern, suggesting that the residuals do not follow a normal distribution. In contrast, for the matched filter hits the points conform to a roughly linear path, implying that in this case the normality condition is fulfilled.

All these results hint at the fact that the concurrence of hits across the wire planes can be strengthened by applying the matched filters.

4.5. VD COLDBOX DATA TAKING

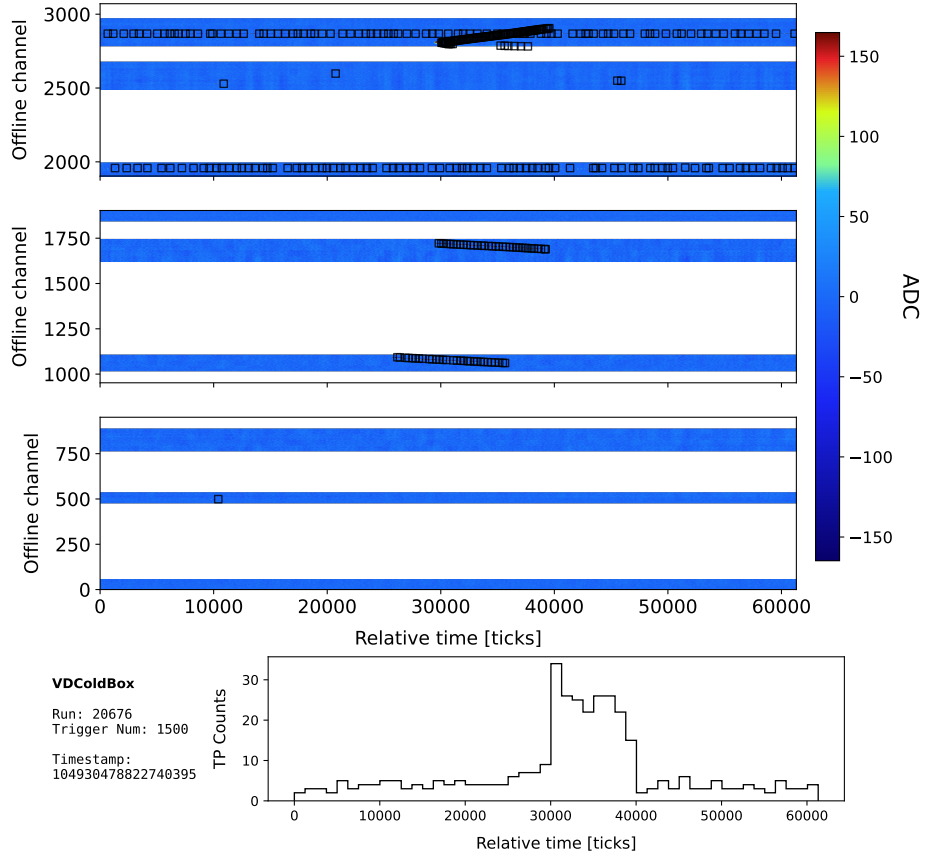


Figure 4.18: Event display of the data taken with the matched filter and HMA trigger at the **VD** ColdBox. The display shows the data from 3 **ADC** links for the full trigger window, with the black squares representing the produced **TPs**. The bottom panel represents the **TP** counts as a function of time in the trigger window.

4.5 VD ColdBox data taking

Between February and April 2023 the vertical drift (**VD**) ColdBox setup at CERN, shown in Fig. 4.17, was recommissioned for cold electronics testing with CRP5. That provided an opportunity for testing the firmware **TP** generation in a real **LArTPC**. However, during the two run periods new software-related complications that were not observed in previous running conditions arose.

These prevented us from taking data with the whole system. As a palliative measure, new configurations were developed that allowed to run with **TP** generation enabled for a subset of the **ADC** links. With these workarounds, we managed to run with up to three

CHAPTER 4. MATCHED FILTER APPROACH TO TRIGGER PRIMITIVES

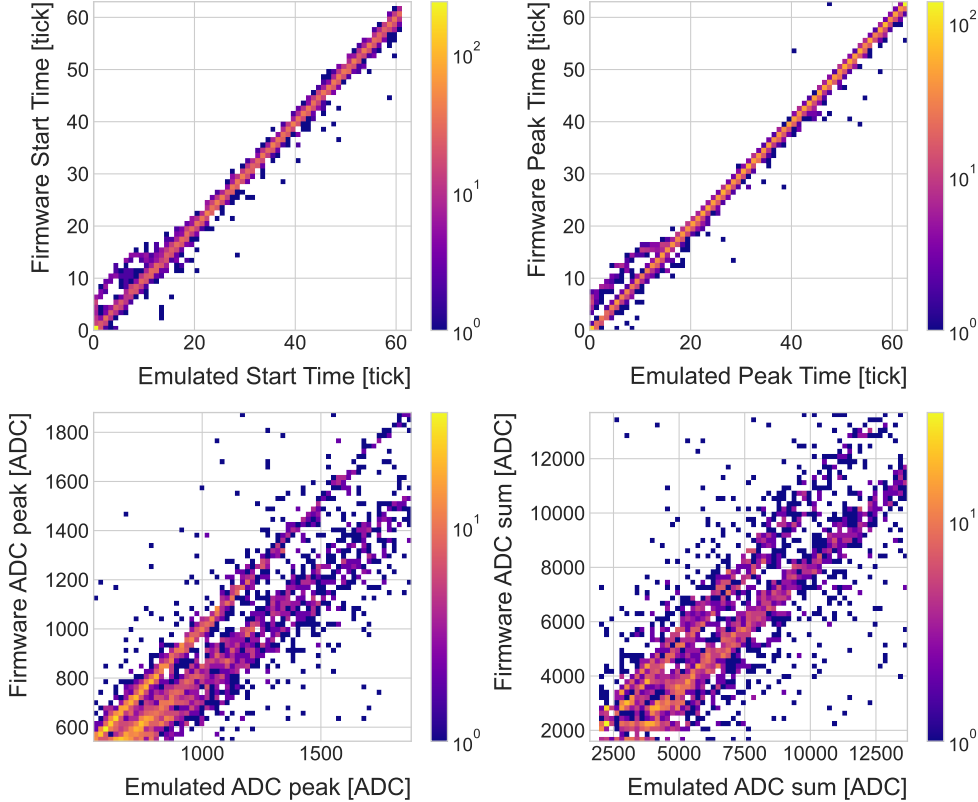


Figure 4.19: Comparison between firmware-produced and simulated [TP](#) quantities for a matched filter run at the [VD](#) ColdBox. From top left to bottom right: start time, peak time, [ADC](#) peak, and [ADC](#) sum.

out of twelve [ADC](#) links and the horizontal muon algorithm ([HMA](#)) trigger.

Additionally, an alternative firmware version was prepared featuring the matched filter coefficients optimised for the induction plane hit finding. The version of the filter we used for the data taking is slightly different from the one of the previous studies, as in this case we needed to apply the same filter coefficients to all channels irrespective of the readout plane they come from. With this, we also managed to run with three [ADC](#) links and the [HMA](#) trigger. Figure 4.18 shows an example event display from the longest run we recorded with the matched filter firmware.

We used the recorded data, together with our standalone [TP](#) generation simulation tool, to perform comparisons between the firmware and simulated [TPs](#). One such comparison for a matched filter run is shown in Fig. 4.19. From this, it can be seen that there is a close agreement between firmware and simulation for the time-related variables

4.6. SUMMARY

(top panels). However, there is a noticeable structure to the [ADC](#) peak and integral distributions (bottom panels). It seems that for the induction planes the simulation systematically overpredicts these values, producing the lines below the main diagonal, while the collection plane [TPs](#) follow the expected behaviour. The reason behind this is still unclear, and is currently being investigated. More details on these comparisons will be included in a planned upcoming publication.

4.6 Summary

The [DAQ](#) system of the [DUNE FD](#) relies on the online identification of hits on channels, the so-called [TPs](#), to form the decisions of what data to store. The goal of this Chapter was to motivate a method to enhance the production of [TPs](#) in the induction channels of the detectors. Forming [TPs](#) from all the charge readout planes will improve the redundancy of the trigger algorithms. Not only that, but this may be the key to have more complex trigger logic that requires directional information. The aspect I focused on to improve the hit finding was the filtering of the waveforms. I introduced the concept of the matched filter in section 4.3. Using a sample of ProtoDUNE-SP cosmic data, I demonstrated that these filters provide significant improvements to the [S/N](#) of the induction channels. A series of studies using [MC](#) samples were presented in section 4.4. These allowed me to study the dependence of the filtering on the orientation and the energy of the tracks. I also used them to assess the impact of this method on the hit sensitivity. Finally, in section 4.5 I briefly summarised the results from the [VD](#) ColdBox runs which featured the matched filter.

The studies presented in this Chapter demonstrate that it is possible to enhance the production of [TPs](#) in the induction planes of the [DUNE FD](#) modules to levels comparable to those of the collection channels. The matched filter approach used here has consistently produced promising results using both ProtoDUNE-SP and [MC](#) data samples. Moreover, the successful [VD](#) ColdBox tests helped establishing it as a feasible candidate for the online data processing of [DUNE](#).

Dark Matter searches with neutrinos from the Sun

He stepped down, trying not to look long at her, as if she were the Sun, yet he saw her, like the Sun, even without looking.

– Leo Tolstoy, *Anna Karenina*

The idea of detecting neutrino signals coming from the core of the Sun to probe DM is not new. The main focus of these searches has usually been high-energy neutrinos originating from DM annihilations into heavy particles [126–129]. However, recent studies have proposed to look at the low-energy neutrino flux arising from the decay of light mesons at rest in the Sun [130–133], previously thought undetectable.

In this Chapter, I demonstrate the capability of DUNE to constrain this kind of DM scenario. I use the neutrino fluxes arising from DM annihilations in the core of the Sun to compute the projected limits that DUNE would be able to set on the annihilation rates of DM particles in the Sun and the DM scattering cross sections.

5.1 Gravitational capture of DM by the Sun

The Sun and the centre of the Earth are possible sources of DM annihilations, and are especially interesting because of their proximity. Their gravitational attraction ensures the capture of DM from the local halo through repeated scatterings of DM particles. Only very weakly interacting particles such as neutrinos produced from DM annihilations

CHAPTER 5. DARK MATTER SEARCHES WITH NEUTRINOS FROM THE SUN

can escape the dense interior of these objects. Therefore, neutrino telescopes are the most useful experimental layouts to pursue **DM** searches from the cores of these astrophysical objects.

The neutrino flux from **DM** annihilations inside the Sun depends on the **DM** capture rate, which is proportional to the **DM** scattering cross section, and the annihilation rate, which is proportional to the velocity-averaged **DM** annihilation cross section. The total number of **DM** particles inside the Sun follows the Boltzmann equation [130]:

$$\frac{dN_{DM}}{dt} = C_\odot - A_\odot N_{DM}^2, \quad (5.1)$$

where C_\odot and A_\odot are the total Sun **DM** capture and annihilation rates respectively. In this expression I neglected the evaporation term, proportional to N_{DM} , which only contribute for $m_{DM} \lesssim 4$ GeV [134]. As the current threshold of neutrino telescopes is a few GeV, this region falls below the probed range but can be important in future low-energy projects like **DUNE**.

This equation has an equilibrium solution:

$$N_{DM}^{eq} = \sqrt{\frac{C_\odot}{A_\odot}}, \quad (5.2)$$

which represents the amount of **DM** inside the Sun if the capture and annihilation have reached equilibrium. As the Sun is approximately 4.6 Gyr old [135], it is usually assumed that equilibrium has been achieved. Therefore, the anomalous neutrino flux from the Sun would be proportional to the **DM** scattering cross section, enabling us to set limits on this quantity. If one does not assume equilibrium, some assumptions on the **DM** annihilation cross section are necessary to extract predictions from the neutrino signals.

A detailed discussion regarding the computation of the capture rates is given in App. B.1.

5.2 Neutrino flux from DM annihilations

When [WIMPs](#) annihilate inside the Sun, a flux of high-energy neutrinos is expected from heavy quarks, gauge bosons and $\tau^+\tau^-$ final states, which decay before losing energy in the dense solar medium [131]. These produce a continuous neutrino spectra up to $E_\nu \sim m_{\text{DM}}$. In the case of direct annihilation into neutrinos, one would have a monochromatic flux with $E_\nu = m_{\text{DM}}$. These kinds of signals have been extensively studied (see e.g. Ref. [136] for a review), allowing strong limits on the [SD WIMP](#)-proton cross section for large m_{DM} . However, the number of high-energy neutrinos per [WIMP](#) annihilation is small and the spectrum depends on the unknown final state. Moreover, although background rejection is easier for large m_{DM} , neutrinos with $E_\nu \gtrsim 100$ GeV are significantly attenuated by interactions in the Sun.

Nevertheless, most [WIMP](#) annihilation final states eventually produce a low-energy neutrino spectrum. In this case one does not just consider the more massive final states but also annihilations into e^+e^- , $\mu^+\mu^-$ and light quarks [130]. In particular, light mesons would be produced and stopped in the dense medium, thus decaying at rest and producing a monoenergetic neutrino signal. The decay-at-rest of kaons will produce a ν_μ flux with $E_\nu = 236$ MeV, while in the case of pions one would have $E_\nu = 29.8$ MeV. In practice, only the K^+ and π^+ contribute to these signals, as the K^- and π^- are usually Coulomb-captured in an atomic orbit and get absorbed by the nucleus. There is also a low-energy neutrino signal coming from muon decays, which are produced in kaon or pion decays, leptonic decays of other hadrons and heavy leptons or even directly from [WIMP](#) annihilations. These can decay at rest and contribute to the previous low-energy neutrino flux with a well known spectrum below 52.8 MeV.

These monoenergetic MeV neutrinos were previously considered undetectable but, due to the large yield, the known spectra and the modern advances in the detector technology, this low-energy neutrino flux can be a good probe of the [SD WIMP](#)-proton cross section in the standard solar [WIMP](#) capture scenario, as it is sensitive to low [WIMP](#) masses and insensitive to the particular final state. A good place to look for

CHAPTER 5. DARK MATTER SEARCHES WITH NEUTRINOS FROM THE SUN

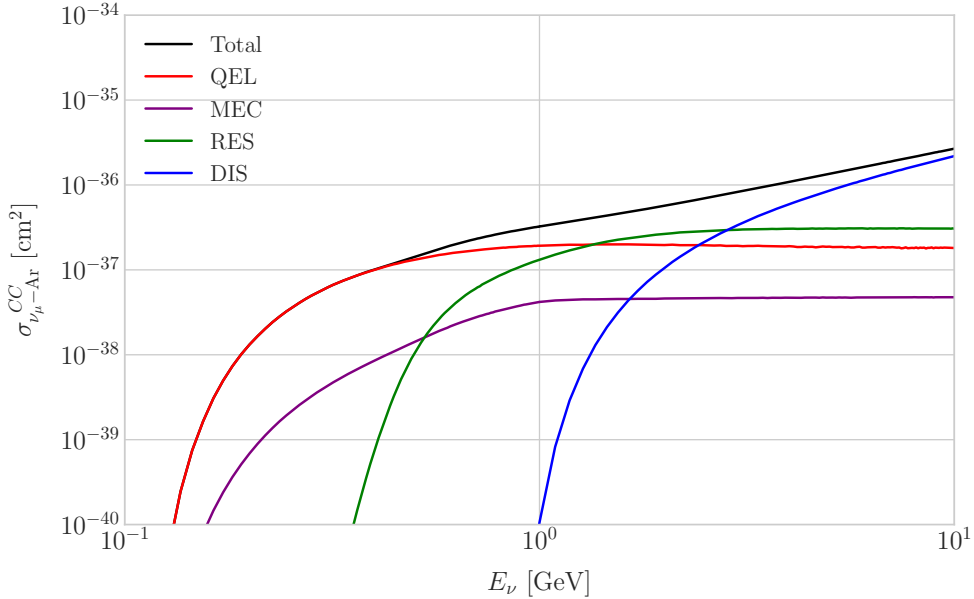


Figure 5.1: NuWro-computed $\nu_\mu - {}^{40}\text{Ar}$ charged-current scattering cross section as a function of the neutrino energy. The black line shows to the total cross section, whereas the others correspond to the different contributions (in red quasi-elastic scattering, in green resonant pion exchange, in blue deep inelastic scattering and in purple meson exchange current).

these signals are next-generation neutrino experiments such as [DUNE](#) [133].

5.3 Computing limits from solar neutrino fluxes

The first step to use these fluxes to search for [DM](#) in the Sun is to determine the expected number of atmospheric background events. For a given exposure, after directionality selection has been applied, this can be written as:

$$N_B = \eta_B \int d\Omega \int_{E_{min}}^{E_{max}} dE_\nu \frac{d^2\Phi_{atm}^\mu}{dE_\nu d\Omega} \times \left(A_{eff}^{(\mu)}(E_\nu) T \right), \quad (5.3)$$

where η_B is the background efficiency, E_{min} and E_{max} the minimum and maximum energies to integrate over, $d^2\Phi_{atm}^\mu/dE_\nu d\Omega$ the double differential flux of atmospheric muon neutrinos in energy and solid angle, $A_{eff}^{(\mu)}$ is the effective area of [DUNE](#) to muon neutrinos, and T is the exposure time. The effective area can be expressed as the product of the neutrino-nucleus scattering cross section and the number of nuclei in the fiducial

5.3. COMPUTING LIMITS FROM SOLAR NEUTRINO FLUXES

volume of the detector. This way, for **DUNE** we have:

$$A_{eff}^{(\mu)}(E_\nu) = (6.0 \times 10^{-10} \text{ m}^2) \left(\frac{\sigma_{\nu-\text{Ar}}^{(\mu)}(E_\nu)}{10^{-38} \text{ cm}^2} \right) \left(\frac{M_{target}}{40 \text{ kT}} \right), \quad (5.4)$$

where $\sigma_{\nu-\text{Ar}}^{(\mu)}$ is the $\nu_\mu - {}^{40}\text{Ar}$ charged-current scattering cross section. In Fig. 5.1 I show the computed value of the cross section as a function of the neutrino energy E_ν , in the range of interest both for the atmospheric background and signal events. It was computed using the **NuWro** Monte Carlo neutrino event generator [137], including the **QE** (red line), **MEC** (purple line), **RES** (green line), and **DIS** (blue line) **CC** contributions.

The background rejection will depend on the resolution of the detector and the selection one applies on the events. A geometry argument can be used to estimate the maximum background rejection one can achieve in this case, considering one can efficiently discriminate all events coming from a direction different from that of the Sun. In that case, the optimal background efficiency will simply be the relative angular coverage of the Sun. Taking the angular diameter of the Sun as seen from the Earth to be approximately 0.5° , one obtains an optimal background efficiency:

$$\eta_B^{(opt)} \simeq \frac{\pi \left(\frac{\delta_\odot}{2} \right)^2}{4\pi} = 4.76 \times 10^{-6}. \quad (5.5)$$

This value gives an optimistic estimate of the number of background events. However, it can be regarded as an upper limit, as it represents the best case scenario.

In Fig. 5.2 I show the fluxes of atmospheric neutrinos at the Homestake mine during solar minimum, taken from Ref. [138]. The values are averaged over the two angular directions. In blue I have the flux of muon neutrinos while in red I indicate the flux of electron neutrinos. Additionally, the dashed lines correspond to both antineutrino species.

Using these values for the muon neutrino and the corresponding total **CC** cross section, one can compute the total number of expected background events by integrating over the given energy range. For this I choose the energy range for the **DUNE FD**

CHAPTER 5. DARK MATTER SEARCHES WITH NEUTRINOS FROM THE SUN

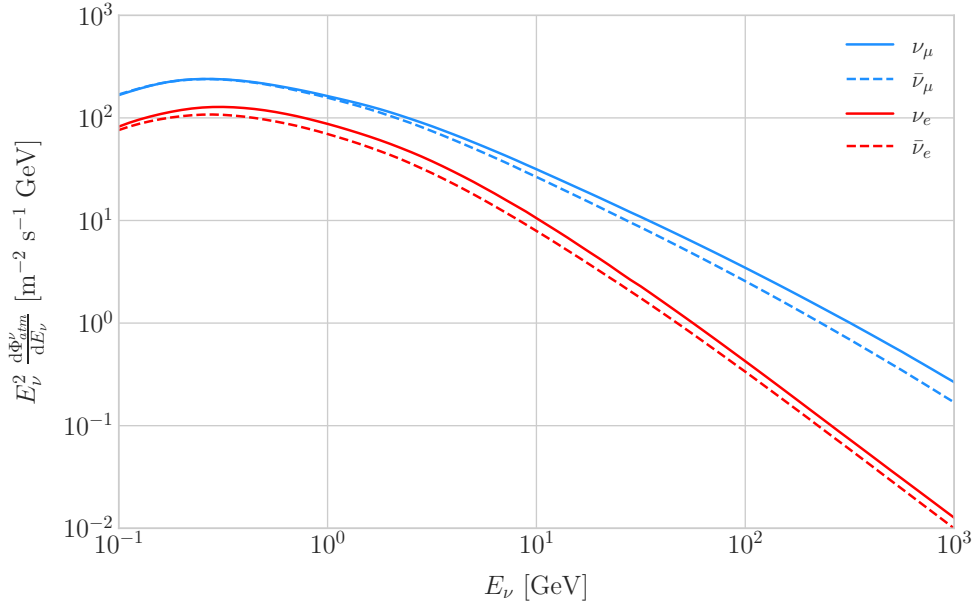


Figure 5.2: Expected atmospheric neutrino flux as a function of the neutrino energy E_ν at Homestake at solar minimum, taken from Ref. [138]. The blue solid (dashed) line correspond to muon neutrinos (antineutrinos) and the red solid (dashed) line correspond to electron neutrinos (antineutrinos).

specified in [96], $E_{min} = 10^{-1}$ GeV and $E_{max} = 10$ GeV. Taking all these into account, I find the total number of background events to be:

$$N_B \simeq \eta_B \times (3.827 \times 10^4) \times \left(\frac{\text{exposure}}{400 \text{ kT yr}} \right). \quad (5.6)$$

To estimate the sensitivity of **DUNE** to this kind of signal, one can consider a hypothetical data set where the number of observed neutrinos is taken to be the expected number of background events rounded to the nearest integer, $N_{obs} = \text{round}(N_B)$ [139]. Now, if I assume that the number of signal and background events seen by **DUNE** are given by Poisson distributions with means equal to the expected number of signal and background events, N_S and N_B , one can denote by N_S^{90} to the number of expected signal events such that the probability of having an experimental run with a number of events greater than N_{obs} is 90%. This number can be obtained as the numerical solution to the equation:

$$1 - \frac{\Gamma(N_{obs} + 1, N_S^{90} + N_B)}{N_{obs}!} = 0.9, \quad (5.7)$$

5.4. HIGH ENERGY DM NEUTRINO SIGNALS

where $\Gamma(x, y)$ is the upper incomplete gamma function. I adopt this method from a previous [DUNE FD](#) analysis which looked for ν_μ CC interactions from decays at rest of charged kaons in the Sun [133].

The number of signal events is related to the neutrino flux from [DM](#) annihilations in a similar way as the background events to the atmospheric neutrino flux. In this case I have:

$$N_S = \eta_S \Gamma_A^{eq} \int_{z_{min}}^{z_{max}} dz \frac{dN_\nu}{dAdN_A dz} \times (A_{eff}^\mu(z)T), \quad (5.8)$$

where η_S is the signal efficiency, Γ_A^{eq} is the total annihilation rate of [DM](#) particles at equilibrium, $\Gamma_A^{eq} = A_\odot (N_{DM}^{eq})^2$, z_{min} and z_{max} the minimum and maximum relative energies to integrate over (given by $z_{min,max} = E_{min,max}/m_{DM}$ for each m_{DM}) and $dN_\nu/dAdN_A dz$ the muon neutrino flux per [DM](#) annihilation in the Sun.

Having obtained N_S^{90} one can use the relation in Eq. (5.8) to compute $\Gamma_A^{eq,90}$ for different values of the [DM](#) mass. Then, I can directly translate those values into the projected sensitivities for [DUNE](#) to the [DM](#) scattering cross sections, for a given exposure. The relation between the annihilation rate and the [DM](#)-nucleon cross section comes from the equilibrium condition through the solar [DM](#) capture rate, discussed above.

5.4 High energy DM neutrino signals

To make accurate estimates of the capability of the [DUNE FD](#) to constrain the parameter space of the [DM](#) using solar neutrino fluxes, I need to account for the detector resolution effects and the topologies of the different signatures. As a starting point, I focus on specific [DM](#) self-annihilation channels. For the case of [DUNE](#), the relevant ones are mainly the hard channels $\tau^+\tau^-$ and $\nu\bar{\nu}$ and the soft channel $b\bar{b}$. For the same [DM](#) mass value, the neutrino spectra from the hard channels are more flat and reach higher energies than the ones from the soft channel, which drop faster as the annihilation products produce other particles in the solar medium. These three are the annihilation channels open for relatively low mass [WIMPs](#) that will actually give sizeable neutrino fluxes. Other channels, like W^+W^- and ZZ , are open for more massive [WIMPs](#). However, those will

CHAPTER 5. DARK MATTER SEARCHES WITH NEUTRINOS FROM THE SUN

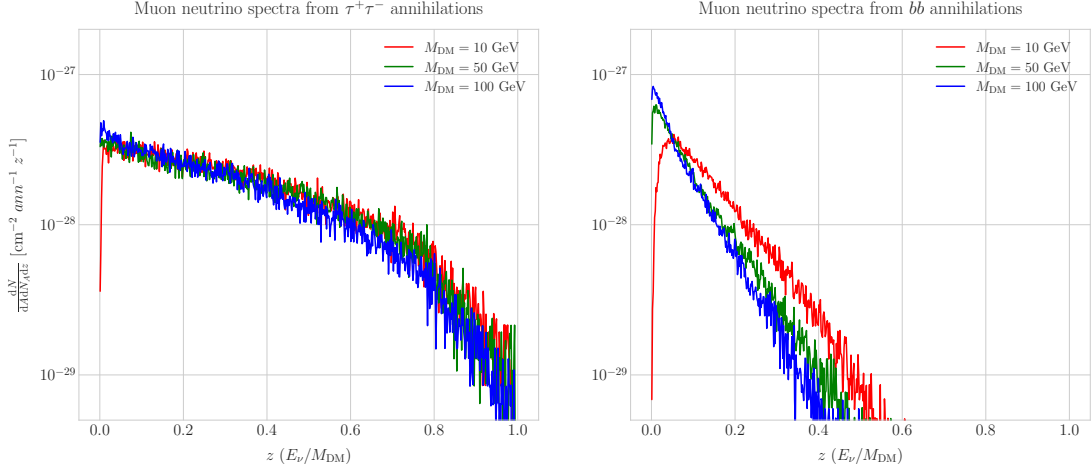


Figure 5.3: Computed spectra of muon neutrinos at the DUNE FD site from $\tau^+\tau^-$ (left panel) and $b\bar{b}$ (right panel) annihilations in the Sun for the DM masses $m_{\text{DM}} = 10 \text{ GeV}$ (red line), 50 GeV (green line) and 100 GeV (blue line), plotted in relative energy units.

produce a higher energy neutrino flux that will be out of reach for DUNE (the maximum neutrino energy for a detector like the DUNE FD is taken to be $E_{\max} = 10 \text{ GeV}$).

In Fig. 5.3 I show the muon neutrino spectra at the DUNE FD location ($44^\circ 20' \text{ N}$, $103^\circ 45' \text{ W}$) generated with `WimpSim` [140] from $\tau^+\tau^-$ (left panel) and $b\bar{b}$ (right panel) annihilations in the core of the Sun, for different DM masses. Here, one can clearly see the meaning of the previous distinction between hard and soft channels.

In this case, I prepared two sets of samples, one for $\tau^+\tau^-$ and the other for $b\bar{b}$, for DM masses in the range from 5 to 100 GeV (for $b\bar{b}$ the first mass point I consider is 7.5 GeV, as this annihilation channel is not kinematically allowed for a WIMP with $m_{\text{DM}} = 5 \text{ GeV}$). For each channel and mass value, I generate 10^5 neutrino events in `WimpSim`, that I then pass to `NuWro` which simulates the neutrino interaction with the argon.

`WimpSim` outputs both a flux file and an event list for the specified channel and mass value. The directions of these events are given in terms of the azimuth and altitude angles viewed from the specified location, so first I need to convert these into the DUNE FD coordinates. Once I have done this, each event is used as input for `NuWro`. I restrict the event generation to charged current interactions, but I allow all

5.4. HIGH ENERGY DM NEUTRINO SIGNALS

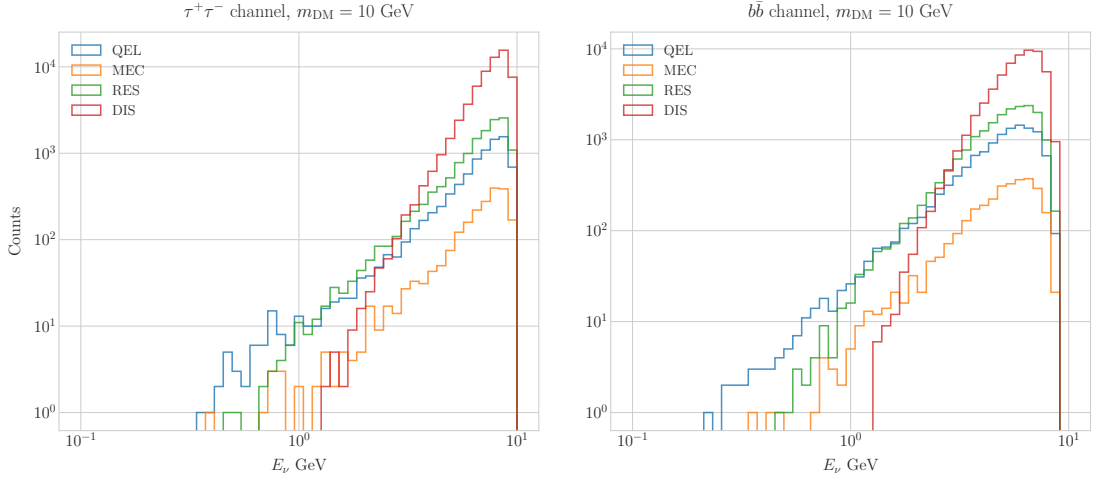


Figure 5.4: Distribution of the muon neutrino energies from the $\tau^+\tau^-$ (left panel) and $b\bar{b}$ (right panel) annihilation channels, for $m_{\text{DM}} = 10$ GeV, separated by CC interaction type: QE (blue), MEC (orange), RES (green) and DIS (red).

the different contributions to the CC cross section, i.e. QE, MEC, RES, and DIS. I exclusively take into account the CC contribution because I am only interested in final states with charged leptons, as we have a better chance of reconstructing the kinematics of these events because of the distinct signature the muons leave in the LArTPC.

For the atmospheric fluxes I follow a similar procedure, using the fluxes binned in azimuth and altitude angles. This way, I transform these to DUNE coordinates and process the fluxes for each bin separated with NuWro, generating a total of 10^5 background events.

At this point, I have two sets of neutrino signal events with different energies and final states. In Fig. 5.4 one can see the distribution of the muon neutrino energies for the case $m_{\text{DM}} = 10$ GeV, both for the $\tau^+\tau^-$ (left panel) and $b\bar{b}$ (right panel) channels, separated by interaction. One can clearly see that there are various energy regimes where different interaction types dominate. This leads to a plurality of event topologies, therefore making it difficult to implement a general approach to the selection of events in detriment of the background. As a way to proceed, I decided to focus on a subset of the samples, based on the different interaction modes and contents of the final state. Thus, I consider a CC DIS sample and a single proton CC QE sample.

CHAPTER 5. DARK MATTER SEARCHES WITH NEUTRINOS FROM THE SUN

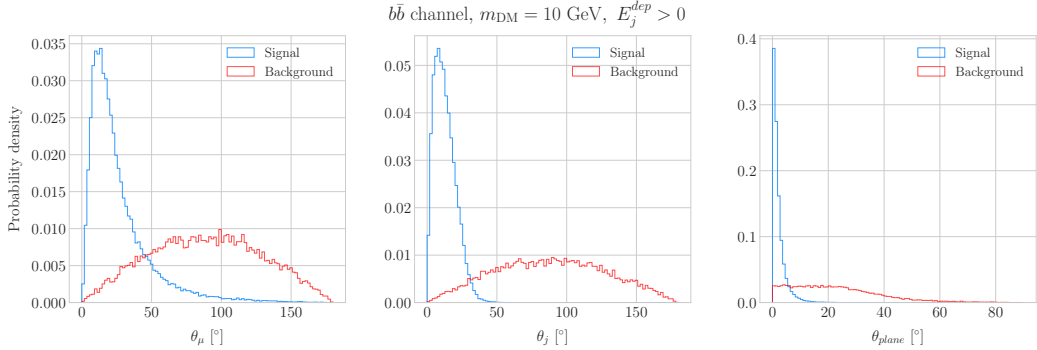


Figure 5.5: Distributions of the muon angle (left panel), jet angle (central panel) and momentum conservation plane angle (right panel) for the $b\bar{b}$ sample with $m_{DM} = 10$ GeV (blue) and the atmospheric background (red).

5.4.1 DIS-like events

To begin with, I consider the high energy part of the neutrino spectrum. In this region **DIS** events dominate, i.e. interactions of the form $\nu_\mu + q_d(\bar{q}_u) \rightarrow \mu^- + q_u(\bar{q}_d)$. Therefore, our final states will contain a muon and a hadronic jet from the fragmentation of the outgoing quark. As all these events have $E_\nu \gtrsim 1$ GeV the momentum transfer to the remnant nucleus is negligible. For this reason, the neutrino energy can be effectively reconstructed just taking into account the momenta of the muon and the jet. This technique was successfully used in Ref. [141] to select monoenergetic **DM** solar neutrino events from the $\nu\bar{\nu}$ annihilation channels.

Using momentum conservation one sees that the plane generated by the momenta of the muon and the jet also needs to contain the momentum of the neutrino. As we are interested in neutrinos coming from the Sun, the direction of the neutrino can be regarded as known beforehand. This will allow us to define the angle of the outgoing muon and jet with respect to the incoming neutrino for each event. Moreover, one can also use that information to reject poorly reconstructed jets, checking for deviations of these from the momentum conservation plane.

To account for the limited angular resolution of the detector, I smeared the momenta of the muons and hadrons. In a **LArTPC** muons are expected to be tracked with high precision, therefore I take the associated angular resolution to be 1° [96]. In the case

5.4. HIGH ENERGY DM NEUTRINO SIGNALS

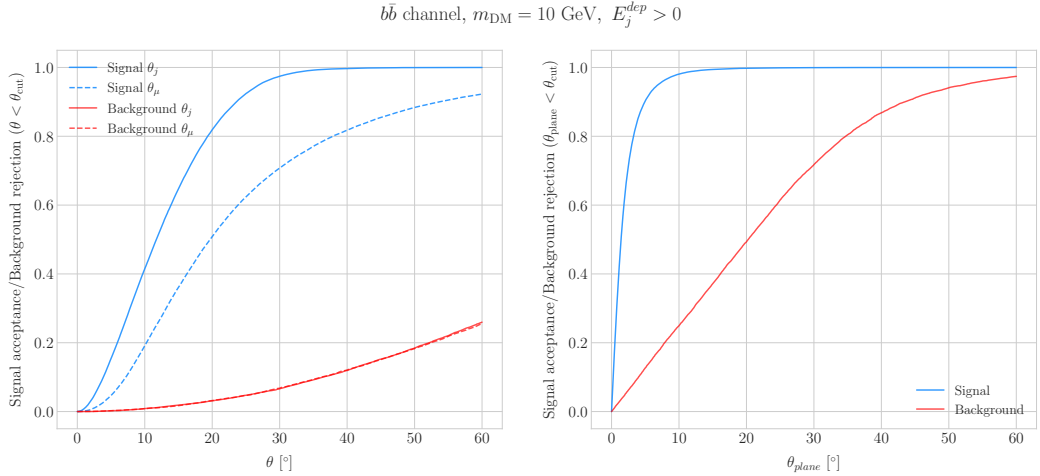


Figure 5.6: Left panel: signal efficiencies (blue lines) and background rejections (red lines) for events passing the cuts $\theta < \theta_{cut}$ for the jet (solid lines) and muon (dashed lines) angles. Right panel: signal efficiency (blue line) and background rejection (red line) for events passing the cut $\theta_{plane} < \theta_{cut}$ for the momentum conservation plane deviation.

of jets, it is expected that for the hadrons dominating the cascade a detector like the **DUNE FD** will have an angular resolution between 1° to 5° [96], so I take the latter for a more conservative estimate.

As a first step, I perform a truth-level pre-selection on the **DIS** events, requiring the **FSI** particles to have kinetic energies above the detection thresholds of **DUNE**. For muons and photons the specified threshold energy is 30 MeV, for charged pions 100 MeV, and for other hadrons 50 MeV [96]. This way, I will drop an event if the outgoing muon has an energy lower than the required threshold. For the case of hadrons and photons, I require at least one particle above the energy threshold, so then one can compute the jet momentum using the (smeared) momenta of the N particles above threshold as:

$$\vec{p}_j = \sum_{i=1}^N \vec{p}_i. \quad (5.9)$$

Additionally, I also estimate the deposited hadronic energy as:

$$E_j^{dep} = \Delta m + \sum_{i=1}^N \sqrt{|\vec{p}_i|^2 + m_i^2}, \quad (5.10)$$

CHAPTER 5. DARK MATTER SEARCHES WITH NEUTRINOS FROM THE SUN

where Δm is the mass difference between the remnant and the initial nucleus. This quantity is useful for selecting events with enough hadronic visible energy in the detector. For events where most of the hadronic energy is scattered across plenty of hadrons with individual energies below the detection threshold, this estimation will give $E_j^{dep} \leq 0$. In these cases it is expected that the jet momentum is poorly reconstructed, and therefore I require events to pass the cut $E_j^{dep} > 0$.

For the events passing the pre-selection, I can compute the angles for the muon and jet with respect to the incoming neutrino as:

$$\cos \theta_\mu = \hat{p}_\nu \cdot \hat{p}_\mu, \quad (5.11)$$

$$\cos \theta_j = \hat{p}_\nu \cdot \hat{p}_j, \quad (5.12)$$

and the deviation from the momentum conservation plane as:

$$\sin \theta_{plane} = \left| \frac{\hat{p}_\mu \times \hat{p}_\nu}{|\hat{p}_\mu \times \hat{p}_\nu|} \cdot \hat{p}_j \right|. \quad (5.13)$$

In Fig. 5.5 I show some distributions of these quantities for the case of the $b\bar{b}$ sample with $m_{DM} = 10$ GeV (blue histograms) and for the atmospheric backgrounds (red). To select the atmospheric events I follow the same criteria as for the signal events. However, because in the signal case I use the true direction of the neutrino as input, as it should be that of the Sun at that time and therefore known, in the atmospheric case I use a set of solar positions as the ansatz for the neutrino direction. From the distributions, one can see that the muon and the jet for the signal events are predominantly forward, and also that the deviations from the momentum conservation plane are peaked at zero, as one should expect.

Now, I can start applying a set of cuts to maximise our signal selection efficiency, while at the same time I try to minimise the amount of atmospheric background events passing the selection. To this end, I need to find some lower and upper cuts for θ_j and θ_μ and an upper bound for θ_{plane} . In Fig. 5.6 I show how upper bound cuts in the

5.4. HIGH ENERGY DM NEUTRINO SIGNALS

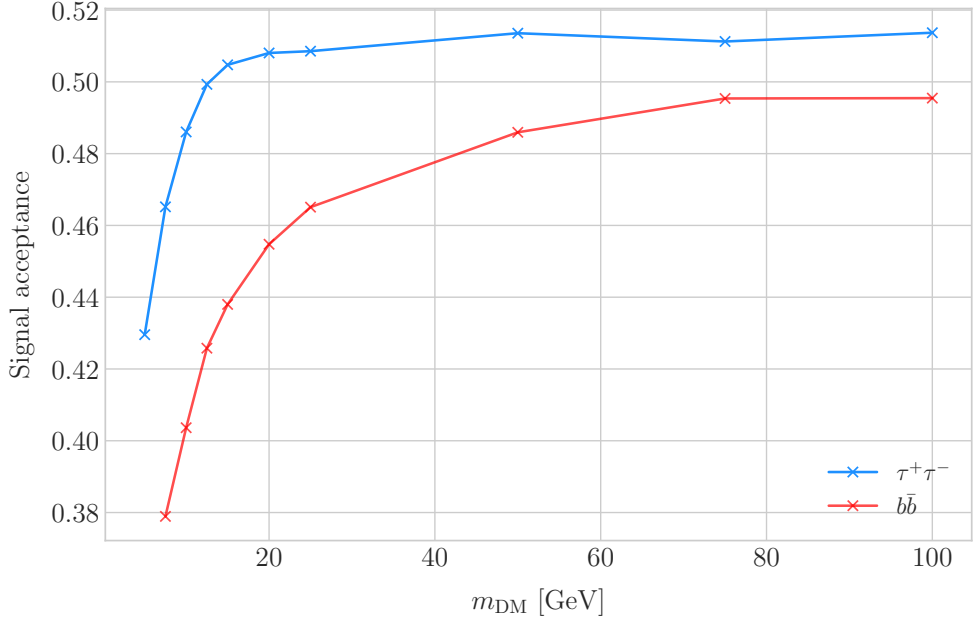


Figure 5.7: Signal efficiencies for the $\tau^+\tau^-$ (blue line) and $b\bar{b}$ (red line) DIS samples as functions of the DM mass, m_{DM} , obtained by applying the optimal angular cuts $\theta_\mu < 27^\circ$, $4^\circ < \theta_j < 26^\circ$ and $\theta_{\text{plane}} < 3.5^\circ$.

different angular variables affect the signal efficiency (blue lines) and the background rejection (red lines). Notice that the signal efficiency behaves in quite a different way when I apply cuts in the jet and the muon angles. On the contrary, the cuts on both variables have a similar effect on the background rejection.

In order to obtain the optimal set of cuts, I perform a multidimensional scan. I do this separately for the $\tau^+\tau^-$ and the $b\bar{b}$ samples. For each case, I scan the possible cuts for every mass point and then I take the mean value of the signal efficiency for each configuration, to get the mean efficiency for each set of cuts. I do a similar scan for the atmospheric sample independently. Then, I take the sets of cuts such that the background rejection achieved is greater than 99.8% and search for the one which maximises the $\tau^+\tau^-$ and $b\bar{b}$ sample efficiencies. Keeping a high background rejection at expense of the signal efficiency is necessary, as this search is dominated by the background.

The cuts were optimised separately for both channels and mass values. However, all the different optimal configurations obtained fell in the same ranges, and the overall performance was not particularly affected when varying the cuts within them. Therefore,

CHAPTER 5. DARK MATTER SEARCHES WITH NEUTRINOS FROM THE SUN

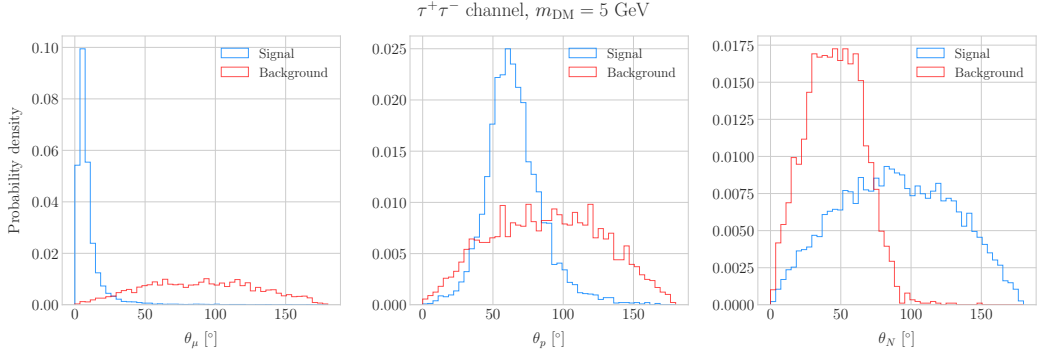


Figure 5.8: Distributions of the muon angle (left panel), proton angle (central panel) and remnant nucleus angle (right panel) for the $\tau^+\tau^-$ QE sample with $m_{\text{DM}} = 5 \text{ GeV}$ (blue) and the atmospheric background (red).

I decided to report a single cut that maximises the mean signal efficiency across the different mass points for the two samples. I found that with the cuts $\theta_\mu < 27^\circ$, $4^\circ < \theta_j < 26^\circ$ and $\theta_{\text{plane}} < 3.5^\circ$ I get a background rejection of 99.80% while achieving 49.40% and 44.92% mean signal efficiencies for the $\tau^+\tau^-$ and $b\bar{b}$ samples, respectively.

In Fig. 5.7 I show the signal efficiencies as a function of the DM mass for the $\tau^+\tau^-$ (blue line) and the $b\bar{b}$ (red line) DIS events, after applying the cuts discussed above, as well as the energy thresholds and hadronic visible energy pre-selections. One can see that the efficiency grows with the mass, as annihilations of more massive DM particles will produce a neutrino spectrum centered at higher energies. This makes it easier to separate the signal from the atmospheric background, which peaks at lower energies. Notice also that the efficiency is higher for the $\tau^+\tau^-$ case at every mass point, as in general this channel produces neutrinos at higher energies than the corresponding $b\bar{b}$ channel.

5.4.2 Single proton QE-like events

Now, one can try to explore the low energy tail of the neutrino energy distributions. This regime is dominated by the QE interactions, i.e. events of the type $\nu_\mu + n \rightarrow \mu^- + p$. The topology of these is very different from that of the DIS events, having typically just a muon and one proton in the final state. I will follow a similar treatment to that in

5.4. HIGH ENERGY DM NEUTRINO SIGNALS

Ref. [133] for the neutrinos from the K^+ decays at rest. However, the events at hand have higher energies and are not monochromatic.

In this case the momentum transfer to the remnant nucleus can be reconstructed from the kinematics of the **FSI** particles. This can be important for events with $E_\nu \leq 1$ GeV. Therefore, I do not make the approximation of assuming that the momentum of the muon and the proton will give an adequate estimation of the reconstructed neutrino energy.

As before, I can take the direction of the incoming neutrino as known. That way, one can estimate the energy of the neutrino as:

$$E_\nu^{reco} = E_\mu + E_p + \Delta m, \quad (5.14)$$

and using momentum conservation I can write the momentum of the remnant nucleus as:

$$\vec{p}_N = \hat{p}_\nu (E_\mu + E_p + \Delta m) - \vec{p}_\mu - \vec{p}_p. \quad (5.15)$$

As in the previous case, I need to drop the events where the muon or the proton fall below the kinetic energy detection threshold [96]. Also, I again apply a smearing to the momenta of the particles, 1% for muons and 5% for protons [96].

Having done that, one can compute the angles of the muon, the proton, and the remnant nucleus with respect to the incoming neutrino as:

$$\cos \theta_\mu = \hat{p}_\nu \cdot \hat{p}_\mu, \quad (5.16)$$

$$\cos \theta_p = \hat{p}_\nu \cdot \hat{p}_p, \quad (5.17)$$

$$\cos \theta_N = \hat{p}_\nu \cdot \hat{p}_N. \quad (5.18)$$

Figure 5.8 shows the distributions of these angular variables for the $\tau^+\tau^-$ **QE** sample with $m_{DM} = 5$ GeV (blue) and the atmospheric background (red). Again, for the atmospheric events I use a random solar position as the ansatz for the incoming neutrino direction. Notice that in this case the proton is typically not as forward as the hadronic

CHAPTER 5. DARK MATTER SEARCHES WITH NEUTRINOS FROM THE SUN

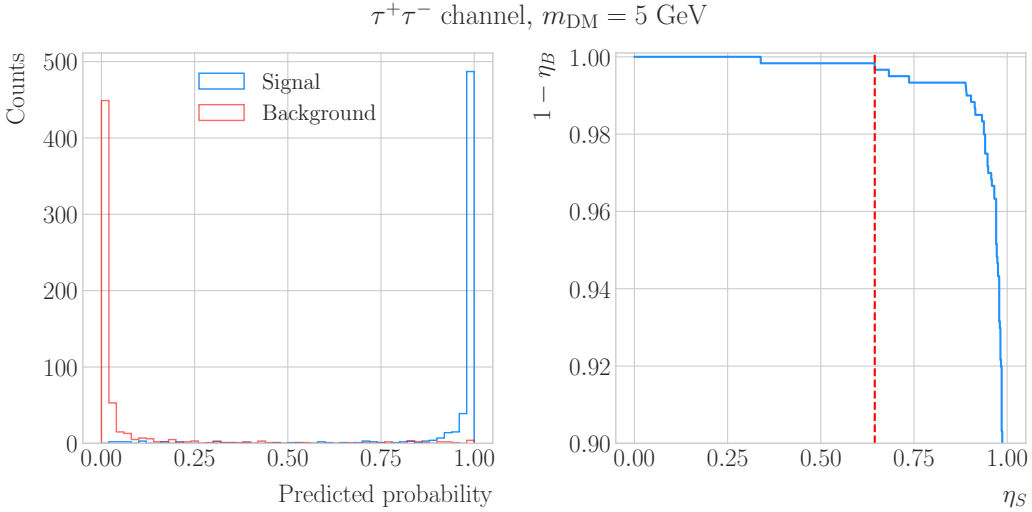


Figure 5.9: Left panel: distributions of the predicted probabilities assigned by the **BDT** classifier to the test sample for the signal (blue) and the atmospheric background (red). Right panel: **ROC** curve in the signal efficiency versus background rejection plane (blue line). The value of η_S for which the target background rejection of 99.8% is achieved is also indicated (dashed red line). In both cases, the signal corresponds to the $\tau^+\tau^-$ **QE** sample with $m_{\text{DM}} = 5$ GeV.

jet is in the **DIS** events. Also, the nucleus angle is uniform for signal events, whereas for the background it is biased towards low values. However, the spread of this angular distribution is significant.

As a consequence of these features, the usual approach of applying simple angular cuts proved to be not as effective as it was in the case of the **DIS** events. Therefore, as a possible solution, I used a boosted decision tree (**BDT**) classifier to separate between signal and background events. In this case, the predicted probability from the classification can be used to form a decision boundary, which will give an estimate of the signal efficiency and the background rejection.

For each **DM** mass value and channel, as well as for the background, I divide the events into training, validation, and test samples. The input variables for the classifier are the angular variables defined in Eqs. (5.16 - 5.18). I use the **BDT** classifier implemented in **scikit-learn** [142], with a maximum depth of four trees, a maximum number of estimators of 400, and early stopping enabled. The rest of the **BDT** parameters are set to their default values. I do not perform a full optimisation of the hyperparameters, as

5.4. HIGH ENERGY DM NEUTRINO SIGNALS

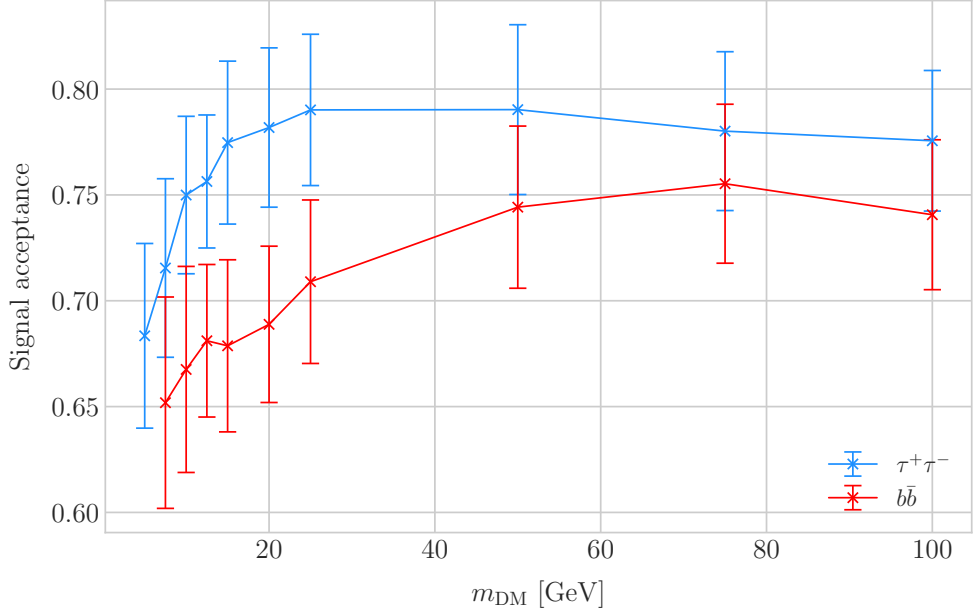


Figure 5.10: Signal efficiencies for the $\tau^+\tau^-$ (blue line) and $b\bar{b}$ (red line) single proton QE samples as functions of the DM mass, m_{DM} , obtained by requiring a background rejection greater than 99.8%.

the goal is simply to demonstrate the power of this method.

The results of the training process for the $\tau^+\tau^-$ QE signal with $m_{\text{DM}} = 5$ GeV are shown in Fig. 5.9. On the left panel I have the distributions of the probabilities predicted by the model, separated in true signal (blue) and background (red) events, for the test sample. On the right panel I show the receiver operating characteristic (ROC) curve for this same sample. This represents the background rejection of the classifier as a function of the signal efficiency. Requiring a background rejection of 99.80% would give a signal efficiency of 64.47% in this case (indicated by the dashed red line).

To obtain a robust estimate of the signal efficiencies, I use a cross-validation approach. In particular, I use the `StratifiedKFold` method in `scikit-learn`. This divides the data into k equal-sized samples (or folds). Then, it performs k training iterations, each time using $k - 1$ of the samples as training data while the remaining fold acts as test sample. In this case, I set $k = 5$ and the metric I extract from the test data is the signal efficiency value which yields a 99.80% background rejection. The final signal efficiency for each channel and mass point is the mean of the metrics obtained from the

CHAPTER 5. DARK MATTER SEARCHES WITH NEUTRINOS FROM THE SUN

cross-validation.

Figure 5.10 shows the result of this procedure. Notice that again the efficiencies for the $\tau^+\tau^-$ channel (blue line) are consistently higher than the ones for the $b\bar{b}$ channel (red line). The angular distributions of the high energy neutrinos are easier to separate from the atmospheric background. Therefore, the signal efficiency grows with the **DM** mass, and benefits from a harder annihilation channel.

5.4.3 Results

To estimate the **DM** cross section sensitivities, the expected number of background events needs to be re-computed. As I am separating events by interaction type, Eq. (5.6) does not hold anymore because in that case I integrated over the total neutrino-argon cross section. In this instance, the expected number of background events for **DIS**-like events is approximately given by:

$$N_B^{DIS} \simeq \eta_B^{DIS} \times (4.655 \times 10^3) \times \left(\frac{\text{exposure}}{400 \text{ kT yr}} \right), \quad (5.19)$$

whereas for **QE**-like events we have:

$$N_B^{QE} \simeq \eta_B^{QE} \times (2.248 \times 10^4) \times \left(\frac{\text{exposure}}{400 \text{ kT yr}} \right). \quad (5.20)$$

Now, using these together with Eqs. (5.7) and (5.8) one can obtain the 90% C.L. upper limit on the total annihilation rate at equilibrium for both kind of events. Then, applying the computed **DM**-nucleons capture rates, I can translate these into limits on the **DM**-nucleon cross section by means of Eq. (5.2).

Figure 5.11 shows the obtained limits on the **SD DM**-nucleon cross section for **DUNE**, using the **DIS** (up triangles) and **QE** (down triangles) events both for the $\tau^+\tau^-$ (blue) and the $b\bar{b}$ (red) samples, for an exposure of 400 kT yr. The coloured bands represent the difference between the realistic efficiencies obtained and the limit of perfect signal efficiency and the optimistic background rejection given by Eq. (5.5). I also include the

5.4. HIGH ENERGY DM NEUTRINO SIGNALS

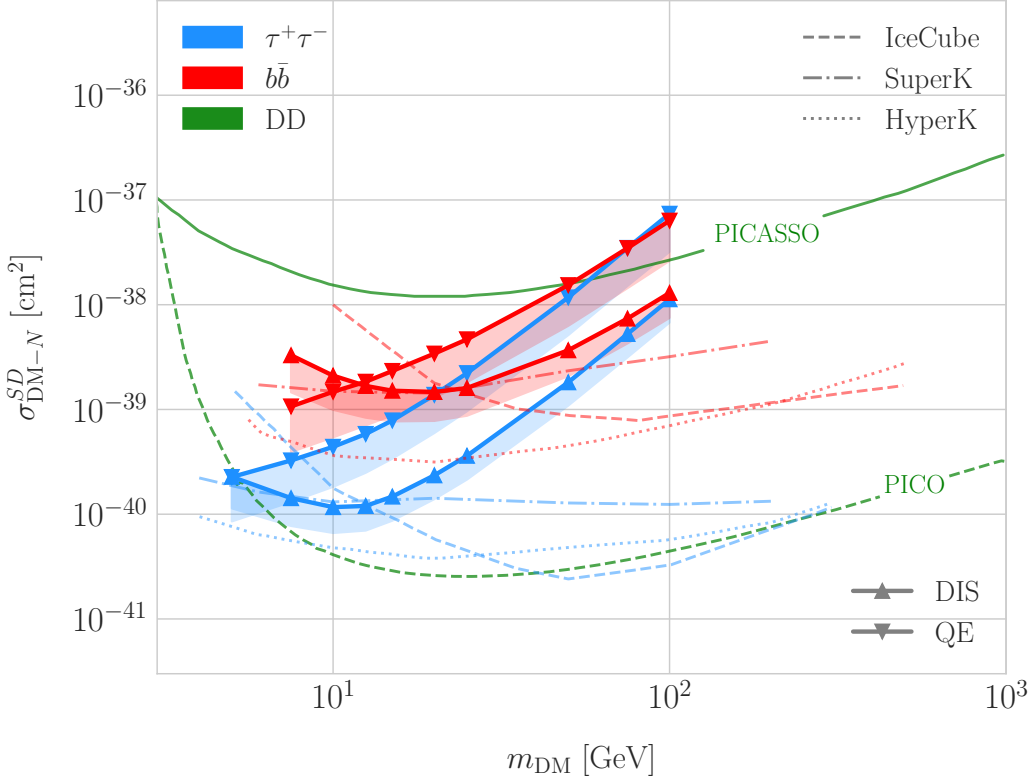


Figure 5.11: Projected 90% confidence level upper limits for DUNE (400 kT yr) on the spin-dependent DM-nucleon scattering cross section as a function of m_{DM} , for the annihilation channels $\tau^+\tau^-$ (blue) and $b\bar{b}$ (red) separated by interaction mode (up triangles denote DIS interactions whereas down triangles represent QE interactions). I also show the previous limits from IceCube [143] (solid lines) and Super-Kamiokande [144] (dash-dotted), and the projected sensitivities for Hyper-Kamiokande [145] (dotted lines), as well as the direct detection limits from PICASSO [146] (solid green line) and PICO-60 C₃F₈ [147] (dashed green line).

corresponding current limits from IceCube [143] (solid lines) and Super-Kamiokande [144] (dash-dotted lines), as well as the projected sensitivities for Hyper-Kamiokande [145] (dotted lines). For comparison, I also show the reported direct detection limits from PICASSO [146] (solid green line) and PICO-60 C₃F₈ [147] (dashed green line).

Notice that, for most of the mass range, the limits one can set using the DIS events are stronger than those of the QE interactions, except for the low mass part of both the $\tau^+\tau^-$ and the $b\bar{b}$ curves where the QE events dominate. In general, the expected sensitivity of DUNE for DM masses ≤ 25 GeV surpasses the stronger current indirect limits. However, experiments like Hyper-Kamiokande are foreseen to have an overall

CHAPTER 5. DARK MATTER SEARCHES WITH NEUTRINOS FROM THE SUN

better sensitivity in this kind of searches, as they have a bigger active volume and accept a broader energy range.

A pending question is what happens when we add the [RES](#) and [MEC](#) charged-current interaction contributions. In that case, it would probably be more convenient to split the samples by final state interaction topologies. Also, another necessary improvement would be adding a full detector simulation and reconstructions. This will also require considering the effect of poorly reconstructed events or final states containing neutral particles, such that they mimic the desired topology at the reconstruction level. The particle identification and tracking capabilities of the detector will also play an important role in the analysis, and are likely to affect the way we extract the variables used in the event selection (either using a cut-based or [BDT](#) approach). However, these fall out of scope for this first sensitivity study.

In Apps. [B.2](#) and [B.3](#) I show the results of two additional studies, where I apply the techniques described before to two specific realisations of the [DM](#) interactions (Kaluza-Klein [DM](#) and leptophilic [DM](#)).

5.5 Systematic uncertainties

The estimation of the [DM](#) cross sections using neutrinos from [WIMP](#) annihilations inside the Sun is affected by systematic uncertainties from different sources, as is the atmospheric background estimation. There are uncertainties common to both types of events, as well as others specific to each. These affect the prediction of the number of background events and the estimation of the [DM](#) annihilation rates, therefore impacting the constraints one can put on the cross sections. Although these are not taken into account for the results presented in this work, in this section I provide a comprehensive summary of the main sources of uncertainty for this analysis, which should be taken into account in any future extensions.

5.5. SYSTEMATIC UNCERTAINTIES

Table 5.1: Systematic uncertainties for the solar **WIMP** signal events. Table adapted from Ref. [148].

Systematic	Value
Form factor	Does not apply to SD [149]
Solar model	3% [149]
Local DM density	Not relevant for relative interpretations [144, 149]
Dynamics of solar system	Negligible [150]
Velocity distributions	20% at 20 GeV [144, 149]
Oscillation parameters	8% for $\tau^+\tau^-$, 5% for $b\bar{b}$ [151]
Neutrino interactions in the Sun	10%
Matter effects in the Earth	10%

5.5.1 Systematic uncertainties in the solar **WIMP** signal

The systematic uncertainties affecting the solar **WIMP** neutrino signal can be divided into two categories. On the one hand, we have those affecting the solar **WIMP** annihilation rate. On the other hand, there are those which modify the neutrino flux resulting from the annihilations reaching our detector.

- **Uncertainties on the annihilation rate.** These include the astrophysical effects that affect the normalisation of the solar **DM** neutrino flux. The main contributions are the solar model choice, the form factor uncertainties (only for **SI** searches), the gravitational effect of other planets, the local **DM** density (not relevant for relative comparisons, as it affects direct detection experiments in the same way), and the **DM** halo and dispersion velocities.
- **Uncertainties on the neutrino flux.** These are related to the oscillation effects, as well as the absorption and regeneration of neutrinos in the Sun. Matter effects inside the Earth also affect the neutrino flux measured by the detectors.

Table 5.1 summarises the contributions of the different sources of uncertainty for the signal events. These are the signal systematic uncertainties that have been taken into account in previous solar **DM** searches with neutrinos [144, 148, 151].

CHAPTER 5. DARK MATTER SEARCHES WITH NEUTRINOS FROM THE SUN

Table 5.2: Systematic uncertainties for the solar WIMP atmospheric background events. Table adapted from Ref. [59].

Systematic	Value
Flux normalisation	25 – 7% for $0.1 < E_\nu \leq 1$ GeV (linear in $\log E_\nu$) 7% up to 10 GeV
$(\nu_\mu + \bar{\nu}_\mu)/(\nu_e + \bar{\nu}_e)$	2% for $E_\nu \leq 1$ GeV 3% for $1 < E_\nu \leq 10$ GeV
$\bar{\nu}_\mu/\nu_\mu$	2% for $E_\nu \leq 1$ GeV 6% for $1 < E_\nu \leq 10$ GeV
K/ π ratio	5% $E_\nu \leq 100$ GeV

5.5.2 Systematic uncertainties in the atmospheric background

For the atmospheric background events, one needs to take into account the systematic uncertainties affecting the atmospheric ν_μ flux. These have been extensively studied in the context of atmospheric neutrino oscillation measurements. Among these, the energy-dependent flux normalisation uncertainty dominates in the low energy regime. Other important contributions to the uncertainty come from the ratios between the muon to electron neutrino and the muon to anti-muon neutrino components of the flux. Additional uncertainty is introduced by the errors in the pion and kaon production rates calculated for the hadronic interactions of cosmic rays in the atmosphere [152].

Table 5.2 shows a summary of the leading contributions to the uncertainty on the atmospheric muon neutrino flux, in the energy range relevant for this analysis.

5.5.3 Common systematic uncertainties

Finally, there are sources of uncertainty common to both signal and backgrounds. These have two different origins:

- **Uncertainties on the neutrino cross section.** These are introduced by the modelling of the neutrino-nucleus interactions. In the context of the solar WIMP analysis, these have been estimated to be 10% for DM masses around 10 GeV [151].

5.6. SUMMARY

- **Uncertainties related to the detector.** They affect the measurement of the neutrino interaction and the final state particles produced. The main detector uncertainties relevant to this analysis are those related to the energy and angular resolutions of the [DUNE FD](#). Other effects, like the timing and triggering efficiencies, will also contribute to the uncertainties. The particular values these will take for this analysis need to be evaluated in the context of [DUNE](#).

5.6 Summary

In this Chapter, I discussed my work on the solar [DM](#) analysis. I explained how the [DUNE FD](#) can be used to probe [DM](#) interactions by measuring the neutrino flux coming from [DM](#) annihilations in the core of the Sun. After introducing the topic of [DM](#) capture and annihilation in a massive object like the Sun in section 5.1, I described what kind of neutrino signals one can expect from such events in section 5.2. Later, in section 5.3 I commented on how [DUNE](#) could constrain the [DM](#) parameter space by performing counting experiments. In section 5.4 I studied the selection efficiency for the $\tau^+\tau^-$ and $b\bar{b}$ channels. I focus on two different kinematic regimes: the high energy neutrinos where [DIS](#) interactions with argon dominate, and the low energy part of the spectrum where neutrinos mainly undergo [QE](#) interactions. This allowed me to compute the projected generator-level [DM](#) cross section sensitivities, showing how [DUNE](#) can be complementary to other indirect [DM](#) searches. Additionally, I presented a summary of the relevant systematic uncertainties in section 5.5.

These studies show the complementarity of the [DUNE FD](#) to other large-volume neutrino detectors in the search for [DM](#) in the Sun. These first results show that the expected sensitivity of [DUNE](#) for [DM](#) masses ≤ 25 GeV surpasses the current limits on the spin-dependent [DM](#)-nucleon cross section set by other indirect detection experiments. Future iterations of this analysis, including full detector simulation and reconstruction and the effect of systematic uncertainties, will give us a clear idea of the capabilities of [DUNE](#) as a solar [DM](#) detector.

6

Particle identification in ND-GAr

I am no bird; and no net ensnares me; I am a free human being with an independent will.

– Charlotte Brontë, *Jane Eyre*

In DUNE Phase II, ND-GAr will fulfill the role of TMS measuring the momentum and sign of the charged particles exiting ND-LAr. Additionally, it will measure neutrino interactions inside the HPgTPC. This way, ND-GAr will constrain certain cross-section systematic uncertainties and study the effect of FSI in CC interactions. To do so, it needs to measure the spectrum of protons and charged pions at low energies, as well as the pion multiplicity. This puts strong requirements on the particle identification (PID) capabilities of the detector, as well as stimulating the relevant developments in the reconstruction.

The goal of the present Chapter is to provide an overview of the current status and design of the GArSoft package, the simulation and reconstruction software of ND-GAr, and present the contributions and upgrades that I have implemented to enhance the reconstruction with the PID in mind. These contributions include:

- developing the calibration of the HPgTPC to enable PID at low momenta using calorimetry,
- designing a strategy to use the information from the ECal and MuID for separating muons and charged pions,

CHAPTER 6. PARTICLE IDENTIFICATION IN ND-GAr

- and using a combination of the [HPgTPC](#) and [ECal](#) to perform a time-of-flight measurement for identifying protons at high momenta.

6.1 GArSoft

GArSoft is a software package developed for the simulation and reconstruction of events in [ND-GAr](#). It is inspired by the LArSoft toolkit [120] used for the simulation of [LArTPC](#) experiments, like the [DUNE FD](#) modules. It is based on [art](#), the framework for event processing in particle physics experiments [153]. Its main dependencies are [ROOT](#) [154], [GENIE](#) [155, 156] and [Geant4](#) [121–123]. It allows the user to run all the steps of a generation-simulation-reconstruction workflow using Fermilab Hierarchical Configuration Language ([FHiCL](#)) files.

6.1.1 Event generation

The standard generator [FHiCL](#) files in GArSoft run the event generation and particle propagation simulation (i.e. [Geant4](#)) in the same job by default. However, it is possible to split them up if needed. The current version of GArSoft provides five different event generators, each of them producing [simb::MCTruth](#) products. The available modules are:

- **SingleGen**: particle gun generator. It produces the specified particles with a given distribution of momenta, initial positions and angles.
- **TextGen**: text file generator. The input file must follow the [hepevt](#) format, the module simply copies the event records into [simb::MCTruth](#) objects.
- **GENIEGen**: GENIE neutrino event generator. The module runs the neutrino-nucleus interaction generator using the options specified in the driver [FHiCL](#) file (flux file, flavour composition, number of interactions per event, t_0 distribution, ...). Current default version is `v3_04_00`, tune `G18`.

6.1. GArSOFT

- **RadioGen**: radiological generator. It produces a set list of particles to model radiological decays.
- **CRYGen**: cosmic ray generator. The module runs the **CRY** event generator [157] with a configuration specified in the **FHiCL** file (for example latitude and altitude of the detector, and energy threshold).

The module **GArG4** searches for all the generated **simb::MCTruth** data products, using them as inputs to the **Geant4** simulation with the specified detector geometry. The current version of the simulated **ND-GAr** geometry is that described in section 3.5.2. A constant 0.5 T magnetic field along the drift coordinate is assumed. The main outputs of this step are **simb::MCParticle** objects for the generated **Geant4** particles, **gar::EnergyDeposit** data products for the energy deposits in the **HPgTPC** and **gar::CaloDeposit** data products for the energy deposits in the **ECal** and muon system.

6.1.2 Detector simulation

The standard detector simulation step in GArSoft is all run with a single **FHiCL**, but the different modules can be run independently as well. First the **IonizationReadout** module simulates the charge readout of the **HPgTPC**, and later the **SiPMReadout** module runs twice, once for the **ECal** and then for the muon system, with different configurations.

The **IonizationAndScintillation** module collects all the **gar::EnergyDeposit** data products, to compute the equivalent number of ionisation electrons for each energy deposit. The **ElectronDriftAlg** module simulates the electron diffusion numerically, both in the longitudinal and transverse directions, and applies an electron lifetime correction factor. The induced charge on the nearest and neighbouring readout pads is modeled using the provided pad response functions. The digitisation of the data is then simulated with the **TPCReadoutSimAlg** module. By default, the **ADC** sampling rate used is 50.505 MHz. The resulting raw waveforms for each channel are stored with zero-suppression, in order to save memory and CPU time. The algorithms keep blocks

CHAPTER 6. PARTICLE IDENTIFICATION IN ND-GAr

of [ADC](#) values above a certain threshold, plus some adjustable additional early and late tick counts. The results of these three steps are `gar::raw::RawDigit` data products.

For the [ECal](#) and the muon system the `SiPMReadout` module calls either the `ECALReadoutSimStandardAlg` or `MuIDReadoutSimStandardAlg` modules. These take all the `gar::CaloDeposit` data products in the corresponding detector, and perform the digitisation depending on whether the hit was in a tile or strip layer. They include single photon statistics, electronic noise, SiPM saturation and time smearing. The resulting objects are `gar::raw::CaloRawDigit` data products.

6.1.3 Reconstruction

The reconstruction in GArSoft is also run as a single job by default. It first runs the hit finding, clustering, track fitting and vertex identification in the [HPgTPC](#), followed by the hit finding and clustering in the [ECal](#) and muon system. After those, it produces the associations between the tracks and the [ECal](#) clusters.

Focusing first on the [HPgTPC](#) reconstruction, the `CompressedHitFinder` module takes the zero-suppressed [ADC](#)s from the `gar::raw::RawDigit` data products. The reconstructed hits largely correspond to the above-threshold blocks, however the hit finder identifies waveforms with more than one maximum, dividing them into multiple hits if they dip below a certain threshold. The data products produced are of the form `gar::rec::Hit`. These are the inputs to the clustering of hits in the `TPCHitCluster` module. Hits close in space and time are merged, and the resulting centroids are found. This module outputs `gar::rec::TPCClusters` objects and associations to the input hits.

The following step prior to the track fitting is the pattern recognition. The module called `tpcvechitfinder2` uses the `gar::rec::TPCClusters` data products to find track segments, typically called vector hits. They are identified by performing linear 2D fits to the positions of the clusters in a 10 cm radius, one fit for each coordinate pair. For each direction, the sum of slopes (in absolute value) in the 2D fits is computed. Setting the independent variable as the direction with the smallest slope sum, a final 3D fit defines

6.1. GARSOFT

the line segment of the vector hit. The clusters are merged into a given vector hit if they are less than 2 cm away from the line segment. The outputs are `gar::rec::VecHit` data products, as well as associations to the clusters. The `tpcpatrec2` module takes the `gar::rec::VecHit` objects to form the track candidates. The vector hits are merged together if their direction matches, their centres are within 60 cm and their direction vectors point roughly to their respective centres. Once the clusters of vector hits are formed, they are used to make a first estimation of the track parameters simply taking three clusters along the track. The module produces `gar::rec::Track` data products and associations between these tracks and the clusters and vector hits.

The track is fitted by means of a Kalman filter in the `tpctrackfit2` module, using the position along the drift direction as the independent variable. Two different fits are performed per track, a forward and a backwards fit, each starting from one of the track ends. The Kalman filter state vector ($y, z, R, \phi, \tan\lambda$) is estimated at each point along the track using a Bayesian update. The track parameters reported in the forward and backwards fits are the ones computed at the opposite end where the fit started. The main outputs of the track fit are the `gar::rec::Track` objects. Additionally, the module stores the fitted 3D positions along the track in the `gar::rec::TrackTrajectory` data products, and the total charge and step sizes for each point also get stored in the form of `gar::rec::TrackIonization` objects.

After the tracking step, the `vertexfinder1` module looks at the reconstructed `gar::rec::Track` products, creating vertex candidates with the track ends that are within 12 cm of each other. The vertices are then fitted using linear extrapolations from the different track ends associated. The results are `gar::rec::Vertex` data products, and associations to the tracks and corresponding track ends.

For the `ECal` and muon tagger, the `SiPMHitFinder` module runs twice with different configurations, adapted to the particular capabilities of both. The module simply takes the `gar::raw::CaloRawDigit` products, applies a calibration factor to convert the `ADC` counts to MeV, and for the strip layer hits it calculates the position along the strip using the times recorded by both SiPMs. This module produces `gar::rec::CaloHit` data

CHAPTER 6. PARTICLE IDENTIFICATION IN ND-GAr

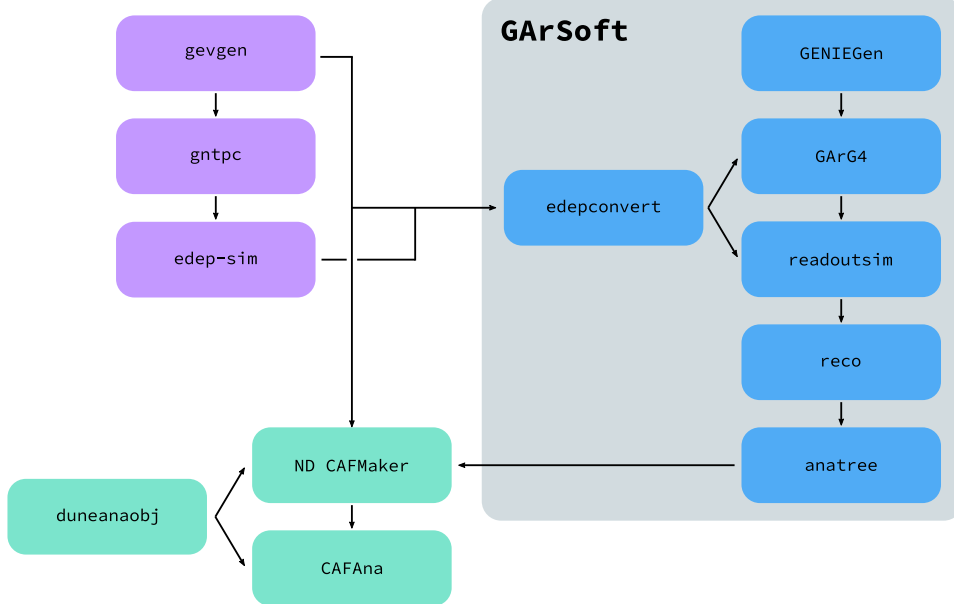


Figure 6.1: Schematic diagram showing the different modules involved in the ND-GAr neutrino event production.

products. Next, these objects are used as inputs to the `CaloClustering` module. It merges the hits based on a simple nearest neighbours (`NN`) algorithm. For the resulting clusters it also computes the total energy and position of the centroid. The results are stored as `gar::rec::Cluster` data products, with associations to the hits.

The last step in the reconstruction is associating the reconstructed tracks in the `HPgTPC` to the clusters formed in the `ECal` and `MuID`. The `TPCECALAssociation` module checks first the position of the track end points, considering only the points that are at least 215 cm away from the cathode or have a radial distance to the centre greater than 230 cm. The candidates are propagated up to the radial position (in the case of clusters in the barrel) or the drift coordinate position (for the end cap clusters) of the different clusters in the collection using the track parameters computed at the end point. The end point is associated to the cluster if certain proximity criteria are met. This module creates associations between the tracks, the end points and the clusters. The criteria for the associations are slightly different for the `ECal` and the `MuID`.

Figure 6.1 shows the simulation and reconstruction workflow of neutrino event

6.2. dE/dx MEASUREMENT IN THE TPC

production in [ND-GAr](#). The diagram also presents other external packages used to produce analysis files.

6.2 dE/dx measurement in the TPC

Among the parameters extracted from the track fitting, ionisation is particularly useful for particle identification, as it is a function of the particle velocity. For the case of relativistic particles this dependence is not very strong, but measuring the track on a large number of points may allow us to estimate the amount of ionisation accurately. This, paired with a measurement of the momentum, may allow us to identify the particle type.

The first calculation of the energy loss per unit length for relativistic particles using a quantum-mechanical treatment is due to H. Bethe [158]. Using this approach, the mean ionisation rate of a charged particle traveling through a material medium is (using natural units $G = \hbar = c = 1$):

$$\left\langle \frac{dE}{dx} \right\rangle = \frac{4\pi Ne^4}{m_e \beta^2} z^2 \left(\log \frac{2m_e \beta^2 \gamma^2}{I} - \beta^2 \right), \quad (6.1)$$

where N is the number density of electrons in the medium, e the elementary charge, m_e is the electron mass, z the charge of the particle in units of e , β is the velocity of the particle, $\gamma = (1 - \beta^2)^{-1}$, and I denotes the effective ionisation potential averaged over all electrons. This relation is known as the Bethe-Bloch formula.

From Eq. (6.1) one can see that the ionisation loss does not depend explicitly on the mass of the charged particle, that for non-relativistic velocities it falls as β^{-2} , then goes through a minimum, and increases as the logarithm of γ . This behaviour at high velocities is commonly known as the relativistic rise. The physical origin of this effect is partly due to the fact that the transverse electromagnetic field of the particle is proportional to γ , therefore as it increases so does the cross section.

It was later understood that the relativistic rise could not grow indefinitely with γ . A way to add this feature in the Bethe-Bloch formula is by introducing the so-called

CHAPTER 6. PARTICLE IDENTIFICATION IN ND-GAR

density effect term. It accounts for the polarisation effect of the atoms in the medium, which effectively shield the electromagnetic field of the charged particle halting any further increase of the energy loss [159]. Denoting the correction as $\delta(\beta)$, one can rewrite Eq. (6.1) as:

$$\left\langle \frac{dE}{dx} \right\rangle = \frac{4\pi Ne^4}{m_e \beta^2} z^2 \left(\log \frac{2m_e \beta^2 \gamma^2}{I} - \beta^2 - \frac{\delta(\beta)}{2} \right). \quad (6.2)$$

In general, the form of $\delta(\beta)$ depends on the medium and its state of aggregation, involving the usage of empirical parametrisations and tabulated values [160].

Another standard method to compute the amount of ionisation a charged particle produces is the so-called photo-absorption ionisation (**PAI**) model proposed by W. Allison and J. Cobb [161]. Within their approach, the mean ionisation is evaluated using a semiclassical calculation in which one characterises the continuum material medium by means of a complex dielectric constant $\varepsilon(k, \omega)$, which is a function of the energy and momentum exchanged between the moving particle and the atoms and electrons in the medium, ω and k . However, in order to model the dielectric constant they rely on the quantum-mechanical picture of photon absorption and collision. Therefore, in the **PAI** model the computation of the ionisation loss involves a numerical integration of the measured photo-absorption cross section for the relevant material.

In a particle physics experiment, the typical way of determining the energy loss per unit length as a function of the particle velocity is studying identified particles over a range of momenta. Once we have established this relation we can use it for other, unknown particles. In this sense, it makes sense to have a regular mathematical expression for this relation that one can use.

It happens that neither the Bethe-Bloch theory nor the **PAI** model from Allison and Cobb offer a closed mathematical form for the ionisation curve. This is the reason why a full parametrisation of the ionisation curves can be useful. A parametrisation originally proposed for the **ALEPH TPC** [162] and later used by the **ALICE TPC** [163] group that

6.2. dE/dx MEASUREMENT IN THE TPC

manages to capture the features of the ionisation energy loss is:

$$f(\beta\gamma) = \frac{P_1}{\beta^{P_4}} \left(P_2 - \beta^{P_4} - \log \left[P_3 + \frac{1}{(\beta\gamma)^{P_5}} \right] \right), \quad (6.3)$$

where P_i are five free parameters. Hereafter, I will refer to Eq. (6.3) as the [ALEPH](#) dE/dx parametrisation.

6.2.1 Truncated dE/dx mean

GArSoft provides a collection of charge deposits for each reconstructed track. In order to obtain the mapping between charge and energy in the [HPgTPC](#), I produced an [MC](#) sample consisting of single, isotropic protons. The starting points of the protons were sampled inside a $50 \times 50 \times 25$ cm box centred at $(100, -150, 1250)$ cm, and their momenta are uniformly distributed in the range $0.25 - 1.75$ GeV. The details of the energy calibration method developed are given in App. [C.1](#).

Once we have a collection of dE/dx values for each track, we can compute the corresponding most probable ionisation loss per unit length of the particle. This is the value predicted by the Bethe-Bloch or the [PAI](#) models, and together with a measurement of the momentum it allows for particle identification.

However, estimating the most probable dE/dx value for each reconstructed track is not a trivial task, as the dE/dx follows a Landau-like distribution [164]. Therefore, one should perform e.g. a LanGauss¹ fit to correctly estimate the most probable values. Automating these kinds of fits is often problematic, as they usually incur in non-convergence problems. Moreover, the reconstructed dE/dx distributions we obtain tend to have relatively low statistics, which may also produce poor fits. In practice, doing these unsupervised fits may degrade our performance, and a more robust method is preferred.

A possibility could be taking the mean of the reconstructed dE/dx distribution for each particle. The problem with this approach is that the high energy Landau tail,

¹I use the term LanGauss to refer to a Landau distribution convolved with a Gaussian. In the literature, this distribution is often referred to as Landau+Gaussian or `langau`.

CHAPTER 6. PARTICLE IDENTIFICATION IN ND-GAR

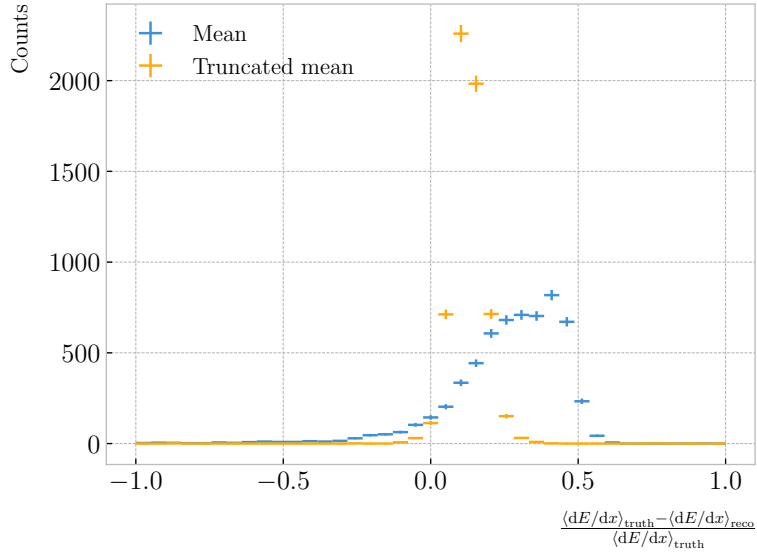


Figure 6.2: Fractional residuals between the true and the reconstructed calibrated dE/dx means (blue) and the 60% truncated means (yellow), for each event in the stopping proton sample.

combined with our limited statistics, can induce large fluctuations in the computation of the mean. Imagine you have two protons with the same kinetic energy, but due to reconstruction problems (or mere chance) in one case you do not get as many charge deposits reconstructed in its high ionisation loss region. If you do not remove the tails, the computed dE/dx means will be significantly different.

In order to avoid those fluctuations, one can compute the mean of a truncated dE/dx distribution instead. By keeping only a given fraction of the lowest energy deposits we obtain an estimate of the mean energy loss that is more resilient to reconstruction inefficiencies and statistical effects. Figure 6.2 shows a comparison between the $\langle dE/dx \rangle$ computed by taking the mean of the full distribution (blue line) and the 60% lowest energy clusters (yellow line), for the stopping proton sample. The fractional residuals are computed for each proton, taking the corresponding means using their collections of true and reconstructed energy deposits. One can see that using the simple mean translates into a high bias and uncertainty in the $\langle dE/dx \rangle$ estimation, whereas applying the truncation reduces both significantly.

The next step is to optimise the level of truncation we are going to apply to our

6.2. dE/dx MEASUREMENT IN THE TPC

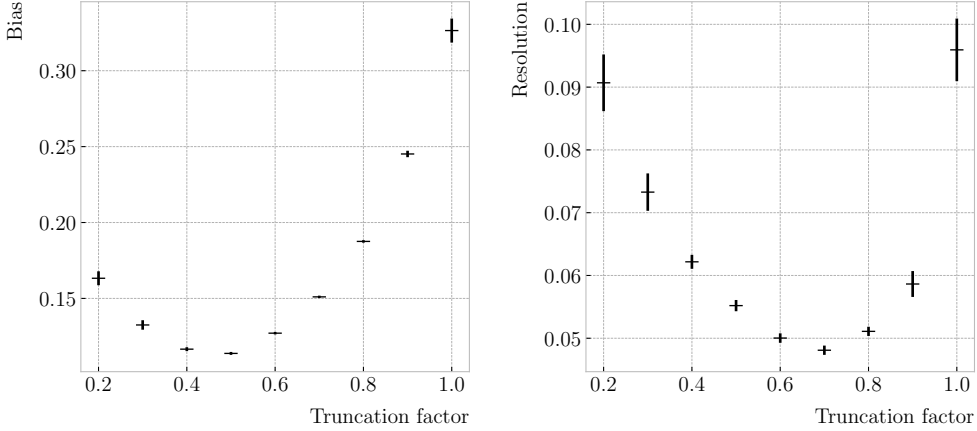


Figure 6.3: Estimated values of the mean dE/dx bias (left panel) and resolution (right panel) obtained using the calibrated data from the stopping proton sample, for different values of the truncation factor.

data. To do so, I use different truncation factors, i.e. the percentage of energy-ordered reconstructed energy deposits we keep to compute the mean calibrated dE/dx values of the stopping proton sample. Then, following the same procedure of computing the fractional residuals as before, I fit the resulting histograms using a double Gaussian function. This is simply the sum of two Gaussian functions of the type:

$$g(x; \mu, \sigma, A) = A e^{-\frac{(x-\mu)^2}{2\sigma^2}}. \quad (6.4)$$

I do not add the classical normalisation factor of the Gaussian, $1/\sqrt{2\pi}\sigma$, therefore the amplitude A simply represents the maximum of the function. One of the two Gaussian functions describes the core part of the distribution, while the other captures the behaviour of the tails.

For each truncation factor, I look at the bias and the resolution I obtain. I define these as the weighted means of the corresponding parameters in the fits:

$$\bar{x} = \frac{A_{core} x_{core} + A_{tail} x_{tail}}{A_{core} + A_{tail}}, \quad (6.5)$$

where A_{core} and A_{tail} are the amplitudes of the core and tail distributions, respectively, and x is either the mean μ or the width σ of said distributions.

CHAPTER 6. PARTICLE IDENTIFICATION IN ND-GAr

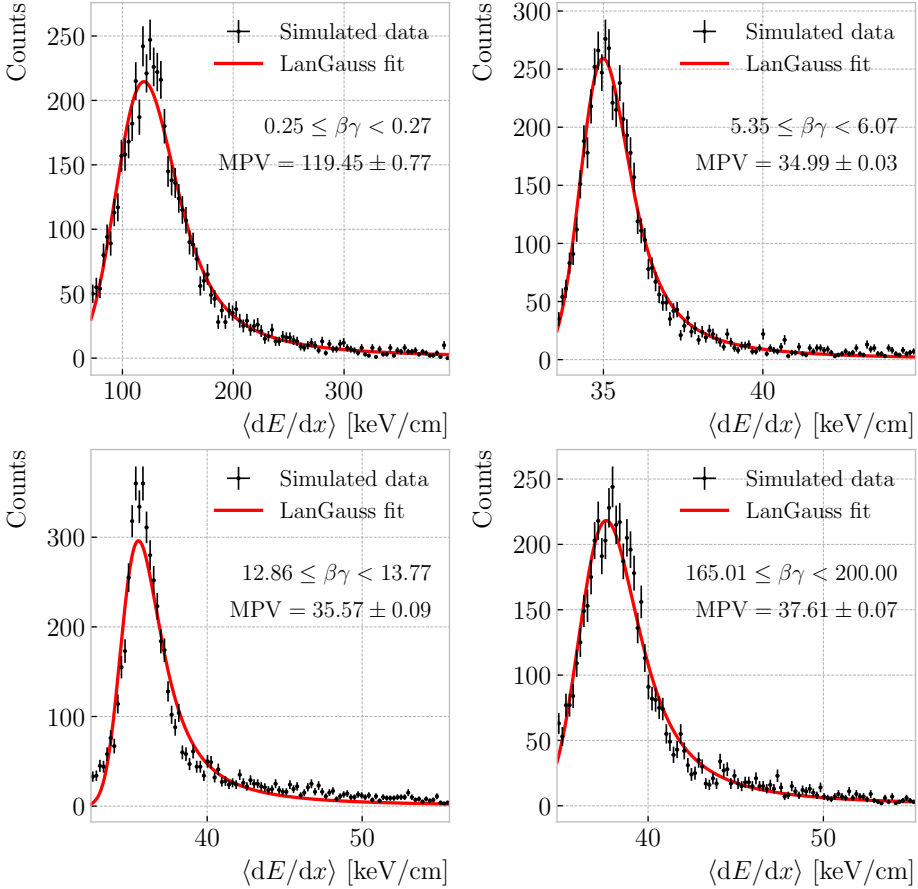


Figure 6.4: Examples of the truncated mean dE/dx LanGauss fits for various $\beta\gamma$ bins, from a simulated [FHC](#) neutrino sample.

Figure 6.3 shows the bias (left panel) and the resolution (right panel) I obtain for the stopping proton sample, using different values of the truncation. From these, it can be seen that a truncation factor of 50% minimises the bias in the estimation, while 70% gives the best resolution. That way, I settled on the intermediate value of 60% truncation, which yields a $\langle dE/dx \rangle$ resolution of 5.00 ± 0.08 % for stopping protons.

6.2.2 Mean dE/dx parametrisation

Now that we have a way to estimate the mean energy loss of a particle in the [HPgTPC](#), we can determine the value of the free parameters in the [ALEPH](#) formula, Eq. (6.3). For this, I produced a sample of 10^5 reconstructed [FHC](#) neutrino events inside [ND-GAr](#). In this case I do not use the stopping proton sample, as we need to cover the full kinematic

6.2. dE/dx MEASUREMENT IN THE TPC

range of interest for the neutrino interactions in our detector.

Among the reconstructed data objects, the sample does not include an estimation of the velocity of the tracks. Instead, the tracks have a value for the reconstructed momentum and the associated [PDG](#) code of the [Geant4](#)-level particle that created the track. Therefore, one can extract some of the tracks in the sample. In this case I select the ones associated to electrons, muons, pions and protons, and compute β and γ using the reconstructed momentum and their mass. In terms of $\beta\gamma$ the mean dE/dx does not depend on the particle species, so one can consider the dataset as a whole. For this fit, I will express β in terms of the $\beta\gamma$ product as:

$$\beta = \frac{\beta\gamma}{\sqrt{1 + (\beta\gamma)^2}}, \quad (6.6)$$

which can be easily proven from the definition of γ .

Next, I bin the sample in $\beta\gamma$. I chose a fine binning so as to capture the different features of the ionisation curve. Instead of fixing the bin width, I select them so each one has approximately the same statistics. Then, for each $\beta\gamma$ slice, I compute the median and the interquartile range ([IQR](#)) of the $\langle dE/dx \rangle$ distribution. Using these, I make a histogram in the range [median – IQR, median + 5 IQR], which I fit to a LanGauss function in order to extract the [MPV](#). Using this range accounts for the asymmetric nature of the distributions, while also helps avoiding a second maximum present at low $\beta\gamma$, probably as a result of reconstruction failures.

A few examples of these fits are shown in Fig. 6.4. The chosen values of $\beta\gamma$ sit at very distinct points along the $\langle dE/dx \rangle$ curve, going from the high ionisation region at low velocities (top left panel), to the minimum point (top right panel), the beginning of the relativistic rise (bottom left panel), and the plateau produced by the density effect (bottom right panel).

I use the resulting most probable $\langle dE/dx \rangle$ values and the centres of the $\beta\gamma$ bins as the points to fit to the [ALEPH](#) formula. For this particular fit, I employ the least-squares method to get a first estimation of the [ALEPH](#) parameters. Applying uniform priors, I

CHAPTER 6. PARTICLE IDENTIFICATION IN ND-GAr

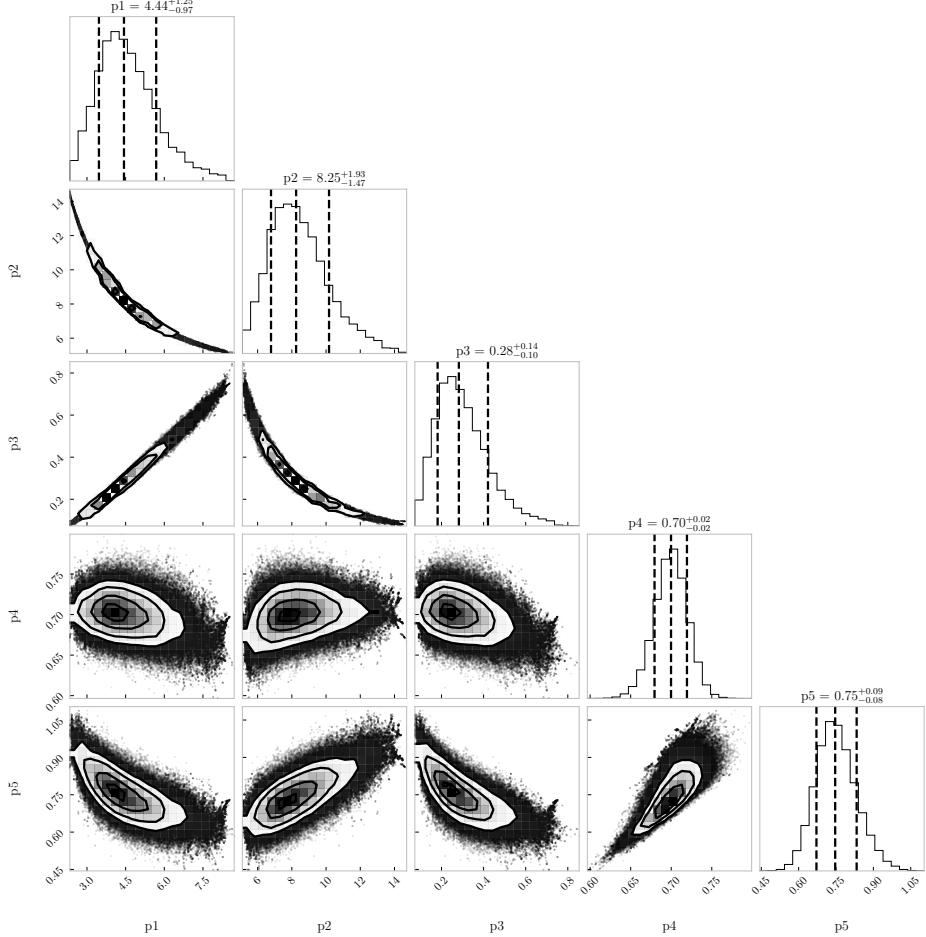


Figure 6.5: Resulting one and two dimensional projections of the posterior probability distributions of the [ALEPH](#) $\langle dE/dx \rangle$ parameters obtained by fitting the 60% truncated mean dE/dx values from a [FHC](#) neutrino sample in [ND-GAr](#). The vertical dashed lines in the 1D distributions represent the 16th, 50th and 84th percentiles.

then use these values as the starting point of a 10^5 step Markov chain [MC](#). Figure 6.5 shows the posterior probability distributions I obtain for each parameter. The reported best fit points are based on the 16th, 50th, and 84th percentiles in the marginalised distributions.

The resulting fit (black line), compared to the data points (red points) and the underlying distribution is shown in Fig. 6.6 (top panel). The overall fit is good, with a reduced chi-squared of $\chi^2/ndf = 1.02$. However, there are some regions where the fit does not describe the data correctly, like the very low $\beta\gamma$ regime, where the fit severely underestimates the dE/dx for energy losses ≥ 50 keV/cm, and the start of the

6.2. dE/dx MEASUREMENT IN THE TPC

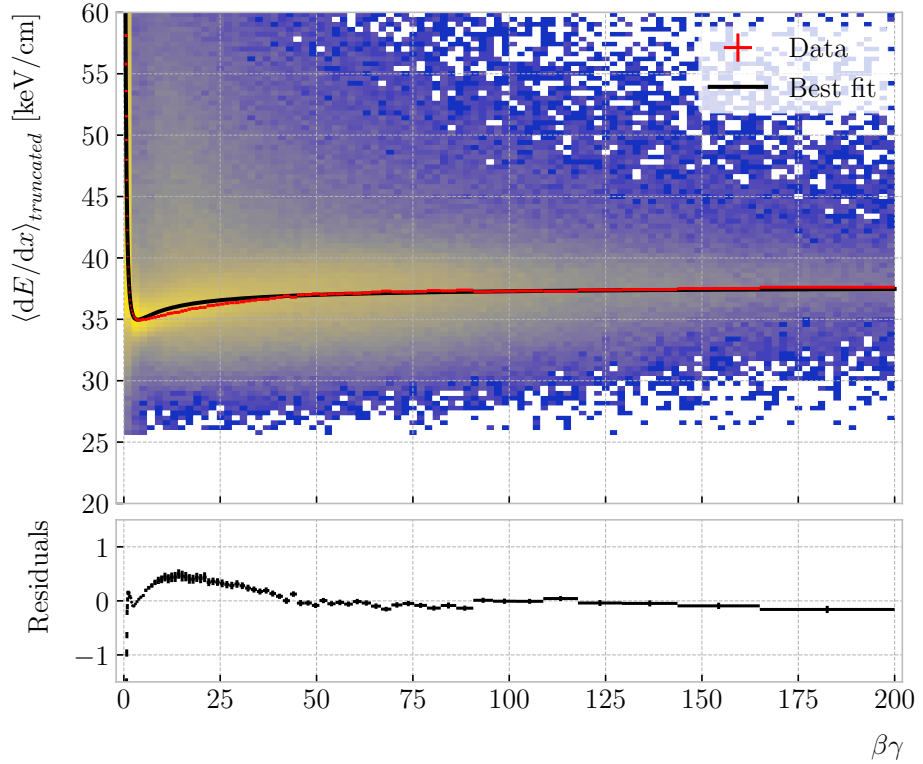


Figure 6.6: Truncated mean dE/dx obtained for the [FHC](#) neutrino sample as a function of the $\beta\gamma$ product (upper panel). Also shown are the fitted most probable values for each $\beta\gamma$ bin (red points) and the best fit obtained using the [ALEPH](#) parametrisation (black line). The residuals resulting from the fit are shown in the lower panel.

relativistic rise, where we have a slight overestimation. This is a result of those points having a larger uncertainty when compared to the ones around the dip or the plateau areas. These differences can be better seen in the residual plot, Fig. 6.6 (bottom panel).

It is interesting to look at the results of the fit in momentum space, for the different particle species. Figure 6.7 shows the truncated mean dE/dx values versus the reconstructed momentum for the neutrino sample. Using a logarithmic scale for the momentum helps with visualising the curves corresponding to the various particles. The resulting fits for electrons, muons, pions and protons are also shown (solid black lines). Notice that each curve stops at a different momentum value, as the fits only extend up to $\beta\gamma = 200$ and translating this limit into momentum depends on the particle.

From Fig. 6.7, the particle separation power of the $\langle dE/dx \rangle$ measurement is evident.

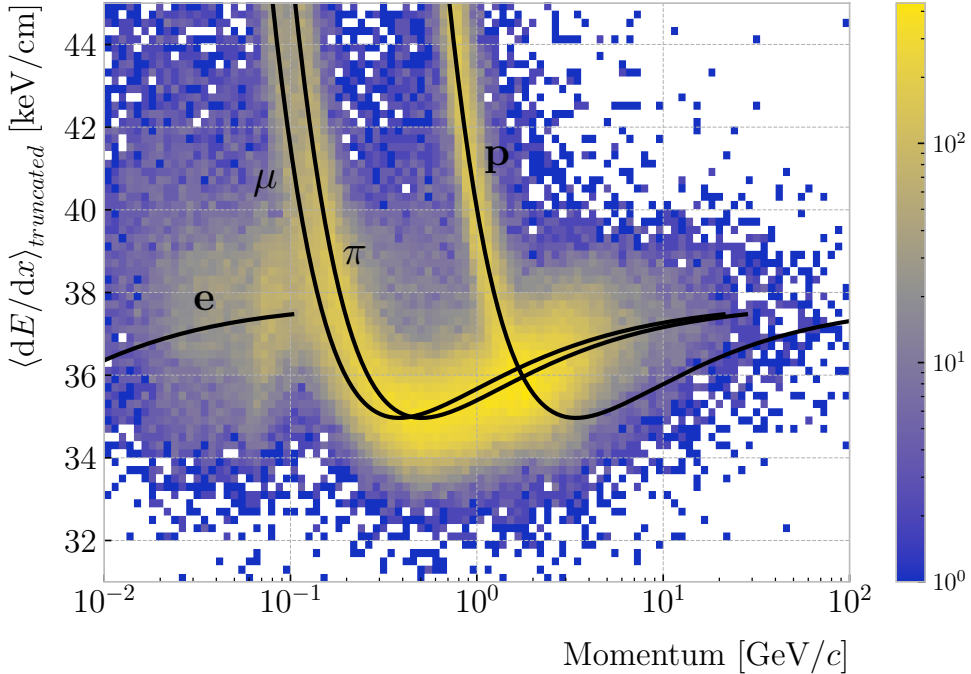


Figure 6.7: Distribution of the 60% truncated mean $\langle dE/dx \rangle$ versus reconstructed momentum for the FHC neutrino sample. The black lines indicate the predictions of the ALEPH parametrisation for electrons, muons, charged pions and protons.

In the low momentum regime, below $300 \text{ MeV}/c$, separating muons and pions should be possible using this method, even if it is with a low significance. On the other hand, protons can be reliably identified up to $1.5 \text{ GeV}/c$.

Relevant to the separating power is the $\langle dE/dx \rangle$ resolution. This can be obtained from the fit, by taking the ratio of the difference between the expected energy loss for a given particle type and momentum and the measured value over the expectation. Then, performing a double Gaussian fit we can extract the bias and the resolution by means of Eq. (6.5). Figure 6.8 presents the values of the $\langle dE/dx \rangle$ bias (left panel) and resolution (right panel) as a function of the momentum for the true protons in the neutrino sample.

When compared to the values for the resolution obtained for the stopping proton sample (see e.g. Fig. 6.3), it appears that the resolution is worse. For that low energy sample the resolution obtained was 5%, whereas now we only achieve those numbers for momenta $\geq 0.75 \text{ GeV}/c$. However, there are several differences between these two cases. The former was obtained for a single proton sample, with tracks fully contained in the

6.3. MUON AND PION SEPARATION IN THE ECAL AND MUID

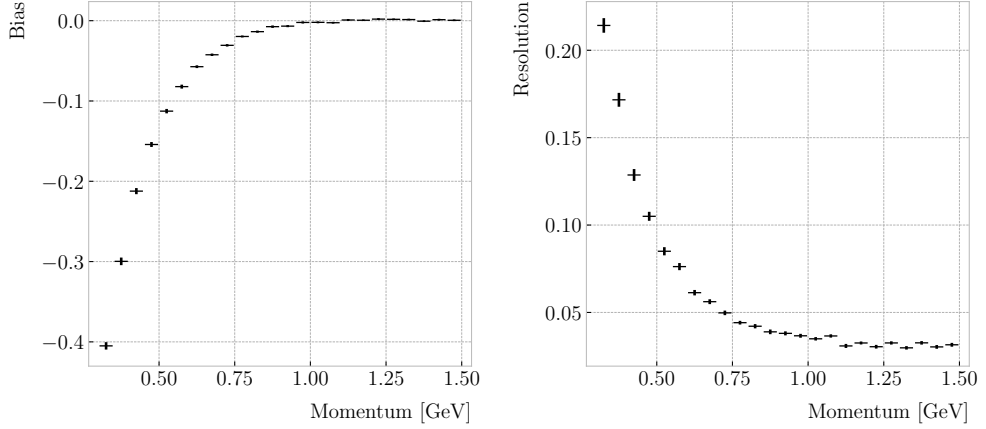


Figure 6.8: Estimated values of the mean dE/dx bias (left panel) and resolution (right panel) obtained for the true protons in the [FHC](#) neutrino sample as a function of the reconstructed momentum.

detector volume. On top of that, I refined the selection requiring a single reconstructed track per event, which eliminates any misreconstruction effects. In this case, we are dealing with tracks that may have fragmented, or even have contributions from different true particles. Also, note that at low energies the $\langle dE/dx \rangle$ for protons is much higher than it is for other particles. Therefore, having a poor resolution in that range does not have an impact on the proton separation.

6.3 Muon and pion separation in the ECal and MuID

As it can be seen from Fig. 6.7, it is not possible to separate muons and charged pions in the [HPgTPC](#) using dE/dx for momenta ≥ 300 MeV/ c . In [ND-GAr](#), approximately 70% of the interactions in [FHC](#) mode will be ν_μ CC (compared to the 47% of $\bar{\nu}_\mu$ CC interactions when operating in [RHC](#) mode), while 24% are neutral currents. Out of these, around 53% and 47% of them will produce at least one charged pion in the final state, respectively. Figure 6.9 shows a comparison between the spectra of the primary muons and the charged pions for ν_μ CC interactions in [ND-GAr](#) producing one or more charged pions. From this, one can see that (i) the majority of muons and charged pions are not going to be distinguishable with a $\langle dE/dx \rangle$ measurement, and that (ii) particle

CHAPTER 6. PARTICLE IDENTIFICATION IN ND-GAr

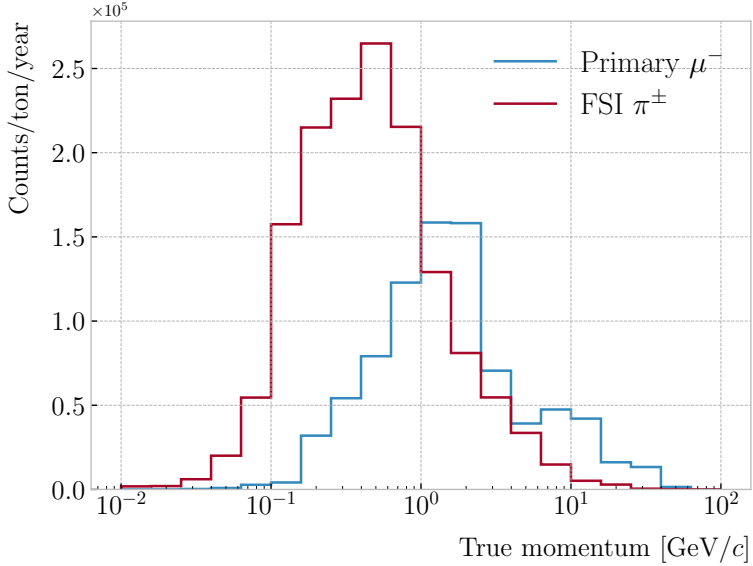


Figure 6.9: True momentum distribution for the primary muon in ν_μ CC $N\pi^\pm$ interactions inside the fiducial volume of ND-GAr (blue line), compared to the post FSI charged pion spectrum (red line).

identification is necessary both to classify correctly the ν_μ CC events and identify the primary muon within them.

ND-GAr features two other subdetectors which can provide additional information for this task, namely the ECal and MuID. The current ECal design, described in section 3.5.2, consists of 42 layers, made of 5 mm of Pb, 7 mm of plastic scintillator, and an additional 1 mm PCB board for the tile layers. The total thickness of this calorimeter is 1.66 nuclear interaction lengths, or 1.39 pion interaction lengths. The MuID design is in a more conceptual stage, however it is envisioned to feature layers with 10 cm of Fe and 2 cm of plastic scintillator. With its three layers, it will have a thickness of 1.87 or 1.53 nuclear or pion interaction lengths, respectively.

Because pion showers are dominated by inelastic nuclear interactions, the signatures of these particles in the calorimeter will look significantly different from those of muons, or in general any minimum ionising particle (MIP). Although our ECal is not thick enough to fully contain the hadronic showers of the charged pions at their typical energies in FHC neutrino interactions, they can still be used to understand whether the original particle was more hadron-like or MIP-like. In Fig. 6.10 I show two examples of energy

6.3. MUON AND PION SEPARATION IN THE ECal AND MuID

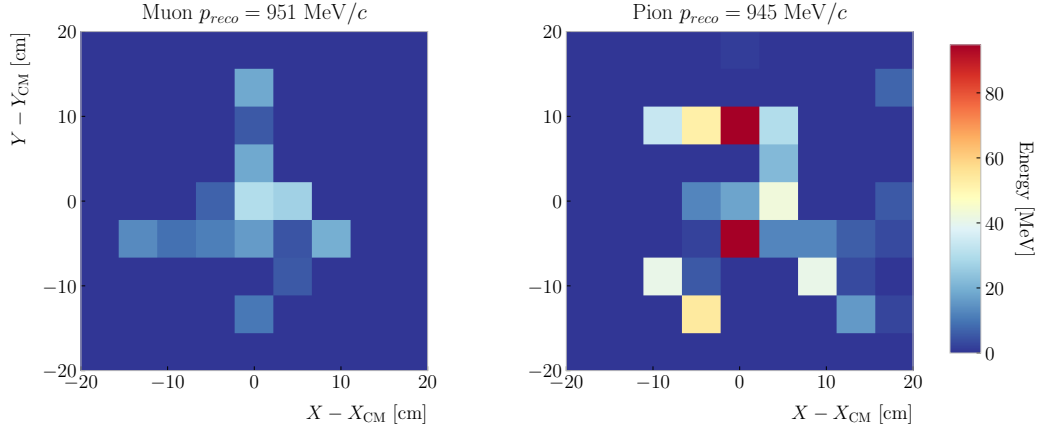


Figure 6.10: Distributions of energy deposits in the [ECal](#) for a muon (left panel) and a charged pion (right panel) with similar momenta. The energy is projected onto the plane perpendicular to the principal component of the hits, and the positions are relative to the centre of the interaction.

distributions created by a muon (left panel) and a charged pion (right panel) of similar momenta interacting in the [ECal](#). These figures represent the transverse development of the interactions. For each of them, I computed the principal component and centre of mass of the interaction, projecting the position of the hits onto the plane perpendicular to that direction, and taking the distances relative to the centre. It can be seen that the muon follows an almost [MIP](#)-like behaviour, with most of the deposited energy located in the central bin. On the other hand, the pion not only deposits more energy overall, but also this energy is more spread-out among the different hits. It is this kind of information that would allow us to distinguish muons from pions.

This way, I identify three main action points that need to be addressed if one wants to use these detectors to distinguish between muons and charged pions. These are:

1. the way we make the associations between tracks in the [HPgTPC](#) to the activities (what in GArSoft we call clusters) in the [ECal](#) and the [MuID](#),
2. what variables or features one can extract from the calorimeters that encapsulate the information we are interested about,
3. and how to carry out the classification problem.

CHAPTER 6. PARTICLE IDENTIFICATION IN ND-GAr

6.3.1 Track-ECal matching

One of the main factors in the muon and pion separation is the way we associate clusters in the ECal to reconstructed tracks in the HPgTPC. Missing some associations or making wrong ones can bias the ECal quantities that we can use for classifying particles. The current algorithm in GArSoft provides precise associations, i.e. most of the associations that it produces are correct, but it appears to miss an important number of them.

The current TPC track-ECal cluster association algorithm is divided in four parts. It first checks whether the track end point fulfils certain conditions to be extrapolated. There are two cut values in this step, one for the drift direction and other for the radial.

If the point can be extrapolated, the code computes the coordinates of the centre of curvature using the Kalman fit estimates at the track end (y , z , $1/R$, ϕ , $\tan\lambda$). It then compares the distance between this and the cluster in the (z, y) plane to R . This introduces another cut in the perpendicular direction.

The next step is different for clusters in the barrel or in one of the end caps. If it is a barrel cluster the algorithm extrapolates the track up to the radial distance of the cluster. There are three possible outcomes, the extrapolated helix can cut the cylinder of radius $r_{cluster}$ two, one or zero times. It gets the cut point that is closer to the cluster and checks that it is either in the barrel or the end caps. Computing the difference between the x coordinates of the cluster and the extrapolated point, the module checks that this is not greater than a certain value. If the cluster is in an end cap, it propagates the track up to the x position of the cluster. Then, the algorithm computes the angle in the (z, y) plane between the centre of curvature and the cluster, α , and the centre of curvature and the propagated point, α' . A cut is applied to the quantity $(\alpha - \alpha')R$.

If the cluster contains more than a certain number N of hits, it applies an extra cut to the dot product of the direction of the track at the propagated point and the cluster direction.

The code makes sure to only associate one end of the track (if any) to a cluster. However, it can associate more than one track to the same cluster. This makes sense,

6.3. MUON AND PION SEPARATION IN THE ECal AND MUID

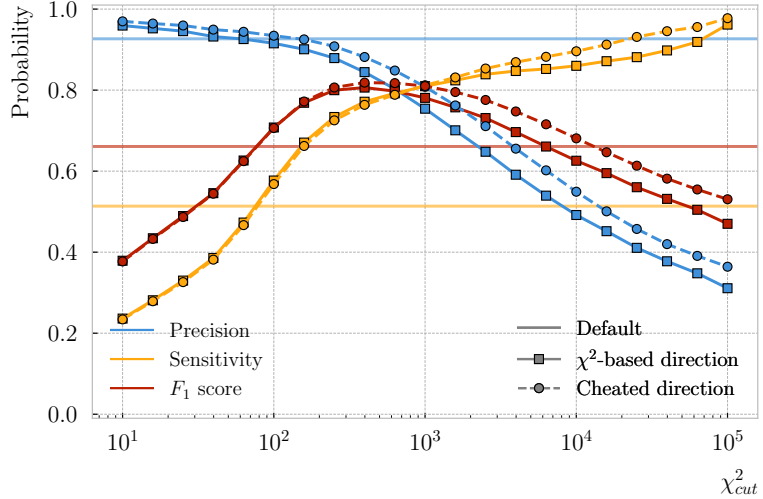


Figure 6.11: Comparison between the precision (blue), sensitivity (yellow) and F_1 score (red) obtained for the default (horizontal lines) and new algorithms, both with the χ^2 -based direction estimator (squares) and cheated directions (circles), for different values of the χ^2 cut.

as different particles can contribute to the same cluster in the [ECal](#), but it makes it difficult to quantify the relative contributions of the tracks to a certain cluster.

As a way of gauging the performance of this algorithm, I developed a new, simpler association module. The goal was to have a simple and robust algorithm, which depends on as few parameters as possible and that can produce a one-to-one matching between tracks and [ECal](#) clusters.

For each reconstructed track, the new algorithm applies the same procedure to the forward and the backward fits irrespective of their end point positions. It first gets the Kalman fit parameters at the corresponding end point, together with the position along the drift direction, x_0 and $(y_0, z_0, 1/R, \phi_0, \tan\lambda)$.

For each [ECal](#) cluster, I compute the radial distance to the centre of the [TPC](#) and find the ϕ value in the range $[\phi_0, \phi_0 + \text{sign}(R)\phi_{max}]$ that makes the propagated helix intersect with the circle defined with such radius. The (x, y, z) position of the helix for the ϕ value found (if any) is then computed. In case there are two intersections, I keep the one that minimises the distance between (y, z) and $(y_{cluster}, z_{cluster})$.

I then calculate a χ^2 value based on the Euclidean distance between the propagated

CHAPTER 6. PARTICLE IDENTIFICATION IN ND-GAR

point and the cluster:

$$\chi^2/ndf = \frac{\sum_{n=0}^2 (x^{(n)} - x_c^{(n)})^2}{3}. \quad (6.7)$$

If there was no intersection I set the stored value to -1 . In the end, for each reconstructed track in the event one ends up with two collections of χ^2 values, one for each [ECal](#) cluster and fit directions.

The current code only supports having [ECal](#) clusters associated to one end of each track. We have two options to decide what track end to keep. The first one tries to cheat the selection, looking at the distance between the two track ends and the true start position of the associated [MC](#) particle. The second one keeps the track end with more χ^2 entries below a certain cut value.

This feature of only considering one track end limits the algorithm, making it unsuitable for reconstructing events with particles originating outside the [HPgTPC](#). However, as for the moment our main concern is the study of neutrino interactions in the gaseous argon volume, this is an acceptable assumption.

In order to associate a cluster to a track, I take all clusters with a χ^2 value in the range $[0, \chi_{cut}^2]$. If a cluster has been assigned to more than one track we leave it with the one with the lowest χ^2 .

This default behaviour of the algorithm can be modified to associate more than one track to each cluster. Not only that, but the χ^2 values can be used to assign relative weights to the different contributions.

To evaluate the performance of the association method, I use a binary classification approach. In this case, I check the leading [MC](#) Track IDs associated to the reconstructed tracks and [ECal](#) clusters. I count an association as true positive (TP) if both Track IDs coincide. An association is considered false positive (FP) when the Track IDs are different. If a cluster has not been associated to any track but it shares the Track ID with a reconstructed track it is counted as a false negative (FN).

For the testing, I produced a sample of 10^4 [FHC](#) neutrino events inside the [HPgTPC](#). Figure 6.11 shows the precision (blue line), sensitivity (yellow line), and F_1 score (red

6.3. MUON AND PION SEPARATION IN THE ECal AND MUID

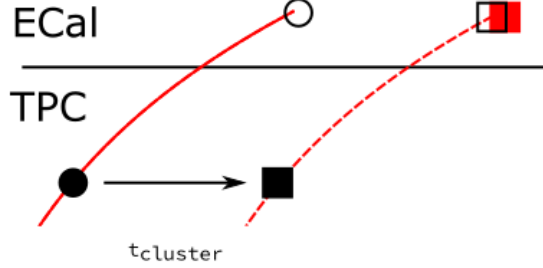


Figure 6.12: Schematics of a possible option to deal with track-**ECal** associations in non-zero t_0 neutrino interaction events, trying to correct for the drift direction uncertainty in a cluster-by-cluster basis using the cluster time, $t_{cluster}$.

line) I obtain for different values of χ^2_{cut} . For comparison, the same metrics computed for the default algorithm with the current configuration are also shown (dashed lines). In the case of the new algorithm, I use both the χ^2 -based method to estimate the track direction described earlier (square markers) and the cheated direction from the **Geant4**-level information (circle markers). For either of these we achieve similar values of the precision compared to the old code, while having a considerably higher sensitivity. It can be seen that cheating the direction of the tracks only makes a difference at high χ^2_{cut} , past the optimal value of the cut around the F_1 score maximum. Therefore, I set the χ^2 method as the default.

One of the possible weak points of this approach is that it relies on the position along the drift direction to make the decisions. Within the current **ND-GAr** design implemented in GArSoft, the timing information is provided by the **ECal**. That effectively means that prior to making the track-**ECal** associations the reconstructed x positions of the track trajectories differ from the simulated ones by an amount:

$$x_{reco}^{(n)} - x_{sim}^{(n)} = v_{drift} t_0, \quad (6.8)$$

where v_{drift} is the mean drift velocity in our medium and the initial time is in the range $t_0 \in [0, t_{spill}]$, with t_{spill} being the spill length. For a 10 μs spill this translates into a maximum 30 cm uncertainty on the drift direction position.

The current default in GArSoft sets $t_0 = 0$, but the functionality to randomly sample

CHAPTER 6. PARTICLE IDENTIFICATION IN ND-GAR

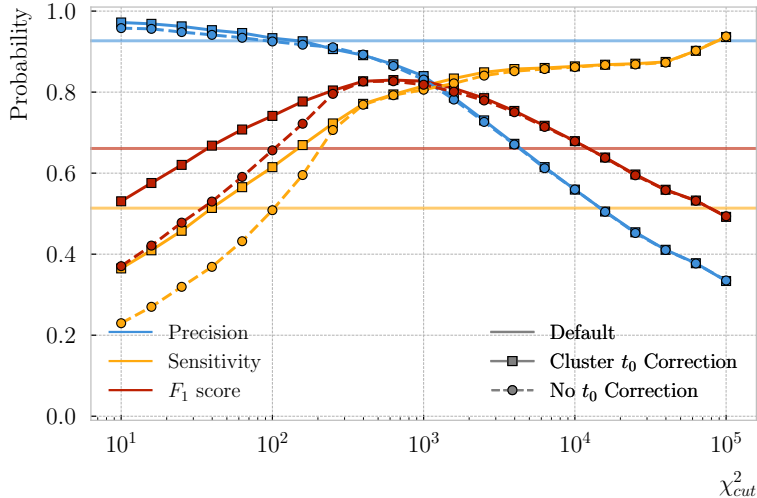


Figure 6.13: Comparison between the precision (blue), sensitivity (yellow) and F_1 score (red) obtained for the new algorithm when applying the cluster t_0 correction (squares) and when no correction is applied (circles), for different values of the χ^2 cut.

this within the spill time is in place. Therefore, we need to understand what is the impact of a non-zero t_0 on the associations algorithm and foresee possible ways of minimising a loss in performance.

Figure 6.12 represents a possible option to tackle the association problem when having events with a non-zero initial time t_0 . The black and white circles represent the original points, whereas the squares indicate the corrected positions. The end points of the track and the propagated points up to the cluster radius are indicated using filled and unfilled markers, respectively. The red square represents the position of the cluster.

Here I try to correct for the drift coordinate position using the time associated to the cluster. Assuming that the drift time is much larger than the propagation time, $t_{cluster}$ could be used as a good estimation of the t_0 . An alternative can be using the earliest time associated to a hit in said cluster. Doing this for each cluster before computing the χ^2 value could be used as an alternative to knowing the specific value of the t_0 , as when the association is correct this will provide the right correction but its impact is small enough to not change the position significantly in the case the cluster does not correspond to a given track.

I tested the effect of this correction again using a sample of 10^4 FHC neutrino events,

6.3. MUON AND PION SEPARATION IN THE ECal AND MuID

this time with t_0 values uniformly distributed within the spill. Figure 6.13 shows the performance of the algorithm for the case where the cluster t_0 correction is applied (square markers), and for the no correction case (circle markers), as a function of χ^2_{cut} . In this case, the differences are particularly noticeable at low values of the cut. This makes sense, as the t_0 effect becomes subdominant when the distance we consider grows large. Overall, the correction increases the sensitivity while keeping the precision almost unchanged. As a result, I apply the t_0 correction to the generated samples by default.

6.3.2 Classification strategy

The problem of the muon and charged pion separation has to be viewed in the broader context of the particle identification in our detector. Focusing on the beam neutrino interactions, it is clear that we are going to have muons and pions spanning a broad momentum range. Not only that, but we will also have other particles with similar characteristics that will make the classification even more challenging. Therefore, we are presented with a task that will depend heavily on the kinematic range we are looking at each time, as both the available information and the possible impurities of other particle species vary.

For instance, distinguishing muons from pions could be difficult at low momenta, as a great number of them do not reach the [Ecal](#). Therefore, we could think of tailoring a version of the classification for that particular case, which could be complemented with a dE/dx measurement. Likewise, for momenta ≥ 1 GeV muons and pions reach the calorimeters efficiently, but so do protons. Because of this, one can try to train another classifier for this energy range, and rely on other methods to remove as many of the protons as possible.

Figure 6.14 shows the momentum distribution of the reconstructed muons (top) and pions (bottom) in a [FHC](#) sample. It also contains the fraction of particles reaching the [Ecal](#) (red) and [MuID](#) (blue), for the different momentum bins. In Fig. 6.15 I show the mean dE/dx of different particles as a function of the momentum, computed using the [ALEPH](#) parametrisation with the best fit parameters found in section 6.2.1.

CHAPTER 6. PARTICLE IDENTIFICATION IN ND-GAr

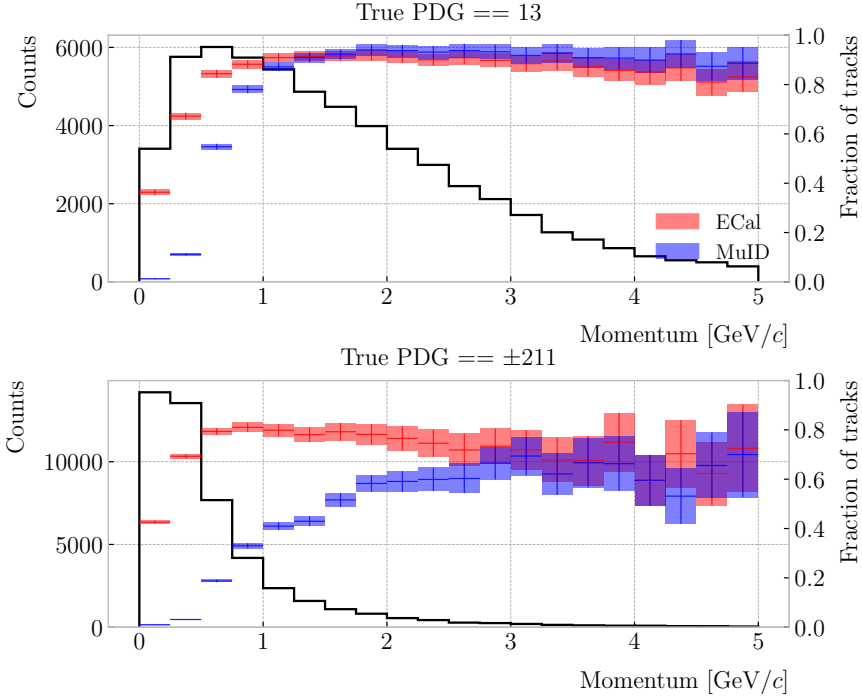


Figure 6.14: Momentum distributions for the reconstructed muons (top panel) and charged pions (bottom panel) in a [FHC](#) neutrino sample, together with the fraction of them reaching the [ECal](#) (red) and [MuID](#) (blue). Each entry corresponds to a reconstructed track, backtracked to a true muon or pion which has not produced any other reconstructed track.

Using these two figures as references, I decided to approach the classification by dividing the problem into six different momentum regions. A summary of these can be found in Tab. 6.1. The idea is to select a number of regions where the basic classification can be complemented with other methods. For the problem at hand, I prepared separate samples of isotropic single muons and pions, with momenta uniformly distributed along the corresponding momentum range. Each sample contains 5×10^4 events of the corresponding particle species. I do not generate samples for the first region, as it is assumed that the separation can be achieved using dE/dx only. For the last region, I generate particles up to a momentum of $10 \text{ GeV}/c$, as that is well above the typical energies of muons and pions from [FHC](#) neutrino interactions in [ND-GAr](#). In all cases, the ratios I keep between the training and testing datasets are 80 : 20.

Additionally, I prepared another sample of 10^5 [FHC](#) neutrino events. For each

6.3. MUON AND PION SEPARATION IN THE ECAL AND MUID

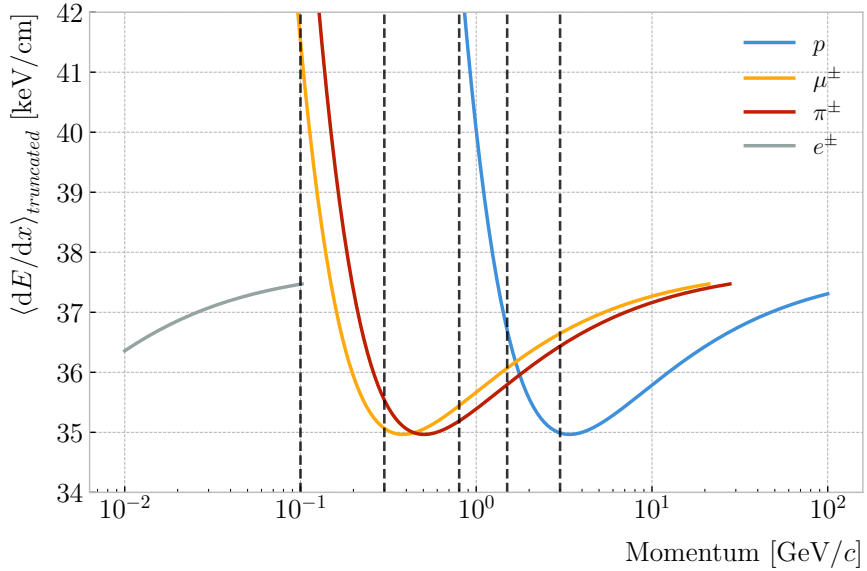


Figure 6.15: Predicted truncated mean dE/dx versus momentum, for electrons, muons, charged pions and protons, obtained using the [ALEPH](#) parametrisation. The vertical dashed lines represent the boundaries of the six regions used for the muon and pion classification training.

interaction, I select the reconstructed particles which were backtracked to true muons or charged pions. I use this dataset to perform validation checks, to see how the models trained with the single particle data generalise to a more realistic scenario.

To tackle this classification problem, I make use of Boosted Decision Trees ([BDT](#)). A decision tree uses a flowchart-like structure to make decisions based on some input data. It starts from a root node, which represents the complete dataset, and then it splits this based on the variable or feature which gives the best separation between classes, creating two new nodes. The process repeats for each node until it reaches a certain limit, like a maximum number of splits or some tolerance criteria. The last set of nodes are often called leaf nodes, and represent the final prediction of the classifier. A good example of the use of [BDT](#)s in particle physics is that from Ref. [165].

Boosting refers to a family of methods to combine the predictions from multiple classifiers, following a sequential approach where each new model learns from the errors of the previous one. The process starts with a simple decision tree, which is used to make predictions on the training data. Then, the data points misclassified by the first

CHAPTER 6. PARTICLE IDENTIFICATION IN ND-GAR

Table 6.1: Momentum ranges and description of the PID approach assumed for the muon and pion classification task.

Momentum range	Description
< 0.1 GeV/c	All tracks can be separated with dE/dx
[0.1, 0.3) GeV/c	Use ECal for reaching muons and pions, dE/dx for the rest
[0.3, 0.8) GeV/c	Use ECal for muons and pions, dE/dx for protons
[0.8, 1.5) GeV/c	Use ECal and MuID for muons and pions, dE/dx for protons
[1.5, 3.0) GeV/c	Use ECal and MuID for muons and pions, ToF for protons
≥ 3.0 GeV/c	Use ECal and MuID for muons and pions, dE/dx and ToF for protons

model are assigned higher weights, and another decision tree is trained on the data with adjusted weights. The predictions of the two trees are then combined, and the cycle repeats for a predefined number of iterations. Gradient boosting uses the direction of the steepest error descent to guide the learning process and improve the accuracy with each iteration.

6.3.3 Feature selection and importance

Using the reconstructed tracks as a starting point, I compute a number of **ECal** and **MuID** variables for each of them. As there can be more than one cluster associated to a track, I collect all associated clusters and compute these variables from the complete collection of associated hits. For the **MuID**, because it only features three layers and typically there will be fewer hits, I also allow single hits to be associated with tracks². I can roughly divide the variables in three types: energy-related, geometry-related and statistical. In the following, I briefly describe the variables related exclusively to the **ECal**:

- **Energy-related ECal**

- **ECal** total energy (`ClusterTotalEnergy`): sum of the energy of all the **ECal** hits.

²At the reconstruction level non-clustered hits are put into single hit clusters, instead of being thrown away. This is necessary to keep the consistency of the track-cluster association code.

6.3. MUON AND PION SEPARATION IN THE ECal AND MUID

- Mean **Ecal** hit energy (HitMeanEnergy): mean of the hit energy distribution.
- Standard deviation **Ecal** hit energy (HitStdEnergy): standard deviation of the hit energy distribution.
- Maximum **Ecal** hit energy (HitMaxEnergy): maximum of the hit energy distribution.

- **Geometry-related ECal**

- Mean distance hit-to-cluster (DistHitClusterMean): mean of the distance distribution between the hits and the corresponding cluster's main axis.
- **RMS** distance hit-to-cluster (DistHitClusterRMS): root mean square of the distance distribution between the hits and the corresponding cluster's main axis.
- Maximum distance hit-to-centre (DistHitCenterMax): maximum of the distance distribution between the hits and the centre of the **HPgTPC**.
- Time-of-Flight velocity (TOFVelocity): slope obtained when fitting a straight line to the hit time versus hit distance to the centre (i.e. $d = v \times t$).

- **Energy and geometry ECal**

- Radius 90% energy (Radius90E): distance in the hit-to-cluster distribution for which 90% of the total energy is contained in the hits that are closer to the axis (i.e. radius that contains 90% of the energy).

- **Statistical ECal**

- Number of hits (NHits): total number of hits associated to the track.
- Number of layers with hits (NLayers): difference between the last and the first layer with hits.

Figure 6.16 shows the distributions of three different **Ecal** variables, separating true muons (blue) and charged pions (red), for the five momentum ranges considered. I chose

CHAPTER 6. PARTICLE IDENTIFICATION IN ND-GAr

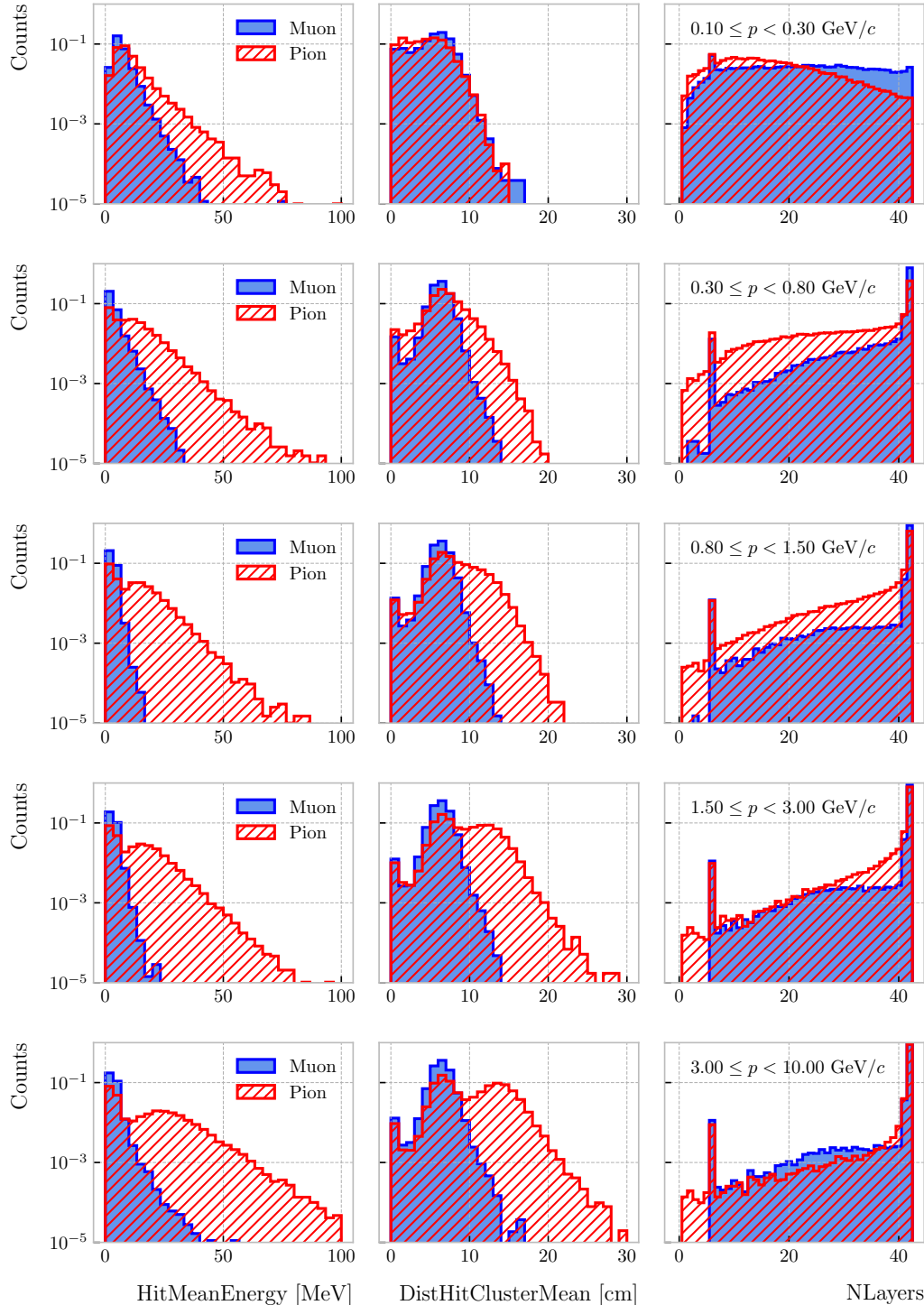


Figure 6.16: Example ECal feature distributions for muons (blue) and charged pions (red) in the five different momentum ranges considered (from top to bottom, in ascending momentum order). From left to right: mean hit energy, mean distance hit-to-cluster, and number of layers with hits.

6.3. MUON AND PION SEPARATION IN THE ECAL AND MUID

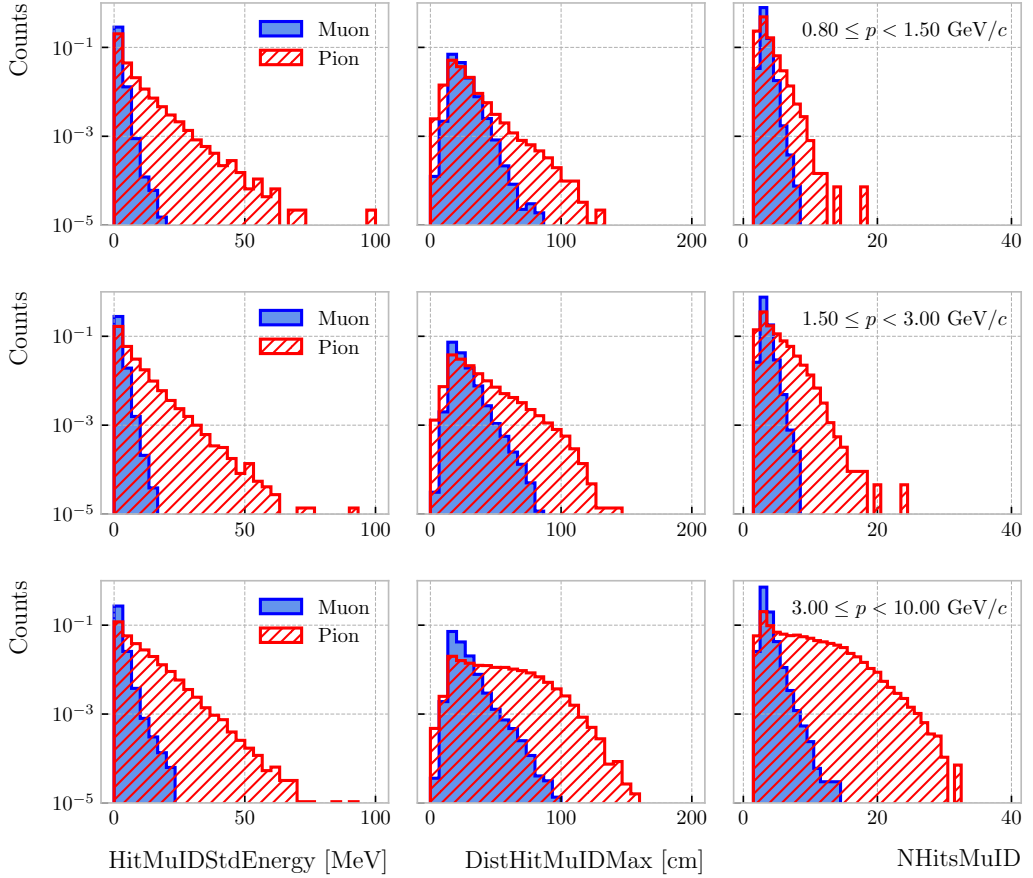


Figure 6.17: Example **MuID** feature distributions for muons (blue) and charged pions (red) in the three different momentum ranges considered (from top to bottom, in ascending momentum order). From left to right: standard deviation hit energy, maximum distance hit-to-hit, and number of hits.

to show one feature from each category, namely the mean energy per hit (left column), the mean distance between the hits and the centre of the cluster (middle column), and the number of **ECal** layers with hits (right column). These give an idea of the separating power of the different features, and how it changes considerably with the energy. In the number of layers with hits distributions, the peak at 6 appears because the first six **ECal** layers sit inside the pressure vessel. Therefore, some of the particles get stopped crossing it, never making it to the seventh layer.

In the case of the **MuID**, because at low momenta a significant fraction of the particles do not make it past the **ECal**, I only consider the information coming from this detector

CHAPTER 6. PARTICLE IDENTIFICATION IN ND-GAR

for momenta $\geq 0.8 \text{ GeV}/c$, i.e. for the last three momentum regions. The variables I extract from it are the following:

- **Energy-related MuID**

- MuID total energy (ClusterMuIDTotalEnergy): sum of the energy of all the MuID hits.
- Mean MuID hit energy (HitMuIDMeanEnergy): mean of the MuID hit energy distribution.
- Standard deviation MuID hit energy (HitMuIDStdEnergy): standard deviation of the MuID hit energy distribution.
- Maximum MuID hit energy (HitMuIDMaxEnergy): maximum of the MuID hit energy distribution.

- **Geometry-related MuID**

- Maximum distance MuID hit-to-hit (DistHitMuIDMax): maximum distance between pairs of MuID hits.
- Maximum distance MuID hit-to-centre (DistHitCenterMuIDMax): maximum of the distance distribution between the MuID hits and the centre of the HPgTPC.

- **Statistical MuID**

- Number of hits (NHitsMuID): total number of MuID hits associated to the track.
- Number of layers with hits (NLayersMuID): difference between the last and the first layer with MuID hits.

Figure 6.17 shows the distributions of three different MuID variables, separating true muons (blue) and charged pions (red), for the three momentum ranges which use the muon tagger information. In this case I decided to show the standard deviation of

6.3. MUON AND PION SEPARATION IN THE ECAL AND MUID

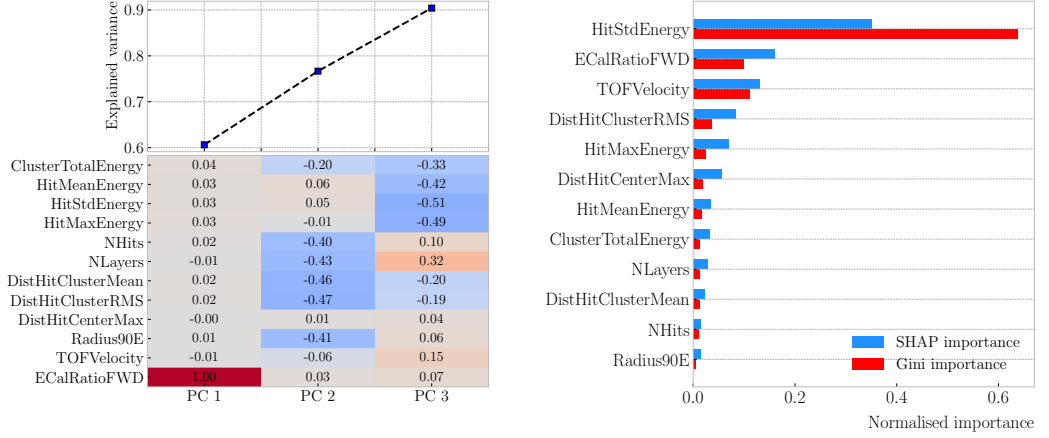


Figure 6.18: Left panel: cumulative explained variance for the first three principal components (top panel) and contribution of the different features to the principal axes in feature space (bottom panel). Right panel: Shapley (blue) and Gini (red) feature importances for the different input features. Both figures correspond to the samples in the momentum range $0.3 \leq p < 0.8$ GeV/c.

the MuID hit energy distribution (left column), the maximum distance between the MuID hit pairs (middle column), and the number of MuID hits (right column). These variables are used together with the ECAL features at high momenta, providing additional disambiguation power.

For both the ECAL and the MuID, I add as an extra feature the ratio between the total energy from the clusters and the momentum measured in the HPgTPC (ECalRatioFWD and MuIDRatioFWD, as I use the momentum value from the forward fit). This variable is typically used for electron discrimination in calorimeters, as the small difference between their momentum and kinetic energy makes it peak around 1. I also include another time-of-flight variable, measured with both the ECAL and MuID from the arrival times to each detector (TOFMuID).

Once our features have been defined, one can do some exploratory analysis to understand how well the variables describe the target class, and avoid the black-box approach by checking which features are most relevant for the learning process. This way, I perform a feature analysis for each of the momentum ranges I divided this classification problem into. It follows three steps: first a principal component analysis (PCA), followed by a feature importance study using Gini [166] and Shapley [167] values, and finally a

CHAPTER 6. PARTICLE IDENTIFICATION IN ND-GAR

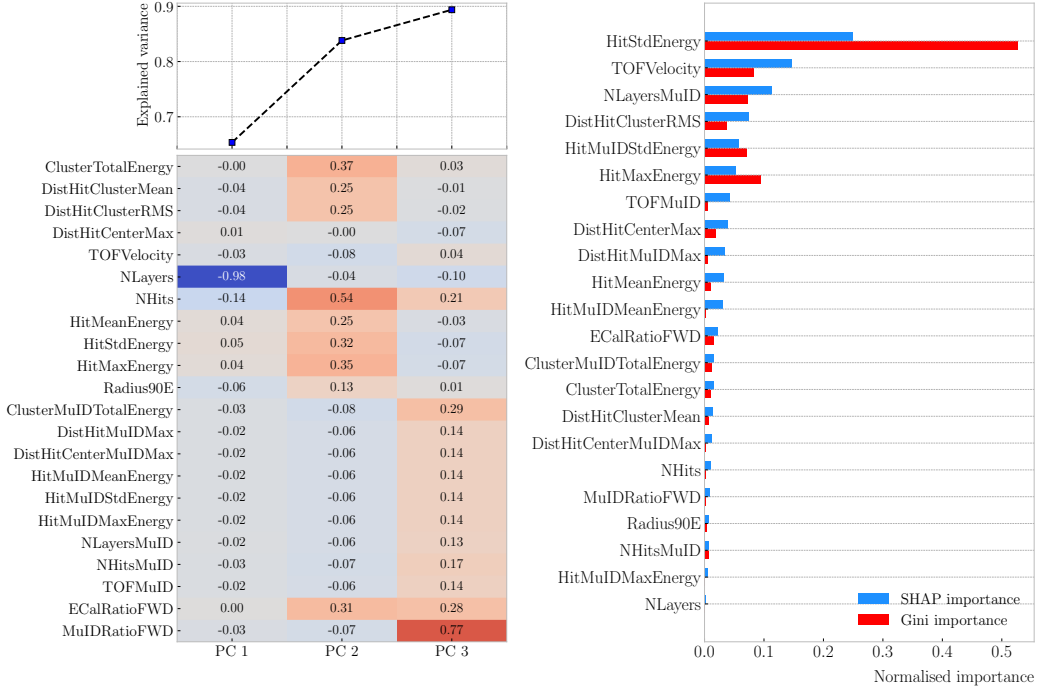


Figure 6.19: Left panel: cumulative explained variance for the first three principal components (top panel) and contribution of the different features to the principal axes in feature space (bottom panel). Right panel: Shapley (blue) and Gini (red) feature importances for the different input features. Both figures correspond to the samples in the momentum range $0.8 \leq p < 1.5$ GeV/c.

feature permutation importance analysis.

The [PCA](#) is useful to understand the variance of the feature space. It is an unsupervised machine learning technique that allows the user to perform a dimensionality reduction [168]. It uses a singular value decomposition ([SVD](#)) of the input features to project them into a lower dimensional space. The idea is to find the matrix \mathbf{C}_q , whose columns are the first q orthonormal eigenvectors of the input covariance matrix. Consider the $n \times p$ real matrix of input data \mathbf{X} , where n is the number of samples and p the number of features. If \mathbf{X} is centred, i.e. the means of its columns are equal to zero, we can write the covariance matrix of \mathbf{X} as $\mathbf{C} = \mathbf{X}^\top \mathbf{X} / (n - 1)$. This matrix can be diagonalised, yielding:

$$\mathbf{C} = \mathbf{V} \mathbf{L} \mathbf{V}^\top, \quad (6.9)$$

where \mathbf{V} is a matrix of eigenvectors and \mathbf{L} a diagonal matrix with eigenvalues λ_i . Then,

6.3. MUON AND PION SEPARATION IN THE ECAL AND MUID

performing [SVD](#) on \mathbf{X} gives us:

$$\mathbf{X} = \mathbf{U} \mathbf{S} \mathbf{W}^\top, \quad (6.10)$$

where \mathbf{U} is a unitary matrix, whose columns are called left singular vectors, \mathbf{S} is a diagonal matrix of singular values s_i , and \mathbf{W} is another unitary matrix, its columns known as right singular vectors. This way, we can write:

$$\mathbf{C} = \mathbf{W} \mathbf{S} \mathbf{U}^\top \mathbf{U} \mathbf{S} \mathbf{W}^\top / (n - 1) = \mathbf{W} \frac{\mathbf{S}^2}{n - 1} \mathbf{W}^\top. \quad (6.11)$$

meaning that the right singular vectors are also the eigenvectors of the covariance matrix. The [SVD](#) can be computed numerically following an iterative approach [169].

This way, taking an input data vector $X \in \mathbb{R}^p$, the resulting feature vector $Y \in \mathbb{R}^q$ is given by:

$$Y = \mathbf{C}_q^\top X. \quad (6.12)$$

The new features capture most of the variance of the original sample, while being lower dimensional, as $q < p$.

Before applying the [PCA](#) reduction one needs to centre and scale the input data. Centring is necessary when using [SVD](#) to obtain the eigenvectors of the covariance matrix, as only in that case we can do the identification with the right singular vectors from the input data. Scaling is needed when variables are on different scales, as some can then dominate the [PCA](#) procedure.

I use the [PCA](#) module of [scikit-learn](#) [142], together with the [RobustScaler](#), which centres the data and scales it based on the interquartile range. In Fig. 6.18 (left panel) and Fig. 6.19 (left panel) I show the results I obtained from the [PCA](#) for the momentum ranges $0.3 \leq p < 0.8 \text{ GeV}/c$ and $0.8 \leq p < 1.5 \text{ GeV}/c$, respectively. Notice that in the second case the number of features increases considerably, as this is the first region which uses the [MuID](#) variables. I find that, in all the cases, adding a fourth [PC](#) does not add additional information. As it can be seen in the top panels of the figures, the cumulative explained variance is already over 80% with three [PCs](#).

CHAPTER 6. PARTICLE IDENTIFICATION IN ND-GAR

The bottom panels show the contribution of the variables to the principal axes. For the two first momentum regions, I observe a tendency of the energy-related and the geometry-related **ECal** variables to be clustered together. For the other ranges, when I include the **MuID** variables, there seems to be a division between **ECal** and **MuID** variables. For these, it seems like the number of **ECal** layers with hits also plays an important role.

The next step in the analysis is to quantify the importance of the features based on two additional metrics, namely the Gini and the Shapley values. The Gini importance, often called mean decrease impurity, is based on how much a feature contributes to the purity improvement at the splits in each decision tree. The purity is measured in terms of the Gini impurity index, defined as [166]:

$$I_G = 1 - \sum_i f_i, \quad (6.13)$$

where f_i is the fractional abundance of the i -th class. Then, for each split one can compute the weighted decrease in impurity as:

$$\Delta_G = \frac{N_t}{N} \left(I_G - \frac{N_t^R}{N_t} I_G^R - \frac{N_t^L}{N_t} I_G^L \right), \quad (6.14)$$

where N represents the total number of samples, N_t the number of samples at the current node, N_t^R and N_t^L the number of samples in the right and left children respectively, I_G is the Gini impurity at the current node, and I_G^R and I_G^L the Gini impurities of the resulting right and left children.

For each decision tree, one will have a normalised vector with the accumulated decrease in Gini impurity for each feature. In the case of a **BDT**, the feature importances are simply the mean for all the estimators in the ensemble.

The concept of Shapley values originated in the context of game theory, and it measures the marginal contribution of a feature in enhancing the accuracy of a classifier [167]. Take F to be the set of all features in a problem, and $S \subseteq F$ a subset of features.

6.3. MUON AND PION SEPARATION IN THE ECAL AND MUID

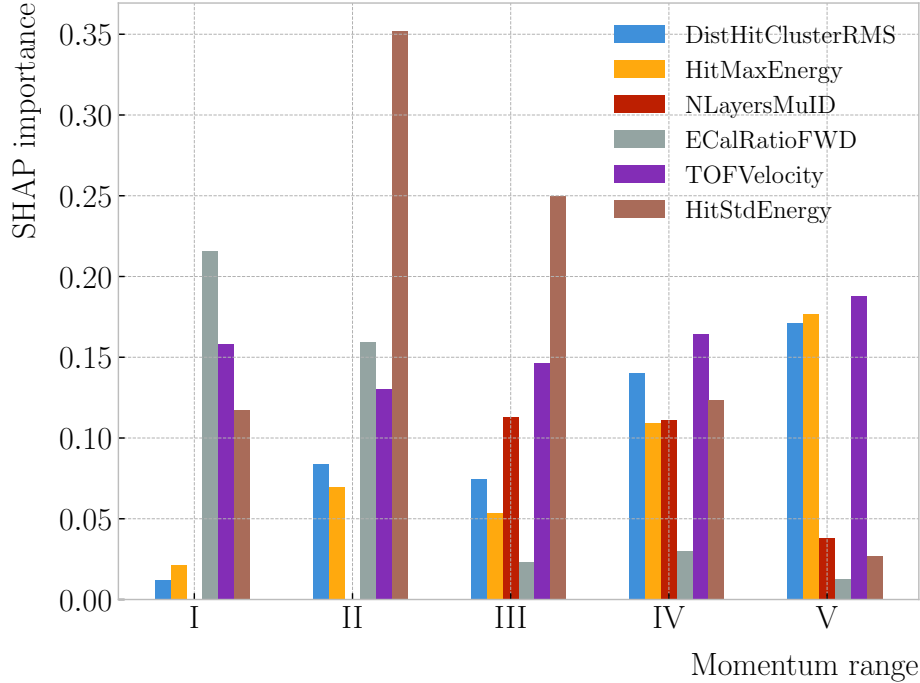


Figure 6.20: Evolution of the SHAP importance for the top six most important features across all five momentum ranges.

To compute the Shapley value of the i -th feature, one has to train a model with that feature present, $f_{S \cup \{i\}}$, and another model trained without it, f_S . This has to be repeated for all possible combinations of subsets $S \subset F \setminus \{i\}$, and evaluating the models predictions on the appropriate sets of data x_S . This way, the Shapley value results [170]:

$$\varphi_i = \sum_{S \subset F \setminus \{i\}} \frac{|S|! (|F| - |S| - 1)!}{|F|!} [f_{S \cup \{i\}}(x_{S \cup \{i\}}) - f_S(x_S)]. \quad (6.15)$$

I train the `GradientBoostingClassifier` from `scikit-learn` with the default configuration in order to evaluate both the Gini and Shapley importances. The Gini scores are automatically computed by `scikit-learn`, using the training data. For the Shapley importance, I use the implementation from the `SHAP` package [170], computing it using the test sample. The results can be seen in Fig. 6.18 (right panel) and Fig. 6.19 (right panel), again for the momentum ranges $0.3 \leq p < 0.8 \text{ GeV}/c$ and $0.8 \leq p < 1.5 \text{ GeV}/c$. The length of the bars denote either the SHAP (blue) or the Gini

CHAPTER 6. PARTICLE IDENTIFICATION IN ND-GAR

(red) importance of the feature. One interesting thing to notice is that, when looking at the Gini importance, there is always one feature that dominates over the rest. This is not the case for the SHAP importance, where importances tend to be more balanced.

Across all momentum ranges, I observe that the most important features are rather consistent. For the five regions considered, only six variables sit in the top five at least once. Figure 6.20 shows the evolution of the SHAP importance of these six features. It is interesting to see that the time-of-flight variable keeps its importance almost unchanged for all momenta. Also, it looks like the `ECal` energy ratio gets less relevant the higher the momentum is, but the `RMS` of the hit-to-cluster distance distribution and the maximum `ECal` hit energy become more important in the high momentum ranges.

The last step in the feature selection analysis is the feature permutation. This technique measures the contribution of each feature to the performance of a model by randomly shuffling its values and checking how some scores degrade. For the present case, I am interested in the precision or purity, and the sensitivity or efficiency, as these two are the most relevant metrics from a physics point of view. The `scikit-learn` module provides the user with a method to perform the permutation scans.

The results of these are shown in Fig. 6.21. For the different momentum ranges I show the permutation importances for the ten most important features. For each of the variables I report the effect the permutations have on the precision (blue) and sensitivity (yellow) of the models. The bars indicate the importance value, with the lighter part representing one standard deviation around the mean (hinted as an additional vertical line). Something to notice is that, in the first momentum region, the feature permutations have an effect on both the precision and the sensitivity. However, for the rest the precision is almost unaffected, while the sensitivity changes are considerably larger.

It is also interesting to see that most of the variables identified as important here are the same as I found when looking at the Shapley values. The behaviour of these across the momentum ranges is also similar, with the same patterns of some features being important at low momenta and then dropping in importance for the high momentum

6.3. MUON AND PION SEPARATION IN THE ECAL AND MUID

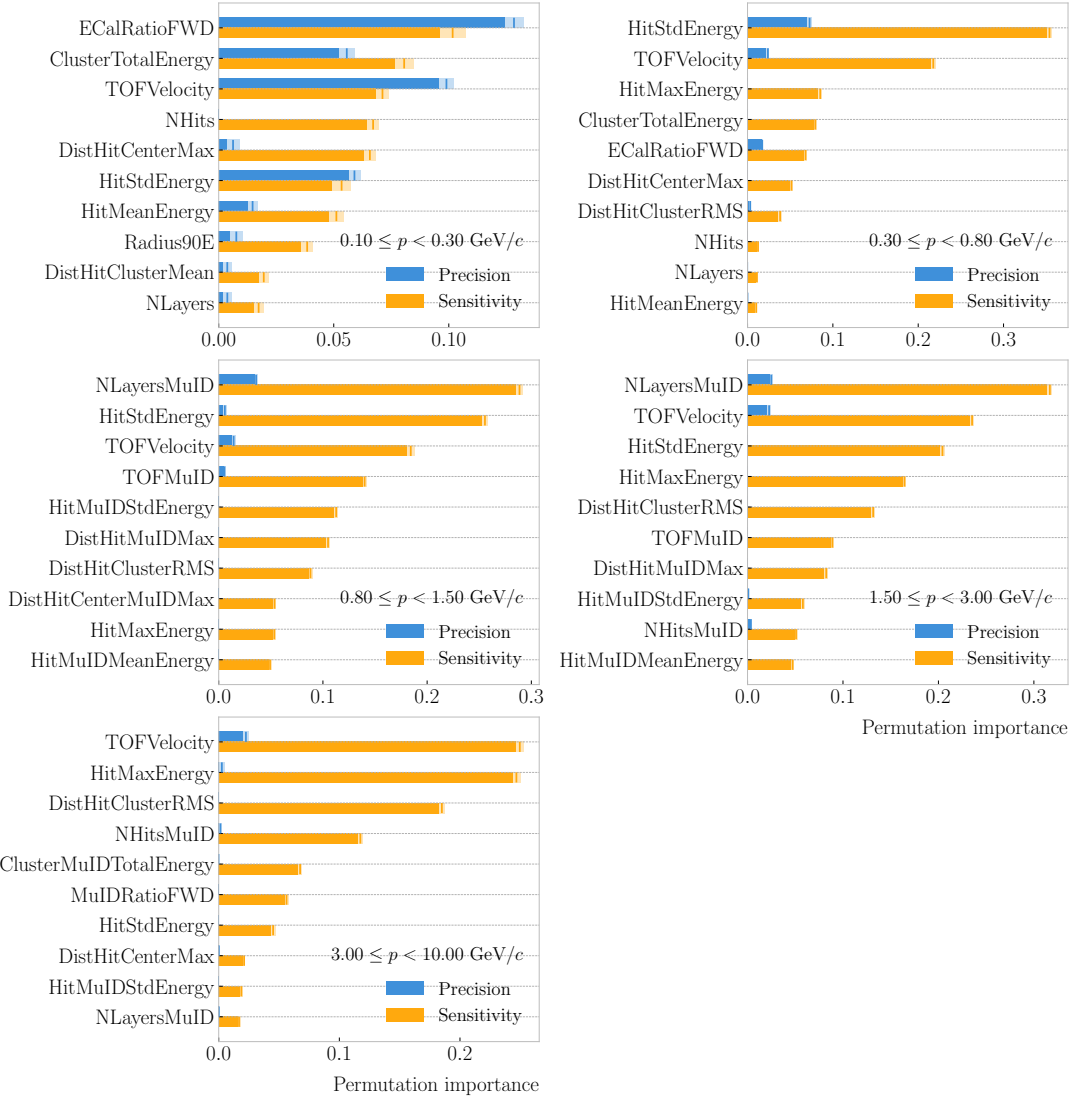


Figure 6.21: Permutation importances for the ten most important features in the different momentum ranges (from left to right, top to bottom, in increasing momentum order). The bars indicate the effect that permutations of each feature have on the purity (blue) and the sensitivity (yellow), the translucent regions representing one standard deviation around the central value.

CHAPTER 6. PARTICLE IDENTIFICATION IN ND-GAR

ranges.

With this, I conclude the study of the features. I have prepared the training and testing datasets and understood which features are likely to have the largest impact on the performance of the classifiers.

6.3.4 Hyperparameter optimisation

Any [BDT](#) requires the user to specify a number of parameters that will dictate its behaviour. They can be divided into two categories: (i) tree-specific parameters, which affect each individual tree in the model, and (ii) boosting parameters, which control the boosting operation in the model. The value of these so-called hyperparameters affect the performance and predictive power of the models. Therefore, one needs to carefully select their optimal values in order to extract as much information as possible from the data.

From all the parameters used to define a tree in the [scikit-learn](#) implementation of the [BDT](#) classifier, I only consider a subset of them. This is due to the fact that some are mutually exclusive, but also because I noticed that others have little effect on the problem at hand. Therefore, the parameters I investigate are the following:

- `min_samples_split`: defines the minimum number of samples required in a node to be considered for splitting. High values prevent a model from learning relations which might be highly specific to the particular sample, but may lead to underfitting.
- `min_samples_leaf`: defines the minimum samples required in a leaf node. For imbalanced problems it should take a low value, as there will not be many cases where the minority class dominates.
- `max_depth`: maximum depth of a tree. Useful to prevent overfitting, as high depths allow the model to learn relations specific to the training sample.

In the case of the boosting parameters, the ones I look at are:

- `learning_rate`: determines the impact of each tree on the final outcome. Low values make the model robust to the specific characteristics of a tree, and thus

6.3. MUON AND PION SEPARATION IN THE ECAL AND MUID

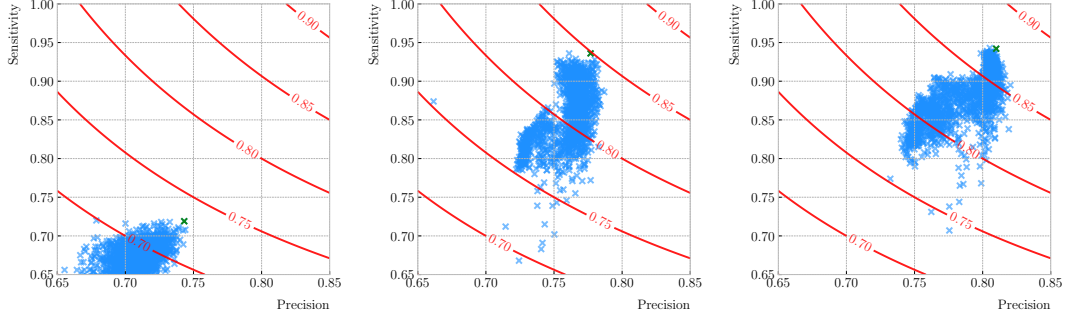


Figure 6.22: Values of the precision and sensitivity obtained for 10^4 BDT hyperparameter configurations, for the momentum regions I, III and V. The red contours indicate the curves of equal F_1 -score, while the green crosses are the selected configurations.

allow it to generalise well. However, that usually requires a large number of trees to model the data properly.

- **n_estimators**: number of sequential trees to be trained. In general, BDTs are fairly robust to high numbers of trees, but they can still overfit at a point.
- **subsample**: fraction of observations to be selected for each tree. Values slightly less than 1 make the model robust by reducing the variance.

In general, hyperparameters depend on each other. Thus, it is not possible to optimise them independently. In the literature, we find two main strategies to explore the hyperparameter space. We could use a grid search, in which one discretises a portion of the space of hyperparameters and evaluates the model at each point. Another approach is the randomised search, where a certain number of random configurations of hyperparameters are explored.

In this case, I use the random search to scan the hyperparameter space. Also, because it is not guaranteed that a set of hyperparameters can be efficiently applied across different datasets, I perform the optimisation for each of the momentum ranges considered. Table 6.2 shows the list of hyperparameters considered, and the range within which I let them vary. I decided to fix the number of estimators to 400 in all cases, as its value is correlated with that of the learning rate.

CHAPTER 6. PARTICLE IDENTIFICATION IN ND-GAR

Table 6.2: Optimal values of the hyperparameters used by the [BDT](#), for each momentum range.

Hyperparameter	Range	Best value				
		I	II	III	IV	V
<code>min_samples_split</code>	[0.001, 1]	0.10	0.06	0.05	0.27	0.06
<code>min_samples_leaf</code>	[0.001, 1]	0.02	0.03	0.01	0.02	0.07
<code>max_depth</code>	{2, 3, ..., 8}	8	2	4	2	7
<code>learning_rate</code>	[0.05, 1]	0.10	0.23	0.07	0.13	0.09
<code>subsample</code>	[0.01, 1]	0.75	0.65	0.79	0.86	0.95

I evaluate 10^4 different hyperparameter configurations for each momentum range. For the hyperparameter tuning, I use subsamples containing 10% of the full datasets, keeping the original proportions between classes, in order to reduce the computational load. The performance of the models was assessed using a stratified 3-fold cross-validation with replacement. Cross-validation involves dividing the data in a number of subsets, training the model using some of them, and testing it with the rest. In our case, I divide the data in 3 equal-sized subsets, maintaining the class proportions of the original dataset. Then, for 3 consecutive iterations, I train the models using 2 of the subsets while I compute the precision and sensitivity scores with the other. This approach provides a more robust estimate of the performance on unseen data.

Figure 6.22 shows the results in the precision versus sensitivity plane, for the momentum regions I, III and V (from left to right). The contours represent the curves of equal F_1 -score, i.e. the harmonic mean of the precision and the sensitivity. The shape of the clusters in this space gives us an idea of the best possible performance of the [BDT](#) when varying the hyperparameters. In order to select the optimal configurations (indicated in the plots with a green cross), I chose the point with the highest F_1 -score.

The results for the different momentum ranges are summarised in Tab. 6.2. One can see some consistency in hyperparameter choices, with models generally preferring small values for the tree-specific parameters, small learning rate, and relatively large subsample sizes.

6.3. MUON AND PION SEPARATION IN THE ECAL AND MUID

Table 6.3: Performance metrics of the **BDTs** with optimal hyperparameters, for the different momentum ranges.

Metric	Value $\pm 1\sigma$				
	I	II	III	IV	V
Accuracy	0.779 ± 0.003	0.812 ± 0.003	0.846 ± 0.002	0.861 ± 0.003	0.874 ± 0.002
Precision	0.769 ± 0.003	0.752 ± 0.005	0.788 ± 0.002	0.805 ± 0.003	0.815 ± 0.003
Sensitivity	0.745 ± 0.009	0.921 ± 0.006	0.965 ± 0.002	0.967 ± 0.002	0.976 ± 0.001
F_1 -score	0.757 ± 0.004	0.828 ± 0.003	0.867 ± 0.002	0.879 ± 0.002	0.889 ± 0.002
ROC AUC	0.868 ± 0.003	0.865 ± 0.003	0.899 ± 0.002	0.902 ± 0.002	0.911 ± 0.001

Now that I have obtained the optimal values of the hyperparameters, I can train the different **BDTs**. In this case I use the complete datasets, keeping 20% of the data for testing. Table 6.3 shows the values of the different performance metrics obtained using the selected hyperparameters and 5-fold cross-validation. The last row indicates the value of the area under the receiver operating characteristic (**ROC**) curve. This represents the sensitivity of a model as a function of the false positive rate. I have included it here as it is a classic model metric used in the machine learning community. Overall, there is a clear trend of models performing better at high momentum.

6.3.5 Probability calibration

So far, the trained **BDTs** are able to provide predictions of the class labels. Ideally, one would like the output of a classifier to give a confidence level about the prediction. However, it is not straightforward to interpret the outputs of our **BDTs** in terms of probabilities.

A way to visualise how well the predictions of a classifier are calibrated is using reliability diagrams [171]. They represent the probability of the positive label versus the probability predicted by the classifier. These can be obtained by binning the predicted probabilities, and then compute the conditional probability $P(y_{true} = 1 | y_i \leq y_{pred} < y_{i+1})$ by checking the fraction of true positive instances in each bin. The reliability diagram of a perfectly calibrated classifier would be a diagonal line.

CHAPTER 6. PARTICLE IDENTIFICATION IN ND-GAR

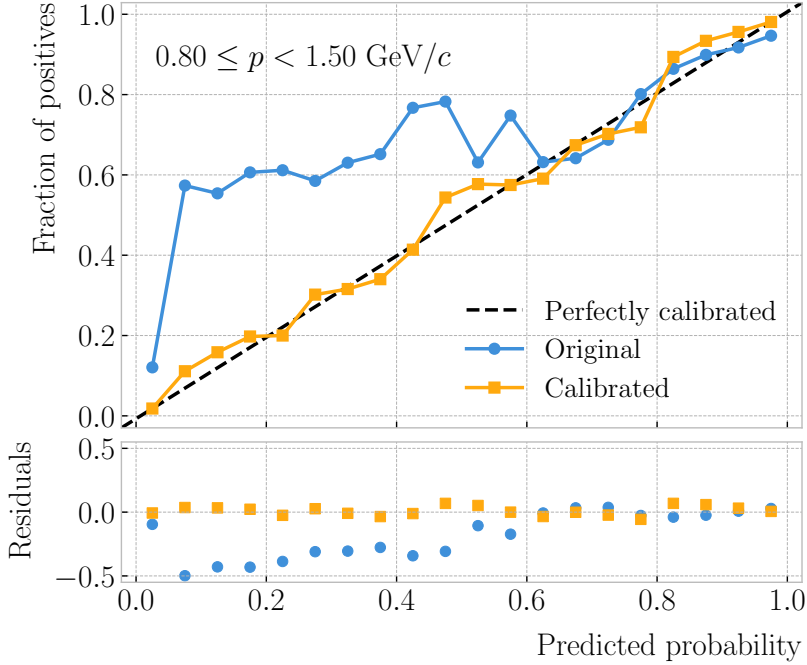


Figure 6.23: Reliability diagrams for the BDT classifier used in the momentum range $0.3 \leq p < 0.8 \text{ GeV}/c$, both for the original (blue circles) and calibrated (yellow squares) responses. For reference, the response of a perfectly calibrated classifier is also shown (black dashed line).

In this case, I try to correct the raw response of the classifiers by applying a sigmoid function:

$$\sigma(x; A, B) = \frac{1}{1 + e^{Ax+B}}, \quad (6.16)$$

where the parameters A and B are real numbers determined using the method of least squares.

For each classifier, I perform a grid search to obtain the optimal values of A and B . For any pair, I compute the predicted probabilities as $y_{pred} = \sigma(y_{raw}; A, B)$, where y_{raw} are the raw predictions of the classifier³. Then, I calculate the corresponding reliability curve, and take the sum of the squared residuals between it and the response of the perfectly calibrated classifier.

Figure 6.23 shows the reliability diagrams for the original (blue) and calibrated (yellow) probability predictions of the classifier for the III momentum range, $0.3 \leq p <$

³In scikit-learn these correspond to the outputs of the `decision_function` method.

6.3. MUON AND PION SEPARATION IN THE ECAL AND MUID

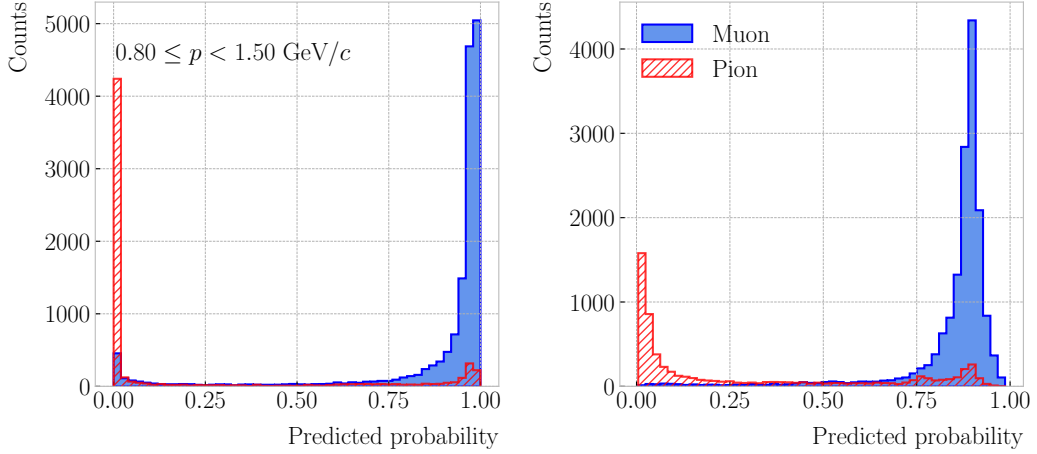


Figure 6.24: Uncalibrated (left panel) and calibrated (right panel) predicted probabilities assigned by the `BDT` classifiers for true muons (blue) and charged pions (red) in the momentum range $0.3 \leq p < 0.8 \text{ GeV}/c$.

$0.8 \text{ GeV}/c$. The original response of the classifier is given by $y_{pred} = \sigma(y_{raw}; -2, 0)$, which is the transformation applied by `scikit-learn` to produce the probability estimate. Notice how the calibrated prediction matches the ideal response much better than the original, across all the probability range.

One can also compare the responses of the uncalibrated and calibrated classifiers broken down by true particle type, as shown in Fig. 6.24. It can be seen that the distributions for both muons (blue) and charged pions (red) smoothen after calibration, but still the separating power of the classifier remains unchanged.

6.3.6 Performance

At this point, having the trained classifiers and the probability calibration parameters, I am able to assess the performance of the classification strategy in a physics-relevant case. For this, I prepared a sample of 10^5 FHC neutrino interaction events in the HPgTPC. Using the truth matching information, I select all true muons and pions, and apply the corresponding `BDT` classifier based on their momentum.

Figure 6.26 shows the resulting calibrated output of the classifiers for the different momentum regions. I do not include the first region, $0.10 \leq p < 0.30 \text{ GeV}/c$, as it only

CHAPTER 6. PARTICLE IDENTIFICATION IN ND-GAR

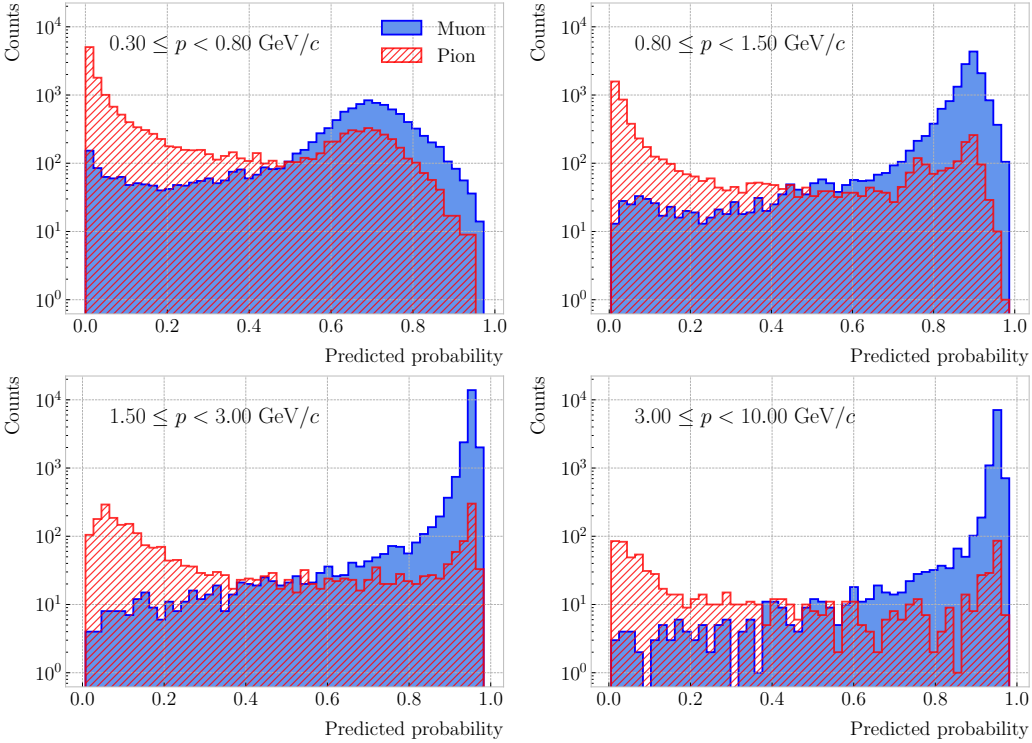


Figure 6.25: Calibrated predicted probabilities assigned by the **BDT** classifiers for the true muons (blue) and charged pions (red) in a **FHC** neutrino sample.

contains a small fraction of signal events. The distributions obtained for this validation sample appear quite consistent with the results found in the single particle case.

I also studied the performance of the muon identification in a track-by-track selection. To do so, I apply a simple cut on the output of the **BDT** classifiers. Every particle with a predicted probability higher than the cut is considered a muon, while the ones not passing the cut are taken to be pions. The results obtained for a cut of 0.50 are shown in Fig. 6.26. Both the efficiency (blue) and the purity (red) of the selection are displayed as a function of the momentum. The binning was chosen so that there were no bins in between different momentum ranges and each had roughly the same number of events. Even without optimising the value of the cut, the performance of the selection is excellent. The only issues appear in the first momentum range, where efficiency and purity sit slightly below 0.50. However, a dE/dx measurement could help enhance the selection there.

6.4. ECAL TIME-OF-FLIGHT

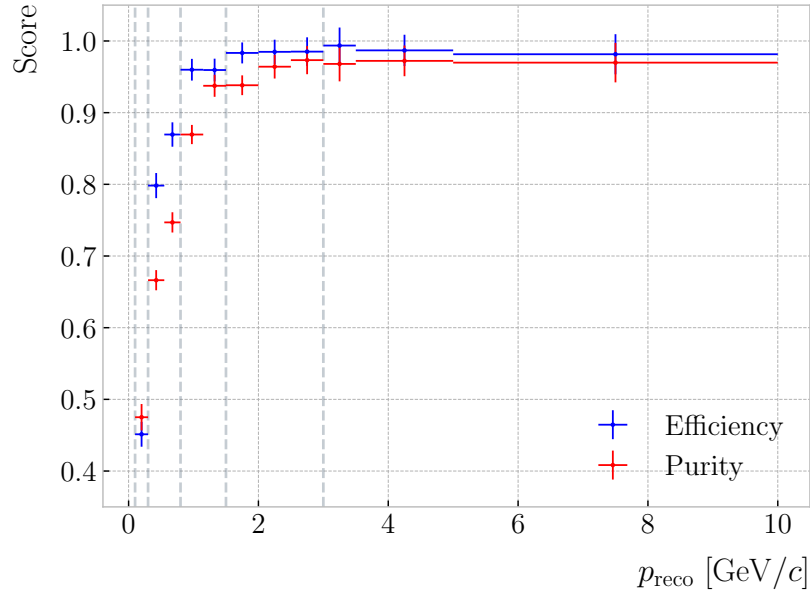


Figure 6.26: Efficiency (blue) and purity (red) of the muon selection as a function of the reconstructed momentum for the FHC neutrino sample.

This shows that the method behaves as expected when using unseen simulated data, generalising without problems from single particle to full neutrino events. In the coming Chapter, I will study how to use the outputs of the BDT, hereafter referred to as muon scores, to perform realistic event selections in ND-GAr.

6.4 ECal time-of-flight

Looking at Fig. 6.15, it is clear that for momentum values in the range $1.0 - 3.0$ GeV/ c it is not possible to separate pions and protons using a $\langle dE/dx \rangle$ measurement in the HPgTPC. However, in the previous section I assumed that protons at those energies could be identified by other means, and therefore were not an issue for the muon and pion discrimination.

Some detectors, like ALICE [172] or the ILD concept [173], complement the PID capabilities of their gaseous trackers with time-of-flight (ToF) measurements. The use of fast timing silicon sensors, with hit time resolutions under 100 ps, would allow for the identification of charged hadrons via a ToF measurement up to 5.0 GeV/ c . In the case

CHAPTER 6. PARTICLE IDENTIFICATION IN ND-GAr

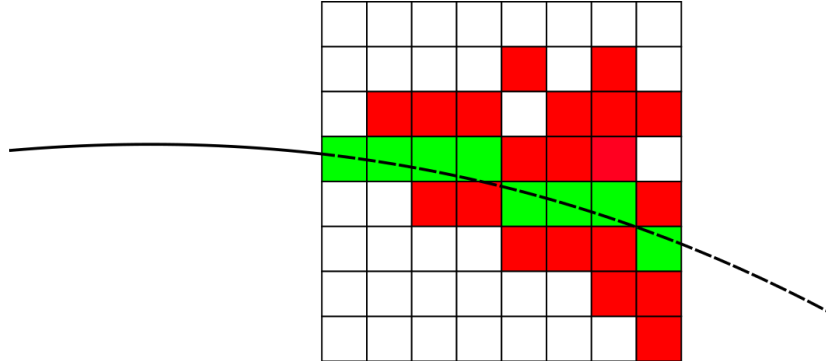


Figure 6.27: Schematic of the hit selection used for the [ToF](#) measurement. The grid represents the layers of the inner [ECal](#), with coloured squares indicating the tiles with hits. Green squares indicate the selected hits.

of [ND-GAr](#), one could think of using the inner layers of the [ECal](#), the ones consisting of high-granularity tiles, to obtain a [ToF](#)-based [PID](#), with some inputs from the [TPC](#).

Measuring the momentum and the velocity of a charged particle allows for a determination of the mass through the relativistic momentum formula:

$$m = \frac{p}{\beta} \sqrt{1 - \beta^2}. \quad (6.17)$$

In our case, the momentum is measured in the [TPC](#), using the curvature and the dip angle of the helix inside the magnetic field. The velocity of the particle can be written as:

$$\beta = \frac{\ell_{track}}{c\tau}, \quad (6.18)$$

where ℓ_{track} is the length of the track, and τ the arrival time to the [ECal](#).

In GArSoft, the track length is computed at the Kalman filter stage. It is simply the sum of the line segments along the track, either in the forward or backward fit. In this case, because we are only interested in the particles that make it to the [ECal](#), I choose the fit direction based on the results of the track-cluster associations.

Additionally, because the last 25 cm of the [HPgTPC](#) radius is uninstrumented, I need to correct for the length of the tracks. Using the track fit parameters to propagate

6.4. ECAL TIME-OF-FLIGHT

the helix to its entry point in the [ECal](#), one can write the total track length as:

$$\ell_{track} = \ell + \left| \frac{\phi_{EP} - \phi}{R^{-1}} \right| \sqrt{1 + \tan^2 \lambda}, \quad (6.19)$$

where ϕ_{EP} is the angle of rotation at the entry point to the calorimeter, and ℓ , ϕ , R and λ are the track length, angle of rotation, radius of curvature and dip angle at the last point in the fit, respectively.

To test the idea of performing a [ToF](#) measurement with the inner [ECal](#), I generated two data samples. Each consists of 10^4 single particle events, either charged pions or protons. Their momenta are uniformly distributed in the range $0.5 - 5.0$ GeV/ c , and their directions are isotropic. I process each sample using different values of the time resolution, from $\Delta\tau = 0$, the perfect time resolution case for comparison, to the current nominal value of $\Delta\tau = 0.7$ ns, and the worse scenario of $\Delta\tau = 1.0$ ns.

6.4.1 Arrival time estimations

In the simulation, the limited time resolution of the [ECal](#) is taken into account by applying a Gaussian smearing to the true hit times. Other effects, like the digitisation of the signals, are not taken into account and fall beyond the scope of this study. After the track-cluster association, one ends up with a collection of [ECal](#) hits associated to each particle. From these, the arrival time of the particle to the [ECal](#) can be extracted.

The simplest possibilities are to either take the time of the earliest hit or the hit closest to the entry point. Because in general these two coincide, I focus only on the earliest hit time. However, this needs to be corrected, to account for the distance travelled from the entry point to the position of the hit:

$$\tau_{earliest} = \tau_{hit} - \frac{d_{EP-hit}}{c}, \quad (6.20)$$

where τ_{hit} is the time of the earliest hit, and d_{EP-hit} is the distance between that hit and the entry point of the particle to the [ECal](#). This is computed as the arc length

CHAPTER 6. PARTICLE IDENTIFICATION IN ND-GAR

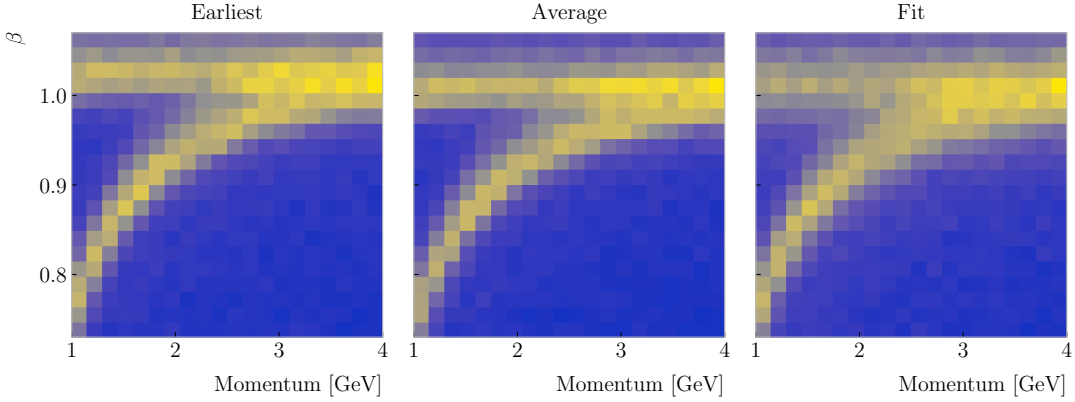


Figure 6.28: Particle velocity versus momentum measured with different [ECal](#) arrival time estimations. From left to right: earliest hit time, average hit time, and fitted hit time. In all cases the time resolution is $\Delta\tau = 0.1$ ns.

between the entry point and the point of the extrapolated helix up to the layer of the hit. This way of correcting the time assumes c for the velocity of the particle, which may lead to biased estimates.

I also tried to estimate the arrival times using information from the rest of the hits. In order to do this, as a simplifying assumption, I approximate the hadronic shower considering only its [MIP](#) component. For each layer, I keep only the hit in the tile closest to the point of the extrapolated track up to that layer. Figure 6.27 shows an example of how this hit selection works. The dashed line represents the extrapolated track, while the coloured squares are the tiles containing hits. I use green to indicate the tile closest to the track in each layer (in the sketch they correspond to the grid columns).

Now, I can use these collections of hits to estimate the arrival times. A possibility is to take the average of the times of the selected hits, denoted $\tau_{average}$. For that to work, one needs to correct these times, in a similar way as in Eq. (6.20), before taking the average. However, as before, this correction assumes that the particle travels at the speed of light inside the [ECal](#). Another option is to perform a linear fit to the hit times and the distances to the entry point. In that case, the arrival time would be the fitted value of the intercept, τ_{fit} . This method would not assume a speed of light propagation.

Figure 6.28 shows the velocity estimations as a function of the particle momentum,

6.4. ECAL TIME-OF-FLIGHT

for the earliest hit time (left panel), average hit time (middle panel), and fitted hit time (right panel), for a time resolution of $\Delta\tau = 0.1$ ns. The two bands correspond to the π^\pm and the p particles. Notice how, for the earliest hit time method, the velocities are significantly biased towards larger values. For the multi-hit methods, the τ_{fit} estimate appears to produce a larger variance than when using the $\tau_{average}$ method.

6.4.2 Proton and pion separation

Once we have the velocities of the particles, one can estimate their masses through Eq. (6.17). The resulting mass spectra are shown in Fig. 6.29. I computed the masses for the three arrival time estimates discussed above, and three different values of the time resolution: $\Delta\tau = 0.00$ (perfect time resolution), $\Delta\tau = 0.10$ ns, and $\Delta\tau = 0.70$ ns. Although in all cases we have the same number of events, it appears as if the entries in the histograms decrease as the time resolution increases. Sometimes, the particles get unphysical values of $\beta > 1$, and in turn they do not contribute to the mass spectra. This is more likely to happen for higher values of $\Delta\tau$.

As noted before, the average hit time method produces the most robust estimates when increasing $\Delta\tau$. Intuitively this makes sense, as by taking the mean one averages out the effect of the Gaussian smearing. Going forward, I will use this arrival time estimator, as it appears to be the best performing one.

It is possible to use the velocity estimations to select a sample of protons. In this case, I do so by dividing the relevant momentum range in bins of 0.1 GeV/ c . For each momentum bin, I compute the expected velocity for the protons via the inverse of Eq. (6.17), and then take the fractional residuals of the measured velocities. Using that distribution, I choose the cut that maximises the F_1 -score of the proton selection.

The results can be seen in Fig. 6.30, for the case $\Delta\tau = 0.10$ ns. As expected from Fig. 6.28, the performance of the selection degrades rapidly with increasing momentum. However, the purity is still around 75% at 3.0 GeV/ c . This is likely to be sufficient, as we do not expect protons or charged pions with higher energies from the beam neutrino interactions.

CHAPTER 6. PARTICLE IDENTIFICATION IN ND-GAr

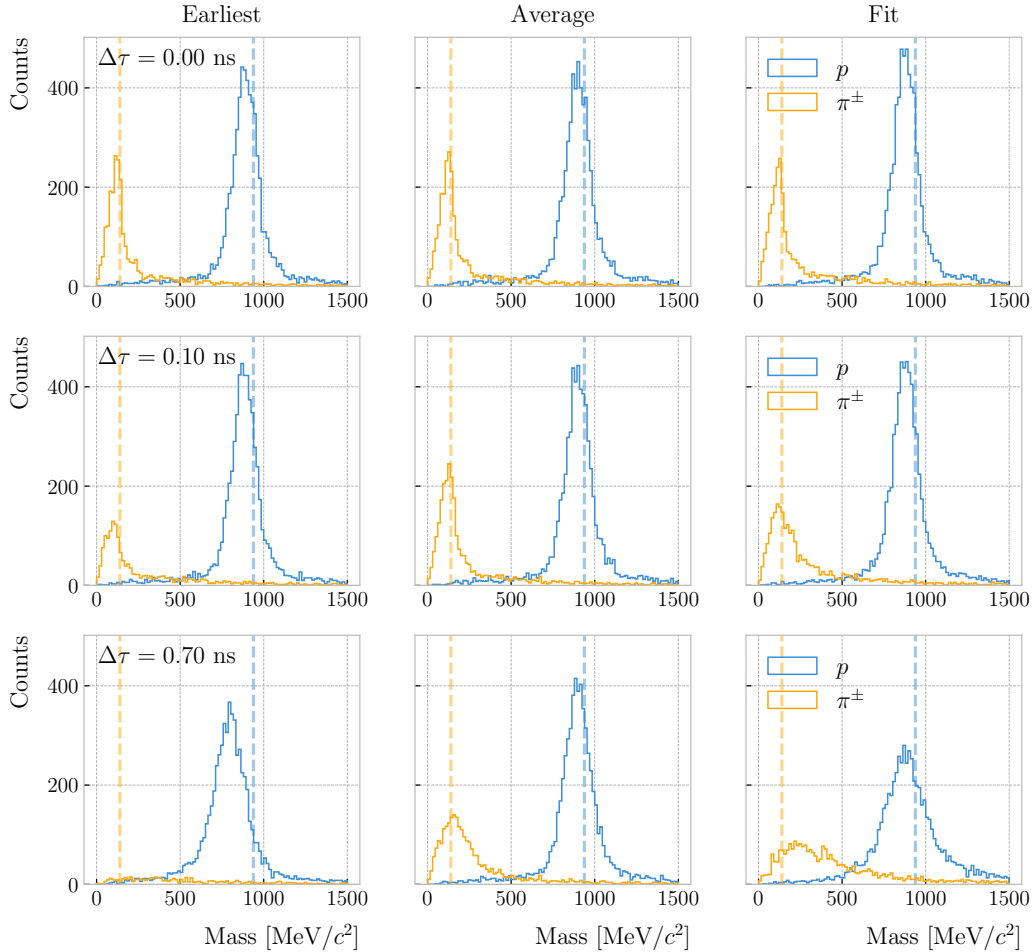


Figure 6.29: Mass spectra for p (blue) and π^\pm (yellow) particles, using different ECal time resolution values (from top to bottom, in ascending order), and arrival time estimates. From left to right: earliest hit time, average hit time, and fitted hit time. The dashed lines indicate the true masses of the particles.

Figure 6.31 shows a few examples of the ToF velocity estimation in a FHC neutrino sample. Here, for the different momentum bins, I have taken the fractional residual of the expected value of β for a proton and the measured values (black data points). The coloured lines represent Gaussian fits to the distributions of the different true particle, with the gray line being the sum of these. It can be seen that, even for momenta close to $2.0 \text{ GeV}/c$, a good proton separation can be achieved. This idea will be explored further later, in the context of the event selection.

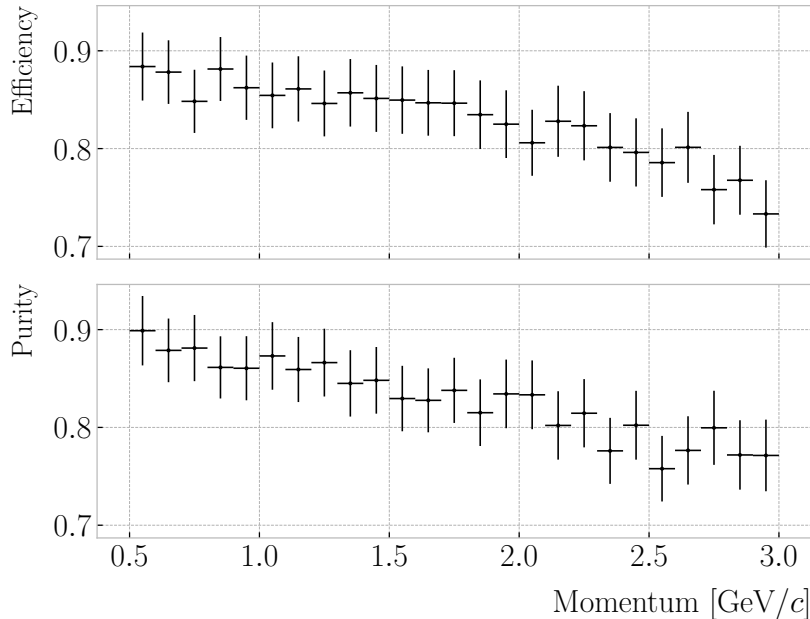


Figure 6.30: Efficiency (top panel) and purity (bottom panel) for the proton selection as a function of the momentum, for $\Delta\tau = 0.10$ ns.

6.5 Integration in GArSoft

All the additions and improvements to the reconstruction discussed in this Chapter had to be integrated in the GArSoft framework. This is necessary both to allow a more streamlined path for development, as this makes testing and adding features straightforward, as well as make the changes usable in future productions of simulated data. In this section, I outline the current status of the integration in GArSoft of the reconstruction work presented above.

The new track-cluster association code has been implemented in GArSoft, under the name of `TPCECALAssociation2`, and has now become the new default in the reconstruction. The structure of the module is similar to the previous implementation, and the data products they output are identical in form. Therefore, any existing code using the association objects does not need to be modified.

The computation of the truncated mean dE/dx of the tracks, the evaluation of the muon score for muon and pion separation, and the estimation of the velocity from

CHAPTER 6. PARTICLE IDENTIFICATION IN ND-GAr

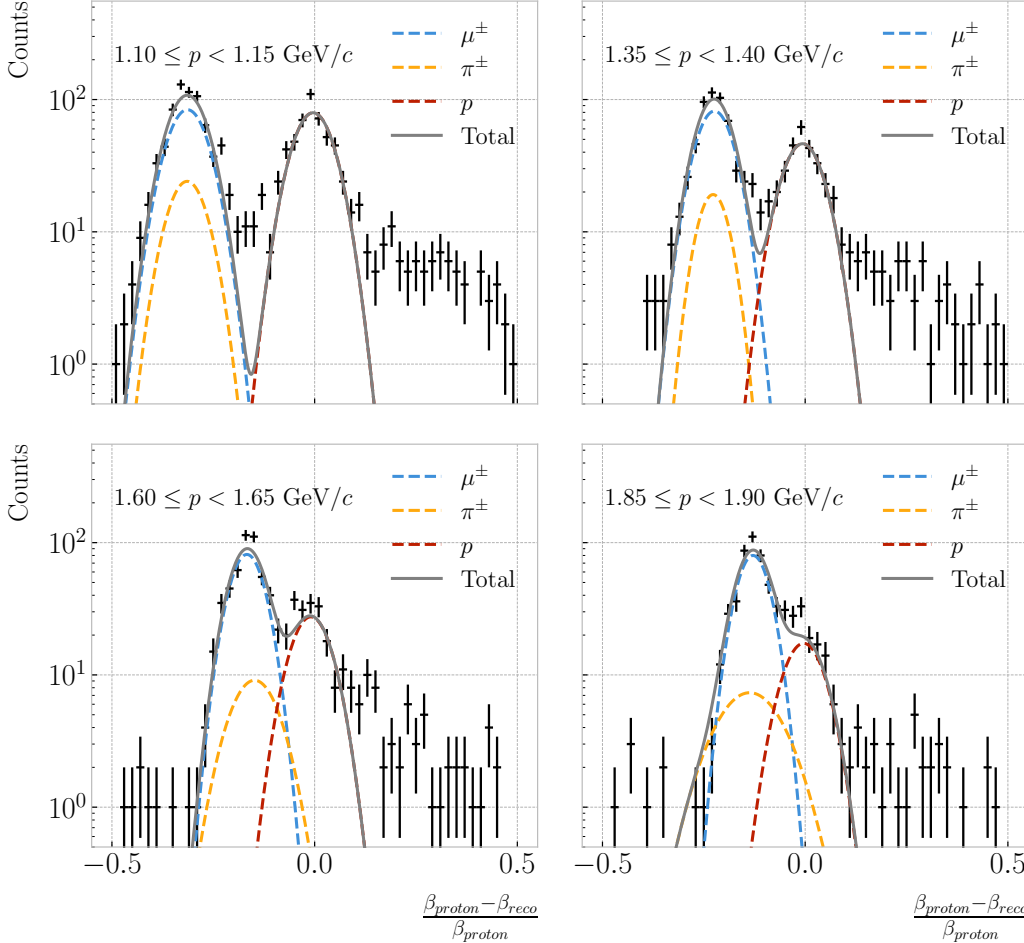


Figure 6.31: Distributions of the velocities measured by ToF with the inner ECal, for different momentum bins, in a FHC neutrino interaction sample. The Gaussian fits are performed around the maxima for each particle species.

time-of-flight are all orchestrated by the new `CreateRecoParticles` module. Each one of these is implemented as a separate algorithm, which is then called by the parent module. It generates the `gar::rec::RecoParticle` products, a new high-level data object in GArSoft. These combine the information from the `HPgTPC`, `ECal`, and `MuID` to create an object useful for analysers. At the moment, these data products are only generated for charged particles. However, in the future the module can be extended to incorporate other algorithms used for the identification of neutral particles, like neutral pions and neutrons.

Additionally, analogous to the muon score, the `gar::rec::RecoParticle` objects

6.5. INTEGRATION IN GArSOFT

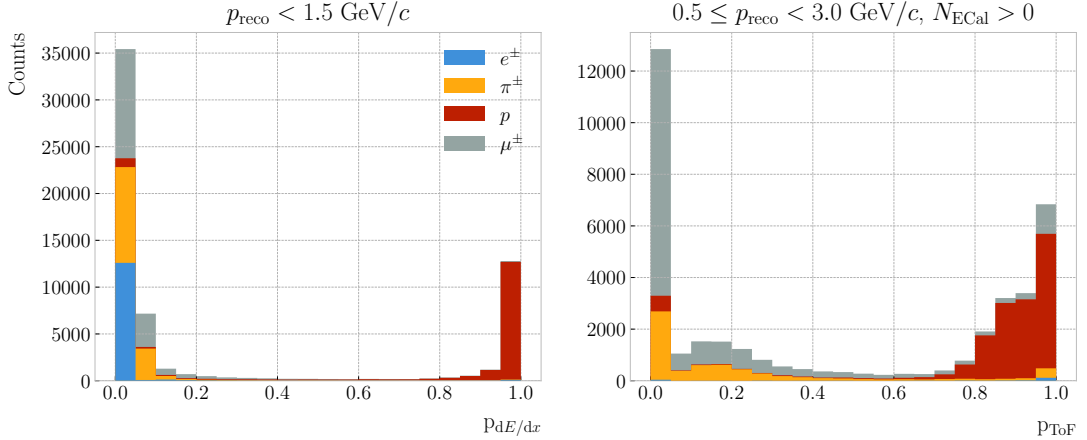


Figure 6.32: Distributions of proton dE/dx (left panel) and ToF (right panel) scores for a sample of 100000 FHC neutrino interactions in the HPgTPC. The distributions are broken down by the true particle type associated to the reconstructed particle.

contain two other scores based on the $\langle dE/dx \rangle$ and ToF estimates which measure the “protoness” of a reconstructed particles. These are obtained in a number of momentum bins, and are a measure of the distance to the point in the corresponding distribution that maximises the F_1 -score for the proton separation. This distance is then transformed applying a sigmoid function, which produces a score in the $0 - 1$ range, with coefficients obtained following a procedure similar to the one used to calibrate the response of the muon score. The dE/dx proton score is defined for all particles with momenta $p_{\text{reco}} < 1.5 \text{ GeV}/c$, whereas the ToF proton score is available for the particles with at least one associated hit in the inner ECal and momentum in the range $0.5 \leq p_{\text{reco}} < 3.0 \text{ GeV}/c$. As an example, Fig. 6.32 shows the distributions of the dE/dx (left panel) and ToF (right panel) proton scores for the reconstructed particles in a 10^5 FHC neutrino sample.

The calculation of the track breakpoint variables for pion decay identification discussed in App. C.2 is currently implemented as an analysis module in GArSoft. It would be interesting to add this information to the `gar::rec::RecoParticle` products, possibly calling the code as an additional algorithm in the `CreateRecoParticles` module. However, the best way to propagate the information to the high-level objects is still unclear.

The new ECal clustering algorithm proposed in App. C.3 is still in a development

CHAPTER 6. PARTICLE IDENTIFICATION IN ND-GAr

phase, and as such it has not replaced the current clustering module. At the moment, its latest version is integrated in GArSoft as the `CaloClustering2` module. The algorithm used is implemented separately, and then invoked in the main code. The module can be run standalone on the outputs of the reconstruction, creating a second instance of the `gar::rec::Cluster` collection. In the future it may replace the current algorithm as the default in the reconstruction chain. However, more work is needed in order to understand its performance in all the different use cases.

6.6 Summary

This Chapter reviews my work on the reconstruction for `ND-GAr`. In section 6.2 I describe how to use the calibrated energy deposits in the `HPgTPC` to compute the mean dE/dx for the reconstructed particles. I finish the section providing a parametrisation for how this depends on the momentum. The problem of the muon and pion separation is the topic of section 6.3. I propose to use the information from the `ECal` to achieve this classification. In this section, I describe the features and the procedure I follow to train the classifier, showing its performance as a function of the particle momentum. In section 6.4 I explore the possibility of performing a `ToF` measurement with the `ECal`. With this, I achieve a separation between pions and protons in a momentum range beyond the reach of the `HPgTPC` alone. Finally, in section 6.5 I describe the status of the integration of the different additions to the reconstruction chain.

The contributions to the reconstruction described in this Chapter represent the first attempt at a realistic `PID` using the end-to-end `ND-GAr` simulation. These `PID` metrics can already be used to explore the event selection capabilities of the detector, which is the topic of the next Chapter. The parallel development of the reconstruction and the selection strategies will allow for a physics-driven optimisation of our algorithms, based on the specific needs of the experiment.

Event selection in ND-GAr

You have power over your mind, not outside events. Realise this, and you will find strength.

– Marcus Aurelius, *Meditations*

As discussed previously, it is necessary to evaluate the capabilities of [ND-GAr](#) at identifying different particles. In the context of the [LBL](#) analysis, we want [ND-GAr](#) to provide data samples containing events of specific topologies, like ν_μ CC $1\pi^\pm$, ν_μ CC $1p1\pi^\pm$, etcetera. Thus, developing a strategy for the event selection using the current reconstruction is required.

In this Chapter, I present the results of a number of preliminary studies focused on the event selection in [ND-GAr](#), particularly the ν_μ CC selection and the pion tagging strategies. I also investigate the neutrino energy reconstruction, as well as the systematic uncertainties relevant for our detector. The objective is to demonstrate that the assumptions made in the [DUNE FD TDR](#) [96] are feasible with a full end-to-end [ND-GAr](#) simulation, as opposed to using a parametrised reconstruction. This means demonstrating that it is possible to reconstruct muon neutrino interactions, select pion exclusive samples, and measure relevant muon and pion quantities (including neutral pions). These preselections can then be used as starting points for the development of selections targeting more complicated topologies, relevant for oscillation or cross section analyses.

7.1 Simulated data sample

For the event selection studies I produced a [MC](#) sample consisting of 10^6 [FHC](#) neutrino interaction events inside the [HPgTPC](#) volume. The version of [GENIE](#) used was [v3_04_00](#), with the [G18](#) configuration. This is a version of the re-tune produced from [CCQE](#), [CC1 \$\pi\$](#) , [CC2 \$\pi\$](#) , and [CC](#) inclusive bubble chamber cross-section data [174]. It uses the local Fermi gas [84] as a description of the nuclear model. The quasielastic-like events are described by the Nieves quasielastic [175] and Valencia $2p2h$ [176] models. The Berger-Seghal model [177, 178] is used for the resonant and coherent pion production. As in all the [GENIE](#) tunes, the Bodek-Yang model [179] describes the [DIS](#) interactions. Finally, the [FSI](#) are described using the effective intranuclear transport model in [INTRANUKE](#).

For this sample, I used [GArG4](#) instead of [edep-sim](#) for the particle propagation. Because both [Geant4](#) wrappers use different configurations for the simulation, the results obtained differ. The default [edep-sim](#) configuration used by the [DUNE ND](#) is appropriate for [ND-LAr](#), where thresholds for particle production are higher. In the case of [ND-GAr](#), these parameters need to be adjusted accordingly. For the time being, in these first productions of analysis files, we use our standalone [Geant4](#) implementation.

The detector simulation and reconstruction used was GArSoft version [v02_21_00](#). I made use of the standard routines for the readout simulation and the reconstruction, which include the additions described in section 6.5. A summary of the GArSoft outputs is extracted in the form of a plain [ROOT TTree](#). These are then used, together with the [GENIE](#) output files, to produce common analysis files ([CAF](#)s). The version of the [CAF](#) format used in this analysis is [duneanaobj v3_07_00](#).

This sample only includes single interaction events. In the future, we will move to simulate full neutrino spills. Also, we will need to include neutrino interactions in the other detector volumes ([ECal](#), magnet, . . .), as well as rock muons making it to [ND-GAr](#). However, this will require a significant amount of work to go into the so-called interaction slicer, the part of the reconstruction in charge of splitting the reconstructed events.

7.1. SIMULATED DATA SAMPLE

Table 7.1: Estimated event rates in [ND-GAr](#), divided by interaction type and pion multiplicity, for two different values of the POT/year.

Process	Events/ton/year	
	1.1×10^{21} POT/year	1.9×10^{21} POT/year
All ν_μ -CC	1.60×10^6	2.83×10^6
CC 0π	5.28×10^5	9.35×10^5
CC $1\pi^\pm$	3.02×10^5	5.34×10^5
CC $1\pi^0$	1.65×10^5	2.92×10^5
CC 2π	3.18×10^5	5.63×10^5
CC 3π	1.36×10^5	2.41×10^5
CC other	1.52×10^5	2.69×10^5
All $\bar{\nu}_\mu$ -CC	7.54×10^4	1.33×10^5
All NC	5.50×10^5	9.73×10^5
All ν_e -CC	2.70×10^4	4.78×10^4

Looking forward, these sort of small samples are useful to prepare before launching a full production of [ND-GAr](#) events. In the original [DUNE TDR LBL](#) analysis, the event rates are calculated with a 1.1×10^{21} POT/year assumption, which assumes a combined uptime and efficiency of the accelerator complex and the [LBNF](#) beamline of 57% [69]. If we have one spill every 1.2 s, that translates into 7.5×10^{13} POT/spill. Therefore, assuming that the POT/spill scales linearly with beam power, in Phase II we will have 1.3×10^{14} POT/spill for the 2.1 MW beam. Or equivalently, 1.9×10^{21} POT/year using the same efficiency. The event rates per year in [ND-GAr](#) computed for these two possible values of the POT/year are shown in Tab. 7.1.

The latest [PRISM](#) plan requires 1.50 POT · years of data on-axis, followed by 0.25 POT · years at each off-axis position (2, 4, 8, 12, 16, 20, 24, and 28 m), both for the [FHC](#) and [RHC](#) mode. This implies that a full on-axis [ND-GAr](#) production will require a total of 2.85×10^{21} POT for both horn currents. The production of these samples is necessary to understand the impact of [ND-GAr](#) on the [LBL](#) sensitivities, and the studies presented here should be considered as a first step towards the realisation of such analysis.

7.2 ν_μ CC selection

In a ν_μ CC inclusive selection, the signal topology we look for is a neutrino-induced muon with or without other final state particles. Here, I also require the neutrino vertex to be located inside the fiducial volume (**FV**) of **ND-GAr**.

The **FV** is defined as a smaller cylinder within the cylindrical volume of the **HPgTPC**. The **FV** has a radius R_{FV} and a half-length L_{FV} . For a particle position to lie within the **FV** it must satisfy:

$$\vec{x}_i \in \left\{ \vec{x} \in \mathbb{R}^3 \mid |x_0| \leq L_{\text{FV}} \wedge \sqrt{x_1^2 + x_2^2} \leq R_{\text{FV}} \right\}, \quad (7.1)$$

in the reference frame of the **HPgTPC**. For convenience, I define:

$$\begin{aligned} \Delta R_{\text{FV}} &= R_{\text{HPgTPC}} - R_{\text{FV}}, \\ \Delta L_{\text{FV}} &= L_{\text{HPgTPC}} - L_{\text{FV}}, \end{aligned} \quad (7.2)$$

where R_{HPgTPC} and L_{HPgTPC} refer to the radius and the half-length of the **HPgTPC**, respectively. Figure 7.1 shows the **HPgTPC** volume with the **FV** inside of it. In that representation, the **FV** is defined as having $\Delta L_{\text{FV}} = 30.0$ cm and $\Delta R_{\text{FV}} = 30.0$ cm. Also shown is the **HPgTPC** reference frame, with x being the drift direction and z aligned along the beam direction.

In some cases, it is interesting to divide the signal events in different categories based on their true interaction mode. In this work, I will distinguish between charged-current quasi-elastic (**CCQE**), meson exchange current (**CCMEC**), resonant (**CCRES**), and deep-inelastic (**CCDIS**) interactions. I also use a separate category for the interactions not included in any of the other categories (**CCOther**).

Any other events are considered backgrounds. For this selection, I use the following categorisation of background events:

- Out of **FV**: if the true neutrino vertex lies outside the defined **FV**.

7.2. ν_μ CC SELECTION

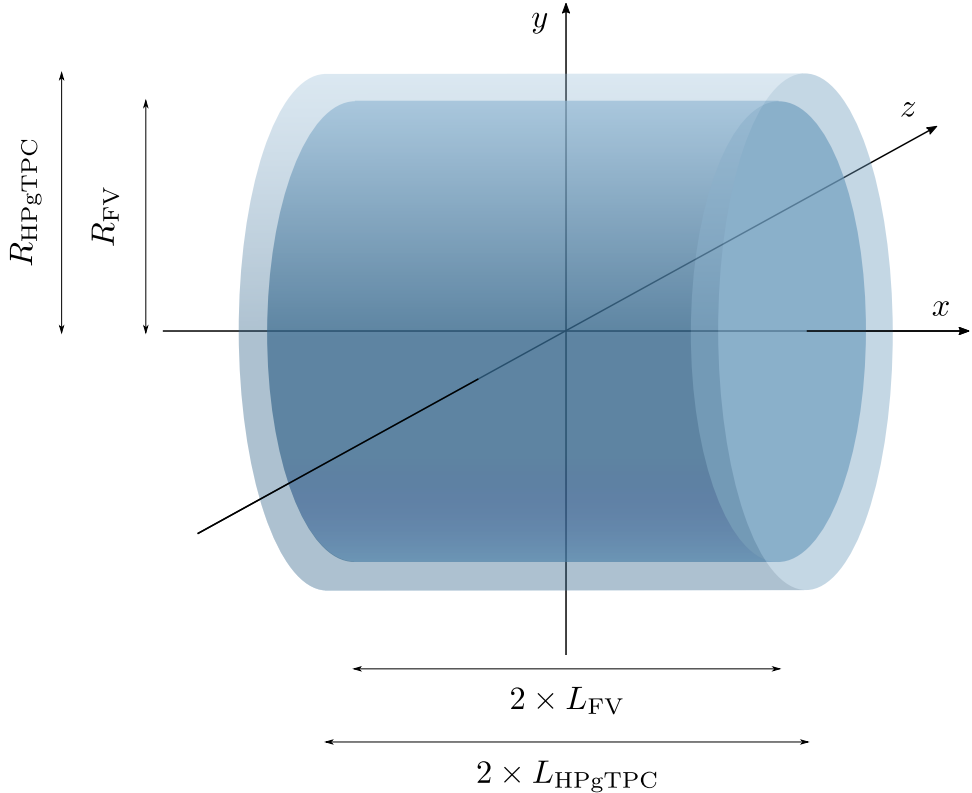


Figure 7.1: Schematic diagram of the HPgTPC including the fiducial volume (FV). In this case the FV is given by $\Delta L_{\text{FV}} = 30.0$ cm and $\Delta R_{\text{FV}} = 30.0$ cm.

- **NC:** if the event is a true neutral-current event.
- **$\bar{\nu}_\mu$ CC:** if the true neutrino candidate is of muon antineutrino flavour.
- Other: if the event is not signal nor falls in any of the other background categories.

The key to the CC selection is the identification of a primary muon candidate. Typically, this is the longest track in the event. However, sometimes protons and pions leave tracks longer than that of the muon. This is particularly important in the GAr medium, as it is considerably less dense than the LAr. For this reason, the muon identification in ND-GAr relies heavily on the capabilities of the ECal.

The selection strategy proposed combines the information coming from the three main detection systems of ND-GAr: the HPgTPC charge readout, and the ECal and MuID detectors. It consists of five steps:

CHAPTER 7. EVENT SELECTION IN ND-GAR

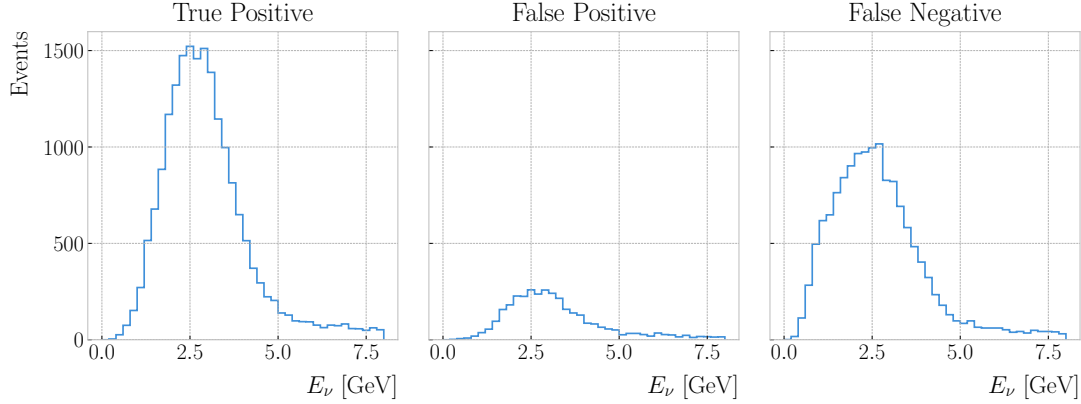


Figure 7.2: True positive (left panel), false positive (middle panel), and false negative (right panel) true neutrino energy distributions for the ν_μ CC selection given by a muon score cut of $\mu_{\text{score}}^{\text{cut}} = 0.75$, and a FV defined as $\Delta L_{\text{FV}} = 30.0$ cm and $\Delta R_{\text{FV}} = 30.0$ cm.

1. Event contains reconstructed particles.
2. Select particles with reconstructed negative charge, $q_{\text{reco}} = -1$.
3. Select particles passing the muon score cut, $\mu_{\text{score}} \geq \mu_{\text{score}}^{\text{cut}}$.
4. Keep reconstructed particle with the highest momentum, $\max [p_{\text{reco}}]$.
5. Check that the remaining particle starts within the FV.

All the events passing these cuts are classified as signal, and the selected particle is regarded as the primary muon candidate.

7.2.1 Selection optimisation

I performed an optimisation of this selection, comparing the performance of a number of configurations. For the muon selection, I varied the value of $\mu_{\text{score}}^{\text{cut}}$ from 0.05 to 0.95, using a step size of 0.05. Additionally, to optimise the FV, I systematically explored a number of different parameter configurations, moving within the 10.0 – 70.0 cm range for ΔL_{FV} and 25.0 – 75.0 cm for ΔR_{FV} , in increments of 10.0 cm and 5.0 cm, respectively.

For each parameter configuration, I extract three different true neutrino energy distributions. These are built combining the results of the selection described previously, which we can refer to as the “reco” selection, and a “true” selection. The later identifies

7.2. ν_μ CC SELECTION

the true ν_μ CC events using the GENIE event records, and checks that the true neutrino vertices are contained in the FV.

The first distribution consists of the events passing both selections, i.e., these are the true ν_μ CC events which pass the “reco” selection. The second distribution contains the events passing the “reco” selection but failing the “true” selection. These are the background events that the selection misidentifies. Finally, the third distribution corresponds to the events picked by the “true” selection but not by the “reco” one. In other words, these are the true ν_μ CC events that our selection misses. In analogy to the machine learning jargon, I refer to these distributions as the true positive (TP), false positive (FP), and false negative (FN) spectra, respectively. Figure 7.2 shows an example of these three distributions for the case $\mu_{\text{score}}^{\text{cut}} = 0.75$, $\Delta L_{\text{FV}} = 30.0$ cm, and $\Delta R_{\text{FV}} = 30.0$ cm.

By making different combinations of these distributions one can compute a series of performance metrics. Using the full information from the spectra allows one to obtain the scores as a function of the true neutrino energy, whereas the totals can be obtained by integrating the histograms. This way, the efficiency of the selection is given by:

$$\begin{aligned} \text{Efficiency} &= \frac{\text{Selected true } \nu_\mu \text{ CC events}}{\text{Total true } \nu_\mu \text{ CC events}} \\ &= \frac{\text{TP}}{\text{TP} + \text{FN}}, \end{aligned} \tag{7.3}$$

while the purity can be written as:

$$\begin{aligned} \text{Purity} &= \frac{\text{Selected true } \nu_\mu \text{ CC events}}{\text{Total selected events}} \\ &= \frac{\text{TP}}{\text{TP} + \text{FP}}. \end{aligned} \tag{7.4}$$

Another scoring metric typically used when quantifying the performance of a selection is the significance. It is defined as:

$$\text{Significance} = \frac{S}{\sqrt{S+B}} = \frac{\text{TP}}{\sqrt{\text{TP}+\text{FP}}}. \tag{7.5}$$

CHAPTER 7. EVENT SELECTION IN ND-GAR

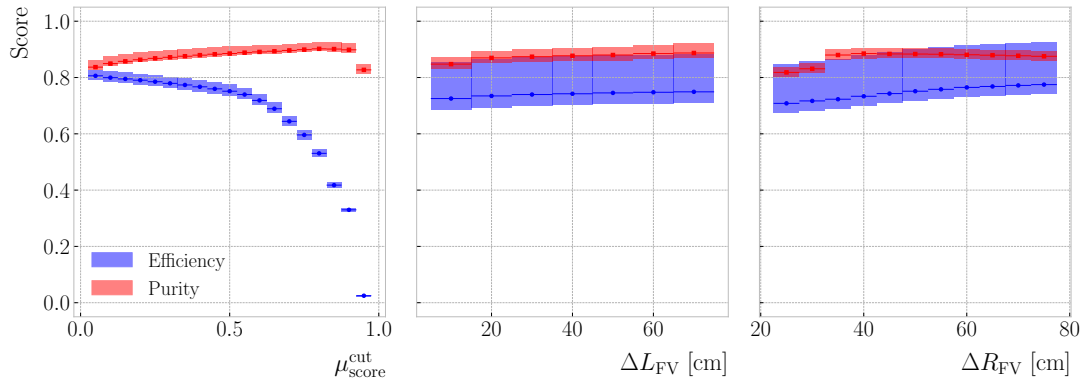


Figure 7.3: Efficiency (blue) and purity (red) for the ν_μ CC selection as a function of the muon score cut (left panel), FV half-length cut (middle panel), and radial cut (right panel). The height of the boxes represents the IQR of the conditional distributions, whereas the horizontal line corresponds to the median.

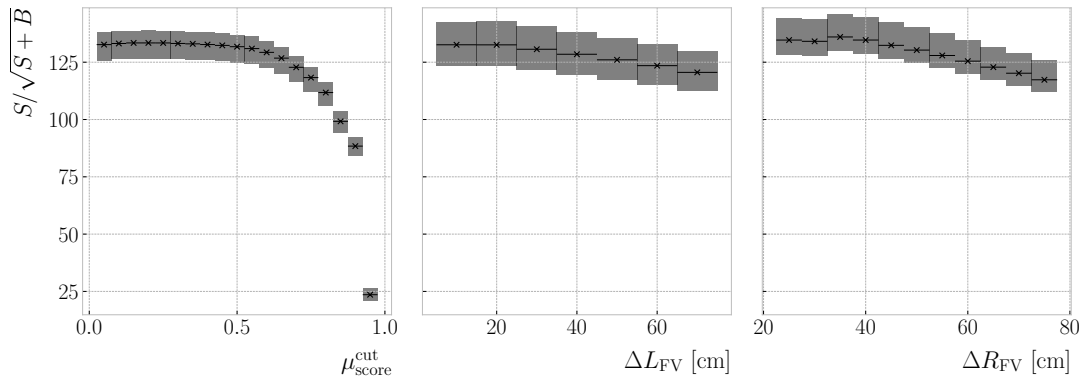


Figure 7.4: Significance for the ν_μ CC selection as a function of the muon score cut (left panel), FV half-length cut (middle panel), and radial cut (right panel). The height of the boxes represents the IQR of the conditional distributions, whereas the horizontal line corresponds to the median.

The significance measures the relative size of the true signal within the selection, $S = \text{TP}$ with respect to one standard deviation of the counting experiment. Assuming Poisson statistics, the variance is equal to the number of observations, and therefore the standard deviation is $\sqrt{N} = \sqrt{S + B} = \sqrt{\text{TP} + \text{FP}}$.

Figure 7.3 shows the change in efficiency (blue) and purity (red) of the ν_μ CC selection as a function of the different cuts. From left to right, I vary $\mu_{\text{score}}^{\text{cut}}$, ΔL_{FV} , and ΔR_{FV} . For each value of the cuts, I compute the median and IQR (represented by the horizontal lines and the heights of the boxes, respectively) of the corresponding

7.2. ν_μ CC SELECTION

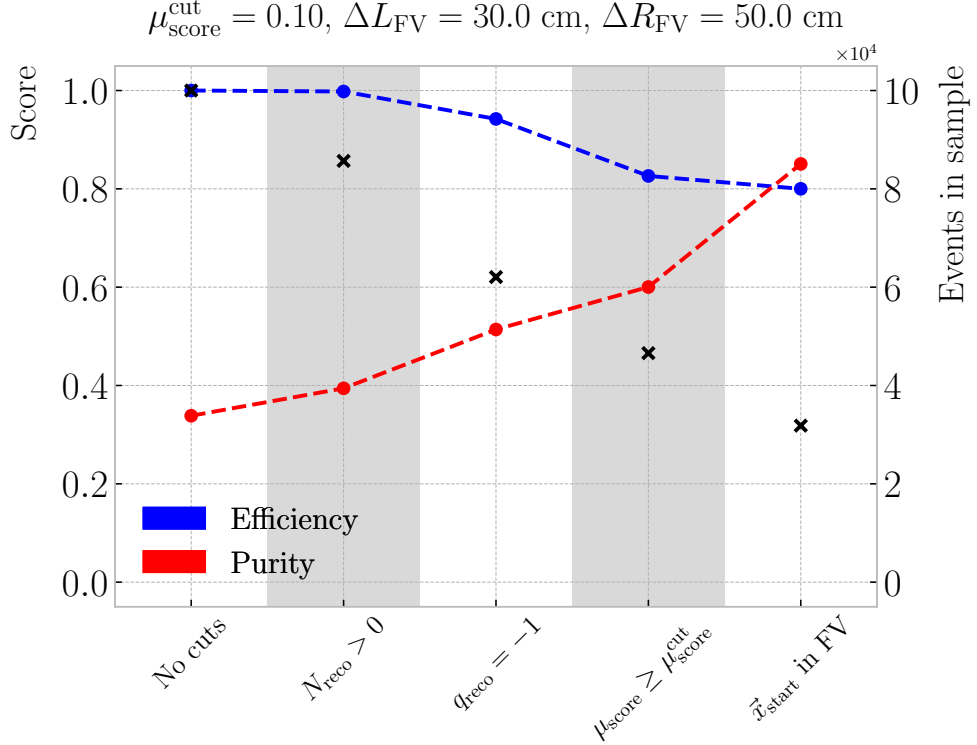


Figure 7.5: Cumulative efficiency (blue) and purity (red) of the ν_μ CC selection. The secondary axis indicates the number of events in the sample after each cut (black crosses).

conditional distributions of efficiency and purity. This representation is useful to get an idea of the general trend the scores follow with the cuts, as well as the spread. It is clear that the muon score cut has the biggest impact on the efficiency, which ranges between 0.05 to 0.80, whereas the purity remains stable with values around 0.85.

A similar depiction of the significance can be found in Fig. 7.4. In this case, one can see that the $S/\sqrt{S+B}$ decreases as the cuts grow tighter. However, there are hints of local maxima at intermediate values.

Selecting the cut configuration with the highest significance, 147 ± 11 for the parameter values explored here, results in an efficiency and purity of 0.754 ± 0.006 and 0.833 ± 0.007 , respectively. However, there are other selections which allow to achieve higher efficiencies and purities, maintaining similar significance values.

Therefore, to get a more refined selection, I first select the configurations with a purity and an efficiency higher than 0.85 and 0.80, respectively. After that, I select the

CHAPTER 7. EVENT SELECTION IN ND-GAR

Table 7.2: Step-by-step ν_μ CC selection cuts and cumulative passing rates. Relative passing rates are indicated in parentheses.

Cut #	Selection cut	Events	Passing rates
0	Total number of events (No cuts)	100000	100.00% (100.00%)
1	At least one reconstructed particle	85680	85.68% (85.68%)
2	Negatively charged particles only	62054	62.05% (72.43%)
3	$\mu_{\text{score}} \geq \mu_{\text{score}}^{\text{cut}}$	46585	46.59% (75.07%)
4	Candidate \vec{x}_{start} in FV	31834	31.83% (68.34%)

tuple of cuts yielding the highest significance. The resulting value for the muon score cut is $\mu_{\text{score}}^{\text{cut}} = 0.10$, and the FV is given by $\Delta L_{\text{FV}} = 30.0$ cm and $\Delta R_{\text{FV}} = 50.0$ cm. With these, one obtains a total efficiency of 0.800 ± 0.007 and purity of 0.851 ± 0.008 , with a significance of 138 ± 11 . Hereafter, I use this optimised selection cuts, unless specified otherwise.

A summary of the selection can be found in Tab. 7.2. It shows the number of events in the selected sample after each selection cut, as well as the absolute and relative passing rates. Figure 7.5 shows the overall efficiencies (blue) and purities (red) after each cut in the event selection is applied. As expected, the efficiency drops while the purity increases with the successive cuts.

Notice how, out of the cuts prior to the FV constraint, the sign selection produces the highest increase in purity. This is one of the advantages of having a magnetised TPC, and can also be used for a $\bar{\nu}_\mu$ CC selection when running in RHC mode.

7.2.2 Selection performance

Using the stored spectra discussed above, the true neutrino energy distribution for the selected events can be recovered computing TP + FP. Similarly, the combination TP + FN gives the true spectrum. Figure 7.6 shows the true (black data points) and selected (coloured stacked histogram) E_ν distributions for the optimised ν_μ CC selection. The colours in the selected spectrum indicate the different signal categories and backgrounds, with the overall statistical uncertainty represented by the gray hatched mess. The ratio

7.2. ν_μ CC SELECTION

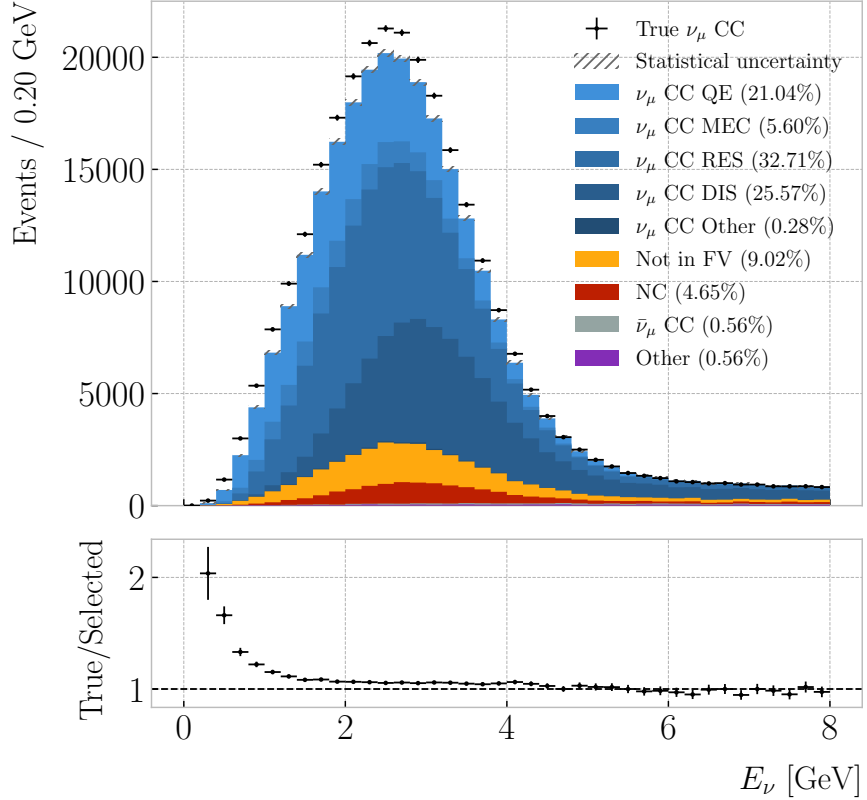


Figure 7.6: True neutrino energy spectra for the ν_μ CC selection. The selected events correspond to the coloured stacked histogram, broken down by signal and background subcategories. The statistical uncertainty is drawn in hatched gray. The true distribution is also shown with the black data points. The bottom panel shows the ratio between the number of true and selected ν_μ CC events per bin.

between the true and selected events is also shown (bottom panel). One can see that it sits around 1 for most of the energy range. However, for energies ≤ 1 GeV there is a significant deficit of selected events.

These spectra also allow to compute the efficiency and purity of the selection as a function of the true neutrino energy, as shown in Fig. 7.7. As it could be expected from the previous ratio plot, the efficiency is low at low neutrino energies. Nonetheless, it rises quickly with the energy, until it stabilises around a value of 0.80. Looking at the purity, one may notice that, although it starts at around 0.90, there is a significant decrease towards the high end of the spectrum.

A variation of the ν_μ CC selection one can try is to apply it without the reconstructed

CHAPTER 7. EVENT SELECTION IN ND-GAR

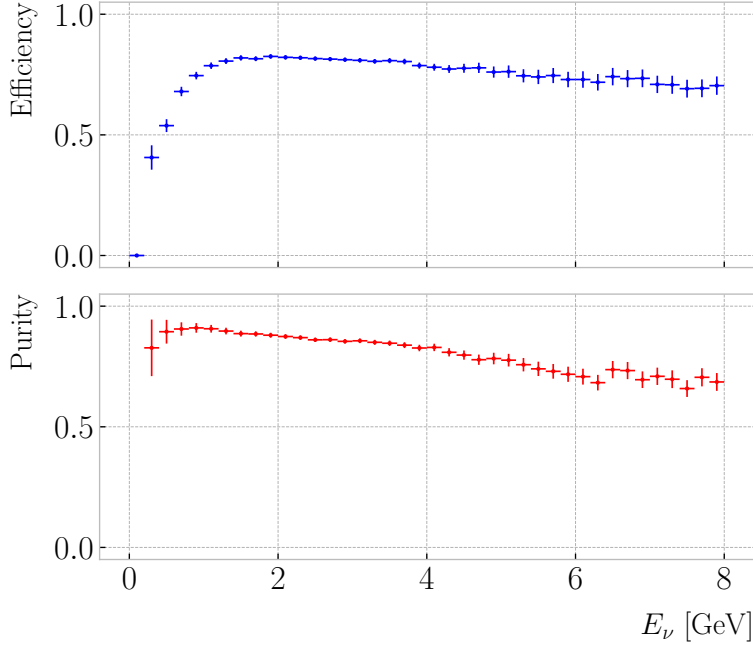


Figure 7.7: Efficiency (top panel) and purity (bottom panel) for the ν_μ CC selection as a function of the true neutrino energy.

charge cut. Figure 7.8 (top panel) shows the E_ν distributions corresponding to the selection with (blue stacked histogram) and without (red stacked histogram) the sign selection. In the former case, the out of FV contamination amounts to 9.06% of the total, while the NC contamination results 4.77% and the wrong-sign contamination 0.57%. For the latter, these backgrounds account for the 10.01%, 10.82%, and 2.18% of the selected events, respectively. As expected, removing the positive particles does not change the FV-related effects noticeably. However, the sign selection proves its worth in the rejection of $\bar{\nu}_\mu$ CC events, which drop almost by one order of magnitude. Additionally, the charge selection cuts the NC events in half, as it reduces the chances of misidentifying a positively charged hadron for a muon.

As an additional check, I explored how the performance of the ν_μ CC selection depends on the position of the neutrino interaction within the HPgTPC. Maps of the selection efficiency for the X, Z (top left panel), X, Y (bottom left panel), and Z, Y (right panel) true vertex position pairs are given in Fig. 7.9. It can be seen that the efficiency remains stable along the drift direction, only slightly degrading close to the

7.2. ν_μ CC SELECTION

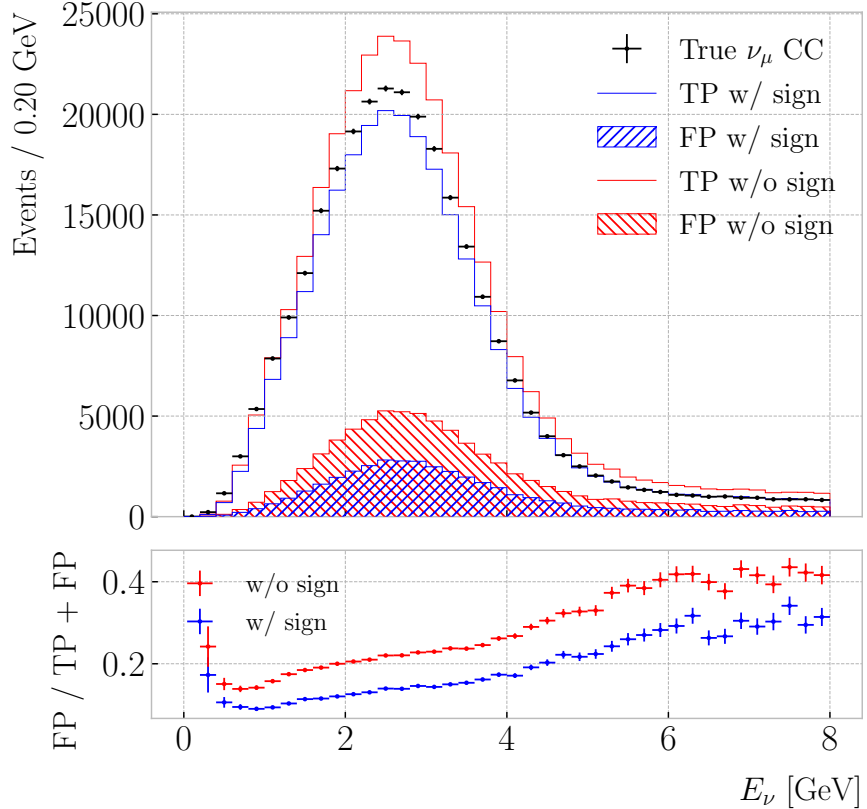


Figure 7.8: True neutrino energy spectrum for the ν_μ CC selection with (blue) and without (red) sign selection. The selected events are broken down by true positives (signal) and false positives (background). The true distribution is also shown (black data points). The bottom panel shows the ratios between the number of false positives and total selected events per bin.

edges of the FV. Regarding the radial direction, it is clear that an important number of events with high $Z_{\text{vtx}}^{\text{truth}}$ are not being selected. Intuitively, the muons arising from these interactions will leave short tracks. As their directions are typically aligned with the beam direction, they enter the ECal shortly after production. This is likely to affect the tracking, and therefore their identification. As a result, the regions with the lowest efficiency are the downstream corners of the HPgTPC, i.e. the areas with high $|X_{\text{vtx}}^{\text{truth}}|$ and $Z_{\text{vtx}}^{\text{truth}}$.

CHAPTER 7. EVENT SELECTION IN ND-GAR

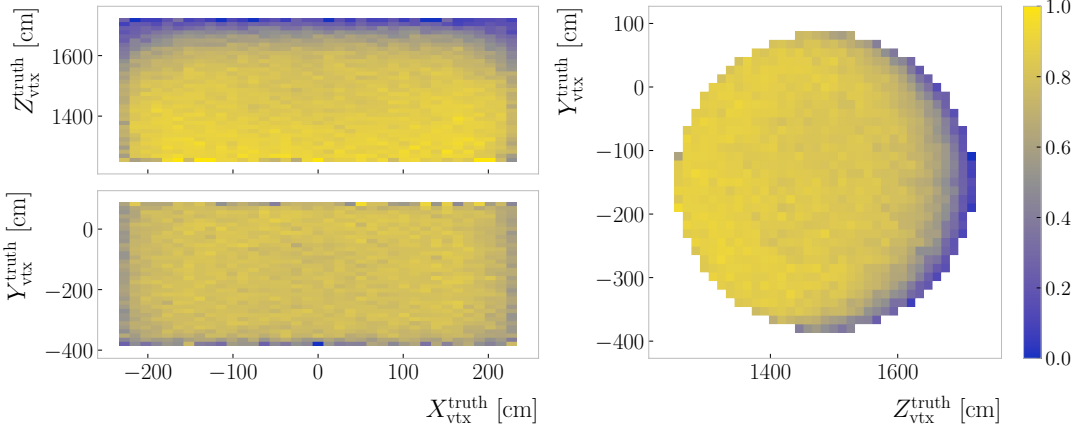


Figure 7.9: Efficiency 2D distributions for the ν_μ CC selection given the true position of the interaction vertex.

7.2.3 Primary muon kinematics

This ν_μ CC selection relies on the identification of the a primary muon, meaning that for each selected event a particle is picked out as the muon candidate. This allows for the study of the kinematics of these selected primary muons.

Figure 7.10 shows a comparison between some of the reconstructed and truth primary muon kinematic variables. From top to bottom, left to right, we have muon momentum, longitudinal momentum, transverse momentum, and beam angle. The histograms are column-normalised, and so the diagonal entries give an idea of the resolution for the different variables. The match between truth and reconstructed values can only be done for the selected true ν_μ CC events, as the others do not have a primary muon. However, for this comparison I do not require the events to start inside the FV.

Notice that, for the reconstructed values, the variables do not necessarily come from a reconstructed particle that matches the true primary muon. In other words, sometimes, even though the event was correctly identified, the primary muon may have been confused with another particle. This means that these distributions include both reconstruction and selection deficiencies.

I also studied the performance of the ν_μ CC selection as a function of the kinematic variables of the primary muon. As before, these metrics are only possible to compute for

7.2. ν_μ CC SELECTION

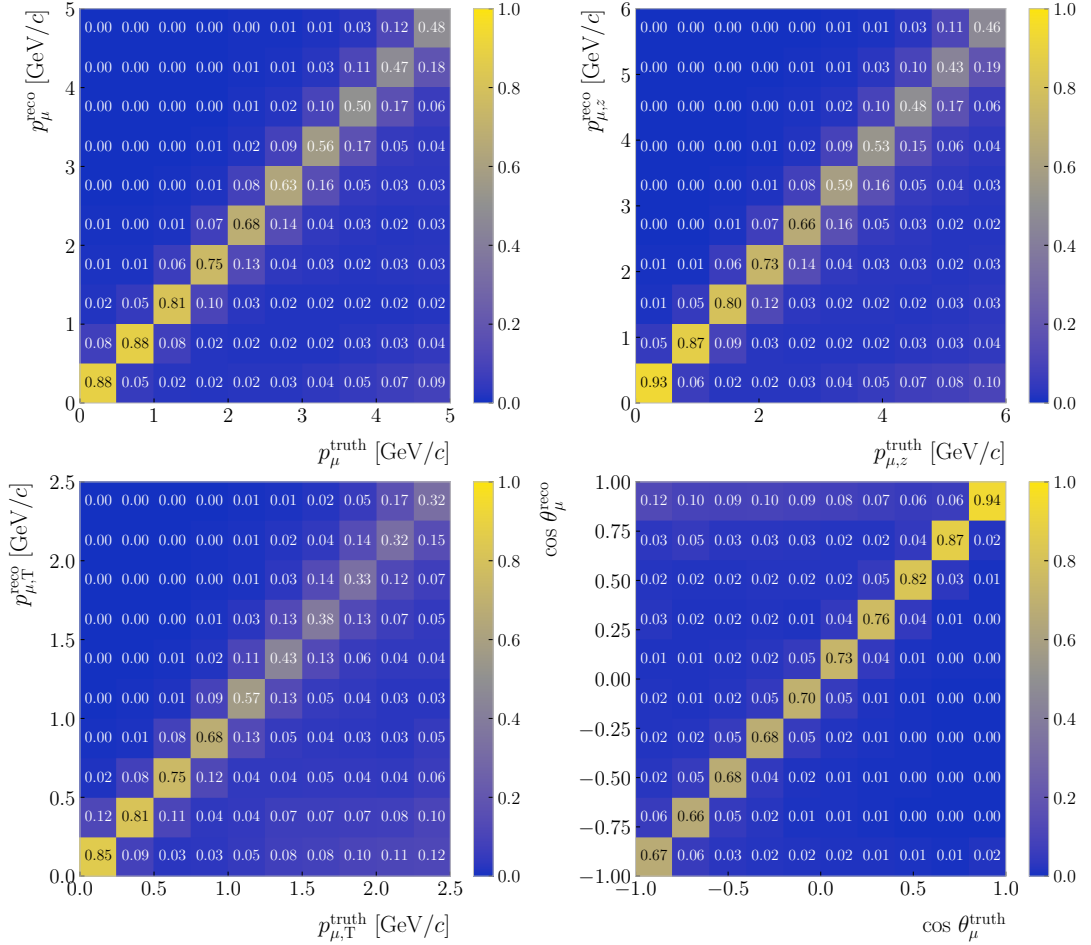


Figure 7.10: Distributions for the reconstructed versus truth generated primary muon momentum (top left panel), longitudinal momentum (top right panel), transverse momentum (bottom left panel), and beam angle (bottom right panel). The reconstructed values correspond to the selected primary muon candidate, whereas the truth values come from the true primary muon in the event.

true ν_μ CC events. The efficiency (top panels) and purity (bottom panels) as a function of the truth muon momentum (left) and beam angle (right) are shown in Fig. 7.11. One can see that there are some similarities in the behaviour of both metrics between the true neutrino energy and the muon momentum cases. This is to be expected, as these two variables are highly correlated. For the efficiency, there is a rapid increase at low momentum values until it peaks at around $1 \text{ GeV}/c$, after which it starts decreasing slowly. The purity remains relatively constant, with a slight drop towards high p_μ^{truth} values. In the case of the muon angle, the decrease in efficiency at high $\theta_\mu^{\text{truth}}$ is more

CHAPTER 7. EVENT SELECTION IN ND-GAR

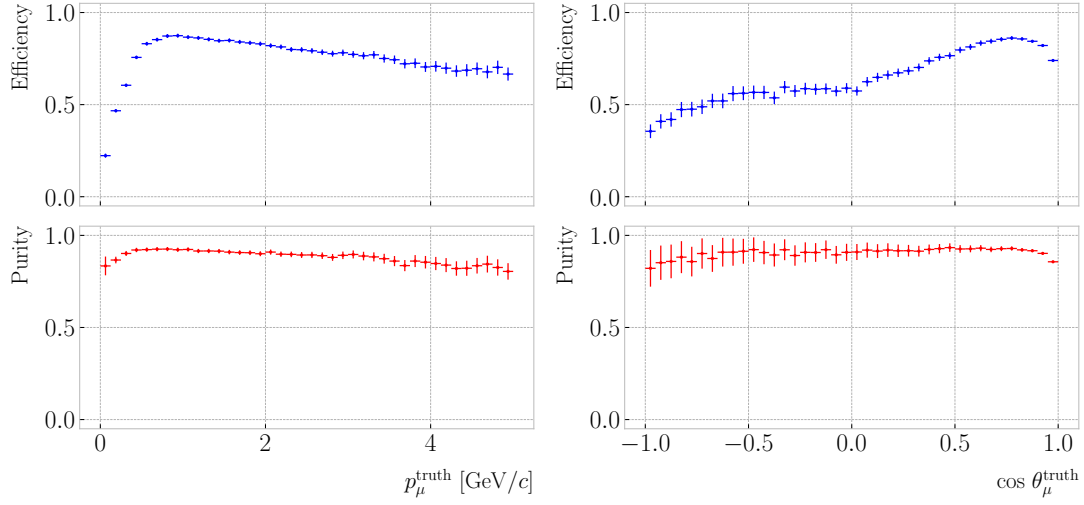


Figure 7.11: Efficiency (blue) and purity (red) of the ν_μ CC selection as a function of the primary muon true momentum (left panel) and beam angle (right panel).

noticeable. However, note that the number of events with backward-going muons is much smaller than those aimed towards the forward direction, as can be seen from the size of the vertical error bars. There is also a decrease in the purity with the beam angle, but this effect is much smaller.

A byproduct of selecting the primary lepton in the interaction is the position of the reconstructed neutrino vertex candidate. Checking how the position of the selected reconstructed primary vertex and the true vertex position compare is needed to understand the validity of our method. Figure 7.12 shows the distributions of fractional residuals between the truth and reconstructed vertex positions in the x (top panel), y (middle panel), and z (bottom panel) directions. Performing a double Gaussian fit to the distributions (red lines), I estimate the reconstructed vertex resolution achieved with this method to be $1.62 \pm 0.08\%$, $1.23 \pm 0.05\%$, and $0.32 \pm 0.05\%$ for the x , y , and z directions, respectively. As expected, the resolution along the drift direction is slightly worse. However, the significant difference in resolution between the two transverse directions is worth noting. Not only is the resolution better for the z direction, but the layout of the residual distribution is highly asymmetrical. This may be related to the variability in the selection efficiency along that direction.

7.2. ν_μ CC SELECTION

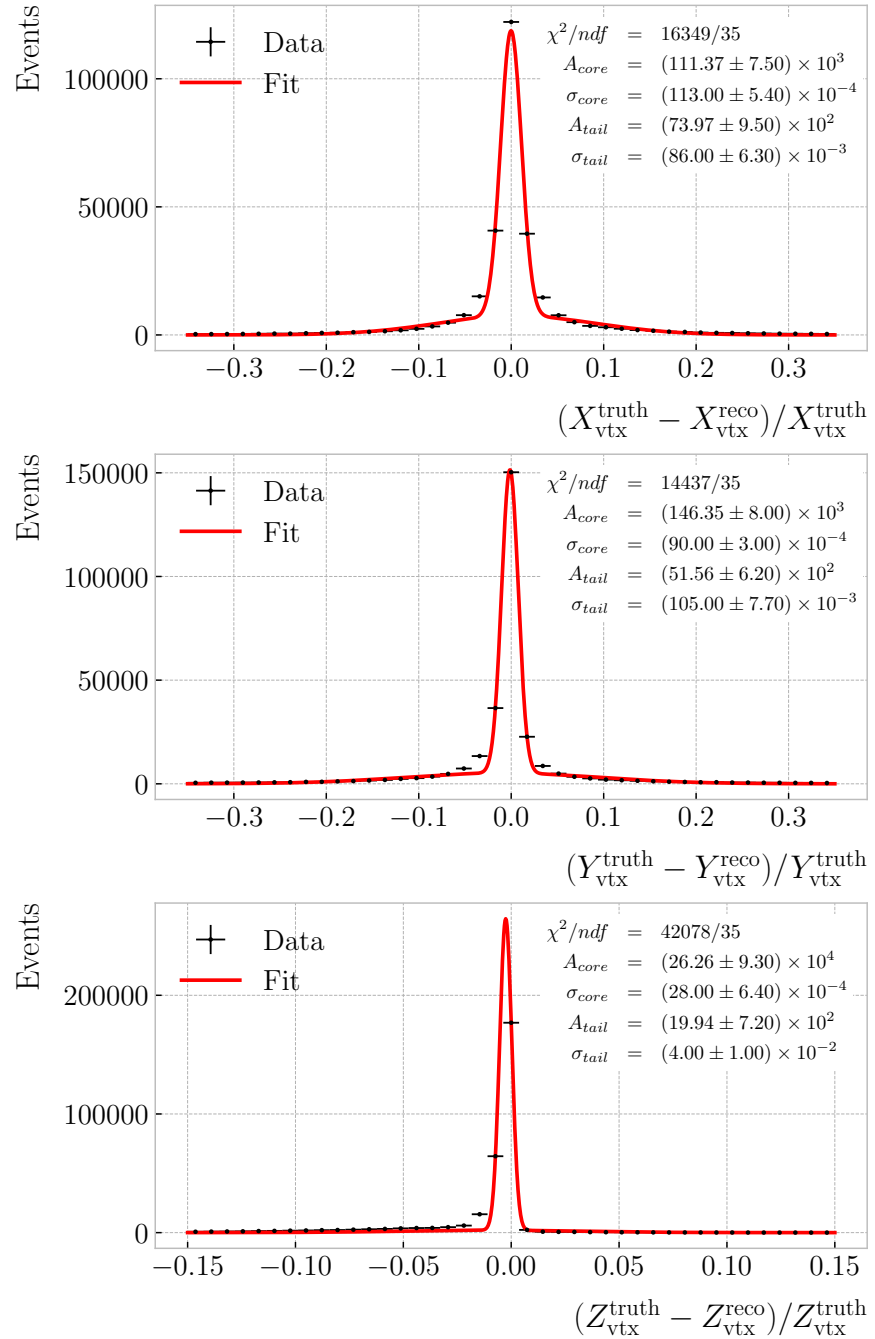


Figure 7.12: Fractional residual distributions for the position of the primary vertex in the ν_μ CC selection. The best fits to a double Gaussian function are also shown (red lines).

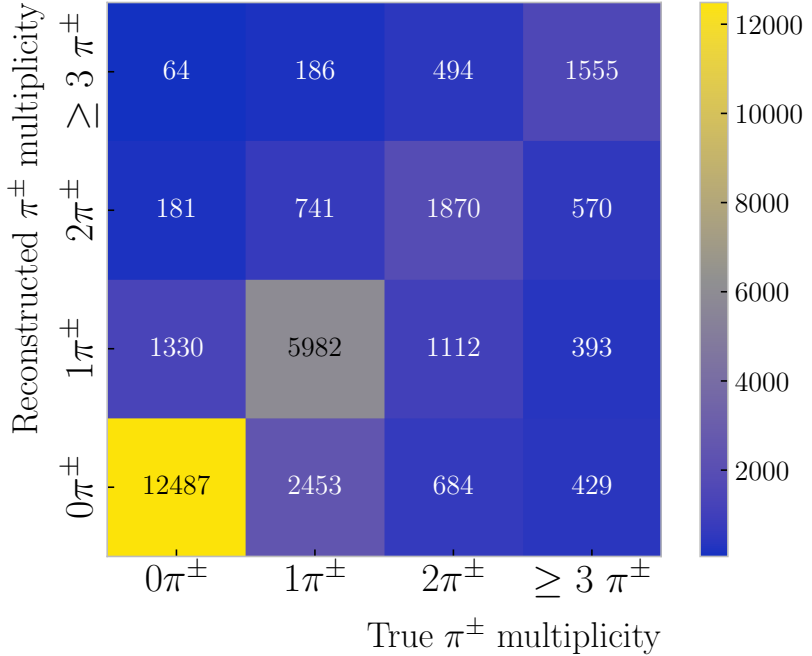


Figure 7.13: Distribution of events based on their true and reconstructed π^\pm multiplicity, for the selection given by $p_{dE/dx}^{\text{cut}} = p_{\text{ToF}}^{\text{cut}} = 0.50$, $\Delta_{dE/dx}^{\pi^\pm} = 0.20$, and $d_\mu^{\text{cut}} = 50.0$ cm.

7.3 Charged pion identification

Now that I have checked the robustness of the proposed ν_μ CC selection, it can be used as a starting point for other, more convoluted, selections. One of the priorities of ND-GAr, as mentioned previously, is the identification of pions. With its lower tracking thresholds, ND-GAr is expected to do better regarding π^\pm identification than the traditional LArTPCs, like ND-LAr. Moreover, it can make use of the different detector subcomponents to tag the charged pions.

The ν_μ CC selection provides a starting point for the pion identification. The first thing one can do is rule out the selected primary muon candidate. Then, by looking at the properties of the rest of the reconstructed particles, one can start the counting of the charged pions.

The two proton scores, the one based on the dE/dx in the HPgTPC and the one obtained from the ToF measurement in the ECal, can be used to separate the protons

7.3. CHARGED PION IDENTIFICATION

from the sample of charged pions. By providing appropriate cuts for these, a good separation can be achieved.

Another source of information available is the dE/dx of the track associated to the reconstructed particle. To select the charged pions, we can require that the measured mean dE/dx is compatible with the expectation for a true π^\pm , in other words:

$$\left\langle \frac{dE}{dx} \right\rangle_{\pi^\pm} (1 - \Delta_{dE/dx}^{\pi^\pm}) \leq \left\langle \frac{dE}{dx} \right\rangle_{\text{meas.}} < \left\langle \frac{dE}{dx} \right\rangle_{\pi^\pm} (1 + \Delta_{dE/dx}^{\pi^\pm}), \quad (7.6)$$

where the parameter $\Delta_{dE/dx}^{\pi^\pm}$ measures the fractional variation one allows around the theoretical expectation. To obtain the expected mean dE/dx of a charged pion with a given momentum, I use the [ALEPH](#) parametrisation with the parameter values obtained previously in section [6.2.2](#).

Also, as we are only interested in the primary pions, and because these are by definition close to the interaction vertex, one can apply an additional distance cut. Using the start position of the muon candidate, we can restrict the starting point of the pions to a certain volume around the vertex.

Combining all these ideas, I propose the following procedure to identify the charged pions in an event:

1. Apply ν_μ [CC](#) selection.
2. Disregard particle selected as primary muon.
3. Remove particles with momentum below threshold.
4. Select particles with proton dE/dx score below threshold.
5. Select particles with proton [ToF](#) score below threshold.
6. Select particles with mean dE/dx around the expected value for a pion.
7. Remove particles with a distance between the start of the track and the primary vertex greater than the cut.

The remaining particles after all these cuts are taken to be charged pion candidates.

CHAPTER 7. EVENT SELECTION IN ND-GAR

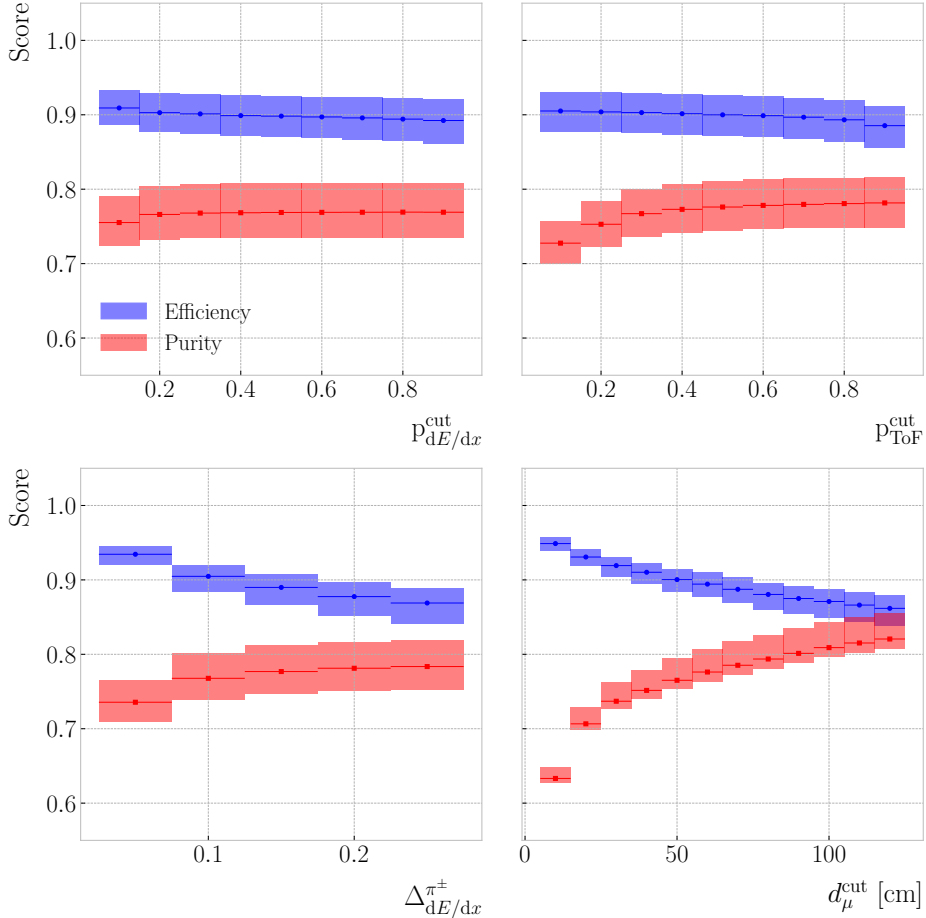


Figure 7.14: Efficiency (blue) and purity (red) for the ν_μ CC $0\pi^\pm$ selection as a function of the proton dE/dx score cut (top left panel), proton ToF score cut (top right panel), pion dE/dx cut (bottom left panel), and distance to muon cut (bottom right panel). The height of the boxes represents the IQR of the conditional distributions, whereas the line corresponds to the median.

7.3.1 Selection optimisation

This counting method depends on four cuts, denoted by $p_{dE/dx}^{\text{cut}}$, $p_{\text{ToF}}^{\text{cut}}$, $\Delta_{dE/dx}^{\pi^\pm}$, and d_μ^{cut} in order of appearance. The momentum threshold is necessary to compare with the true multiplicity. For values of the kinetic energy lower than $10 - 20$ MeV, we do not expect to be able to tag individual pions. Such low energy particles just leave small traces in the TPC which, together with the busy environment of the neutrino interaction vertex, leaves one with no other option but to only account for their energy calorimetrically. As such, the true pion counting also features this momentum threshold.

7.3. CHARGED PION IDENTIFICATION

I performed an optimisation of the charged pion counting by scanning the space of possible cut configurations. For the two proton scores, I let them vary between 0.10 to 0.90, in increments of 0.10. Similarly, the parameter $\Delta_{dE/dx}^{\pi^\pm}$ takes values in the range 0.05 – 0.25, with a step size of 0.05. Finally, the distance cut changes in 10 cm steps, from 10 to 120 cm.

For each combination of selection cuts, I compare the true charged pion multiplicity given by GENIE with the number of charged pion candidates I count with this method, hereafter referred to as the reconstructed π^\pm multiplicity. The result of this comparison is a matrix, with columns and rows indicating true and reconstructed charged pion multiplicity, respectively. An example of one of these matrices, obtained for a certain configuration of cuts, can be seen in Fig. 7.13. From these multiplicity matrices one can extract performance metrics, like efficiency, purity, and significance.

Given a multiplicity matrix \mathbf{M} , the efficiency for the i -th multiplicity value can be computed as:

$$\text{Efficiency}|_i = \frac{M_{ii}}{\sum_j M_{ij}}, \quad (7.7)$$

or in other words, dividing the corresponding diagonal entry by the sum of all the entries in the same column. On the other hand, the purity is given by:

$$\text{Purity}|_i = \frac{M_{ii}}{\sum_j M_{ji}}, \quad (7.8)$$

which is just the ratio between the diagonal entry and the sum of the entries in the corresponding row. Similarly, the significance is obtained by taking the square root of the denominator in the previous expression:

$$\text{Significance}|_i = \frac{S}{\sqrt{S+B}}|_i = \frac{M_{ii}}{\sqrt{\sum_j M_{ji}}}. \quad (7.9)$$

Figures 7.14 and 7.15 show the efficiency (blue) and the purity (red) for the ν_μ CC $0\pi^\pm$ and $1\pi^\pm$ selections, respectively, as a function of the different cut values. In the figures, each box represents the IQR of the conditional distribution for the fixed

CHAPTER 7. EVENT SELECTION IN ND-GAR

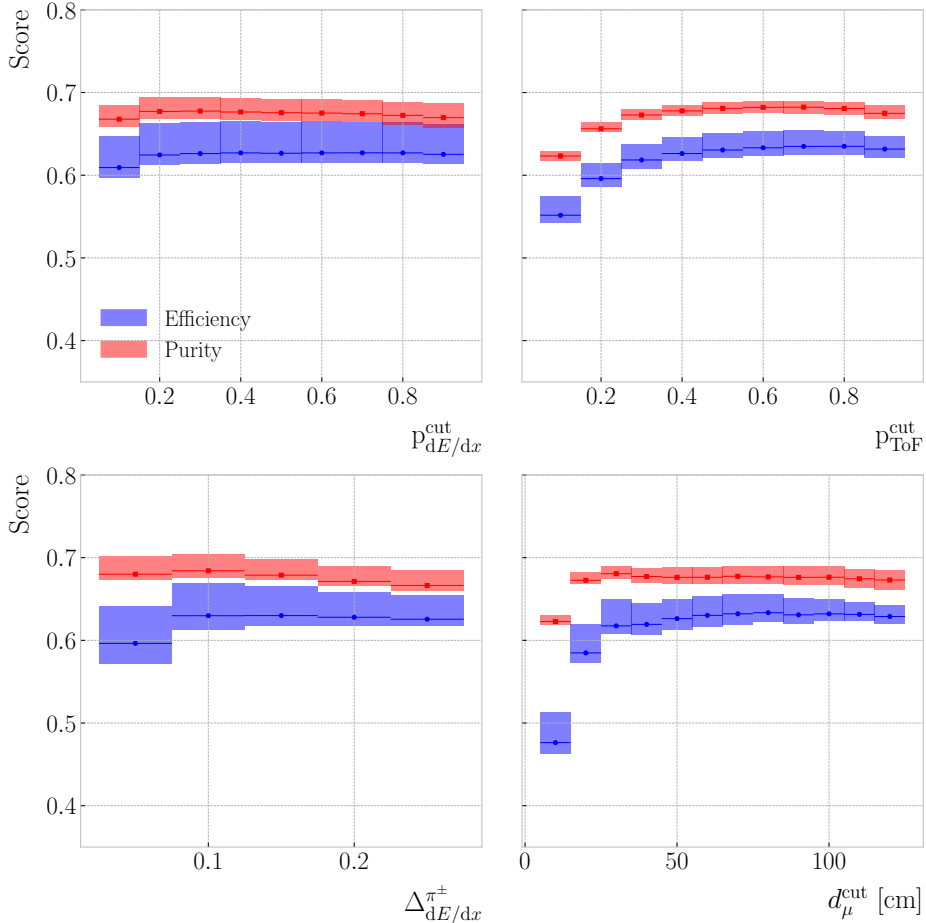


Figure 7.15: Efficiency (blue) and purity (red) for the ν_μ CC $1\pi^\pm$ selection as a function of the proton dE/dx score cut (top left panel), proton ToF score cut (top right panel), pion dE/dx cut (bottom left panel), and distance to muon cut (bottom right panel). The height of the boxes represents the IQR of the conditional distributions, whereas the line corresponds to the median.

value of the corresponding cut, and the horizontal lines correspond to the medians. The first thing one notices is that the efficiency is always higher than the purity in the $0\pi^\pm$ selection, while the opposite is true for the $1\pi^\pm$ selection. Also, it is clear that these metrics are able to reach higher values for the $0\pi^\pm$ selection than they do for the $1\pi^\pm$ case. This shows that it is easier to assess that no charged pions are present in the event, rather than actually tagging them.

For the ν_μ CC $0\pi^\pm$ selection, the performance metrics follow the expected tendency. As the purity grows with a cut value, the efficiency decreases. Interestingly, this is not

7.3. CHARGED PION IDENTIFICATION

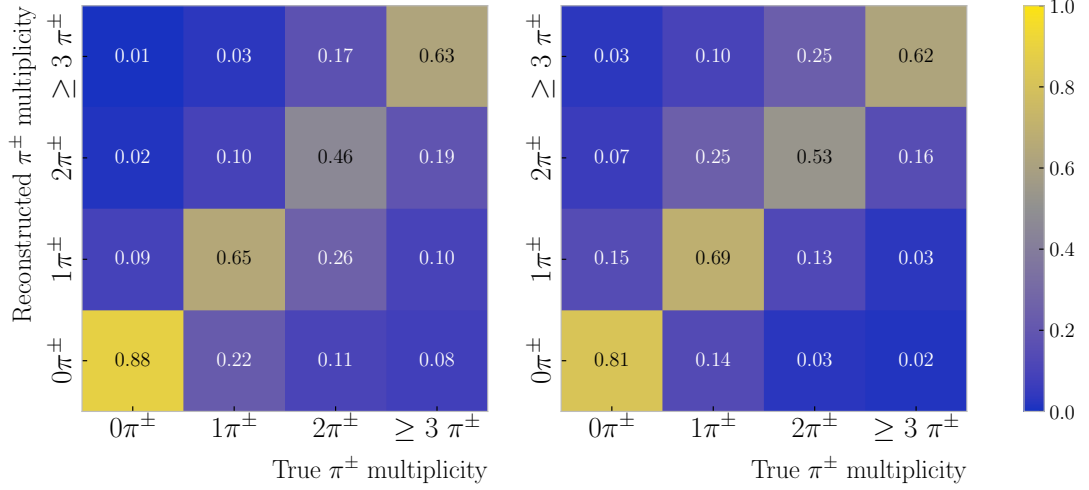


Figure 7.16: Distribution of events given their true and reconstructed π^\pm multiplicity, both column-wise (left panel) and row-wise (right panel) normalised, for the selection that maximises the significance of the ν_μ CC $1\pi^\pm$ selection. The column normalisation yields the efficiency in the diagonal entries, whereas the row normalisation reveals the purity.

the case for the $1\pi^\pm$ selection, where both efficiency and purity follow roughly the same trends along the different cuts. This makes sense when one comprehends that this is not a traditional cut-based selection, but more of a counting exercise. Some restrictive cut configurations will not tag any particles as pions. On the contrary, loose cuts will render every particle as a π^\pm . Therefore, when looking at a specific multiplicity, the relations between the cut value and the performance metrics are not obvious. Thus, sometimes efficiency and purity can both increase, as the cuts refine the definition of a reconstructed pion.

To have a working point for our studies, I chose the cut configuration that yields the maximum significance for the ν_μ CC $1\pi^\pm$ selection. Of course, other cuts would be more appropriate in certain scenarios. However, this provides us with a starting point to understand the performance of the selection. A significance of 66 ± 7 for the $1\pi^\pm$ selection is achieved for the cut values $p_{dE/dx}^{\text{cut}} = 0.30$, $p_{\text{ToF}}^{\text{cut}} = 0.70$, $\Delta_{dE/dx}^{\pi^\pm} = 0.10$, and $d_\mu^{\text{cut}} = 110.0$ cm.

Figure 7.16 shows the multiplicity matrices resulting from this optimised ν_μ CC $1\pi^\pm$ selection. Although both matrices are produced with the same selection cuts, one is

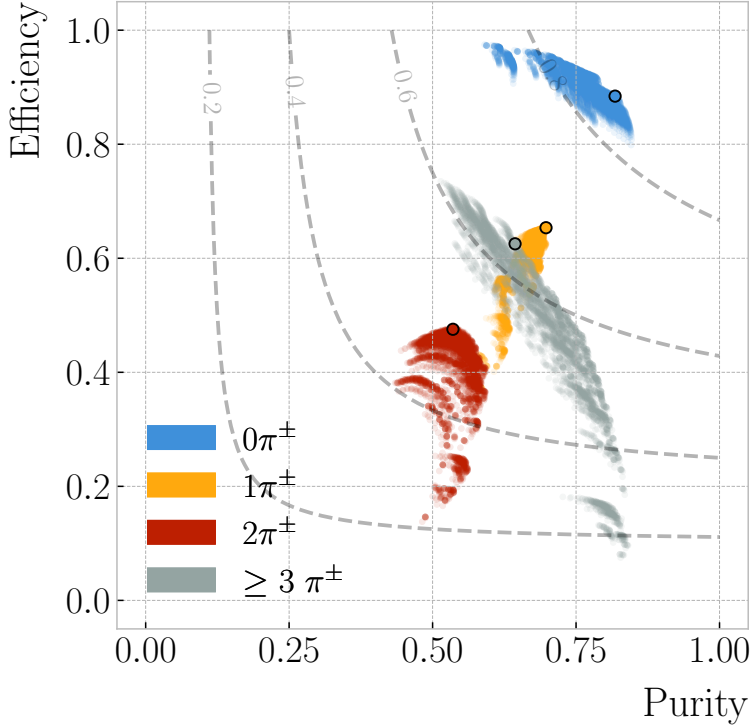


Figure 7.17: Purity versus efficiency achieved for the different cut configurations explored separated by the various ν_μ CC $N\pi^\pm$ selections. The outlined points indicate the state for each possible multiplicity when using the configuration that maximises the significance of the ν_μ CC $1\pi^\pm$ selection. The contours indicate the surfaces of equal F_1 -score.

column normalised (left panel), whereas the other is row normalised (right panel). It follows from the definitions in Eqs. (7.7) and (7.8) that the diagonal entries of these matrices correspond to the efficiencies and the purities, respectively, for each of the possible charged pion multiplicity selections.

An additional check to make is understand how this configuration performs when applied to the other selections, like ν_μ CC $0\pi^\pm$, and how it compares to the other possible configurations. A comparison between the different pion multiplicity selections, indicated with colours, in the purity versus efficiency space is shown in Fig. 7.17. The envelopes of these clusters of points represent the best possible performance of the different selections when varying the cut values, similar to ROC curves. For each of the possible multiplicity choices, the performance obtained for the $1\pi^\pm$ optimised selection

7.3. CHARGED PION IDENTIFICATION

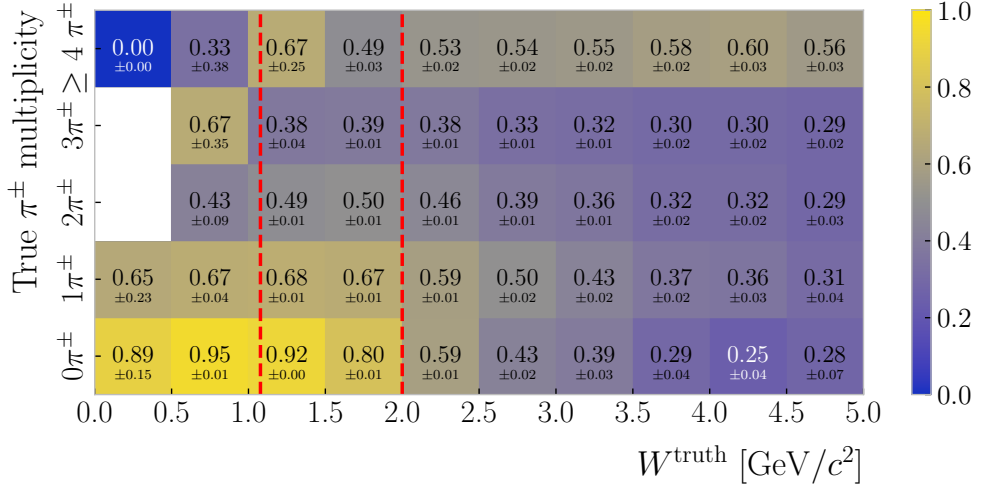


Figure 7.18: Efficiency of the various ν_μ CC $N\pi^\pm$ selections as a function of the true hadronic invariant mass. The dashed vertical lines correspond (from left to right) to the values $m_p + m_{\pi^\pm}$ and $2.0 \text{ GeV}/c^2$, which define the shallow inelastic scattering region.

is indicated by an outlined point. From this, one can see that the selected configuration performs reasonably well, within the limits of what can be achieved in each case, across the different multiplicities.

At this point, one can study the charged pion selection performance as a function of other quantities of interest. A natural variable to check is the hadronic invariant mass. It is defined as:

$$W = \sqrt{-Q^2 + 2m_n q_0 + m_n^2} \quad (7.10)$$

where Q^2 is the momentum transfer from the neutrino to the primary muon, q_0 the energy transfer, and m_n the mass of the nucleon. This quantity is related to the elasticity of the neutrino interaction, and defines the transitions between the **QE**, **RES** and **DIS** regions. An interesting invariant mass range for **DUNE** is the one that extends between the mass of the Δ resonance, even though this is typically extended down to $m_p + m_{\pi^\pm}$, and $2.0 \text{ GeV}/c^2$. It is estimated that roughly 7 in every 10 events in our **ND** will take place in this region. Although the **RES** production dominates at these W values, this range also includes the transition to the **DIS** regime. Thus, it is often called the shallow inelastic scattering (**SIS**) region.

CHAPTER 7. EVENT SELECTION IN ND-GAR

Within these boundaries, the resonant events produce either 1 or 2 charged pions, whereas the multipion events are typically associated to non-resonant production. Therefore, our ability to correctly select events with $\geq 2\pi^\pm$ in the **SIS** region will impact our ability to constrain this poorly understood regime. Figure 7.18 shows the efficiency of the various charged pion multiplicity selections in a number of hadronic invariant mass bins. The two red dashed lines indicate the boundaries of the **SIS** region. One can see that, although not as good as the single pion selection, the efficiency for the multipion events is reasonable in the relevant invariant mass range. The total efficiency for the ν_μ CC $\geq 2\pi^\pm$ selection in the **SIS** regime is estimated to be 0.65 ± 0.01 .

7.3.2 ν_μ CC $1\pi^\pm$ selection

By focusing on the $1\pi^\pm$ selection, one can study the kinematics of the selected pion. This allows one to understand how well the charged pions are tagged. This is difficult to do using only the multiplicity matrices, as with them one can only check that the number of charged pions is the same as in the truth. Sometimes, even if the estimated pion multiplicity is correct, the identified particles may not be true pions.

Figure 7.19 displays the distributions of various reconstructed kinematic variables for the selected pion candidate. The different colours indicate the ID of the true particle associated to the reconstructed pion candidate.

First, we have the kinetic energy distribution. For this set of reconstructed particles, because they have been tagged as charged pions, the kinetic energy is computed using their momentum assuming the pion hypothesis. One can see that most of the backgrounds sit in the low energy range, up to around 0.2 GeV.

The next distribution presents the ratio between the energy deposited in the **ECal** associated to the particle over the momentum measured in the **HPgTPC**. This variable is restricted to particles with at least one associated hit in the **ECal**. It is interesting to see a two peak structure in the true pion distribution. The first one presumably corresponds to the pions punching-through the **ECal**, while the latter is probably due to the ones stopping in it. On the other hand, the misidentified particles, other than the

7.3. CHARGED PION IDENTIFICATION

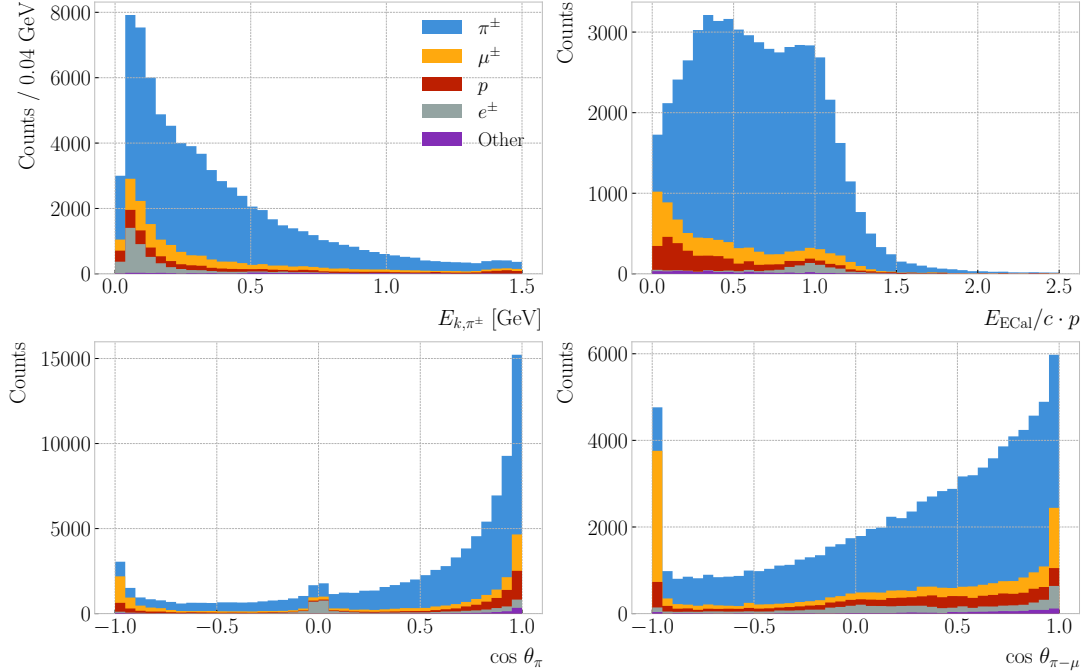


Figure 7.19: Reconstructed kinematic distributions for the pion candidate in the ν_μ CC $1\pi^\pm$ selection, broken down by true ID of the particle. From left to right, top to bottom, we have the kinetic energy given the pion hypothesis, the ratio between the energy deposited in the ECal and the momentum, the pion angle, and the angle between the muon and pion candidates.

electrons, tend to lower ratios. This is expected for protons, as this could not be higher than 0.5 for momenta ≤ 1 GeV/ c even if they stopped, but for the muons it may point to a misreconstruction problem.

Figure 7.19 also shows the angle of the pion candidates with respect to the beam direction. Although most of them are aimed in the forward direction, it can be noted that an important number of the misidentified muons seem to be backward-going. This is likely a reconstruction artifact, produced by broken tracks that got assigned the wrong propagation direction. Also, there is a sizeable number of true electrons with directions perpendicular to the beam, probably delta electrons from the primary muon.

Finally, I included the reconstructed pion-muon angular distribution. Even though it shares some similarities with the previous distribution, as the primary muon typically goes forward, the pion distribution is not as prominently forward-going in this case. Also, it may be noted that approximately 25% of the muons misidentified as pions have

CHAPTER 7. EVENT SELECTION IN ND-GAR

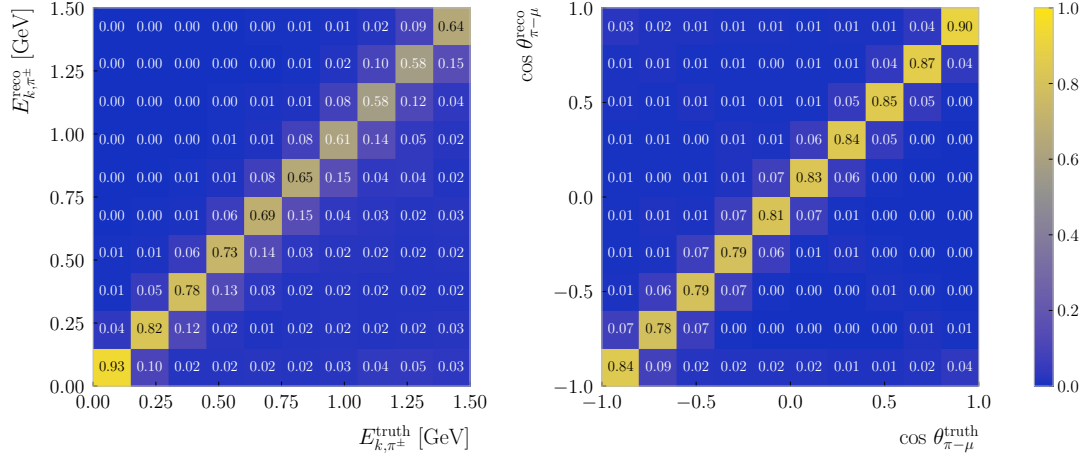


Figure 7.20: Distributions for the reconstructed versus truth generated pion kinetic energy (left panel) and cosine of the angle between the pion and muon (right panel). The reconstructed values correspond to the selected primary muon and pion candidates in the ν_μ CC $1\pi^\pm$ selection, whereas the truth values come from the true primary muon and pion in the events.

$\cos \theta_{\pi-\mu} \leq -0.95$. Therefore, putting an additional angular cut improves the purity of the charged pion selection from 0.74 ± 0.01 to 0.77 ± 0.01 , while not loosing a substantial amount of true pions.

A comparison between the true and the reconstructed values of the pion kinetic energy (left panel) and pion-muon angle (right panel) is shown in Fig. 7.20. The distributions are column normalised, which allows one to see the fraction of events in the correct bins. For this, I select the events where only one reconstructed pion and one true pion were identified, as that is the only case where a pairing of the variables is possible. It shows the excellent agreement between the reconstruction and the truth information.

One can also study the performance of the pion selection as a function of the truth pion kinematics. Fig. 7.21 shows the selection efficiency versus the true kinetic energy (left panel) and the angle between the true primary pion and muon (right panel). The efficiency is computed from the events with a single true and reconstructed pion, comparing their number to the total of events with one true pion. Notice how the efficiency, although it starts with relatively low values, plateaus around 0.70 quickly after 0.20 GeV. In terms of the pion-muon angle, the efficiency looks relatively flat, only

7.4. NEUTRAL PION IDENTIFICATION

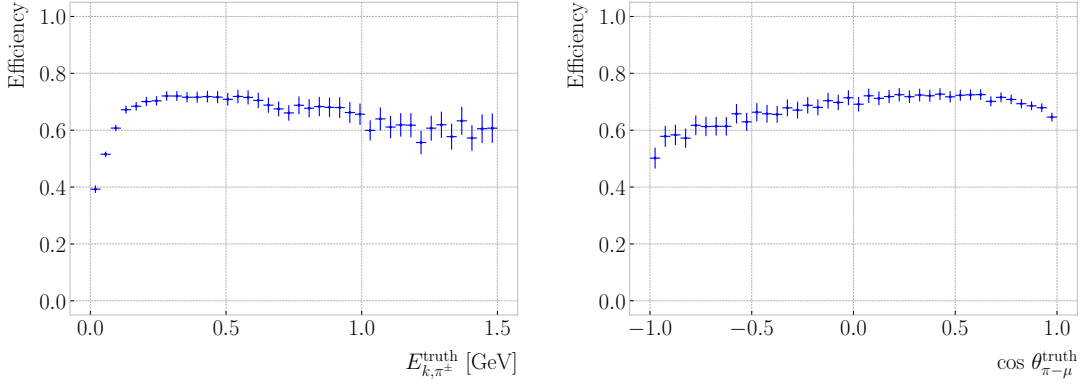


Figure 7.21: Efficiency of the ν_μ CC $1\pi^\pm$ selection as a function of the true pion kinetic energy (left panel) and pion-muon angle (right panel).

dropping slightly towards the back-to-back case.

7.4 Neutral pion identification

The ν_μ CC selection can also be used as a stepping stone for the identification of neutral pions. Although these particles do not leave any traces in the HPgTPC, they can be identified using a combination of the different detectors within ND-GAr. Being able to tag the neutral pions is a valuable asset for the estimation of the reconstructed neutrino energy, as both their kinetic and mass components can then be added in the calculation.

In the case that both photons from the π^0 decay do not undergo pair production to an e^+e^- pair, they will reach the ECal where they will produce an electromagnetic shower. This activity inside the ECal will not be associated to any charged particle track inside the HPgTPC, unless there is a reconstruction failure. Thus, having a neutrino interaction vertex candidate from the ν_μ CC selection, one can reconstruct the mass of the π^0 using the energy and position of the photons.

The idea is to look for all the ECal clusters that were not associated to tracks in each event. Then, if two or more were identified, compute the invariant mass for all possible combinations as:

$$m_{\gamma\gamma} = \sqrt{2E_1E_2(1 - \cos \theta)}, \quad (7.11)$$

CHAPTER 7. EVENT SELECTION IN ND-GAR

where E_i are the energies of the photons and θ the opening angle between them. At this point, I select the pair whose invariant mass is the closest to m_{π^0} , remove the pairs containing any of the two selected clusters from the collection, and iterate until no more pairs can be formed.

I repeat this procedure for the events with 0, 1, 2 and 3 or more true neutral pions. For each of them, I extract the invariant mass of the first three cluster pair candidates (in order of proximity to m_{π^0}), in case they can be formed. If the number of the cluster pair is lower than the true neutral pion multiplicity of the event, that entry will be counted as signal. The additional candidates for an event of a given multiplicity are considered background. The resulting distribution is shown in Fig. 7.22 (black data points).

I fit the signal distribution to a double-sided Crystal Ball function [180]:

$$f_s(x; \alpha_{L,R}, n_{L,R}, \mu, \sigma, N) = N \begin{cases} A_L (B_L - \frac{x-\mu}{\sigma})^{-n_L}, & \text{for } \frac{x-\mu}{\sigma} < -\alpha_L, \\ e^{-\frac{(x-\mu)^2}{2\sigma^2}}, & \text{for } -\alpha_L \leq \frac{x-\mu}{\sigma} \leq \alpha_R, \\ A_R (B_R + \frac{x-\mu}{\sigma})^{-n_R}, & \text{for } \frac{x-\mu}{\sigma} > \alpha_R, \end{cases} \quad (7.12)$$

where $A_{L,R}$ and $B_{L,R}$ are given by:

$$\begin{aligned} A_{L,R} &= \left(\frac{n_{L,R}}{|\alpha_{L,R}|} \right)^{n_{L,R}} e^{-\frac{|\alpha_{L,R}|^2}{2}}, \\ B_{L,R} &= \frac{n_{L,R}}{|\alpha_{L,R}|} - |\alpha_{L,R}|. \end{aligned} \quad (7.13)$$

The tails of this distribution accommodate the asymmetric shape due to the misreconstruction effects. The values obtained for the best fit parameters are indicated in Fig. 7.22 (blue box).

The background is characterised by an exponential function of the form:

$$f_b(x; x_0, \tau) = x_0 e^{-x/\tau}. \quad (7.14)$$

Similarly, the best fit values can be seen in Fig. 7.22 (red box).

Figure 7.22 also shows the results of the fits for the signal plus background (blue line)

7.4. NEUTRAL PION IDENTIFICATION

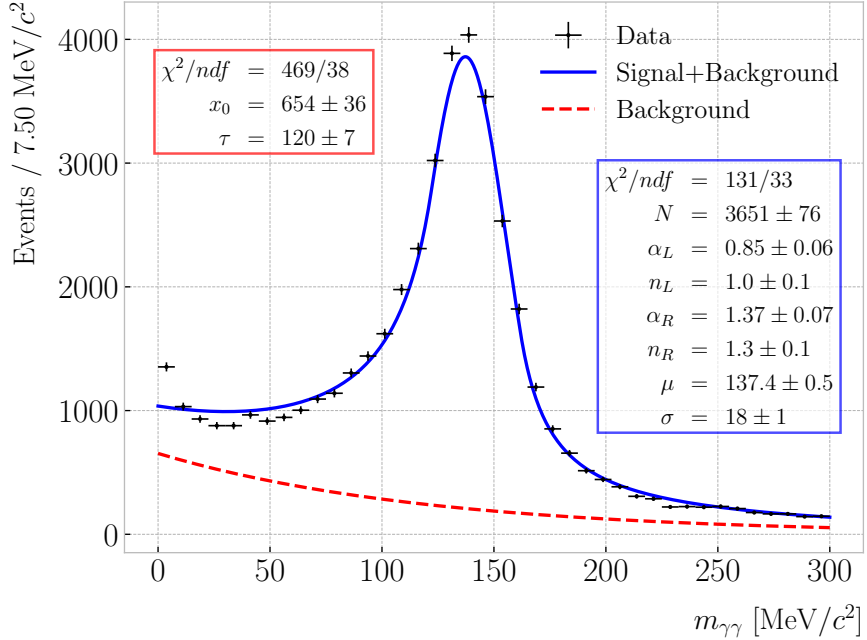


Figure 7.22: Invariant mass distribution obtained for the unassociated ECal cluster pairs in the event. The best fits for signal plus background (solid blue line) and background only (dashed red line) are also shown.

and the background only (dashed red line) cases. Using these, I estimate the tagging efficiency of this method to be 0.90 ± 0.01 with a purity of 0.85 ± 0.01 , when selecting the candidates with an invariant mass in the range $54.0 - 288.0 \text{ GeV}/c^2$.

This is a robust method to identify the photon pair from the π^0 decay. However, this approach is not enough to efficiently identify all the events containing neutral pions in the sample. A quick calculation reveals that only 20% of the ν_μ CC $1\pi^0$ events can be correctly identified with it.

This approach can be complemented with the identification of the secondary vertices from the e^+e^- conversions. This will make it possible to cover the cases where either one or both photons convert in the HPgTPC. In those cases, one can try pairing the e^+e^- with unassociated activities in the ECal, or matching pairs of secondary vertices. However, this will require further work on the reconstruction, and thus falls out of the scope of this analysis.

7.5 Neutrino energy reconstruction

In a neutrino-nucleus [CC](#) interaction, where alongside the charged lepton N nucleons are knocked out and M mesons produced, the reconstructed neutrino energy can be computed as:

$$E_{\text{rec}} = S_n + E_\ell + \sum_{i=0}^N E_{k,n_i} + \sum_{j=0}^M E_{m_j}, \quad (7.15)$$

where S_n is the average single-nucleon separation energy, E_ℓ the energy of the primary lepton, E_{k,n_i} is the kinetic energy of the i -th knocked-out nucleon and E_{m_j} the total energy of the j -th produced meson.

This represents the ideal scenario, where all the kinetic energy of the nucleons is visible in the detector and one can identify all mesons produced in the interaction. In a real experiment, some of these energy components will be missed, and this needs to be accounted for in any estimation of the reconstructed energy.

For instance, in [ND-GAr](#) neutrons are complicated to account for, as they do not produce tracks in the [TPC](#). They may be identified either from scatterings off Ar nuclei in the [HPgTPC](#), or from a [ToF](#) measurement in the [ECal](#). However, these methods are not fully mature in the current reconstruction, and their development is beyond the scope of this study. So, in the following, I will completely ignore the contribution of neutrons.

Also, with a real detector we can not expect to tag all the charged pions irrespective of their energy. This is why one has to introduce detection thresholds in the energy estimation. Thus, in the reconstructed energy calculation I will add only the kinetic energy for the charged pions below the threshold, and the total energy for the pions above the threshold.

Likewise, the identification of all neutral pions in the sample is challenging. As discussed in the previous section, with our [ECal](#) we are able to identify the photons from the π^0 decays, but that selection still needs to be completed with other methods. Therefore, for this first study I do not take into account the energy contribution of the

7.5. NEUTRINO ENERGY RECONSTRUCTION

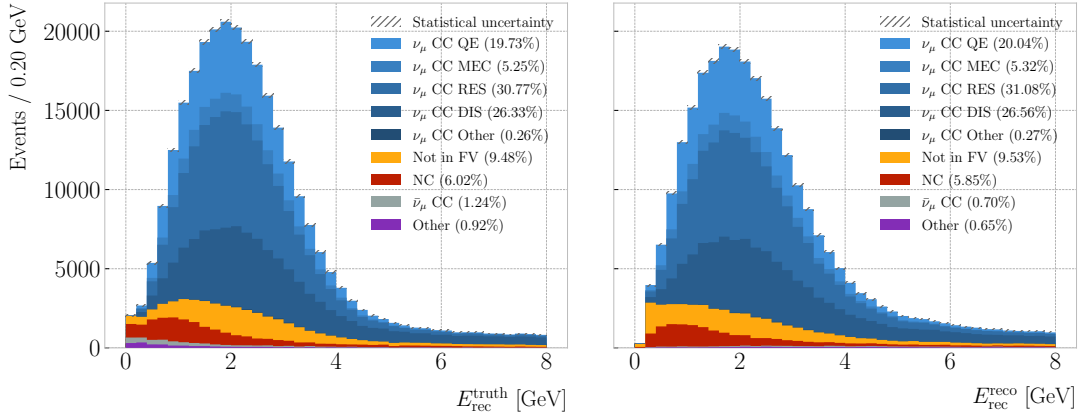


Figure 7.23: Reconstructed neutrino energy spectra for the ν_μ CC selection obtained using the truth (left panel) and reconstructed (right panel) information. The selected events are broken down by signal and background subcategories. The statistical uncertainty is drawn in hatched gray.

neutral pions.

With all this in mind, using the truth information from the events I compute the reconstructed neutrino energy as:

$$E_{\text{rec}}^{\text{truth}} = S_n + E_\ell + \sum_{i=0}^{N_p} E_{k,p_i} + \sum_{j=0}^{M_{\pi^\pm}^<} E_{k,\pi_j^\pm} + \sum_{k=0}^{M_{\pi^\pm}^>} E_{\pi_k^\pm}, \quad (7.16)$$

where N_p is the number of protons, and $M_{\pi^\pm}^<$ and $M_{\pi^\pm}^>$ the number of charged pions below and above the threshold, respectively. As before, I assume a kinetic energy threshold of 20 MeV for the charged pions.

At the reconstruction level, I use the energy of the primary muon candidate, computed from its momentum, as the starting point for the neutrino energy calculation. Then, I add the total energy contributions from the identified charged pions, again using their momenta. After that, I try to identify the protons by looking at the two proton scores. If any of them are above threshold (here the thresholds used are the same as for the pion identification), the kinetic energy of the particle is added to the total. Finally, I check if any of the remaining particles are fully contained within the FV. I add their kinetic contributions using the total energy they deposited in the HPgTPC.

CHAPTER 7. EVENT SELECTION IN ND-GAR

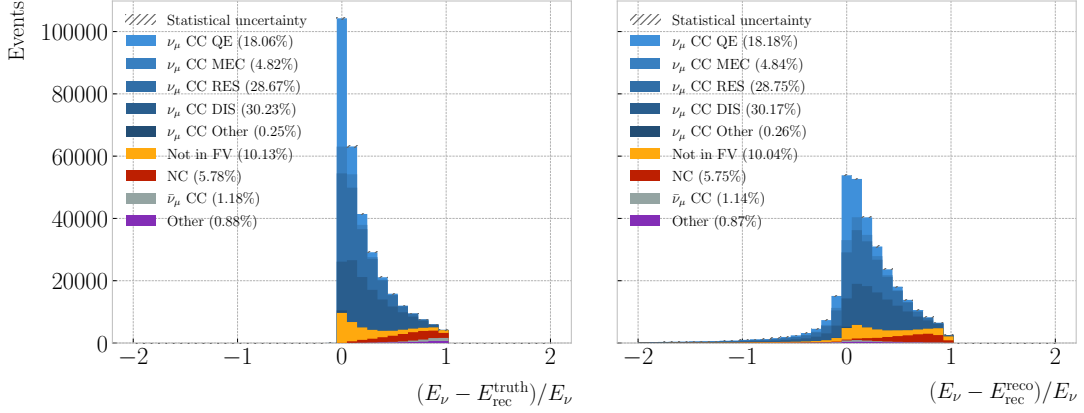


Figure 7.24: Neutrino energy residuals distributions for the ν_μ CC selection obtained using the truth (left panel) and reconstructed (right panel) information. The selected events are broken down by signal and background subcategories. The statistical uncertainty is drawn in hatched gray.

Figure 7.23 shows the resulting distributions of reconstructed neutrino energy obtained from the truth (left panel) and reconstructed (right panel) particle collections. The overall shape of the distributions is similar, with the reconstructed one having a slightly larger high energy tail. Note also that the background events from outside the FV tend to have a smaller energy in the reconstructed case. This is likely due to a misreconstruction of the primary muon, which clearly does not affect the other computation.

I also compared the reconstructed energies to the true energy of the neutrino. Figure 7.24 displays the ratio of the energy residuals to the true energy for the truth (left panel) and reconstructed (right panel) cases. As expected, using the true particles one never overestimates the neutrino energy. Also, using the reconstructed objects one is more prone to underestimate the neutrino energy, due to deficiencies in the reconstruction.

This constitutes a really promising first estimation of the energy reconstruction capabilities of the detector using the end-to-end reconstruction. Possible improvements may come from the addition of the contributions from neutral pions and photons, as well as the neutron tagging.

7.6 Systematic uncertainties

Although the implementation and study of the systematic uncertainties relevant for [ND-GAr](#) is out of the scope of this preliminary analysis, in this section I give an extended overview of the topic. These can be classified in three categories: neutrino flux uncertainties, neutrino-nucleus interaction model uncertainties, and detector response uncertainties.

7.6.1 Flux uncertainties

The neutrino flux prediction is affected by systematic uncertainties arising from two sources: the uncertainties in the production of hadrons in the target and the uncertainties in the design parameters of the beamline itself. These fluxes and their uncertainties are generated with the G4[LBNF](#) simulation [96], a Geant4 implementation of the [LBNF](#) beamline, and the Package to Predict the FluX ([PPFX](#)) framework, originally developed for [MINERvA](#) [181].

The hadron production uncertainties are associated to the kinematic distributions of the hadrons produced when the protons interact with the carbon target, as well as the possible interactions of the hadrons with the beamline materials. The [PPFX](#) package estimates these uncertainties by performing a number of random throws of the production model parameters [182]. This way, different predictions of the [LBNF](#) flux are generated, which can be compared to the nominal prediction to build a matrix of the covariances between neutrino energies, flavours and running modes (either [FHC](#) or [RHC](#)). The resulting hadron production uncertainties are described by the eigenvectors associated to the largest eigenvalues in this matrix, obtained performing a [PCA](#) analysis.

The other set of uncertainties affecting the neutrino flux prediction come from the limited precision with which we know the parameters of the different components in the beamline. These include the specifications of the target, the dimensions of the decay pipe, and the current and alignment of the magnetic horns. The effects on the flux predictions of these uncertainties are estimated using the G4[LBNF](#) simulation. For each

CHAPTER 7. EVENT SELECTION IN ND-GAR

of the parameters, the simulation runs with said parameter shifted by $\pm 1\sigma$ from the nominal value, and the resulting flux prediction is compared to the nominal one.

7.6.2 Cross-section uncertainties

As discussed previously in section 2.6, the neutrino-nucleus interaction model is of great importance for neutrino experiments, as it maps the true neutrino energy to the kinematics of the final state particles. The uncertainties on the cross-section model are implemented in three ways: varying the parameters used in the **GENIE** simulation, using weights that parametrise cross-section effects not accounted for in **GENIE**, and comparing the **GENIE** predictions to other interaction models.

Within the **DUNE TDR LBL** analysis, the default interaction model was that implemented in **GENIE v2_12_10** [133]. A summary of the cross section systematic parameters present in **GENIE** used in that analysis is presented in Tab. 7.3. The additional systematic parameters used in the analysis are described in Tab. 7.4.

In this default **GENIE** configuration, the initial state of the nucleons is described by the Bodek-Ritchie global Fermi gas model [183]. The model is known to give a poor agreement when compared to neutrino-nucleon data [184]. Because of the limitations of the model, the current versions of **GENIE** use the local Fermi gas approach, which takes into account the correlation between the momentum of the nucleons and their location within the nucleus.

For the **CCQE** events, the dominant model uncertainties arise from the axial form factor of the nucleon, for which a dipole parametrisation is used, and the nuclear correlation effects computed using the random phase approximation (**RPA**). In the analysis, a parametrisation of the Valencia **RPA** effect [176] is used. This consists of a third-order Bernstein polynomial up to $Q^2 = 1.2 \text{ GeV}^2$ followed by an exponential decay (**BeRPA**), originally proposed by the **T2K** collaboration [185].

The $2p2h$ interactions are included using the Valencia model [176], with an additional correction following the observation of an underprediction of these events in **MINERvA** [186]. Additional uncertainties for the energy dependence of the missing strength were

7.6. SYSTEMATIC UNCERTAINTIES

Table 7.3: Neutrino interaction systematic parameters implemented in GENIE used in the DUNE TDR LBL analysis. Events with low W that are not QE are mainly RES, whereas DIS events dominate at high W . The initials BY refer to the Bodek-Yang model. Table adapted from Ref. [133].

Systematic	1σ value
Quasielastic	
Axial mass for CCQE	$+0.25_{-0.15}$ GeV
CCQE vector form factor shape	N/A
Fermi surface momentum for Pauli blocking	$\pm 30\%$
Low W	
Axial mass for CC resonance	± 0.05 GeV
Vector mass for CC resonance	$\pm 10\%$
θ_π distribution for Δ decay	N/A
High W (BY model)	
A_{HT}	$\pm 25\%$
B_{HT}	$\pm 25\%$
C_{v1u}	$\pm 30\%$
C_{v2u}	$\pm 40\%$
Other neutral current	
Axial mass for NC resonance	$\pm 10\%$
Vector mass for NC resonance	$\pm 5\%$
Intra-nuclear	
Nucleon charge exchange	$\pm 50\%$
Nucleon elastic reaction	$\pm 30\%$
Nucleon inelastic reaction	$\pm 40\%$
Nucleon absorption	$\pm 20\%$
Nucleon π -production	$\pm 20\%$
π charge exchange	$\pm 50\%$
π elastic reaction	$\pm 10\%$
π inelastic reaction	$\pm 40\%$
π absorption	$\pm 20\%$
π π -production	$\pm 20\%$

CHAPTER 7. EVENT SELECTION IN ND-GAR

Table 7.4: Neutrino interaction systematic parameters used in the [DUNE TDR LBL](#) analysis not present in [GENIE](#). I have omitted the parameters only relevant for the [FD](#). Table adapted from Ref. [133].

Systematic	Mode	Description
BeRPA	1p1h/QE	Nuclear model suppression
ArC2p2h	2p2h Ar/C	Electron scattering SRC pairs
E_{2p2h}	$2p2h$	$2p2h$ energy dependence
CC non-resonant	CC DIS 1π	$\nu + n/p \rightarrow \ell + 1\pi$
Other non-resonant	DIS Nπ	$1 < W < 5 \text{ GeV}/c^2$
NC normalisation	NC	$\pm 20\%$ to all NC events at the ND

added. Also, the uncertainties in the scaling from carbon to argon are included, based on measurements of electron scattering off short-range correlated ([SRC](#)) nucleon pairs on multiple targets [187].

In this version of [GENIE](#), the Rein-Sehgal model describes the single pion resonant production events [188]. It includes 16 different resonances, with no interference between them. Two parameters account for the uncertainties on the axial and vector masses of the resonances. In subsequent [GENIE](#) tunes, like the one used in the studies presented in this Chapter, the Berger-Sehgal model is used [177]. This is an improved version of the Rein-Sehgal model, which includes the lepton mass effects in the calculations.

The Bodek-Yang parametrisation is used to describe the [DIS](#) events [179]. The parameters A_{HT} and B_{HT} account for higher twist effects in the scaling variable, while C_{v1u} and C_{v2u} control the form of the valence quark K factors. For the analysis, the uncertainties on the values of these parameters are taken into consideration. Also, due to the difficulties of [GENIE](#) at describing the transition region between [RES](#) and [DIS](#) events, a set of systematic parameters affecting the different non-resonant pion production channels were developed, following the example of [NOvA](#) [189]. There are independent parameters for the interactions on protons and neutrons, except for the [CC DIS 1 \$\pi\$](#) case where they are merged. All start with an uncertainty of 50% for $W \leq 3 \text{ GeV}/c^2$, which linearly decreases until reaching a 5% at $W = 5 \text{ GeV}/c^2$.

For the [TDR](#) analysis, an additional 20% normalisation uncertainty was added to all

7.6. SYSTEMATIC UNCERTAINTIES

NC events in the ND. It was implemented to understand if the NC events passing the selection cuts affected the results of the analysis [133].

Finally, the effective intranuclear transport model (often denoted as hA) is a part of GENIE, implemented in the INTRANUKE module. GENIE features a large number of parameters for the uncertainties on the intranuclear cascade model, which are summarised in the last portion of Tab. 7.3. In following GENIE releases, updated versions of the INTRANUKE model are used.

Although part of this cross-section systematic treatment is outdated, as the tunes currently used feature different models, it gives a good idea of what systematic effects are relevant for the different measurements we may want to perform in the future. At the moment, a significant effort is channeled to the creation of new tunes specifically tailored for DUNE, including the development of parametrisations particularly relevant for ND-GAr.

7.6.3 Detector uncertainties

The DUNE ND CDR [102] presents a number of studies on the performance of ND-GAr. These were based on the reference design described in section 3.5. Because the detector is still in an R&D stage, with the design continually evolving, these performance metrics will need to be revisited in the future. However, they still provide valuable information. These studies help understand what detector requirements are needed to achieve the physics goals of the experiment, and on what design aspects we need to improve.

Since the reference design of ND-GAr repurposes the ALICE MWPCs and other hardware components, the ALICE TPC operation experience is a point of reference for the spatial resolution performance. They reported a single hit resolution of 0.25 mm and 1.50 mm in the directions perpendicular and parallel to the drift direction, respectively [107]. Nevertheless, the MWPCs are not the leading option for the charge readout anymore. Current efforts focus on the study of the effects of different pixelisation choices, relevant for the GEMs setups.

For other performance metrics, a fairer comparison for the ND-GAr HPgTPC could

CHAPTER 7. EVENT SELECTION IN ND-GAR

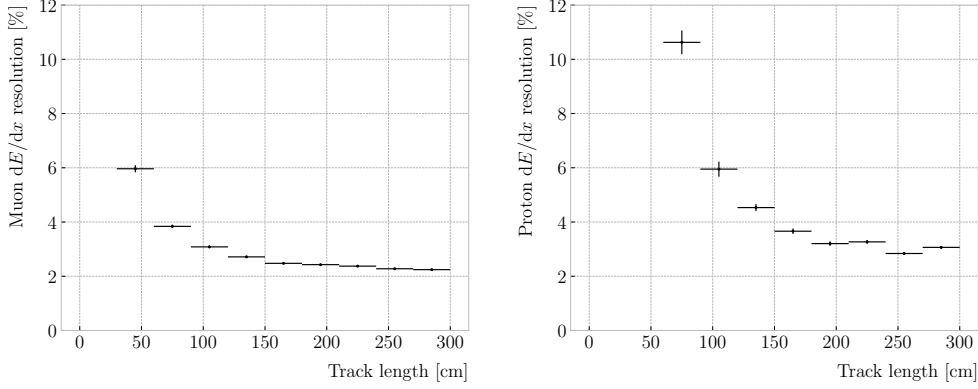


Figure 7.25: Estimated dE/dx resolution as a function of the track length for true muons (left panel) and protons (right panel) in a ν_μ CC sample.

be the PEP-4 detector. It operated with a 80:20 Ar:CH₄ mixture at 8.5 bar, achieving a two-track separation of 1 cm [190, 191]. This metric is particularly relevant in our case, as the neutrino interaction vertex can be an area of very high track multiplicity. Thus, our track separation capabilities will have a direct impact on the primary vertex identification and resolution. There are several difference between our HPgTPC and PEP-4. The operating pressure of ND-GAr will be higher, and the gas mixture likely to contain a higher fraction of Ar.

In terms of the ionisation measurement, both the experience from ALICE and PEP-4 are relevant, as this depends on the readout and the running conditions (pressure and gas mixture). They obtained resolutions of 4.5% and 3.0% for typical track lengths of 160 and 75 cm, respectively. According to previous studies on the dE/dx resolution in gaseous detectors [192], ND-GAr can achieve a 2% resolution for a typical track length of 200 cm. Figure 7.25 shows the values of the resolution I estimate for muon (left panel) and proton (right panel) tracks with different lengths, using the procedure described in section 6.2.

The tracking capabilities of ND-GAr were studied in the context of ν_μ CC interactions. Using a sample of reconstructed tracks from true muons and charged pions, the tracking efficiency was estimated to be above 90% for momenta ≥ 40 MeV/ c , with it steadily rising with the momentum. As a function of the angle with respect to the beam direction,

7.6. SYSTEMATIC UNCERTAINTIES

the efficiency was almost flat for particles with $p \geq 200$ MeV/ c . In the case of protons, the tracking performs well for kinetic energies ≥ 20 MeV. A machine learning algorithm is being developed for low energy proton track identification near the interaction vertex. Preliminary results show an efficiency of 30% at 5 MeV for this method.

The same samples used for the tracking studies were employed to estimate the momentum resolution. The momentum is computed from the curvature of the tracks in the magnetic field, and is therefore limited by the track length in the direction perpendicular to the field. Focusing on the tracks associated to true muons, a double Gaussian fit revealed a width of 2.7% and 12% for the core and tails of the momentum distribution. This same study determined the 3D angular resolution in the [HPgTPC](#) to be 0.80°.

The main source of uncertainty in the momentum measurement is the value of the magnetic field. The magnetic field simulations indicate that the overall uncertainty on the central field value is < 0.05%. A preliminary study investigated the use of K_s^0 decays in the [HPgTPC](#) to measure any deviations of the magnetic field from its nominal 0.5 T value. This showed that even a magnetic field bias of 1% will shift the reconstructed invariant mass distribution significantly.

The results presented for the [ECal](#) in Ref. [102] use an outdated version of the geometry, where the entire [ECal](#) sits outside of the pressure vessel and the layers consist of 5 mm of scintillator and 2 mm of Cu. The sample used consists of single photons in a 20° cone aligned with the beam direction. In the simulation, an energy threshold of 200 keV and a time resolution of 0.25 ns are assumed.

The energy resolution of the photons is obtained from a Gaussian fit. The resulting resolutions are then fitted to a function of the form:

$$\frac{\sigma_E}{E} = \frac{A}{\sqrt{E}} \oplus \frac{B}{E} \oplus C, \quad (7.17)$$

where A is the stochastic term, B the noise term and C the constant term. The best fit finds the values $A = 6.1\%$, $B = 1.6\%$, and $C = 4.5\%$. The photon angle is estimated

CHAPTER 7. EVENT SELECTION IN ND-GAr

Table 7.5: Expected performance for ND-GAr, both from simulation studies and extrapolated from ALICE and PEP-4. Table adapted from Ref. [102].

Parameter	Value
Perpendicular hit resolution	0.25 mm
Parallel hit resolution	1.50 mm
Two-track separation	1.00 cm
dE/dx resolution	5% for protons, 2% for muons
Tracking efficiency	> 90% for 40 MeV/c
Momentum resolution	2.7% core, 12% tails
Angular resolution	0.80°
Proton detection threshold	5 MeV
ECal energy resolution	$6\%/\sqrt{E} \oplus 1.6\%/E \oplus 4\%$
ECal pointing resolution	$8.17^\circ/\sqrt{E} + 4.18^\circ$

using a PCA analysis of the associated ECal cluster, taking it from the direction of the first principal component. The angular resolution is computed from a Gaussian fit to the core of the distribution. As a function of the photon energy, the values obtained are $\frac{8.17}{\sqrt{E}} + 4.18$ °. Different arrangements of the layers and alternative absorber choices may improve these results.

The different detector effects discussed above and the performance expected for ND-GAr are summarised in Tab. 7.5.

7.7 Summary

In this Chapter I applied the PID strategies discussed previously to the event selection in ND-GAr. I start by describing a method for selecting ν_μ CC events in section 7.2. This is mainly based on the muon score derived from the muon/pion classification I developed. Additionally, I perform an optimisation of the FV. As part of this study, I also examined the kinematics of the selected primary muon and the reconstruction of the interaction vertex. Next, in section 7.3 I explore the capabilities of ND-GAr and its reconstruction at identifying charged pions. I optimise a selection based on the reconstructed charged pion multiplicity, for events with 0, 1, 2, and $\geq 3\pi^\pm$ in the final state. I assess the performance

7.7. SUMMARY

of the selection as a function of the truth hadronic invariant mass, as well as the true pion kinematics for the ν_μ CC $1\pi^\pm$ case. I briefly discuss the possibility of tagging events with neutral pions by reconstructing the invariant mass of the photon pairs from their decay in section 7.4. Lastly, in section 7.5 I study the neutrino energy reconstruction of the selected ν_μ CC events using a calorimetric approach. For this, I compare the values obtained using generator-level and reconstructed information. Additionally, I described the systematic uncertainties relevant for ND-GAr in the context of the LBL analysis in section 7.6.

In the DUNE FD TDR [96], the assumptions made regarding the ν_μ CC reconstruction and the selection of exclusive samples in ND-GAr were backed by studies based on smeared truth samples. The studies in this Chapter demonstrate for the first time that ND-GAr is capable of selecting ν_μ CC events, generating pion exclusive samples, and estimating the neutrino energy using the end-to-end simulation and reconstruction.

Conclusion and outlook

Our plans miscarry because they have no aim. When a man does not know what harbour he is making for, no wind is the right wind.

– Lucio Anneo Seneca, *Epistulae morales ad Lucilium*

This thesis is a compilation of three different projects within **DUNE**. However, the idea behind each one of them is the same. The common theme is the prospect of improving or extending the physics of **DUNE**. In the first case, by enhancing the production of trigger primitives in the induction channels what I seek is to provide more useful information to the far detector data selection. The investigations with both data and MC, as well as the opportunity to run with a live detector, showed that such an enhancement is possible and should be pursued. Next, the solar dark matter analysis adds to the already rich beyond the Standard Model physics programme of **DUNE**. With the results of these preliminary studies, I want to show that **DUNE** can be complementary to the large-volume neutrino detectors in these kinds of searches. Finally, the goal of the **ND-GAr** reconstruction improvements was the development of the particle identification strategy of the detector. For this, I tried to extract all the possible information from its different subcomponents. With the particle identification at hand, it is possible to form the selections of the different **ND-GAr** samples, as I have shown in this work. These will help understand how the detector is going to further constrain the neutrino interaction uncertainties in **DUNE** Phase II, which will eventually allow **DUNE** to reach its ultimate physics goals.

CHAPTER 8. CONCLUSION AND OUTLOOK

In Chapter 4 I showed that the matched filter puts the production of trigger primitives in the induction and collection planes on the same level. The natural next step will be to understand the impact that this has in the context of the current trigger algorithms. Then, one could explore the development of new trigger routines, like triggers based on coincidence across planes. At the same time, these alternative hit finder chains should be implemented in the trigger simulations currently under development.

At this stage, the solar dark matter analysis presented in Chapter 5 already shows the potential of DUNE to explore these scenarios. However, including the full simulation and reconstruction of the events will be necessary moving forward. At the moment, a significant effort is aimed towards the reconstruction of atmospheric neutrinos in the DUNE far detector, which could be relevant for the case at hand. Also, following iterations of the analysis should include all the relevant systematic uncertainties, summarised in section 5.5.

The goal of the reconstruction developments discussed in Chapter 6 was establishing a robust particle identification strategy for ND-GAr, that allows to reconstruct the multiplicity of pions and other hadrons in the neutrino interactions final states. Following the integration efforts described in section 6.5, the next steps include continue developing other aspects of the reconstruction.

The studies in Chapter 7 constitute the first try at an event selection in ND-GAr using the end-to-end simulation and reconstruction. It will serve as a stepping stone for the development of other selections and analyses. Ultimately, the goal is to quantify the impact of ND-GAr on the long baseline neutrino oscillation analysis in DUNE. This will allow for a physics-driven optimisation of the detector design. For this, including the effect of the systematic uncertainties outlined in section 7.6 will be necessary. Future work will also include the study of proton exclusive samples, neutral pion identification and neutron tagging, as well as comparisons with ND-LAr + TMS. Additionally, these studies will go towards a publication on the capabilities of ND-GAr and the additional physics potential that it will allow for DUNE.

A

Additional material on Matched Filter

A.1 Low-pass FIR filter design

To optimise the frequency response of a digital filter, we can use the Parks-McClellan algorithm, where one finds a set of N real coefficients that give the best response for the specified pass-band and order of the filter [193].

Taking the detector ticks as the time unit, the Nyquist frequency will simply be $1/2 \text{ ticks}^{-1}$. The current implementation of the filter seems to have as pass-band the range $[0, 0.1] \text{ ticks}^{-1}$. This can be seen in Fig. A.1, where I show the power spectrum, in decibels, of that filter implementation (blue solid line). The Park-McClellan algorithm finds the optimal Chebyshev FIR filter [194] taking as input the boundaries of the target pass-band and stop-band, which can be written in the form:

$$\left\{ \begin{array}{l} [0, f_c] \\ [f_c + \delta f, f_N] \end{array} \right. , \quad (\text{A.1})$$

where f_c is the cut-off frequency, δf is the transition width and f_N is the aforementioned Nyquist frequency. A filter with a similar behaviour to the previous one can be obtained by setting $f_c = 0$ and $\delta f = 0.1 \text{ ticks}^{-1}$. The response of the resulting filter is also shown in Fig. A.1 (blue solid line). Notice that the suppression of the stop-band is enhanced for this optimal filter. For comparison, I include the power response of the filter obtained by taking the integer part of the coefficients resulting from the Parks-McClellan method (red dashed line). One can see that it does not suppress that much the stop-band, in a

CHAPTER A. ADDITIONAL MATERIAL ON MATCHED FILTER

similar way to the current implementation of the filter.

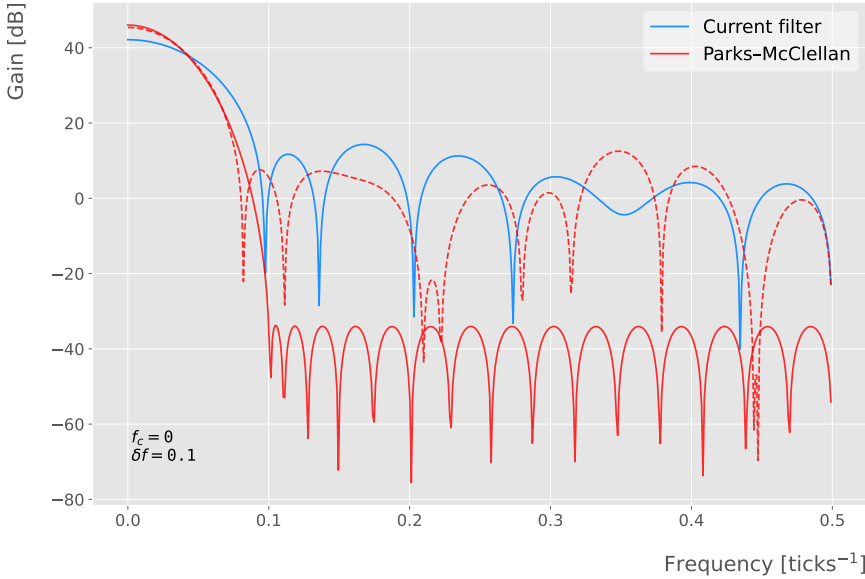


Figure A.1: Power spectrum in decibels for the current implementation of the low-pass **FIR** filter in **dtp-firmware** (blue line), compared to the response of an optimal filter obtained using the Parks-McClellan algorithm for the same pass-band (red line). Also for comparison I include the spectrum of the optimal filter when taking only the integer part of the coefficients (red dashed line).

At this point, I tried to improve the performance of the **FIR** filter using the Park-McClellan method, i.e. maximise the overall **S/N**, using the available data captures. I did so by varying the values of the two quantities that parametrise the pass-band and stop-band, the cut-off frequency f_c and the transition width δf .

Figure A.2 shows the average relative change in the **S/N** (i.e. the ratio between the value of the **S/N** after and before the filtering) for capture **felix-2020-07-17-21:31:44**, when using filters designed with the Parks-McClellan algorithm for the specified values of the cut-off frequency f_c and the transition width δf , restricted to integer values for the filter coefficients. One can clearly distinguish different regions where we get an improvement of up to a factor of 1.35 for the U plane. For large values of $f_c + \delta f$ the ratio tends to 1, as expected. In that limit the width of the stop-band goes to 0, meaning that no frequencies are filtered out and thus the waveform remains the same.

As it can be seen in Fig. A.2 (bottom right panel) the configuration which gives the

A.1. LOW-PASS FIR FILTER DESIGN

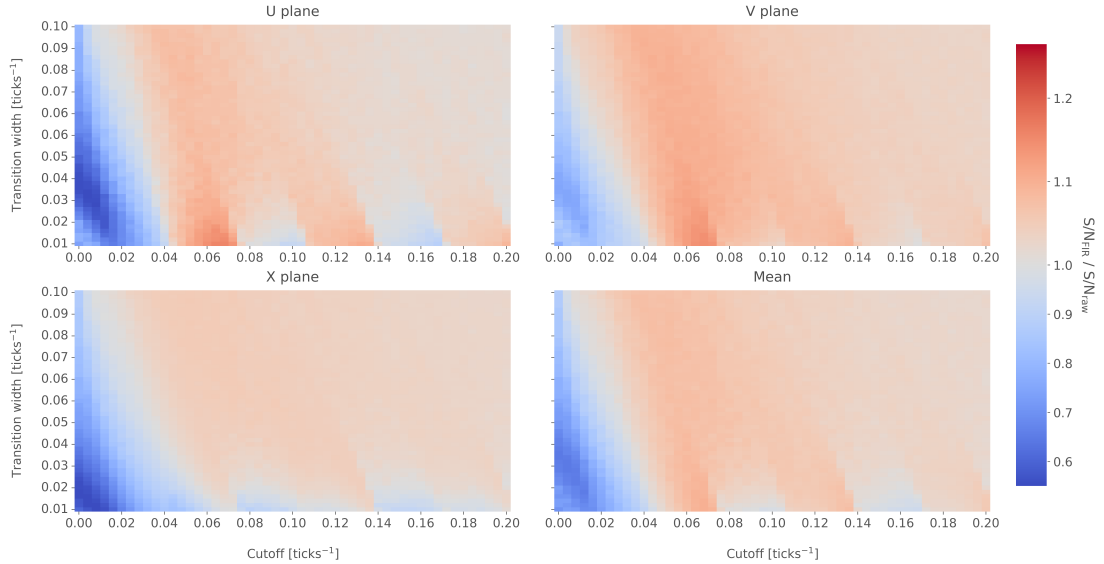


Figure A.2: Relative change in the S/N for the ProtoDUNE-SP raw data capture `felix-2020-07-17-21:31:44`, using different values of the cutoff frequency f_c and the transition width δf . The optimal Chebyshev filters were applied using just the integer part of the coefficients given by the Parks-McClellan algorithm.

best mean performance for the three planes is $f_c = 0.068 \text{ ticks}^{-1}$ and $\delta f = 0.010 \text{ ticks}^{-1}$. We can use these to see how the filter affects the different channels. Figure A.3 shows the distribution of the S/N improvement values for all the channels in the raw `ADC` capture `felix-2020-07-17-21:31:44`, separated by wire plane, after the optimal Chebyshev filter was applied. One can see that there is a clear improvement for both U and V induction planes, obtaining a mean change of 1.25 and 1.30 for them, respectively. However, in the case of the X collection plane the distribution peaks around 1, meaning that an important fraction of channels in that plane get a slightly worse S/N after the filter is applied. This is not a big issue, as the S/N for collection channels is usually much higher than the one for induction channels.

The results I obtained optimising the low pass filter with the Parks-McClellan method are promising. Nonetheless, the improvement found is rather marginal. Thus, I explored alternative approaches to the filtering problem, which may yield better outputs. This way, I found a possible solution in matched filters. By construction, this kind of filters offer the best improvement on the S/N .

CHAPTER A. ADDITIONAL MATERIAL ON MATCHED FILTER

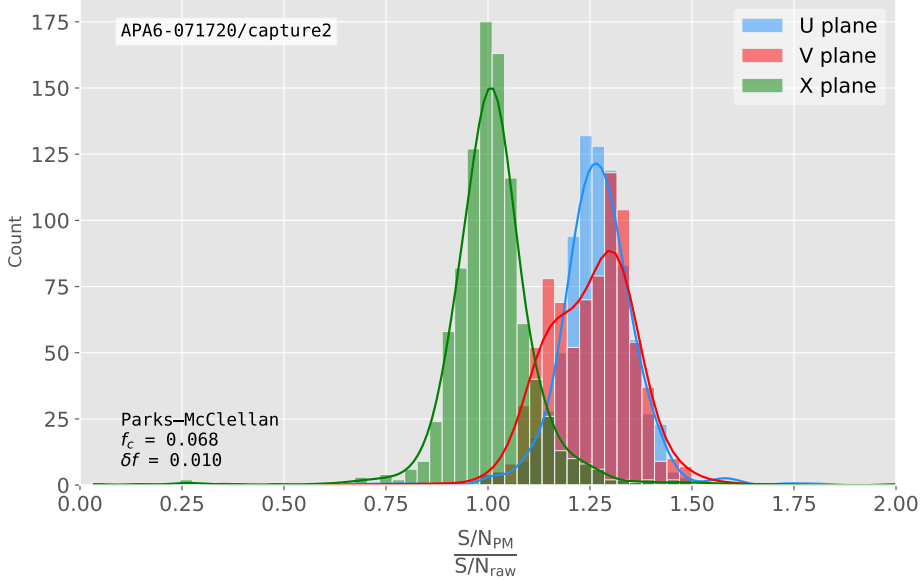


Figure A.3: Distribution of the relative change of the S/N on the different wire planes from the ProtoDUNE-SP raw data capture `felix-2020-07-17-21:31:44` after the optimal Chebyshev filter was applied. The filter was computed with the Parks-McClellan algorithm using a cutoff of $f_c = 0.068 \text{ ticks}^{-1}$ and a transition width $\delta f = 0.010 \text{ ticks}^{-1}$.

A.2 Matched filter impulse-response function

Given a known signal sequence $s(t)$ and another (a priori unknown) noise sequence $n(t)$, the input signal can be written as:

$$x(t) = s(t) + n(t). \quad (\text{A.2})$$

Now, considering a linear time-invariant filter, whose impulse-response function I will refer to as $h(t)$, one can write the output signal as:

$$\begin{aligned} y(t) &= x(t) * h(t) \\ &= (s(t) + n(t)) * h(t) \\ &= y_s(t) + y_n(t), \end{aligned} \quad (\text{A.3})$$

where $y_s(t)$ and $y_n(t)$ are simply the outputs of the filter due to the signal and the noise components respectively.

A.2. MATCHED FILTER IMPULSE-RESPONSE FUNCTION

The goal of the matched filter is to detect the presence of the signal $s(t)$ in the input sample $x(t)$ at a certain time t_0 , which effectively means that we need to maximise the **S/N** at that given time. This way, what one wants is to have a filter which gives a much bigger output when the known signal is present than when it is not. Putting it in other words, the instantaneous power of the signal output $y_s(t)$ should be much larger than the average power of the noise output $y_n(t)$ at some time t_0 .

For the case of the filtered signal, one can easily re-write it as an inverse Fourier transform:

$$y_s(t) = \frac{1}{2\pi} \int_{-\infty}^{\infty} d\omega H(\omega)S(\omega)e^{i\omega t}, \quad (\text{A.4})$$

where $H(\omega)$ and $S(\omega)$ are the Fourier transforms of the impulse-response function (i.e. the transfer function of the filter) and of the input signal, respectively.

Now, focusing on the noise part, we can use the Wiener-Khinchin theorem [195] to write the mean power of the noise after filtering as:

$$E|y_n(t)|^2 = \frac{1}{2\pi} \int_{-\infty}^{\infty} d\omega |H(\omega)|^2 S_n(\omega), \quad (\text{A.5})$$

where $S_n(\omega)$ is the power spectral density of the noise.

Having these, one can write the instantaneous **S/N** at time t_0 as:

$$\begin{aligned} \left(\frac{S}{N} \right)_{t_0} &= \frac{|y_s|^2}{E|y_n(t)|^2} \\ &= \frac{1}{2\pi} \frac{\left| \int_{-\infty}^{\infty} d\omega H(\omega)S(\omega)e^{i\omega t_0} \right|^2}{\int_{-\infty}^{\infty} d\omega |H(\omega)|^2 S_n(\omega)}. \end{aligned} \quad (\text{A.6})$$

Once we have this expression, we need to find its upper limit to determine what would be the optimal choice for the transfer function. For this, we use the Cauchy-Schwarz inequality, which in the present case takes the form:

$$\left| \int_{-\infty}^{\infty} dx f(x)g(x) \right|^2 \leq \int_{-\infty}^{\infty} dx |f(x)|^2 + \int_{-\infty}^{\infty} dx |g(x)|^2, \quad (\text{A.7})$$

CHAPTER A. ADDITIONAL MATERIAL ON MATCHED FILTER

for any two analytical functions $f(x)$ and $g(x)$. One can prove that making the choice:

$$\begin{aligned} f(x) &= H(\omega) \sqrt{S_n(\omega)} e^{i\omega t_0}, \\ g(x) &= \frac{S(\omega)}{\sqrt{S_n(\omega)}}, \end{aligned} \quad (\text{A.8})$$

leads to the following upper bound for the [S/N](#):

$$\left(\frac{S}{N} \right)_{t_0} \leq \frac{1}{2\pi} \int_{-\infty}^{\infty} d\omega \frac{|S(\omega)|^2}{S_n(\omega)}. \quad (\text{A.9})$$

From Eqs. [\(A.6\)](#), [\(A.7\)](#) and [\(A.8\)](#) one can also derive the form of the transfer function such that the upper bound is exactly reached [\[196\]](#):

$$H(\omega) \propto \frac{S^*(\omega) e^{-i\omega t_0}}{S_n(\omega)}. \quad (\text{A.10})$$

From this last expression we can clearly see the way the matched filter acts. As the transfer function is proportional to the Fourier transform of the signal it will try to only pick the frequencies present in the signal [\[197\]](#).

The matched filter transfer function can be greatly simplified if the input noise is Gaussian. In that case, the power spectral density of the noise is a constant, so it can be re-absorbed in the overall normalisation of the transfer function. Moreover, considering that the input signal is a real function, one can simply set $S^*(\omega) = S(-\omega)$, which gives:

$$H(\omega) \propto S(-\omega) e^{-i\omega t_0}. \quad (\text{A.11})$$

For a discrete signal, one can think of the input and impulse-response sequences as vectors. Then, the matched filter tries to maximise the inner product of the signal and the filter while minimising the output due to the noise by choosing a filter vector orthogonal to the latter. In the case of additive noise, that leads to the impulse-response vector:

$$h = \frac{1}{\sqrt{s^\dagger R_n^{-1} s}} R_n^{-1} s, \quad (\text{A.12})$$

A.3. DISTORTION AND PEAK ASYMMETRY

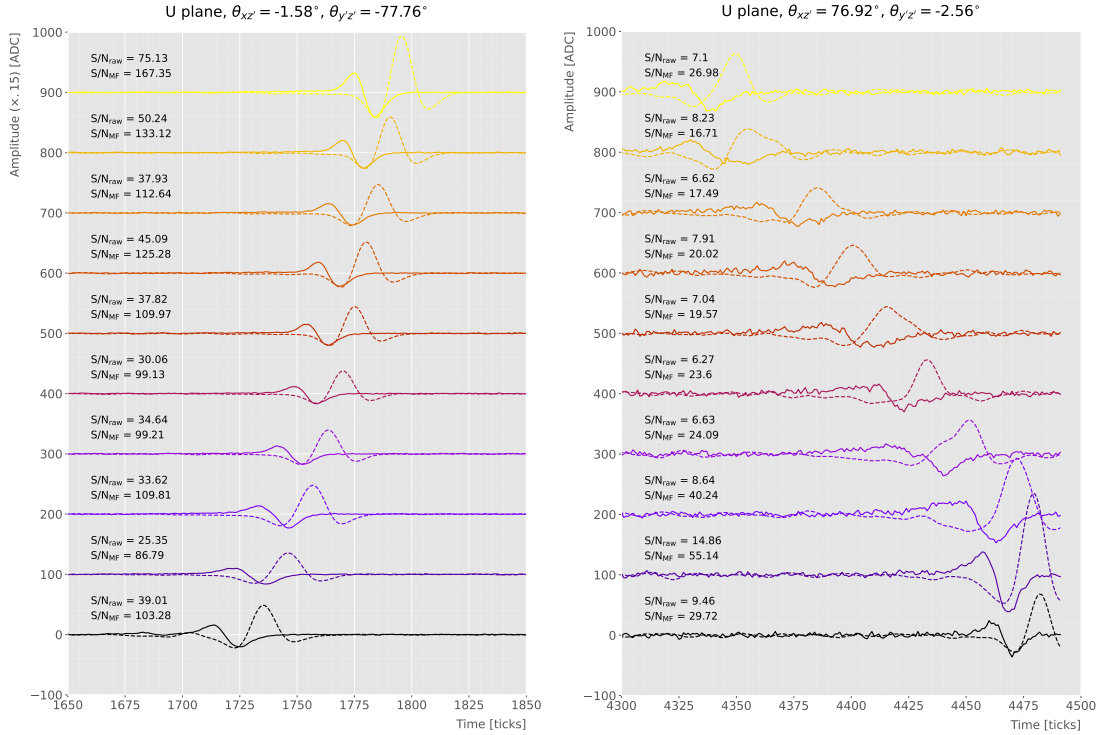


Figure A.4: Selected consecutive waveforms corresponding to two monoenergetic $E_k = 100$ MeV muon events, one is parallel to the [APA](#) and to the wires in the U plane (left panel) and the other is normal to the [APA](#) plane and perpendicular to the U plane wires (right panel). The solid lines represent the raw waveforms whereas the dashed lines correspond to the waveforms after the matched filter was applied. The waveforms on the left panel have been scaled by a factor of 0.15 to have similar amplitudes to the ones on the right panel.

where s is a reversed signal template sequence of length N equal to the order of the filter and R_n is the covariance matrix associated with the noise sequence n . For the Gaussian noise case, the covariance matrix is simply the unit matrix, so the above expression simplifies again to:

$$h = \frac{s}{|s|}. \quad (\text{A.13})$$

A.3 Distortion and peak asymmetry

As a case study using the [MC](#) sample, I select two of the simulated $E_k = 100$ MeV monoenergetic muon events. With respect to the U induction plane, one is parallel to the

CHAPTER A. ADDITIONAL MATERIAL ON MATCHED FILTER

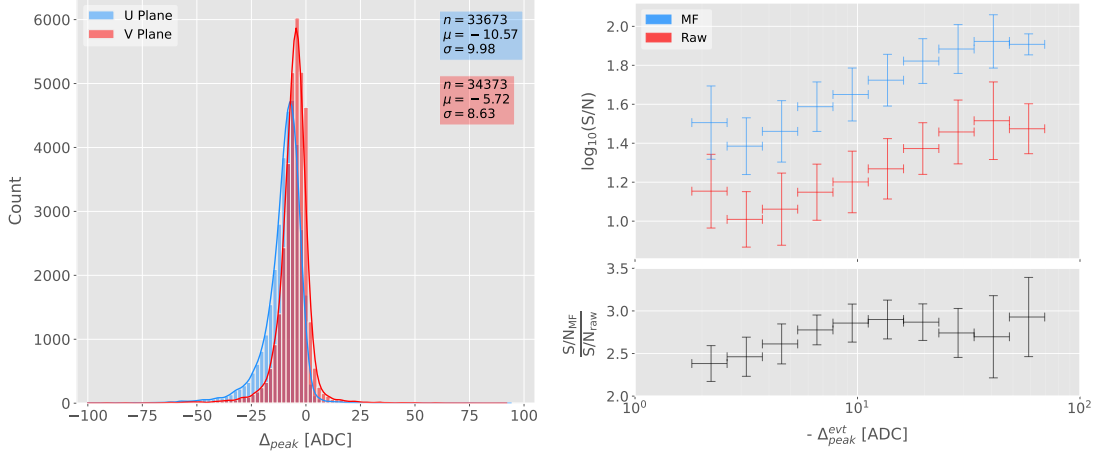


Figure A.5: Left panel: peak asymmetry distribution for the case of the monoenergetic $E_k = 100$ MeV muon sample. Each value corresponds to a single bipolar signal peak from a channel in any event. The blue distribution represents the peaks on U plane channels, whereas the red corresponds to signal peaks in V wires. Right panel: relation between the mean peak asymmetry per event with the S/N for U channel waveforms from the $E_k = 100$ MeV muon sample. The top subplot shows the decimal logarithm of the mean S/N for the raw (red) and the matched filtered (blue) waveforms. The bottom subplot contains the mean S/N improvement ratio after the matched filter was applied.

APA (low $\theta_{xz'}$) and to the wires (high $\theta_{y'z'}$) and the other is normal to the APA plane (high $\theta_{xz'}$) and perpendicular to the wires (low $\theta_{y'z'}$). As expected from the results on the angular dependence discussed above, the former has a higher S/N (both before and after the filtering) when compared to the latter. An interesting thing to notice about these two samples is that, even though one has a much larger S/N than the other, it is the one with the smallest S/N the one that gets a more significant averaged S/N improvement. In Tab. A.1 I include all the relevant parameters of these two $E_k = 100$ MeV muon events, namely the angles with respect to the $xy'z'$ reference frame, the values of the S/N, the S/N change and also the so-called peak asymmetry Δ_{peak} , that I will define next.

One can try to understand better the nature of these two events by looking at the raw and filtered data from some of their active channels. Figure A.4 shows a selection of consecutive raw and filtered U plane waveforms from the event with high S/N (left panel) and the one with low S/N (right panel). To show both collections of waveforms at a

A.3. DISTORTION AND PEAK ASYMMETRY

Table A.1: Characteristic parameters of the two monoenergetic muon events selected, relative to the U plane: projected angles in the xz' and $y'z'$ planes, S/N values for the raw and filtered waveforms, mean improvement of the S/N and peak asymmetry.

	$\theta_{xz'} (\circ)$	$\theta_{y'z'} (\circ)$	S/N_{raw}	S/N_{MF}	$\frac{S/N_{\text{MF}}}{S/N_{\text{raw}}}$	$\Delta_{\text{peak}} (\text{ADC})$
High (“parallel”)	-1.58	-77.76	41.65	112.44	2.83	-35.73
Low (“normal”)	76.92	-2.56	8.07	25.46	3.12	-10.38

similar scale I had to apply a factor of 0.15 to the waveforms with high S/N . Additionally, next to each waveform I include the values of the raw and matched filtered S/N for the corresponding channel. The first thing to notice is that the amplitude of the signal peaks from the normal track have a much smaller amplitude, and also appear quite distorted when compared to the others. On the other hand, although the matched filtered S/N for each channel are still smaller, the relative improvements are larger than in the parallel case.

A way to quantify the difference between the shape of the waveforms of these two events is using their peak asymmetry. I define the peak asymmetry as the (signed) difference between the positive and the negative peaks of the bipolar shape, i.e.:

$$\Delta_{\text{peak}} \equiv h_+ - h_-, \quad (\text{A.14})$$

where both heights h_+ and h_- are positive. Figure A.5 (left panel) shows the distribution of this peak asymmetry for all the waveforms corresponding to channels in the U (blue) and V (red) planes for the monoenergetic muon sample. One can see that these distributions are clearly shifted to negative values, with means $\mu_{\Delta}^{\text{U}} = -10.57 \text{ ADC}$ and $\mu_{\Delta}^{\text{V}} = -5.72 \text{ ADC}$, respectively. Notice how the peak asymmetry value of the selected event with the high S/N sits at the left tail of the distribution, whereas the corresponding value of the sample with the low S/N lies around the mean.

It is possible to correlate the peak asymmetry with the S/N and the S/N change per event. Figure A.5 (right panel) shows the result of comparing the mean peak asymmetry per event to the averaged raw (red) and matched filtered (blue) S/N per event (top

CHAPTER A. ADDITIONAL MATERIAL ON MATCHED FILTER

subplot). The horizontal lines sit at the mean value obtained in the fit and represent the width of the $-\Delta_{peak}$ bins used, while the vertical lines indicate one standard deviation around that mean value. Notice how there is an approximate linear relation between the peak asymmetry and the S/N , except for peak asymmetry values bigger than -5 ADC where the S/N remains constant.

Also, in the bottom subplot of Fig. A.5 (right panel) I show the relation between the peak asymmetry and the mean S/N change. In this case, one can see that there is a clear maximum at $\Delta_{peak} \sim -10$ ADC. As mentioned previously, this is also the value of the mean of the peak asymmetry distribution. In fact, it is expected that our filter favours the signal peaks with the most common values of the peak asymmetry, as this was one of the features I target in our filter coefficient optimisation through the parameter δ .

These results suggest that events with poorer values of the mean S/N , usually associated to non-favourable track orientations, tend to have smaller values of the mean peak asymmetry (in absolute value). Nonetheless, because our matched filters have been optimised to account for these asymmetries, the improvement on the S/N for these events is sizeable if not better than the one for events which already had a high S/N .

B

Additional material on Solar DM

B.1 Gravitational capture of DM by the Sun

In this work I consider three possible scenarios for the **DM** interactions: **DM** scattering off electrons, spin-dependent (**SD**) and spin-independent (**SI**) interactions with nuclei. For these last two, the cross sections will be given in terms of the **SD** and **SI** elastic scattering **DM** cross section off protons (assuming that the **DM** interactions with protons and neutrons are identical), σ_p^{SD} and σ_p^{SI} , as [130, 198]:

$$\sigma_i^{\text{SD}} = \left(\frac{\tilde{\mu}_{A_i}}{\tilde{\mu}_p} \right)^2 \frac{4(J_i + 1)}{3J_i} |\langle S_{p,i} \rangle + \langle S_{n,i} \rangle|^2 \sigma_p^{\text{SD}}, \quad (\text{B.1})$$

$$\sigma_i^{\text{SI}} = \left(\frac{\tilde{\mu}_{A_i}}{\tilde{\mu}_p} \right)^2 A_i^2 \sigma_p^{\text{SI}}, \quad (\text{B.2})$$

where $\tilde{\mu}_{A_i}$ is the reduced mass of the **DM**-nucleus i system, $\tilde{\mu}_p$ is the reduced mass of the **DM**-proton system, A_i and J_i the mass number and total angular momentum of nucleus i , and $\langle S_{p,i} \rangle$ and $\langle S_{n,i} \rangle$ the expectation value of the spins of protons and neutrons averaged over all nucleons, respectively (see Ref. [199] for a review on spin expectation values).

Since the Sun is mainly composed of hydrogen, the capture of **DM** from the halo is expected to occur mainly through **SD** scattering. However, since the **SI** cross section is proportional to the square of the atomic mass, heavy elements can contribute to the capture rate (even though they constitute less than 2% of the mass of the Sun). Heavy elements can also contribute to the **SD** cross section if the **DM** also has momentum-

CHAPTER B. ADDITIONAL MATERIAL ON SOLAR DM

dependent interactions [200].

DM particles can get captured by the Sun if after repeated scatterings off solar targets their final velocity is lower than the escape velocity of the Sun. In the limit of weak cross sections, this capture rate can be approximately written as [201]:

$$C_{\odot}^{\text{weak}} = \sum_i \int_0^{R_{\odot}} dr \ 4\pi r^2 \int_0^{\infty} du_{\chi} \frac{\rho_{\chi}}{m_{\chi}} \frac{f_{v_{\odot}}(u_{\chi})}{u_{\chi}} \omega(r) \int_0^{v_e(r)} dv \ R_i^-(\omega \rightarrow v) |F_i(q)|^2, \quad (\text{B.3})$$

where the summation extends over all possible solar targets. In this expression, R_{\odot} is the radius of the Sun, ρ_{χ} is the local **DM** density, m_{χ} the mass of the **DM** particle, $f_{v_{\odot}}(u_{\chi})$ the **DM** velocity distribution seen from the Sun's reference frame, $R_i^-(\omega \rightarrow v)$ is the differential rate at which a **DM** particle with velocity v scatters a solar target of mass m_i to end up with a velocity ω and $|F_i(q)|$ is the nuclear form factor of target i .

The differential scattering rate takes a rather simple form when considering velocity-independent and isotropic cross sections. In that case, this quantity is given by [198, 201]:

$$R_i^-(\omega \rightarrow v) = \frac{2}{\sqrt{\pi}} \frac{\mu_{i,+}^2}{\mu_i} \frac{v}{\omega} n_i(r) \sigma_i \left[\chi(-\alpha_-, \alpha_+) + \chi(-\beta_-, \beta_+) e^{\mu_i(\omega^2 - v^2)/u_i^2(r)} \right], \quad (\text{B.4})$$

where μ_i is the ratio between the **DM** mass and the mass of target i , $\mu_{i,\pm}$ is defined as:

$$\mu_{i,\pm} \equiv \frac{\mu_i \pm 1}{2}, \quad (\text{B.5})$$

$n_i(r)$ is the density profile of target i in the solar medium, $u_i(r)$ is the most probable velocity of target i given by:

$$u_i(r) = \sqrt{\frac{2T_{\odot}(r)}{m_i}}, \quad (\text{B.6})$$

where $T_{\odot}(r)$ is the temperature of the Sun, the quantities α_{\pm} and β_{\pm} are defined as:

$$\alpha_{\pm} \equiv \frac{\mu_{i,+}v \pm \mu_{i,-}\omega}{u_i(r)}, \quad (\text{B.7})$$

$$\beta_{\pm} \equiv \frac{\mu_{i,-}v \pm \mu_{i,+}\omega}{u_i(r)}, \quad (\text{B.8})$$

B.1. GRAVITATIONAL CAPTURE OF DM BY THE SUN

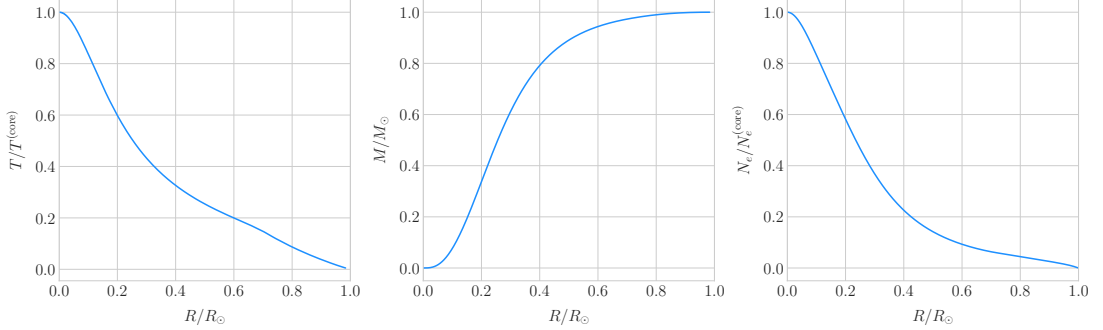


Figure B.1: Input solar parameters used in the capture rate computation as a function of the solar radius, from left to right: temperature (with respect to the temperature at the core), mass (in solar masses) and electron number density (with respect to the electron density at the core). All quantities shown correspond to the standard solar model BS2005-OP [26].

and the function $\chi(a, b)$ is a Gaussian integral of the form:

$$\chi(a, b) \equiv \int_a^b dx e^{-x^2}. \quad (\text{B.9})$$

Finally, if one assumes the **DM** halo velocity distribution in the galactic rest frame to be a Maxwell-Boltzmann distribution, one can write the halo velocity distribution for an observer moving at the speed of the Sun with respect to the **DM** rest frame as:

$$f_{v_\odot}(u_\chi) = \sqrt{\frac{3}{2\pi}} \frac{u_\chi}{v_\odot v_d} \left(e^{-\frac{3(u_\chi - v_\odot)^2}{2v_d^2}} - e^{-\frac{3(u_\chi + v_\odot)^2}{2v_d^2}} \right), \quad (\text{B.10})$$

where:

$$\omega^2(r) = u_\chi^2 + v_e^2(r), \quad (\text{B.11})$$

is the **DM** velocity squared, v_\odot the relative velocity of the Sun from the **DM** rest frame and $v_d \simeq \sqrt{3/2}v_\odot$ the velocity dispersion.

For the case of strong scattering cross sections, Eq. (B.3) ceases to be valid, as it escalates indefinitely with the cross section. In that limit, the capture rate saturates to the case where the probability of interaction is equal to one, which can be written as

CHAPTER B. ADDITIONAL MATERIAL ON SOLAR DM

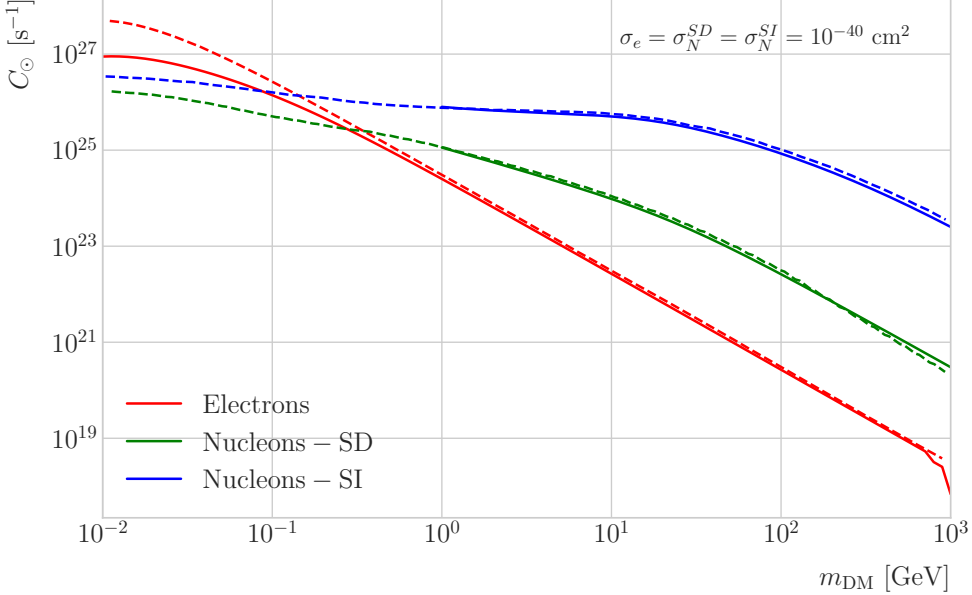


Figure B.2: Capture rates as a function of the **DM** mass for the **DM**-electron interactions (red lines), **SD** **DM**-nucleons interactions (green lines), and **SI** **DM**-nucleons interactions (blue lines). Solid lines represent the values computed in this work while the dashed lines are the one given in Ref. [198]. All the rates are shown for a choice of scattering cross section of $\sigma_i = 10^{-40} \text{ cm}^2$.

[202]:

$$C_\odot^{\text{geom}} = \pi R_\odot^2 \left(\frac{\rho_\chi}{m_\chi} \right) \langle v \rangle \left(1 + \frac{3}{2} \frac{v_e^2(R_\odot)}{v_d^2} \right) \xi(v_\odot, v_d), \quad (\text{B.12})$$

where $\langle v \rangle = \sqrt{8/3\pi} v_d$ is the mean velocity in the **DM** rest frame and the factor $\xi(v_\odot, v_d)$ accounts for the suppression due to the motion of the Sun:

$$\xi(v_\odot, v_d) = \frac{v_d^2 e^{-\frac{3v_\odot^2}{2v_d^2}} + \sqrt{\frac{\pi}{6}} \frac{v_d}{v_\odot} (v_d^2 + 3v_e^2(R_\odot) + 3v_\odot^2) \text{Erf}\left(\sqrt{\frac{3}{2}} \frac{v_\odot}{v_d}\right)}{2v_d^2 + 3v_e^2(R_\odot)}. \quad (\text{B.13})$$

Having these into account, one can write the total capture rate as a combination of both contributions, allowing a smooth transition between the two, as [130]:

$$C_\odot = C_\odot^{\text{weak}} \left(1 - e^{C_\odot^{\text{geom}} / C_\odot^{\text{weak}}} \right). \quad (\text{B.14})$$

I computed the capture rate from Eq. (B.14) in the case of interactions with

B.1. GRAVITATIONAL CAPTURE OF DM BY THE SUN

electrons. To do so, I used the standard solar model BS2005-OP [26]. Fig. B.1 shows the three parameters from the solar model that are needed for the computation, the solar temperature (left panel), mass (central panel) and electron density (right panel) profiles.

For the case of the interactions off nuclei, the computations are more convoluted as one needs to add up the contributions of the different most abundant nuclei in the Sun. Also, in contrast to the electron scenario where the form factor is trivially $|F_e(q)|^2 = 1$, for any nucleus i one would need to consider some appropriate nuclear density distribution (either a Gaussian approximation, a Woods-Saxon distribution, etc) which would complicate the calculations even further.

That is the reason why, at this stage of the study, I decided to take an alternative approach to the computation of the **DM**-nucleus capture rates. I used the **DarkSUSY** software, that allows us to compute these quantities performing a full numerical integration over the momentum transfer of the form factors [203]. The default standard solar model used by **DarkSUSY** is BP2000¹ [204].

In Fig. B.2 I show the results I obtain for the capture rates, for the case of interactions off electrons (red solid line), **SD** (green solid line) and **SI** (blue solid line) interactions of nucleons. In all cases I use a value of the scattering cross sections of $\sigma_i = 10^{-40} \text{ cm}^2$. Note here one of the limitations of the **DarkSUSY** approach, one can not extend the computation below $m_{\text{DM}} = 1 \text{ GeV}$. Nevertheless, this is not something to worry about in this case, as I will discuss next. As a comparison, I added also the values computed in Ref. [198] (same color scheme, dashed lines). One can see there is good agreement between these and the **DarkSUSY** computation of the **SD** and **SI** interactions for $m_{\text{DM}} \geq 1 \text{ GeV}$. In this regime their computations also matches quite well the results for the electron capture rate. However, these start to differ significantly below $m_{\text{DM}} = 1 \text{ GeV}$, being their estimate up to a factor of 5 bigger than ours for low masses. This could be due to the use of a different solar model in the calculation.

Let me comment briefly about the assumption I made before about not including

¹This is what they say in their manual, but I fear it is somewhat outdated. It appears to me this model is relatively old and do not see why they are not using others like [26]. Maybe one can double-check in the code to make sure.

CHAPTER B. ADDITIONAL MATERIAL ON SOLAR DM

an evaporation term in the Boltzmann equation. If I include this term in the equation, which is proportional to the number of **DM** particles, the equilibrium solution takes the form:

$$N_{DM}^{eq} = \sqrt{\frac{C_\odot}{A_\odot}} \frac{1}{\kappa + \frac{1}{2} E_\odot \tau_{eq}}, \quad (\text{B.15})$$

where E_\odot is the total evaporation rate, τ_{eq} is the equilibrium time in the absence of evaporation:

$$\tau_{eq} = \frac{1}{\sqrt{C_\odot A_\odot}}, \quad (\text{B.16})$$

and κ is defined as:

$$\kappa \equiv \sqrt{1 + \left(\frac{E_\odot \tau_{eq}}{2} \right)^2}. \quad (\text{B.17})$$

Now, it is easy to proof that in the case evaporation dominates $\kappa \gg 1$ and therefore:

$$N_{DM}^{eq} \simeq \frac{C_\odot}{E_\odot}. \quad (\text{B.18})$$

In contrast, if evaporation is irrelevant $\kappa \simeq 1$ and one recovers Eq. (5.2).

In this way, one can define the evaporation mass as the mass for which the number of **DM** particles in equilibrium approaches Eq. (B.18) at 10% level:

$$\left| N_{DM}^{eq}(m_{evap}) - \frac{C_\odot(m_{evap})}{E_\odot(m_{evap})} \right| = 0.1 N_{DM}^{eq}(m_{evap}). \quad (\text{B.19})$$

This can be regarded as the minimum testable mass one can reach using the annihilation products of the **DM** in the Sun.

It was reported in Ref. [198] that, in the case of both **SD** and **SI DM** interactions off nuclei, this value ranges from 2 to 4 GeV depending on the specific scattering cross section value, compatible with the usual assumptions in the literature. What is interesting is the case of the electron capture. It was found that, when one applies a cutoff in the velocity distribution of the **DM** trapped in the Sun slightly below the escape velocity, the evaporation mass for the **DM**-electron interaction decreases remarkably. For a moderate choice of $v_c(r) = 0.9 v_e(r)$ one gets an evaporation mass of around 200 to

B.2. EXAMPLE: KALUZA-KLEIN DARK MATTER

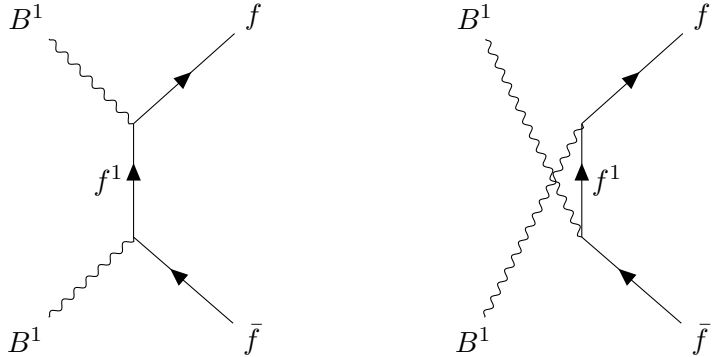


Figure B.3: Feynman diagrams for $B^1 B^1$ annihilation into SM fermions.

600 MeV. This possibility opens a region of the parameter space that could be tested with the next generation of neutrino detectors.

B.2 Example: Kaluza-Klein Dark Matter

Even though there are plenty of BSM theories which provide viable DM candidates, the Kaluza-Klein (KK) type of models [205, 206] within the universal extra dimensions (UED) paradigm naturally predict the existence of a massive, stable particle that can play the role of the DM. In the UED scenario all the SM fields can propagate in one or more compact extra dimensions [207], as opposed to the idea of brane worlds [208, 209], where just gravity can propagate in the bulk while SM particles live at fixed points.

Furthermore, in UED there is no violation of the translational invariance along the extra dimensions, thus leading to degenerate KK modes masses and also the conservation of the KK number in the effective four dimensional theory. At loop level, radiative corrections and boundary terms shift the masses of the KK modes and break KK number conservation into a KK parity. As a result, this theory only contains interactions between an even number of odd KK modes, and therefore the lightest among the first KK excitations will be stable. This particle is usually denoted as the lightest Kaluza-Klein particle (LKP) and its mass is proportional to $1/R$, being R the size of the extra dimension.

A viable DM candidate needs to be electrically neutral and non-baryonic, therefore

CHAPTER B. ADDITIONAL MATERIAL ON SOLAR DM

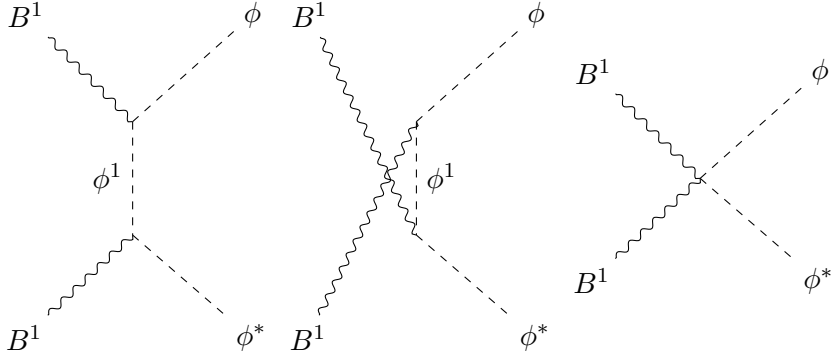


Figure B.4: Feynman diagrams for $B^1 B^1$ annihilation into a Higgs boson pair.

good candidates among the first Kaluza-Klein excitations would be the [KK](#) neutral gauge bosons and the [KK](#) neutrinos [210]. Another possible candidate is the first [KK](#) excitation of the graviton, which receives negligible radiative contributions to its mass and therefore has a mass almost equal to $1/R$. However, it has been shown that the lightest eigenstate from the mixing of the gauge mass states (B^1 , W_3^1) would be lighter, as these receive negative radiative corrections [211]. It is also understood that, when these corrections become sizeable, the eigenstates become approximately pure B^1 and W_3^1 states, as the Weinberg mixing angle grows small with the [KK](#) number [211]. In that case, the [LKP](#) can be well-approximated as being entirely B^1 .

To estimate the sensitivity of [DUNE](#) to this particular [DM](#) model, I first need to compute the neutrino flux produced by the annihilations of the [LKP](#) in the core of the Sun, taking into account their propagation in the solar medium, as well as neutrino oscillations. To this end I use [WimpSim](#) [140, 212] to generate 10^6 annihilation events in the Sun over a time span of four years, and propagate them to the [DUNE FD](#) location ($44^\circ 20' \text{ N}$, $103^\circ 45' \text{ W}$), for different values of M_{LKP} . The different Feynman diagrams for the annihilation of the B^1 into a pair of [SM](#) fermions and scalars are shown in Figs. B.4 and B.4. The relative annihilation fractions of the B^1 used by [WimpSim](#) can be found in Ref. [213].

In Fig. B.5 I show the obtained muon neutrino spectra arriving to the detector from [LKP](#) annihilations in the Sun, per unit area and per annihilation, plotted in relative

B.2. EXAMPLE: KALUZA-KLEIN DARK MATTER

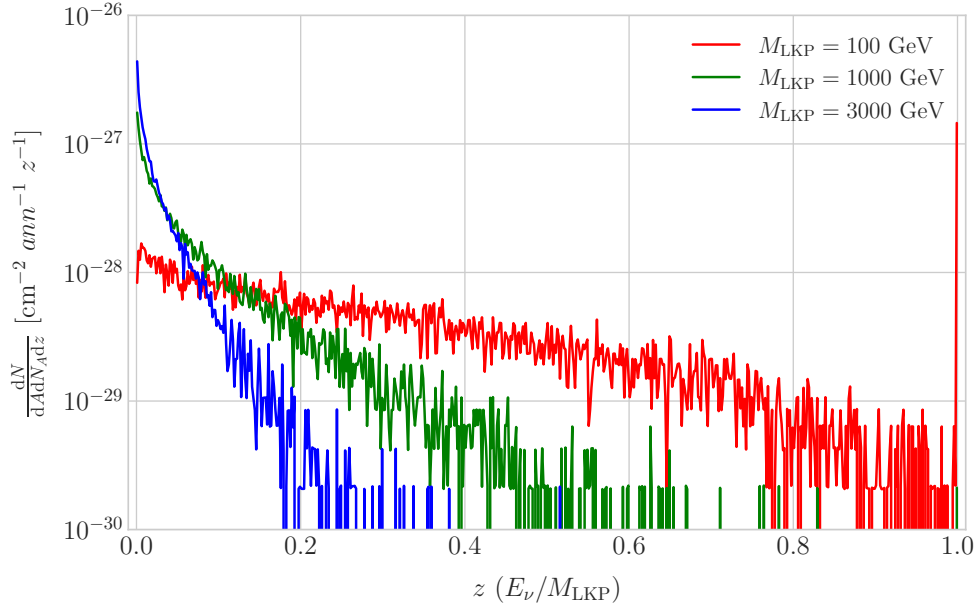


Figure B.5: Computed spectra of muon neutrinos at the [DUNE FD](#) site from B^1 annihilations in the Sun for three different values of M_{LKP} , plotted in relative energy units for legibility.

energy units for different values of the [LKP](#) mass. As one could expect the spectra get steeper the higher is the mass, due to the absorption of high-energy neutrinos in the solar medium. Also, one can see the peak at $z = 1$ due to the direct annihilation into neutrinos $B^1 B^1 \rightarrow \nu \bar{\nu}$.

Now, one can estimate the sensitivity of [DUNE](#) to this particular model by using the method I previously discussed. I use the optimistic estimation of the background efficiency in Eq. (5.5) to get an upper bound of the sensitivity. Using it, one can directly compute the number of expected background events to be $N_B = 0.11$ for an exposure of 400 kT yr. Then, Eq. (5.7) give us a value of $N_S^{90} = 2.20$ for the 90% exclusion number of expected signal events. Thanks to the cross sections generated with [NuWro](#) and the computed neutrino fluxes from B^1 annihilations in the Sun, I can estimate the limits on the [SD](#) and [SI DM](#)-nucleus cross section using the relation in Eq. (5.2) and the capture rates I obtained from [DarkSUSY](#).

In Fig. B.6 I show the projected sensitivity for [DUNE](#) on the spin-dependent B^1 -proton scattering cross section versus the mass of the [LKP](#), for a exposure of

CHAPTER B. ADDITIONAL MATERIAL ON SOLAR DM

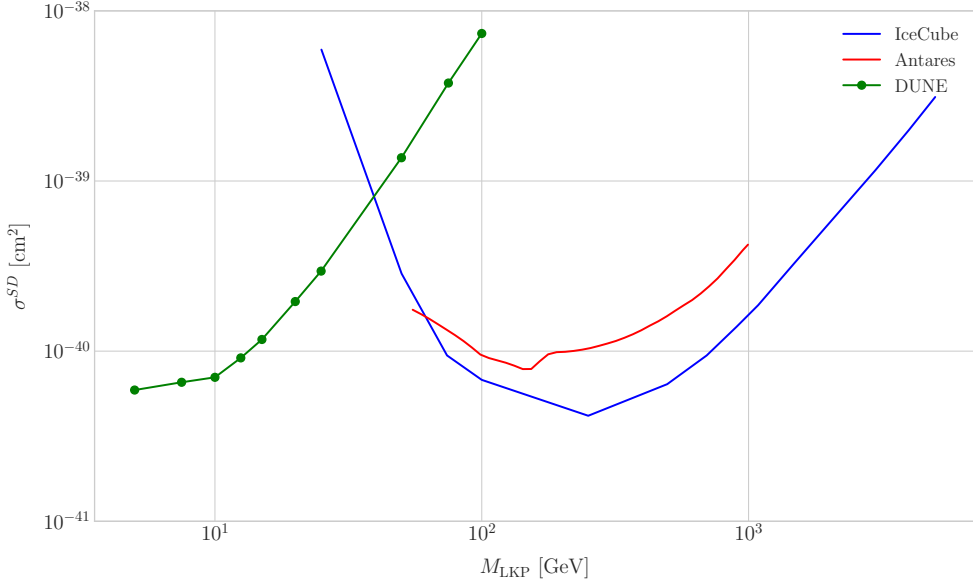


Figure B.6: Projected 90% confidence level upper limit for **DUNE** (400 kT yr) on the spin-dependent B^1 -proton scattering cross section as a function of M_{LKP} (green dots). I also show the previous limits from **IceCube** [214] (blue line) and **Antares** [215] (red line) on the **LKP** cross section. The shaded area represents the disfavoured region (at 95% confidence level) on the mass of the **LKP** from **LHC** data [216].

400 kT yr (green dots). I also include the previous results from **IceCube** [214] (blue line) and **Antares** [215] (red line). The shaded area represents the disfavoured region from combined searches for **UED** by **ATLAS** and **CMS** [216].

From the experimental point of view, this estimation lacked a detailed simulation of the detector response and thus this must be regarded as a mere optimistic sensitivity computation. However, it shows the potential of **DUNE** to constrain this kind of exotic scenarios, showing the region where it will be in a position to compete with other neutrino telescopes. A more detailed analysis is needed if I am to make a realistic estimation. Even though the region of the parameter space where **DUNE** would be sensitive to this particular model is quite constrained by collider searches [216] and other rare decay measurements [217, 218], it still constitutes an alternative indirect probe.

B.3 Example: Leptophilic Dark Matter

In general, the capture rate of **DM** particles by the Sun via interactions with electrons is several orders of magnitude smaller than the capture via **DM**-nucleus scattering. Thus, it would be sub-leading even when nucleon capture is loop suppressed [219]. As I showed in Fig. B.2, the capture rate via scattering off electrons only surpasses the capture rates via **DM**-nucleon interactions for **DM** masses $\lesssim 100 - 500$ MeV.

However, if one considers a model where **DM**-nucleon interactions are forbidden even at loop level, then electron interactions will be the sole contributor to **DM** capture in the Sun. One can describe such scenario where the **DM** particles couple to leptons but not to the quark sector using effective operators.

Assuming that the **DM** particle is a Dirac fermion, the dimension six operators describing the interaction between two **DM** particles and two leptons can be written as:

$$\mathcal{L}_{eff} = G \sum_i (\bar{\chi} \Gamma^i_\chi \chi) (\bar{\ell} \Gamma^i_\ell \ell), \quad (B.20)$$

where $G = 1/\Lambda^2$ is the effective coupling strength, Λ the cut-off of the effective field theory and ℓ denotes any lepton. In principle, one should consider all the possible Lorentz structures Γ_f^i in order to have a complete set of effective operators.

However, some combinations will induce interactions with nucleons at loop level. As we are specifically interested in interactions which forbid any communication with the quark sector, I will not consider those [219]. In addition, some of the effective operators give rise to velocity-suppressed scattering cross sections between **DM** particles and leptons. I will also neglect them, as the suppression goes with the square of the **DM** halo velocity, which in units of the speed of light is $\sim 10^{-6}$.

This way, the only Lorentz tensor structure that do not induce interactions with quarks at loop level and gives a contribution to the scattering cross section that is not velocity-suppressed is the axial-axial interaction. The effective Lagrangian is then given

CHAPTER B. ADDITIONAL MATERIAL ON SOLAR DM

by:

$$\mathcal{L}_{eff} = \frac{c_A^\chi c_A^\ell}{\Lambda^2} (\bar{\chi} \gamma^\mu \gamma^5 \chi) (\bar{\ell} \gamma_\mu \gamma^5 \ell), \quad (B.21)$$

where c_A^χ and c_A^ℓ are the couplings for the different species. As the **DM** coupling appears as a common factor for any lepton choice, I redefine the corresponding coupling c_A^ℓ to absorb c_A^χ . Also, for simplicity, I will assume that the couplings between the **DM** particles and the leptons are flavour independent, i.e. I have just two couplings, c_A^e for charged leptons and c_A^ν for neutrinos.

In the case of a scalar **DM** particle, the lowest order effective interaction with leptons happens through a dimension five operator, generating scalar and pseudoscalar interactions. However, the former induces interactions with quarks at two loop level whereas the latter gives a velocity suppressed scattering cross section.

From the effective Lagrangian in Eq. (B.21), it can be shown that the axial-axial contribution to the scattering cross section for the fermionic **DM** and a charged lepton is given by:

$$\sigma_{DM-e}^{AA} = 3 (c_A^e)^2 \frac{m_e^2}{\pi \Lambda^4}. \quad (B.22)$$

If the **DM** interacts exclusively with fermions, then the only annihilation channels that will give us measurable neutrino fluxes coming out of the Sun are $\tau^+ \tau^-$ and $\nu \bar{\nu}$. The former channel, already explored previously in the mainstream scenario of the **DM** capture via scattering off nucleons, is open only for $m_{DM} > m_\tau \simeq 1776.86 \pm 0.12$ MeV [220], a mass region where the solar **DM** capture by electrons is at least one order of magnitude smaller than the capture via interactions with nucleons. On the contrary, the latter allows us to explore a region where the capture rate via scattering off electrons dominates over the rest.

One downside of focusing in such low mass range is that it falls below the usual limit of $m_{evap} \sim 4$ GeV usually explored in the literature. The pretext to explore this region is the result discussed previously reported in Ref. [198], where **DM** evaporation in the Sun for the case of capture via electron scattering could be negligible for masses as low as $m_{evap} \sim 200$ MeV. This result is quite sensitive to the high velocity tail of

B.3. EXAMPLE: LEPTOPHILIC DARK MATTER

the **DM** velocity distribution in equilibrium inside the Sun, and therefore full numerical simulations would be needed to assess the impact of this effect. However, this is out of the scope of this work.

In this case, as I have an specific realisation of the interaction between the **DM** and leptons, I can estimate the relic density of our **DM** for different values of the couplings and the effective field theory scale Λ . The first step to do so is compute the self-annihilation cross section. Because I consider cold relics, at the freeze-out time our **DM** particles were non-relativistic and so one can expand the annihilation cross section in terms of the relative velocity v between two annihilating **DM** particles as [221]:

$$\sigma_{ann}^{AA}|v| \approx \frac{1}{2\pi\Lambda^4} \sum_{\ell} \left(c_A^{\ell} \right)^2 m_{\chi}^2 \sqrt{1 - \frac{m_{\ell}^2}{m_{\chi}^2}} \left[\frac{m_{\ell}^2}{m_{\chi}^2} + \frac{1}{12} \left(2 - \frac{m_{\ell}^2}{m_{\chi}^2} \right) v^2 \right], \quad (\text{B.23})$$

where the sum includes all the possible lepton final states with mass m_{ℓ} .

Solving the Boltzmann equation for the evolution of the **DM** density gives as a solution a relic density of:

$$\Omega_{\chi} h^2 \approx \frac{(1.04 \times 10^9) x_F}{M_{Pl} \sqrt{g_*} (a + 3b/x_F)}, \quad (\text{B.24})$$

where $x_F = m_{\chi}/T_F$ being T_F the freeze-out temperature, g_* the number of relativistic degrees of freedom at freeze-out and a and b the terms in the annihilation cross section expansion $\sigma_{ann}|v| \approx a + bv^2 + \mathcal{O}(v^4)$. Using the current best fit for the relic **DM** density $\Omega_{\chi} h^2 = 0.1198 \pm 0.0012$ [222] one can use these relations to compute the required effective theory scale Λ at which the correct density is achieved for any combinations of m_{χ} and c_A^{ℓ} .

As discussed before, in the low **DM** mass region **QE** interactions dominate. Moreover, if I focus on direct annihilation to neutrinos, the energy of the muon neutrino flux is known. This must be equal to the mass of the **DM** particle, $E_{\nu} = m_{\chi}$. That way, now I do not need to use Eq. (5.14) in order to estimate the momentum transfer to the

CHAPTER B. ADDITIONAL MATERIAL ON SOLAR DM

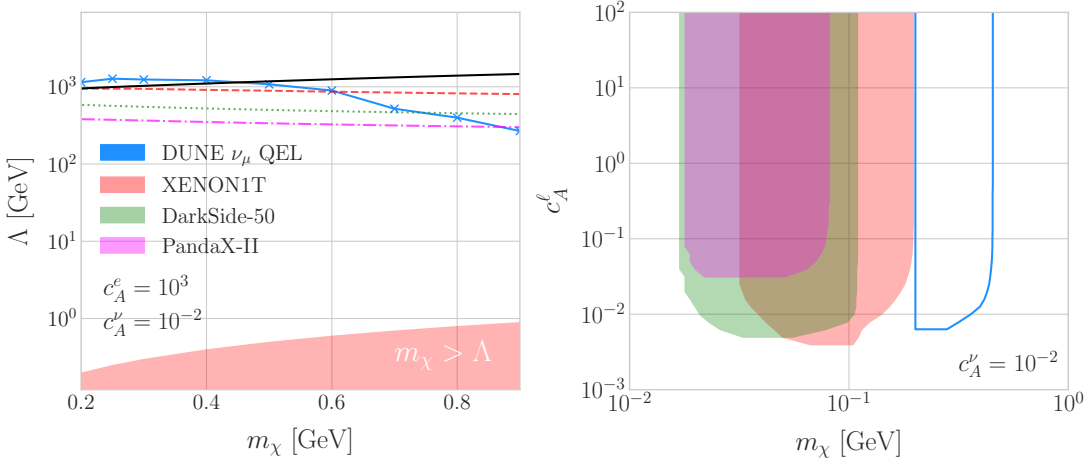


Figure B.7: Left panel: Projected 90% confidence level sensitivity of [DUNE](#) (400 kT yr) to the scale Λ of an [EFT](#) containing only leptophilic [DM](#) axial-axial interactions (blue line), for the coupling values $c_A^e = 10^3$ and $c_A^\nu = 10^{-2}$. The black line represents the values for which the correct relic density is achieved. Right panel: Excluded values of c_A^e as a function of the [DM](#) mass, for a fixed value $c_A^\nu = 10^{-2}$. In both cases the corresponding limits from [XENON1T](#) [223] (red), [DarkSide-50](#) [224] (green) and [PandaX-II](#) [225] (magenta) are also shown.

remnant nucleus, I can simply take:

$$\vec{p}_N = \hat{p}_\nu m_\chi - \vec{p}_\mu - \vec{p}_p. \quad (\text{B.25})$$

To estimate the signal efficiency and background rejection for this case I use again the [BDT](#) classifier from [scikit-learn](#), using the same specifications as before. The only difference now is that I add also the reconstructed neutrino energy as one of the features to train the classifier with, because the characteristic monoenergetic flux for each m_χ value will help to distinguish between signal and background events.

In this case, for masses below ~ 500 MeV I obtain a signal efficiency close to unity while keeping a background rejection of 99.9%. For bigger values of the mass, the signal efficiency drops significantly if I require to keep the background acceptance under 0.01%. However, because this kind of search is dominated by the background, sacrificing the signal acceptance to keep the background rejection to a minimum enhances the reach of the analysis. This way, for [DM](#) masses of the order of $m_\chi \sim 1$ GeV I end up with

B.3. EXAMPLE: LEPTOPHILIC DARK MATTER

efficiencies as low as 1%.

Now, estimating the number of background events using Eq. (5.20) one can go on and apply Eqs. (5.7) and (5.8) together with Eq. (B.22) to derive the sensitivity of **DUNE** to this kind of model. Fig. B.7 (left panel) shows the potential reach of **DUNE** to constrain the **EFT** scale Λ of this model containing only leptophilic **DM** axial-axial interactions (blue line), for a choice of couplings $c_A^e = 10^3$ and $c_A^\nu = 10^{-2}$. I also include the current limits on the **DM**-electron scattering cross section from XENON1T [223] (dashed red line), DarkSide-50 [224] (dotted green line) and PandaX-II [225] (dash-dotted magenta line), reworked with Eq. (B.22) to show their implications for the **EFT** scale. The values of Λ for which the correct **DM** relic density value is achieved for each mass are also shown (black line). This tells us that, for that specific choice of couplings, **DUNE** would be sensitive to **DM** configurations allowed by the relic density constraint up to a mass of $m_\chi \sim 400$ MeV.

In Fig. B.7 (right panel) I show similar limits for the excluded values of c_A^e as a function of the **DM** mass, for a fixed $c_A^\nu = 10^{-2}$. I do not show the limits for other values of c_A^ν , as this parameter has little effect on the phenomenology at hand. From this view, one can see that **DUNE** would be able to offer complementary information to the low energy **DM**-electron interaction searches performed by direct detection experiments, in a slightly higher mass range.

With the present example, although it focuses on a very specific realisation of the **DM** interactions, I show the potential of **DUNE** to constrain exotic **DM** scenarios. Thanks to its low backgrounds and superb angular resolution, **DUNE** will be able to help with the searches for dark sectors physics.

C

Additional material on ND-GAr PID

C.1 Energy calibration

In order to obtain the amount of energy loss by a charged particle due to ionisation in our [HPgTPC](#) we need to determine the conversion between the charge deposited in our readout planes and the actual energy depositions. This procedure is known as energy calibration.

In general, the first step of the calibration involves a non-uniformity correction, to make sure that the detector response is uniform throughout the [TPC](#). These are typically divided into three categories, non-uniformities in the transverse (y, z) plane, non-uniformities along the drift direction x , and variations of the detector response over time (would not apply to us as the detector is not built yet). These would correct for effects such as electron diffusion and attenuation, space charge effects or channel misconfiguration. However, because at the moment I am only interested in making sure we recover a sensible result from our simulation, I will not apply uniformity corrections to our charge deposits.

Other effects, like electron-ion recombination or [ADC](#) saturation, lead to a non-linear relation between the observed charge and the deposited energy in the detector, with the observed readout charge saturating at high ionisation energies. Because we are dealing with gaseous argon, recombination is not as important as in [LAr](#). Therefore, we do not simulate recombination effects in the [HPgTPC](#). Even so, the simulation of the electronic response will still introduce charge saturation, and one needs to correct for it in order to

CHAPTER C. ADDITIONAL MATERIAL ON ND-GAr PID

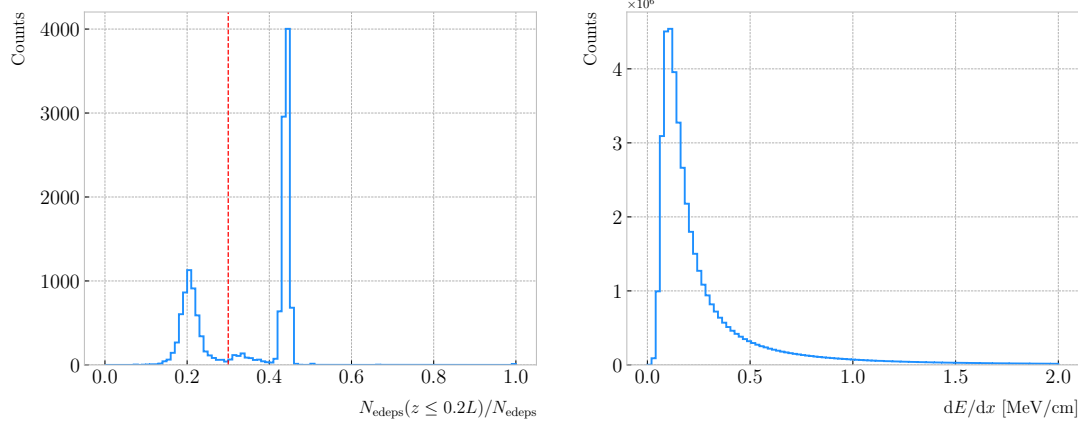


Figure C.1: Left panel: distribution of the fraction of Geant4-level energy deposits per track with residual range less than 20% of the total track length, for the isotropic proton sample. Right panel: distribution of the ionisation per unit length of the energy deposits in the proton sample after removing the tracks with less than 30% of their energy deposits in the last 20% of the track.

obtain the exact amount of energy loss due to ionisation.

By default, the track fitting algorithm in GArSoft provides a `TrackIonization` object associated to each reconstructed track. It contains two collections of charge deposits, one for each fitting direction, consisting on pairs of charge values (dQ , in [ADC](#)) and step sizes (dx , in cm).

For studying the energy loss of the protons, I select the reconstructed tracks that range out (i.e. slow down to rest) inside the [HPgTPC](#). A characteristic feature of the energy loss profile of any stopping ionising particle is the so-called Bragg peak, a pronounced peak that occurs immediately before the particle comes to rest. From Eq. (6.1) we can see that this behaviour is expected, as the energy loss for non-relativistic particles is inversely proportional to β^2 . In data, a way of identifying the Bragg peak, and thus select the stopping particles, is checking the number of energy deposits towards the end of the track. In this case, I count the fraction of the Geant4-simulated energy deposits with a residual range value (the distance from a given energy deposit to the last deposit in the track trajectory) less than a 20% of the corresponding track length¹.

¹As we are applying this selection at the Geant4-level we could have simply selected the stopping protons using the `EndProcess` labels from the simulation. However, the Bragg peak identification method displayed here could serve as a starting point for a selection of stopping protons in real data.

C.1. ENERGY CALIBRATION

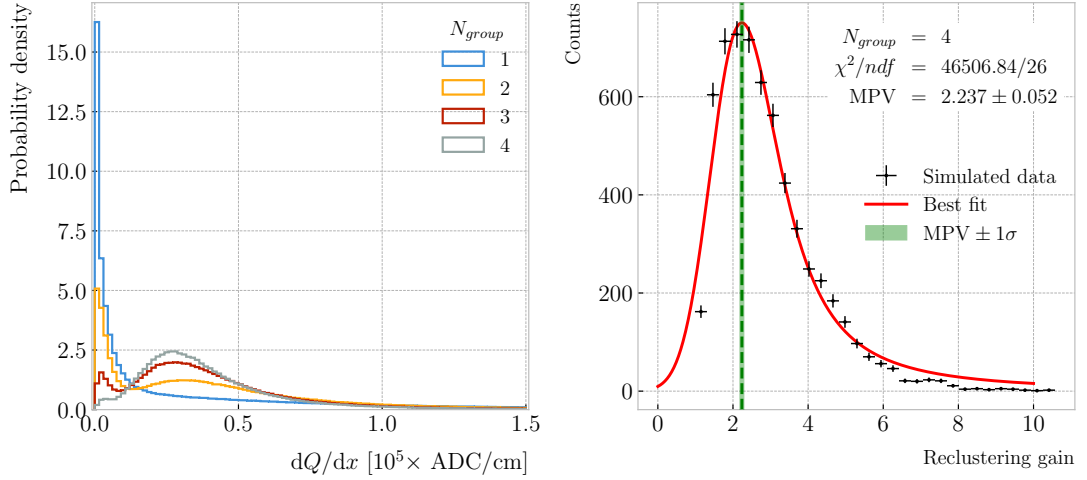


Figure C.2: Left panel: distribution of the reconstructed ionisation charge per unit length for our MC stopping proton sample. The different colors indicate how many consecutive dQ/dx pairs were grouped together. Right panel: distribution of the median change in dQ/dx per track after $N_{group} = 4$ clusters were reclustered together.

The distribution of this fraction of energy deposits for the proton sample is shown in Fig. C.1 (left panel). We can clearly see two well separated peaks in this distribution, one centered at 0.2 and another, narrower one centered at a higher value. The first one corresponds to non-stopping protons, as in that case the number of energy deposits towards the end of the track is uniformly distributed due to the absence of the Bragg peak. In that way, I apply a cut in this distribution, requiring that at least 30% of the simulated energy deposits sit in the last 20% of the tracks, to ensure that the Bragg peak is present.

Figure C.1 (right panel) shows the distribution of the energy loss per unit length for the Geant4-simulated energy deposits of the selected stopping protons. We can see that it follows the expected shape of a Landau distribution, which describes the fluctuations of the ionisation energy losses [164]. This distribution has a characteristic asymmetric PDF, with a long right tail that translates into a high probability for high-energy ionisation losses. The origin of these fluctuations is mainly the possibility of transferring a high enough energy to an electron, so it becomes a ionising particle itself.

Now, from the point of view of the reconstruction, the objects that we have available

CHAPTER C. ADDITIONAL MATERIAL ON ND-GAr PID

to extract the ionisation information for the different reconstructed tracks are the collections of dQ and dx pairs, as stated before. The dQ values come from adding up the amplitude of all the reconstructed hits in a cluster, which are the input objects to the Kalman fit.

Figure C.2 (left panel) shows the distribution of the ionisation charge deposits per unit length for the tracks in the stopping proton sample (blue line). As one may notice, this distribution does not resemble the expected shape of the Landau PDF. This distribution peaks sharply at 0 and has a heavy-tailed behaviour. Notice, however, how the distribution changes its shape as we group together N_{group} consecutive charge deposit pairs (red, purple and green lines). The distribution in the $N_{group} = 4$ case already has a shape which resembles that of the Geant4-level ionisation per unit length, so I will proceed using this amount of reclustering for the reconstruction-level depositions.

An extra factor I need to account for, when reclustering is applied, is how the overall dQ/dx per track changes. To do so, we can look at the ratio between the median dQ/dx before and after the reclustering. Figure C.2 (right panel) shows the median enhancement in dQ/dx per track for the stopping proton sample in the case $N_{group} = 4$. Fitting a LanGauss distribution, I estimate the most probable value of this ratio to be $G_{group} = 2.24 \pm 0.05$.

At this point, I am left with determining the conversion between the charge deposits per unit length dQ/dx and the energy deposits per unit length dE/dx . To this end, we need a way of comparing the two. I can use the residual range z to get a prediction of the most probable dE/dx by using the following empirical parametrisation:

$$\frac{dE}{dx}(z) = \frac{z^{\frac{1}{p}-1}}{p\Lambda^{\frac{1}{p}}}, \quad (C.1)$$

which is quoted in the literature as the Bragg-Kleeman formula [226]. In order to obtain the p and Λ parameters I perform a fit using the energy losses and the residual ranges given by the Geant4 stage of our proton sample.

Within our simulation, the residual range is sampled with a maximum size of

C.1. ENERGY CALIBRATION

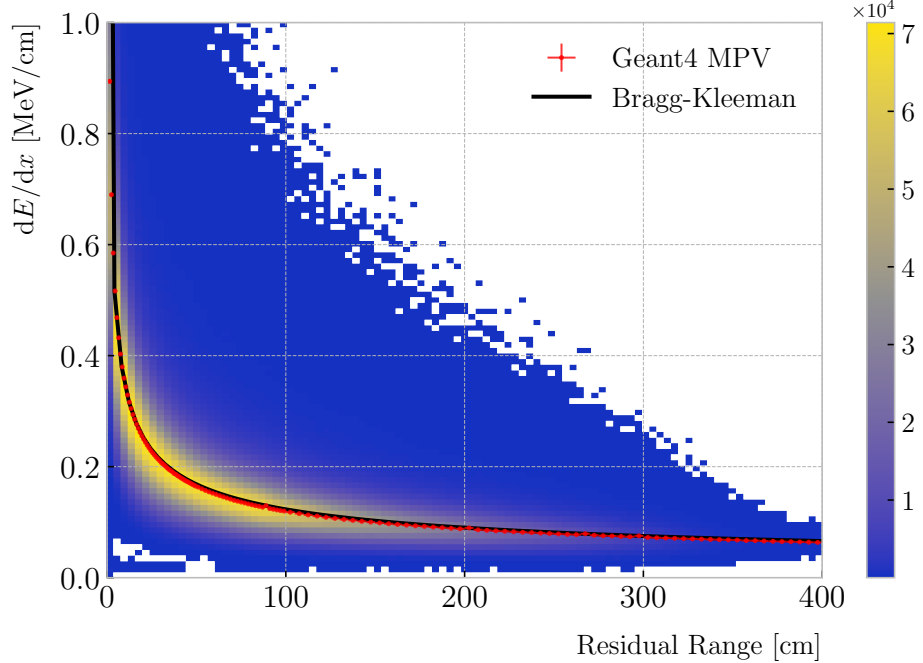


Figure C.3: Distribution of the **Geant4**-simulated energy losses per unit length versus residual range for the stopping proton sample. The overlaid points represent the fitted most probable value of the dE/dx distribution in each residual range bin, whereas the curve is their best fit to the Bragg-Kleeman formula from Eq. (C.1).

5 mm. Therefore, to perform the fit to the Bragg-Kleeman formula we can use a fine-grained residual range binning. For each of the residual range bins I extract the dE/dx distribution and fit it to a LanGauss distribution, to obtain the value of the most probable dE/dx in the bin together with a statistical uncertainty. I then fit Eq. (C.1) to these most probable values and the centres of the residual range bins. This procedure is depicted in Fig. C.3, where I show the distribution of the energy loss per unit length versus the residual range, together with the most probable dE/dx values and their uncertainty in each bin (red points) and the curve with the best fit of the Bragg-Kleeman relation to those values (black line). The best fit is obtained for the parameter values $p = 1.8192 \pm 0.0005$ and $\Lambda = 0.3497 \pm 0.0008 \text{ cm}/\text{MeV}^{p^2}$.

Having an analytical expression that relates the residual range to dE/dx , I can take our reconstruction-level residual ranges from the stopping proton sample and compute

²These strange units for Λ come from dimensional analysis, just to keep the Bragg-Kleeman formula (C.1) consistent.

CHAPTER C. ADDITIONAL MATERIAL ON ND-GAr PID

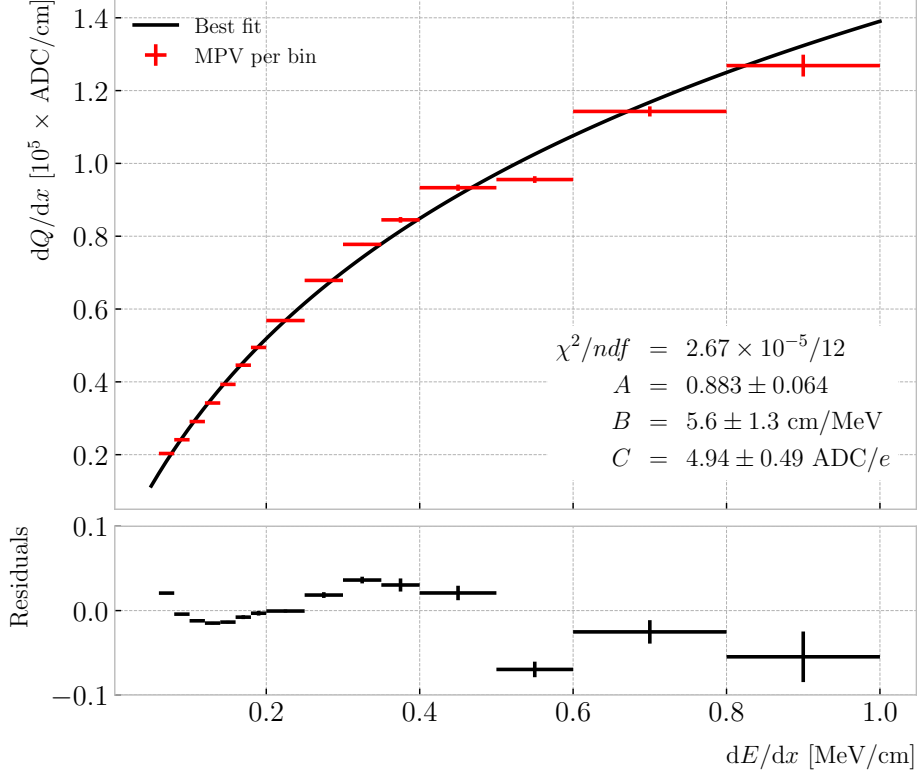


Figure C.4: Fitted most probable dQ/dx values for each dE/dx bin (red points), obtained from the stopping proton sample. The overlaid curve (black line) represents the best fit to the logarithmic calibration function from Eq. (C.2).

the most probable energy loss associated.

In order to parametrise the charge saturation, we can use the following logarithmic function inspired by the modified box model for recombination [227]:

$$\frac{dE}{dx} = \frac{e^{\frac{dQ}{dx}B\frac{W_{ion}}{G_{group}C}} - A}{B}, \quad (\text{C.2})$$

where A and B are the calibration parameters we need to determine, W_{ion} is the average energy to produce an electron-ion pair, G_{group} is the gain from the reclustering discussed above, and C is the calibration constant to convert the number of electrons to [ADC](#) counts, commonly refer to as gain (also to be obtained in the fit). In this case, I use a value for the electron-ion production energy of $W_{ion} = 26.4$ eV [228]. This value, used in our simulation as well, was measured for gaseous argon in normal conditions,

C.1. ENERGY CALIBRATION

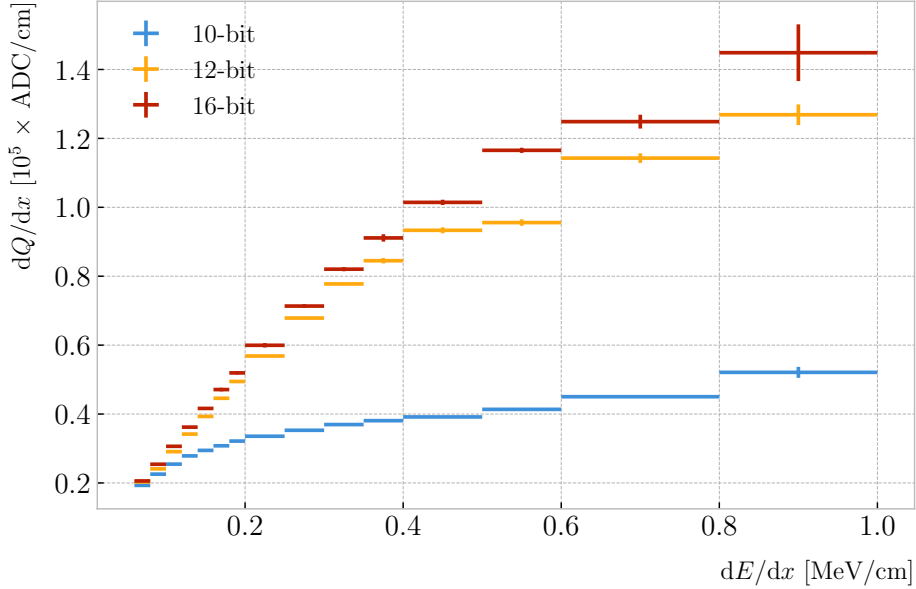


Figure C.5: Fitted most probable dQ/dx values for each dE/dx bin for three different ADC bit limits, 10 (blue points), 12 (default, yellow points) and 16-bit (red points).

and therefore should be checked in the future to describe correctly the high-pressure argon-CH₄ mixture of ND-GAr.

For the calibration fit I follow a procedure similar to the previous one for Eq. (C.1). Binning the dE/dx range, I fit a LanGauss function to the corresponding dQ/dx distribution to obtain the most probable value. The resulting data points (red bars) are shown in Fig. C.4 (top panel), the horizontal error bars depict the width of the dE/dx bin whereas the vertical bars represent the error associated to the most probable value estimation. A fit to the logarithmic function in Eq. (C.2) is also shown (black line). For this I weighted the data points using the inverse of their relative error, obtaining a reduced chi-square value of $\chi^2/ndf = 2.22 \times 10^{-6}$. The best fit parameters I found from this fit are $A = 0.883 \pm 0.064$, $B = 5.6 \pm 1.3$ cm/MeV and $C = 4.94 \pm 0.49$ ADC/e. Figure C.4 (bottom panel) shows the residuals between the data points and the fit.

The value for the gain I obtained from the fit is in reasonable agreement with our expectation. This value is set in GArSoft to 5 ADC/e by default.

One interesting thing to check is what induces this non-linear relation between charge and energy. The only effects that modify the amount of electrons reaching the readout

CHAPTER C. ADDITIONAL MATERIAL ON ND-GAr PID

Table C.1: Calibration parameters obtained from the fit of the ND-GAr simulated stopping proton sample to the calibration function from Eq. (C.2). The fits were performed for the 10, 12, and 16-bit **ADC** limits.

		Best fit $\pm 1\sigma$		
χ^2/ndf		<i>A</i>	<i>B</i> (cm/MeV)	<i>C</i> (ADC/e)
10-bit	$1.83 \times 10^{-6}/12$	-9.3 ± 3.9	270 ± 69	27.1 ± 5.4
12-bit	$2.67 \times 10^{-5}/12$	0.883 ± 0.064	5.6 ± 1.3	4.94 ± 0.49
16-bit	$1.44 \times 10^{-5}/12$	0.949 ± 0.024	3.53 ± 0.58	4.52 ± 0.29

planes in the simulation are the transverse diffusion and the finite electron lifetime. Once the electrons reach the readout chambers, the pad response functions are applied, together with an electrons-to-**ADC** conversion and the **ADC** saturation limit.

By default, GArSot applies a 12-bit **ADC** limit, which can be changed in the simulation configuration. However, it can only be increased up to 16-bit, as we represent the **ADC** collection as a `std::vector<short>`. This way, I tried to change the saturation parameter to see how it affects the relation between reconstructed charge and energy. Figure C.5 shows a comparison between the most probable dQ/dx for 10, 12 and 16-bit **ADC** limits. As expected, the lower the limit is the sooner the charge saturates. For higher **ADC** limits the relation between energy and charge remains linear up to higher dE/dx values, but even for the 16-bit limit the saturation is noticeable for ionisations ≥ 0.5 MeV/cm.

Table C.1 shows the results of fitting the samples with 10, 12, and 16-bits **ADC** limits to the calibration function from Eq. (C.2), using the weights based on their relative error as described previously. One interesting feature to notice is how different the best fit parameters look for the 10-bit **ADC** saturation when compared to the other two, which are consistent with each other.

At this point we can compare the dE/dx distribution one gets from **Geant4**, i.e. the true energy loss distribution, and the distribution I found by applying the calibration function to our collection of reconstructed dQ/dx values. Figure C.6 (top panel) shows the true (solid grey) and reconstructed (blue) distributions together. The dashed vertical

C.1. ENERGY CALIBRATION

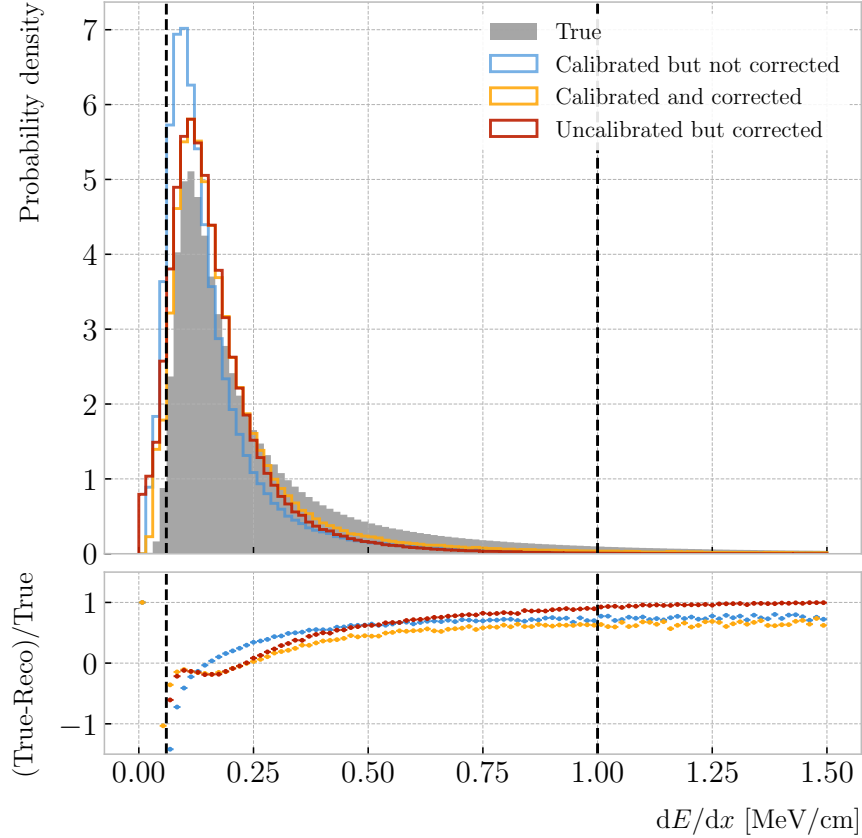


Figure C.6: Top panel: area normalised dE/dx distributions for the true (solid grey) and the reconstructed energy deposits in the stopping proton sample, both after applying the calibration (blue) and the calibration and the normalisation correction (yellow). Also shown is the distribution obtained by applying a correction factor to the dQ/dx values but not the calibration (red). Bottom panel: fractional residuals for the uncorrected (blue), corrected (yellow) and uncalibrated (red) samples.

lines indicate the region of validity of the calibration fit, i.e. the left and right edges of the first and last dE/dx bins, respectively. Notice that these histograms are area-normalised, as the total number of true energy deposits is much higher than the number of reconstructed charge deposits. This is due to a combination of effects, like the finite spatial resolution of the detector, the hit clustering used in the track fitting and the reclustering we have applied here.

The two distributions are significantly different. That can be seen clearly when looking at the fractional residuals, shown in Fig. C.6 (bottom panel). In particular, the position of the peak is off, which could bias the mean energy loss predictions. It

CHAPTER C. ADDITIONAL MATERIAL ON ND-GAr PID

seems like the difference between these may be due to an overall scaling factor. One possibility is to scale the most probable value of the reconstructed distribution to the most probable value predicted by **Geant4**. I do this by fitting both distributions using a LanGauss function, obtaining $dE/dx_{MPV, true} = 0.1145 \pm 0.0005$ MeV/cm and $dE/dx_{MPV, reco} = 0.0928 \pm 0.0005$ MeV/cm for the true and reconstructed most probable values, respectively. These can be translated into an scaling factor $S = 0.579 \pm 0.006$.

The result of applying the scaling correction can be seen in Fig. C.6 (top panel). The calibrated and corrected dE/dx distribution (yellow) peaks around the same value the true distribution does, as expected. Moreover, the high energy region is also slightly better described. For low ionisations, below the lower limit of the calibration fit, the differences between true and reconstructed are still significant. This low energy excess may be a migration of some events from the peak region. The overall effect of the correction can be seen in the fractional residual plot in Fig. C.6 (bottom panel).

One can also check what happens if instead of applying the logarithmic calibration we simply scale the dQ/dx distribution (after reclustering) to have the same most probable value as the true dE/dx distribution. In this case, following an analogous procedure to the one described earlier, I found the scaling factor $S_{uncalibrated} = 0.414 \pm 0.002$ MeV/ADC³. The resulting uncalibrated but corrected distribution (red) is also shown in in Fig. C.6 (top panel). The behaviour of the new distribution is similar to the corrected case at low energy losses, around the peak of the true distribution, but it is worse at describing the high energy tail. This is expected, as it is in the high ionisation regime where saturation effects apply and therefore calibration is needed.

C.2 Charged pion decay in flight

As discussed previously, in GArSoft the **HPgTPC** tracks are formed after a pattern recognition algorithm and a Kalman filter are applied to the **TPC** clusters. These two steps can find discontinuities in the track candidates (e.g. due to a particle decay) when

³Notice that now the scaling factor is not dimensionless, as it acts like a conversion factor here.

C.2. CHARGED PION DECAY IN FLIGHT

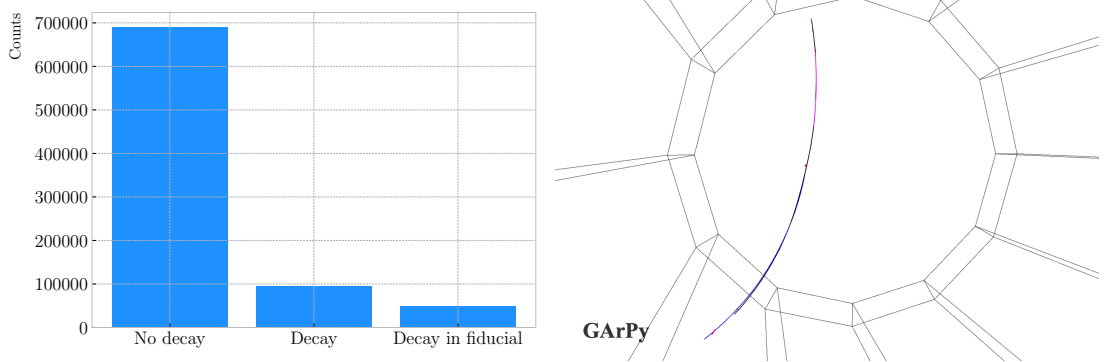


Figure C.7: Left panel: number of non-decaying, decaying and decaying in the fiducial volume pions for a MC sample of 10^5 , $p = 500$ MeV/c isotropic positively charged pions inside the TPC. Right panel: event display for a positive pion decaying inside the fiducial volume, with a single reconstructed track for the pion and muon system.

these so-called breakpoints are large enough. However, for some, more subtle, cases they may miss them and form a single reconstructed track. It has been noted in the literature that Kalman filters offer, as a by-product, additional information to form test statistics to identify these breakpoints [229, 230].

Considering the mean life of the charged pion, $\tau = (2.6033 \pm 0.0005) \times 10^{-8}$ s, one can estimate that about 12% of the pions with momentum $p \sim \mathcal{O}(500 \text{ MeV}/c)$ (roughly the peak of the pion momentum distribution in ν_μ CC interactions off argon) decay inside the TPC. Figure C.7 (left panel) shows the amount of charged pions decaying in the full and fiducial HPgTPC volumes from an isotropic, monoenergetic sample of 10^5 negatively charged pions with $p = 500$ MeV/c. We see that about 10% of those decayed, with more than half of them decaying inside the TPC fiducial volume.

Figure C.7 (right panel) shows an example event display of a charged pion (magenta line) which decays in flight inside the TPC. However, because the angle of the muon (blue line) is small both were reconstructed as one single track (black line). In this case, the composite track reaches the ECal, where it undergoes a muon-like interaction, thus being classified as a muon.

A way to understand what decaying pion tracks were totally or partially reconstructed together with the daughter muon is looking at the relative energy contributions to the reconstructed track. In order to select a sample of such events, I require that a minimum

CHAPTER C. ADDITIONAL MATERIAL ON ND-GAr PID

50% of the total energy comes from the pion and at least 20% from the muon.

C.2.1 Track breakpoints

To identify potential decays we can use the information we obtain from the Kalman filter at each step of the fitted track. The simplest test we can think about is computing the χ^2 of the mismatch between all the parameters in the forward and the backward fits:

$$\chi_k^{2(FB)} = (\hat{x}_k^B - \hat{x}_k^F)^T [V^{(\hat{x}_k, B)} + V^{(\hat{x}_k, F)}]^{-1} (\hat{x}_k^B - \hat{x}_k^F), \quad (\text{C.3})$$

where \hat{x}_k^F , \hat{x}_k^B are the Kalman filter state vector estimates at step k in the forward and backward fits, and $V^{(\hat{x}_k, F)}$, $V^{(\hat{x}_k, B)}$ the covariance matrices of \hat{x}_k^F and \hat{x}_k^B , respectively. Using the values of the χ^2 at measurement k for the forward and backward fits we can compute another χ^2 value that characterises the overall track fit:

$$\chi_{track}^2 = \chi_k^{2(F)} + \chi_k^{2(B)} + \chi_k^{2(FB)}, \quad (\text{C.4})$$

which remains approximately constant for all k .

An alternative approach proposed in the context of the [NOMAD](#) experiment was using a fit with a more elaborated breakpoint hypothesis, so we can perform a comparison of the χ^2 with and without breakpoints. This can be achieved by using an alternative parametrisation, which allows some of the track parameters to be discontinuous at certain points. A decay changes the momentum magnitude and direction, so we can use the new state vector:

$$\alpha = (y, z, 1/R_F, 1/R_B, \phi_F, \phi_B, \tan\lambda_F, \tan\lambda_B)^T. \quad (\text{C.5})$$

As we already have the estimates from the standard Kalman filter and their covariance matrices at each point, we do not need to repeat the Kalman fit for the new parametrisation. Instead, I can compute the values of α at each point k that minimise

C.2. CHARGED PION DECAY IN FLIGHT

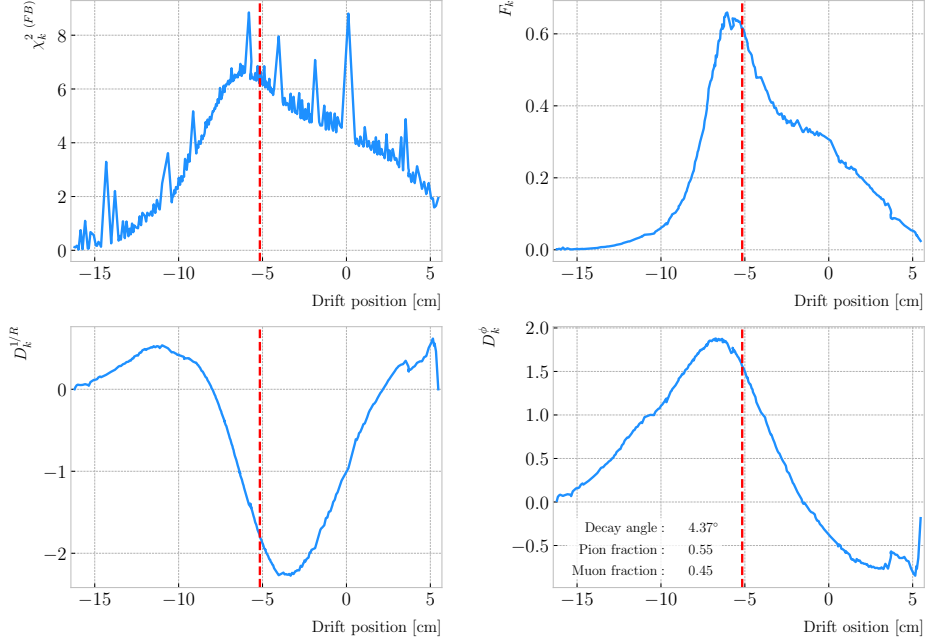


Figure C.8: Values of $\chi_k^2(FB)$ (top left panel), F_k (top right panel), $D_k^{1/R}$ (bottom left panel) and D_k^ϕ (bottom right panel) versus position along the drift direction for a reconstructed track in a positive pion decay event. The vertical red dashed line indicates the true location of the decay point.

the χ^2 resulting from comparing them to $\{\hat{x}_k^B, \hat{x}_k^F\}$. Introducing the two 5×8 matrices:

$$H^F = \begin{pmatrix} 1 & 0 & 0 & 0 & 0 & 0 & 0 & 0 \\ 0 & 1 & 0 & 0 & 0 & 0 & 0 & 0 \\ 0 & 0 & 1 & 0 & 0 & 0 & 0 & 0 \\ 0 & 0 & 0 & 0 & 1 & 0 & 0 & 0 \\ 0 & 0 & 0 & 0 & 0 & 0 & 1 & 0 \end{pmatrix}, \quad H^B = \begin{pmatrix} 1 & 0 & 0 & 0 & 0 & 0 & 0 & 0 \\ 0 & 1 & 0 & 0 & 0 & 0 & 0 & 0 \\ 0 & 0 & 0 & 1 & 0 & 0 & 0 & 0 \\ 0 & 0 & 0 & 0 & 0 & 1 & 0 & 0 \\ 0 & 0 & 0 & 0 & 0 & 0 & 0 & 1 \end{pmatrix}, \quad (C.6)$$

we can write this as:

$$\begin{aligned} \chi_k^2(FB)(\alpha) &= (\hat{x}_k^F - H^F \alpha)^T \left[V^{(\hat{x}_k, F)} \right]^{-1} (\hat{x}_k^F - H^F \alpha) \\ &\quad + (\hat{x}_k^B - H^B \alpha)^T \left[V^{(\hat{x}_k, B)} \right]^{-1} (\hat{x}_k^B - H^B \alpha). \end{aligned} \quad (C.7)$$

The minimum of $\chi_k^2(FB)(\alpha)$ is found when the measured new state vector takes the value:

$$\hat{\alpha}_k = V^{(\hat{\alpha}_k)} H^T (V^{(\hat{x}_k)})^{-1} \hat{X}, \quad (C.8)$$

CHAPTER C. ADDITIONAL MATERIAL ON ND-GAr PID

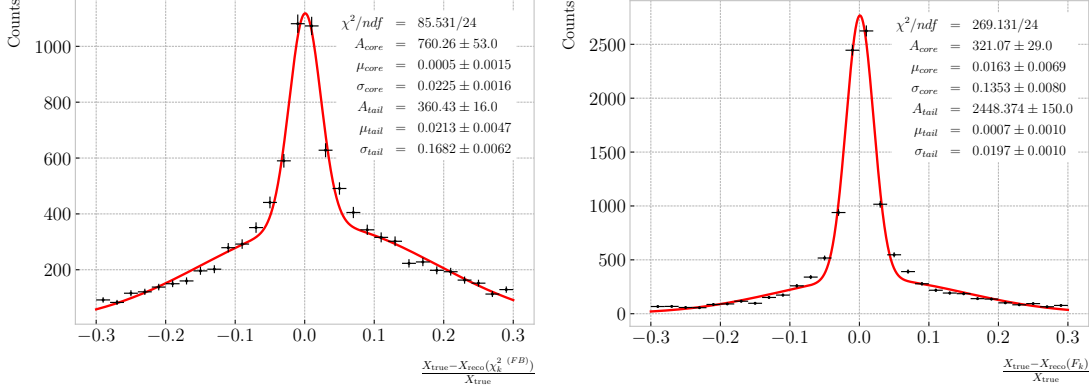


Figure C.9: Fractional residual distributions of the true and reconstructed decay position along the drift coordinate, using the position of the maximum of $\chi_k^2(FB)$ (left panel) and F_k (right panel) as estimates of the decay position. Also shown are double Gaussian fits to these points (red lines).

where $\hat{\mathbf{X}} = \{\hat{\mathbf{x}}_k^B, \hat{\mathbf{x}}_k^F\}$, $V^{(\hat{\mathbf{x}}_k)}$ is the block diagonal matrix formed by $V^{(\hat{\mathbf{x}}_k, F)}$ and $V^{(\hat{\mathbf{x}}_k, B)}$ and $V^{(\hat{\alpha}_k)}$ is the covariance matrix of $\hat{\alpha}_k$, given by:

$$V^{(\hat{\alpha}_k)} = \left(H^T (V^{(\hat{\mathbf{x}}_k)})^{-1} H \right)^{-1}. \quad (\text{C.9})$$

From these new fit estimates we can compute the F statistic, which tells us whether the model with breakpoint provides a statistically significant better fit:

$$F_k = \left(\frac{\chi_{\text{track},k}^2 - \chi_{\text{full},k}^2}{8 - 5} \right) / \left(\frac{\chi_{\text{full},k}^2}{N - 8} \right). \quad (\text{C.10})$$

One can also compute the signed difference of the duplicated variables divided by their standard deviation at each point. These represent how significant the discontinuity in each variable is. For any variable η we can write it as:

$$D_k^\eta = \frac{\hat{\eta}_k^B - \hat{\eta}_k^F}{\sqrt{\text{Var}[\hat{\eta}_k^F] + \text{Var}[\hat{\eta}_k^B] - 2\text{Cov}[\hat{\eta}_k^F, \hat{\eta}_k^B]}}. \quad (\text{C.11})$$

In our case, the relevant ones to look at are $D_k^{1/R}$ and D_k^ϕ .

Figure C.8 shows the values of $\chi_k^2(FB)$, F_k , $D_k^{1/R}$ and D_k^ϕ as functions of the position along the drift direction, for an example reconstructed track with 55.5% of the energy

C.2. CHARGED PION DECAY IN FLIGHT

coming from the charged pion and 45.5% from the daughter muon. The true position of the decay is indicated (dashed red lines). Notice how $\chi_k^2(FB)$ and F_k , $D_k^{1/R}$ reach their maxima near the decay point. In the former case this indicates a large forward-backward difference in the track fit. In the later it represents that the extended state vector improves the fit particularly around that point.

I can estimate the decay position finding resolution by computing the difference between the X position of the maxima of $\chi_k^2(FB)$ and F_k and the X position of the true decay. Figure C.9 represents the fractional residual distributions for both cases, from the sample of tracks containing pion decays. Fitting a double Gaussian to the distributions (red lines) I find a resolution of $(3.31 \pm 0.15)\%$ and $(6.94 \pm 0.31)\%$ respectively.

In principle, the F -statistic should follow a Fisher distribution with $(8 - 5)$ and $(N - 8)$ degrees of freedom under the null hypothesis. In most of our cases $N \sim \mathcal{O}(100)$, so the probability density functions will look very similar. In this case, it is safe to take the limit $N \rightarrow \infty$ in the Fisher PDF:

$$\begin{aligned}\tilde{f}(x; a - b) &= \lim_{N \rightarrow \infty} f(x; a - b, N - a) \\ &= \frac{2^{-\frac{a-b}{2}}}{\Gamma\left(\frac{a-b}{2}\right)} (a - b)^{\frac{a-b}{2}} x^{\frac{a-b}{2}-1} e^{-\frac{a-b}{2}x}.\end{aligned}\tag{C.12}$$

In our case $a - b = 8 - 5 = 3$, so we would obtain a p-value of 0.05 at $x = 2.60$.

Figure C.10 contains the distributions of the maxima of $\chi_k^2(FB)$, F_k and D_k^ϕ and the minima of $D_k^{1/R}$ for a sample of non-decaying pion tracks (blue) and another sample of reconstructed tracks containing part of the pion and the daughter muon from a decay inside the fiducial volume (red). Notice that, even though the values of $F_k^{(max)}$ for the decay sample are typically larger than for the non-decaying one, just a small fraction of the events go beyond the aforementioned value of $F = 2.60$. Therefore, from a practical point of view, it is not the most efficient variable to use for selecting the decay events.

However, looking at the $D_k^{1/R \text{ (min)}}$ distribution we can see there is a big difference between non-decaying and decaying events in this variable. One can use a combination of these four variables to distinguish between the pion decay events (signal) and the

CHAPTER C. ADDITIONAL MATERIAL ON ND-GAr PID

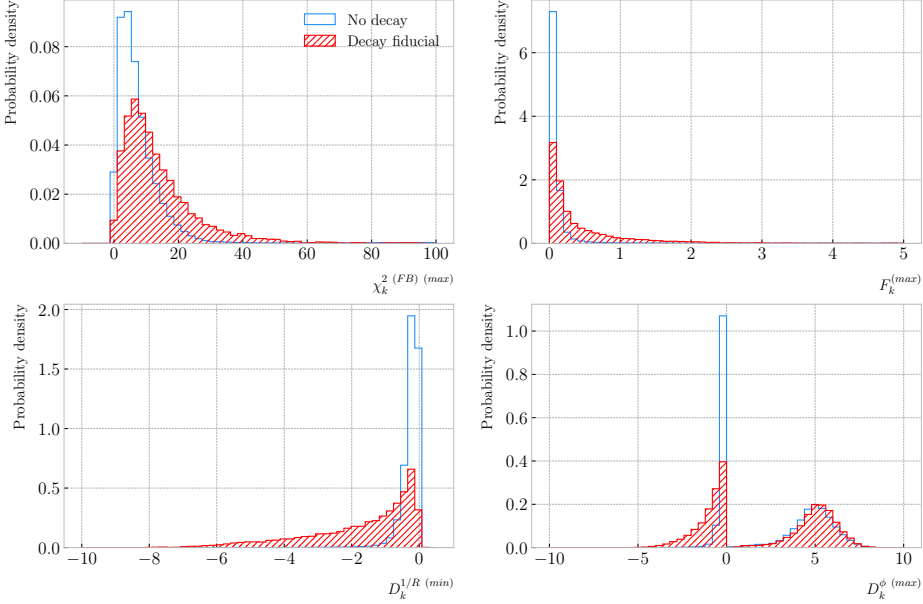


Figure C.10: Distributions of the extrema of $\chi_k^2(FB)$ (top left panel), F_k (top right panel), $D_k^{1/R}$ (bottom left panel) and D_k^ϕ (bottom right panel) for non-decaying reconstructed pion tracks (blue) and tracks which include the decay inside the fiducial volume (red).

non-decaying pions (background).

An approach to this classification could be using a **BDT**. Training a **BDT** with 400 estimators and a maximum depth of 4 I can obtain an efficient classification without overtraining. Figure C.11 (left panel) shows the distribution of probabilities predicted by the **BDT** for a test sample. The signal efficiency as a function of background acceptance, the so-called ROC curve, is shown in Fig. C.11 (right panel). With a relative importance of 0.83, the most important variable turned out to be $D_k^{1/R} \text{ (min)}$.

One thing we can check is how the resolution to the decay and the signal efficiency in the classification changes with the true decay angle. Using an equal-frequency binning for the decay angles, we can repeat the previous steps for each bin.

Figure C.12 (left panel) shows the dependence on the decay angle of the decay finding resolution. We can see that for the $\chi_k^2(FB)$ maximum location method the resolution consistently lies between 12 to 16%. However, the $F_k^{(max)}$ approach gives a significantly better resolution for high angle values, reaching the 4 – 6% range for decay angles $\geq 4^\circ$.

C.2. CHARGED PION DECAY IN FLIGHT

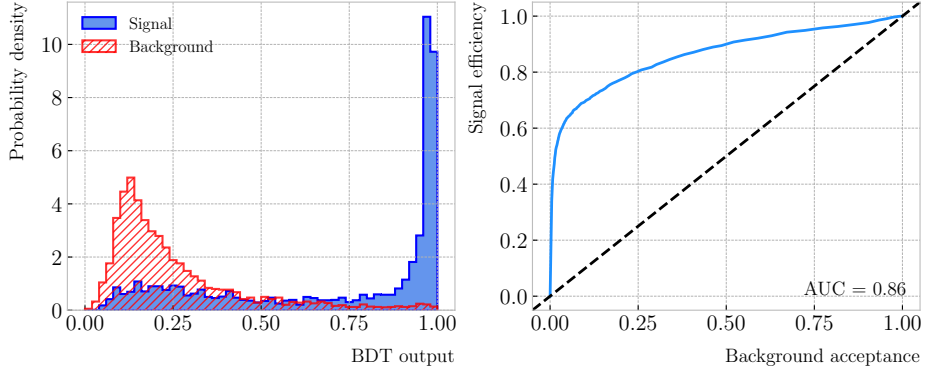


Figure C.11: Left panel: distributions of the predicted probabilities assigned by the **BDT** classifier for a test sample of decaying pion+muon tracks (blue) and non-decaying pion tracks (red). Left: signal efficiency versus background acceptance (ROC curve) obtained from the **BDT** for the test sample.

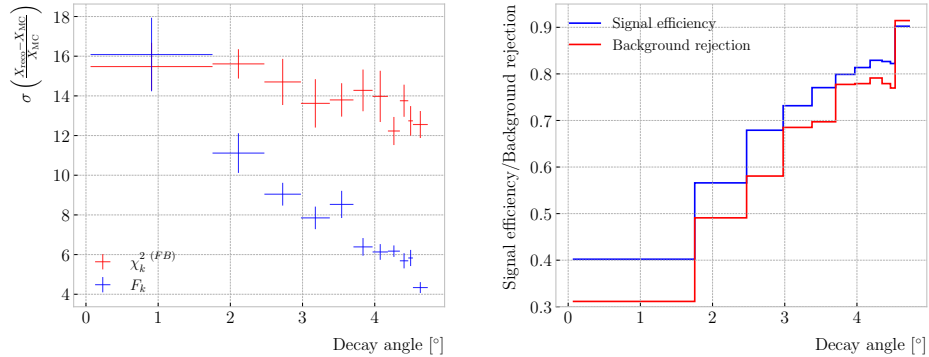


Figure C.12: Left panel: dependence of the decay position finding resolution on the true value of the decay angle for the $\chi_k^2(FB)$ (red) and F_k (blue) methods. Right panel: signal efficiency (blue line) and background rejection (red line) from the **BDT** classifier versus true decay angle.

For the classification dependence on the angle, I use the same classifier I trained before but evaluating the test sample for each individual angular bin. I compute the signal efficiency in each bin for a fixed value of the background rejection, in this case 90%. Similarly, for the background rejection estimation I use a fixed signal efficiency value of 90%. Figure C.12 (right panel) represents the change in signal efficiency (blue) and background rejection (red) with the value of the true decay angles.

C.3 Neutral particle identification

C.3.1 ECal clustering

Another important reconstruction item is the clustering algorithm of [ECal](#) hits in GArSoft. The default module features a [NN](#) algorithm that treats all hits in the same way, independently of the layer each hit comes from. However, the current [ECal](#) design of [ND-GAr](#) has two very different types of scintillator layers. The inner layers are made out of tiles, which provide excellent angular and timing resolutions. On the other hand, the outer layers are cross scintillator strips. That way, an algorithm that treats hits from both kinds of layers differently may be able to improve the current performance.

Inspired by the reconstruction of [T2K](#)'s ND280 downstream [ECal](#) [231], the idea was to put together a clustering module that first builds clusters for the different [ECal](#) views (tiles, strips segmented in the x direction and strips segmented in y direction), and then tries to match them together to form the final clusters.

Working on a module-by-module basis, the algorithm separates the hits depending on the layer type they come from. Then, it performs a [NN](#) clustering for the 3 sets of hits separately. For the tile hits it clusters together all the hits which are in nearest-neighbouring tiles and nearest-neighbouring layers. For strip hits it looks at nearest-neighbouring strips and next-to-nearest-neighbouring layers (as the layers with strips along the two directions are alternated). For strip clusters an additional cut in the direction along the strip length is needed.

After this first clustering I then apply a recursive re-clustering for each collection of strip clusters based on a PCA method. In each case, the algorithm loops over the clusters with $N_{hits} \geq 2$, computing the centre of mass and three principal components. Propagating these axes up to the layers of the rest of the clusters, we check if the propagated point and the centre of mass of the second cluster are within next-to-nearest-neighbouring strips. An additional cut in the direction along the strip length is also needed. Moreover, I require that the two closest hits across the two clusters are at most

C.3. NEUTRAL PARTICLE IDENTIFICATION

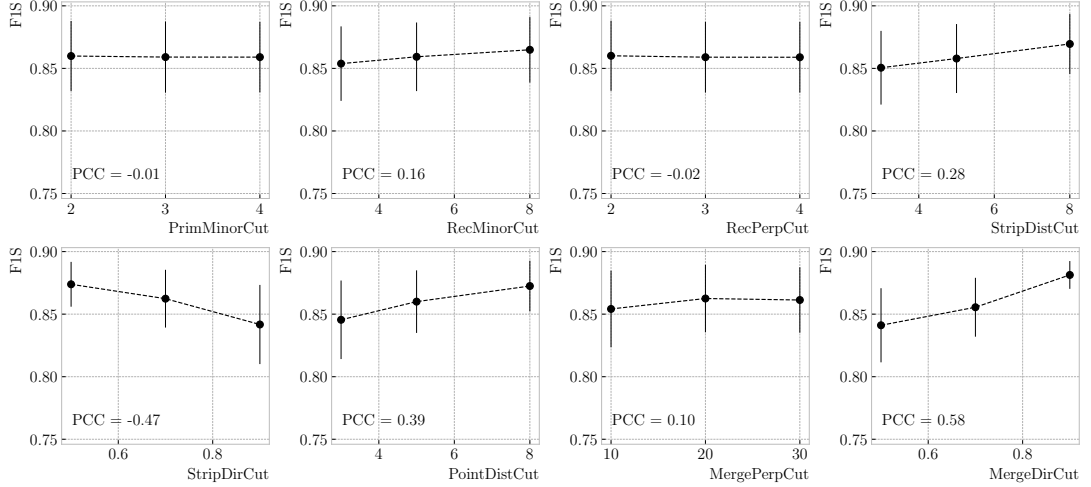


Figure C.13: Mean values of the F_1 -score marginal distributions for the different free parameters of the new clustering algorithm, with the error bars representing one standard deviation around the mean. The F_1 -score values were computed for the 6561 possible parameter configurations using 1000 ν_μ CC interaction events.

in next-to-nearest-neighbouring strips. I merge the clusters if these three conditions are satisfied. The re-clustering is repeated until no more cluster pairs pass the cuts.

The clusters in each strip view are combined if their centres of mass are close enough and they point in the same direction. An alternative approach for the strip cluster merging could be to compute the overlap between the ellipsoids defined by the principal axes of the clusters, and then merge the pair if the overlap exceeds some threshold. Further study is needed to understand if this change would have an impact in the overall clustering performance.

To merge the tile clusters to the combined strip clusters, I propagate the principal axis of the strip cluster towards the inner layers, up to the centre of mass layer of the tile cluster. I merge the clusters if the distance between the propagated point and the centre of mass is below a certain cut.

The last step is to check if clusters in neighbouring modules should be merged together, both across two barrel modules, across end cap modules and between barrel end cap modules. I check the distance between the two closest hits in the pair of clusters and merge them if it passes this and an additional directional cut.

CHAPTER C. ADDITIONAL MATERIAL ON ND-GAr PID

Table C.2: Summary of parameters and sampled values used in the optimisation of the clustering algorithm.

Name	Units	Sampled values	Description
PrimMinorCut	strips	2, 3, 4	Distance along strip length in NN clustering
RecMinorCut	strips	3, 5, 8	Distance between propagated point and CM along strip length in re-clustering
RecPerpCut	strips	2, 3, 4	Closest hit pair distance in re-clustering
StripDistCut	strips	3, 5, 8	Distance between CMs in strip cluster merging
StripDirCut	cos	0.5, 0.7, 0.9	Main axes direction cut in strip cluster merging
PointDistCut	tiles	3, 5, 8	Distance between propagated point and CM in strip-tile matching
MergePerpCut	cm	10, 20, 30	Closest hit pair distance in module merging
MergeDirCut	cos	0.5, 0.7, 0.9	Main axes direction cut in module merging

This algorithm has a total number of eight free parameters that need to be optimised.

I used a sample of 1000 ν_μ [CC](#) interactions in order to obtain the optimal configuration of clustering parameters. This sample was generated up to the default [ECal](#) hit clustering level, so then I could run the new clustering algorithm each time with a different configuration of parameters. As the number of parameters is relatively large, I only performed a coarse-grained scan of the parameter space. Sampling each of the eight parameters at three different points each I obtain 6561 different configurations. These parameters, together with the used values, are summarised in Tab. [C.2](#).

In order to measure the performance of the clustering, I use a binary classification approach. For each formed cluster, I identify the [Geant4](#) Track ID of the matching [MC](#) particle and the energy fraction of each hit. Then, I assign to each cluster the Track ID with the highest total energy fraction. For each of the different Track IDs associated to the clusters, I select the cluster with the highest energy (only from the hits with the same Track ID). I identify such a cluster as the main cluster for that Track ID. I count as true positives (TPs) the hits with the correct Track ID in each main cluster. False positives (FPs) are the hits with the incorrect Track ID for the cluster they are in, not only main clusters. The false negatives (FNs) are the hits with the correct Track ID in

C.3. NEUTRAL PARTICLE IDENTIFICATION

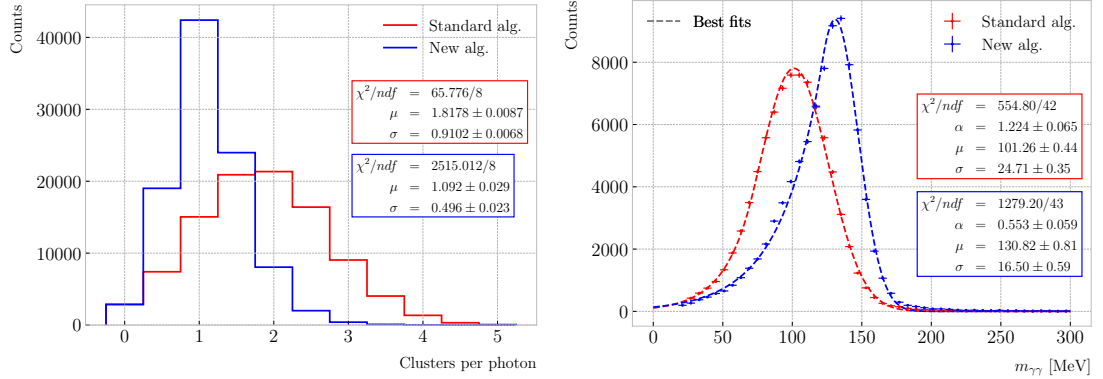


Figure C.14: Left panel: distributions of the number of ECal clusters per photon from π^0 decays for the standard (red) and new (blue) clustering algorithms. Right panel: reconstructed invariant mass distributions for photon pairs from single π^0 events using the standard (red) and new (blue) ECal clustering algorithms.

clusters other than the main.

Figure C.13 shows the computed F_1 -score values for the different cuts. In each case, the central value represents the mean of the F_1 -score distribution for the specified value of the corresponding variable, and the vertical error bar represents one standard deviation around the mean. Also shown are the Pearson correlation coefficients of these central values. We can see that five of the variables have a sizeable effect on the F_1 -score, with an absolute difference between the last and first values as big as 4%.

The working configuration is obtained as follows. I first select all configurations with purity $\geq 90\%$. Among those, I choose the combinations that yield the maximum F_1 -score. If more than one configuration remains, I select the one with the highest sensitivity. Doing so, I end up with a parameter configuration with an efficiency of 88% and a 90% purity. Compared with the default algorithm, which gives an efficiency of 76% and a purity of 91% for the same sample, I have managed to improve the efficiency by a factor of 1.16.

C.3.2 π^0 reconstruction

One of the potential applications of the new ECal hit clustering is the reconstruction of neutral particles, in particular pions. Neutral pions decay promptly after being produced,

CHAPTER C. ADDITIONAL MATERIAL ON ND-GAr PID

through the $\pi^0 \rightarrow \gamma\gamma$ channel ($98.823 \pm 0.034\%$) of the time [52]. The photon pair does not leave any traces in the [HPgTPC](#) (unless one or both of them converts into an electron-positron pair), but each of them will produce an electromagnetic shower in the [ECal](#).

To test the potential impact of the new algorithm on the π^0 reconstruction, I generated a [MC](#) sample of single, isotropic neutral pions inside the [HPgTPC](#). All pions were generated with a momentum of 500 MeV/ c , and their initial positions were uniformly sampled inside a $2 \times 2 \times 2$ m box aligned with the centre of the [HPgTPC](#). I ran both the default and the new clustering algorithms, using for the latter the optimised configuration discussed above.

The first thing to notice is that the number of clusters produced per photon has decreased. Figure C.14 (left panel) shows these distributions for the default (red) and new (blue) algorithms. Using a simple Gaussian fit, we see that the mean number of [ECal](#) clusters per photon went from 1.82 ± 0.01 to 1.09 ± 0.03 . This effectively means that with the new algorithm the [ECal](#) activity of one true particle is typically reconstructed as a single object. From the reconstruction point of view this can be an advantage. As now most of the photon energy ends up in a single [ECal](#) cluster, I can simply use cluster pairs to identify the π^0 decay.

In general, one calculates the invariant mass of the photon pair as:

$$m_{\gamma\gamma} = \sqrt{2E_1E_2(1 - \cos \theta)}, \quad (\text{C.13})$$

where E_i are the energies of the photons and θ the opening angle between them. In this case, I can use the energies deposited in the [ECal](#) and their incident directions. This quantity is computed for all possible pairs of clusters, using their position together with the true decay point. In a more realistic scenario, e.g. ν_μ [CC](#) interaction, one could use the position of the reconstructed primary vertex instead. I also tried to use the principal direction of the clusters, but that approach gave considerably worse results. For each event, I only keep the pair with the invariant mass closest to the true π^0 mass value.

C.3. NEUTRAL PARTICLE IDENTIFICATION

Figure C.14 (right panel) shows the invariant mass distributions for the photon pairs I get using the default (red) and the new (blue) ECal clustering algorithms. For the fit I use a modified version of the Crystal Ball function [180], obtained by taking the limit where the parameter controlling the power-law tail goes to infinity:

$$f(x; N, \mu, \sigma, \alpha) = N \cdot \begin{cases} e^{\frac{\alpha(2x-2\mu+\alpha\sigma)}{2\sigma}}; & x \leq \mu - \alpha\sigma, \\ e^{-\frac{(x-\mu)^2}{2\sigma^2}}; & x > \mu - \alpha\sigma. \end{cases} \quad (\text{C.14})$$

Comparing the fitted mean and standard deviation values for the Gaussian cores, we see that the distribution for the new algorithm is a 67% narrower and also peaks much closer to the true m_{π^0} value, going from 101.3 ± 0.4 MeV to 130.8 ± 0.6 MeV.

Bibliography

- [1] S.L. Glashow, *Partial-symmetries of weak interactions*, *Nuclear Physics* **22** 579. 33, 35
- [2] S. Weinberg, *A model of leptons*, *Physical Review Letters* **19** 1264. 33, 35
- [3] A. Salam, *Weak and Electromagnetic Interactions*, *Conf. Proc. C* **680519** (1968) 367. 33, 35
- [4] J. Erler and M. Schott, *Electroweak Precision Tests of the Standard Model after the Discovery of the Higgs Boson*, *Prog. Part. Nucl. Phys.* **106** (2019) 68 [[1902.05142](#)]. 33
- [5] L. Canetti, M. Drewes and M. Shaposhnikov, *Matter and Antimatter in the Universe*, *New J. Phys.* **14** (2012) 095012 [[1204.4186](#)]. 33
- [6] G. Bertone, D. Hooper and J. Silk, *Particle dark matter: Evidence, candidates and constraints*, *Phys. Rept.* **405** (2005) 279 [[hep-ph/0404175](#)]. 33
- [7] S.F. King, A. Merle, S. Morisi, Y. Shimizu and M. Tanimoto, *Neutrino Mass and Mixing: from Theory to Experiment*, *New J. Phys.* **16** (2014) 045018 [[1402.4271](#)]. 33
- [8] A.D. Sakharov, *Violation of CP Invariance, C asymmetry, and baryon asymmetry of the universe*, *Pisma Zh. Eksp. Teor. Fiz.* **5** (1967) 32. 33
- [9] M.B. Gavela, P. Hernandez, J. Orloff and O. Pene, *Standard model CP violation and baryon asymmetry*, *Mod. Phys. Lett. A* **9** (1994) 795 [[hep-ph/9312215](#)]. 33

BIBLIOGRAPHY

- [10] E.K. Akhmedov, V.A. Rubakov and A.Y. Smirnov, *Baryogenesis via neutrino oscillations*, *Phys. Rev. Lett.* **81** (1998) 1359 [[hep-ph/9803255](#)]. 33
- [11] B.W. Lee and S. Weinberg, *Cosmological Lower Bound on Heavy Neutrino Masses*, *Phys. Rev. Lett.* **39** (1977) 165. 34
- [12] G. Jungman, M. Kamionkowski and K. Griest, *Supersymmetric dark matter*, *Phys. Rept.* **267** (1996) 195 [[hep-ph/9506380](#)]. 34
- [13] G. Arcadi, D. Cabo-Almeida, M. Dutra, P. Ghosh, M. Lindner, Y. Mambrini et al., *The Waning of the WIMP: Endgame?*, [2403.15860](#). 34
- [14] DUNE collaboration, *Deep Underground Neutrino Experiment (DUNE), Far Detector Technical Design Report, Volume I Introduction to DUNE*, *JINST* **15** (2020) T08008 [[2002.02967](#)]. 34, 61, 62, 63, 69, 79, 80, 81, 82
- [15] W. Pauli, *Dear radioactive ladies and gentlemen*, *Phys. Today* **31N9** (1978) 27. 35
- [16] F. Reines and C.L. Cowan, *Detection of the free neutrino*, *Phys. Rev.* **92** (1953) 830. 35
- [17] C.A. Argüelles et al., *New opportunities at the next-generation neutrino experiments I: BSM neutrino physics and dark matter*, *Rept. Prog. Phys.* **83** (2020) 124201 [[1907.08311](#)]. 35
- [18] A. Pich, *The Standard Model of Electroweak Interactions*, in *2010 European School of High Energy Physics*, pp. 1–50, 1, 2012 [[1201.0537](#)]. 36, 38
- [19] M. Goldhaber, L. Grodzins and A.W. Sunyar, *Helicity of neutrinos*, *Physical Review* **109** 1015. 36
- [20] F. Englert and R. Brout, *Broken symmetry and the mass of gauge vector mesons*, *Physical Review Letters* **13** 321. 38
- [21] P.W. Higgs, *Broken symmetries and the masses of gauge bosons*, *Physical Review Letters* **13** 508. 38

BIBLIOGRAPHY

- [22] G.S. Guralnik, C.R. Hagen and T.W.B. Kibble, *Global conservation laws and massless particles*, *Physical Review Letters* **13** 585. 38
- [23] ALEPH, DELPHI, L3, OPAL, SLD, LEP ELECTROWEAK WORKING GROUP, SLD ELECTROWEAK GROUP, SLD HEAVY FLAVOUR GROUP collaboration, *Precision electroweak measurements on the Z resonance*, *Phys. Rept.* **427** (2006) 257 [[hep-ex/0509008](#)]. 39
- [24] E.G. Adelberger et al., *Solar fusion cross sections II: the pp chain and CNO cycles*, *Rev. Mod. Phys.* **83** (2011) 195 [[1004.2318](#)]. 40
- [25] R. Davis, D.S. Harmer and K.C. Hoffman, *Search for neutrinos from the sun*, *Physical Review Letters* **20** 1205. 40
- [26] J.N. Bahcall, A.M. Serenelli and S. Basu, *New solar opacities, abundances, helioseismology, and neutrino fluxes*, *Astrophys. J. Lett.* **621** (2005) L85 [[astro-ph/0412440](#)]. 41, 253, 255
- [27] J.N. Bahcall, N.A. Bahcall and G. Shaviv, *Present Status of the Theoretical Predictions for the ^{37}Cl Solar-Neutrino Experiment*, *Physical Review Letters* **20** 1209. 40
- [28] B.T. Cleveland, T. Daily, R. Davis, Jr., J.R. Distel, K. Lande, C.K. Lee et al., *Measurement of the solar electron neutrino flux with the Homestake chlorine detector*, *Astrophys. J.* **496** (1998) 505. 40
- [29] SAGE collaboration, *Measurement of the solar neutrino capture rate with gallium metal. III: Results for the 2002–2007 data-taking period*, *Phys. Rev. C* **80** (2009) 015807 [[0901.2200](#)]. 40, 53
- [30] F. Kaether, W. Hampel, G. Heusser, J. Kiko and T. Kirsten, *Reanalysis of the GALLEX solar neutrino flux and source experiments*, *Phys. Lett. B* **685** (2010) 47 [[1001.2731](#)]. 40, 53

BIBLIOGRAPHY

- [31] Q.R. Ahmad, R.C. Allen, T.C. Andersen, J.D. Anglin, G. Bühler, J.C. Barton et al., *Measurement of the Rate of $\nu_e + d \rightarrow p + p + e^-$ Interactions Produced by 8B Solar Neutrinos at the Sudbury Neutrino Observatory*, *Physical Review Letters* **87** 071301. 41
- [32] Q.R. Ahmad, R.C. Allen, T.C. Andersen, J. D. Anglin, J.C. Barton, E.W. Beier et al., *Direct Evidence for Neutrino Flavor Transformation from Neutral-Current Interactions in the Sudbury Neutrino Observatory*, *Physical Review Letters* **89** 011301. 41
- [33] T.K. Gaisser and M. Honda, *Flux of atmospheric neutrinos*, *Annual Review of Nuclear and Particle Science* **52** 153. 42
- [34] K. Hirata, T. Kajita, M. Koshiba, M. Nakahata, S. Ohara, Y. Oyama et al., *Experimental study of the atmospheric neutrino flux*, *Physics Letters B* **205** 416. 42
- [35] D. Casper, R. Becker-Szendy, C.B. Bratton, D.R. Cady, R. Claus, S.T. Dye et al., *Measurement of atmospheric neutrino composition with the IMB-3 detector*, *Physical Review Letters* **66** 2561. 42
- [36] M. Ambrosio, R. Antolini, C. Aramo, G. Auriemma, A. Baldini, G. C. Barbarino et al., *Measurement of the atmospheric neutrino-induced upgoing muon flux using MACRO*, *Physics Letters B* **434** 451. 42
- [37] W. Allison, G. Alner, D. Ayres, W. Barrett, C. Bode, P. Border et al., *Measurement of the atmospheric neutrino flavour composition in soudan 2*, *Physics Letters B* **391** 491. 42
- [38] SUPER-KAMIOKANDE collaboration, *Evidence for oscillation of atmospheric neutrinos*, *Phys. Rev. Lett.* **81** (1998) 1562 [[hep-ex/9807003](#)]. 42, 43
- [39] M.C. Gonzalez-Garcia and M. Maltoni, *Phenomenology with Massive Neutrinos*, *Phys. Rept.* **460** (2008) 1 [[0704.1800](#)]. 43

BIBLIOGRAPHY

- [40] P. Minkowski, *$\mu \rightarrow e\gamma$ at a Rate of One Out of 10^9 Muon Decays?*, *Phys. Lett. B* **67** (1977) 421. 45
- [41] M. Gell-Mann, P. Ramond and R. Slansky, *Complex Spinors and Unified Theories*, *Conf. Proc. C* **790927** (1979) 315 [[1306.4669](#)]. 45
- [42] T. Yanagida, *Horizontal gauge symmetry and masses of neutrinos*, *Conf. Proc. C* **7902131** (1979) 95. 45
- [43] R.N. Mohapatra and G. Senjanovic, *Neutrino Mass and Spontaneous Parity Nonconservation*, *Phys. Rev. Lett.* **44** (1980) 912. 45
- [44] J. Schechter and J.W.F. Valle, *Neutrino Masses in $SU(2) \times U(1)$ Theories*, *Phys. Rev. D* **22** (1980) 2227. 45
- [45] B. Pontecorvo, *Mesonium and anti-mesonium*, *Sov. Phys. JETP* **6** (1957) 429. 46
- [46] M. Gell-Mann and A. Pais, *Behavior of neutral particles under charge conjugation*, *Physical Review* **97** 1387. 46
- [47] B. Pontecorvo, *Neutrino Experiments and the Problem of Conservation of Leptonic Charge*, *Zh. Eksp. Teor. Fiz.* **53** (1967) 1717. 46
- [48] B. Pontecorvo, *Inverse beta processes and nonconservation of lepton charge*, *Zh. Eksp. Teor. Fiz.* **34** (1957) 247. 47
- [49] Z. Maki, M. Nakagawa and S. Sakata, *Remarks on the unified model of elementary particles*, *Prog. Theor. Phys.* **28** (1962) 870. 47
- [50] C. Giganti, S. Lavignac and M. Zito, *Neutrino oscillations: The rise of the PMNS paradigm*, *Prog. Part. Nucl. Phys.* **98** (2018) 1 [[1710.00715](#)]. 48
- [51] C. Jarlskog, *Commutator of the quark mass matrices in the standard electroweak model and a measure of maximal cp nonconservation*, *Physical Review Letters* **55** 1039. 50

BIBLIOGRAPHY

- [52] PARTICLE DATA GROUP collaboration, *Review of particle physics*, *Phys. Rev. D* **110** (2024) 030001. 50, 288
- [53] L. Wolfenstein, *Neutrino Oscillations in Matter*, *Phys. Rev. D* **17** (1978) 2369. 50
- [54] S.P. Mikheev and A.Y. Smirnov, *Resonant amplification of neutrino oscillations in matter and solar neutrino spectroscopy*, *Nuovo Cim. C* **9** (1986) 17. 50
- [55] B.T. Cleveland, T. Daily, R. Davis, Jr., J.R. Distel, K. Lande, C.K. Lee et al., *Measurement of the solar electron neutrino flux with the Homestake chlorine detector*, *Astrophys. J.* **496** (1998) 505. 53
- [56] G. Bellini et al., *Precision measurement of the ${}^7\text{Be}$ solar neutrino interaction rate in Borexino*, *Phys. Rev. Lett.* **107** (2011) 141302 [[1104.1816](#)]. 53
- [57] SUPER-KAMIOKANDE collaboration, *Solar neutrino measurements in super-Kamiokande-I*, *Phys. Rev. D* **73** (2006) 112001 [[hep-ex/0508053](#)]. 53
- [58] SNO collaboration, *Combined Analysis of all Three Phases of Solar Neutrino Data from the Sudbury Neutrino Observatory*, *Phys. Rev. C* **88** (2013) 025501 [[1109.0763](#)]. 53
- [59] SUPER-KAMIOKANDE collaboration, *Atmospheric neutrino oscillation analysis with external constraints in Super-Kamiokande I-IV*, *Phys. Rev. D* **97** (2018) 072001 [[1710.09126](#)]. 53, 136
- [60] ICECUBE collaboration, *Measurement of Atmospheric Neutrino Oscillations at 6–56 GeV with IceCube DeepCore*, *Phys. Rev. Lett.* **120** (2018) 071801 [[1707.07081](#)]. 53
- [61] KAMLAND collaboration, *Reactor On-Off Antineutrino Measurement with KamLAND*, *Phys. Rev. D* **88** (2013) 033001 [[1303.4667](#)]. 53
- [62] RENO collaboration, *Measurement of Reactor Antineutrino Oscillation Amplitude and Frequency at RENO*, *Phys. Rev. Lett.* **121** (2018) 201801 [[1806.00248](#)]. 53

BIBLIOGRAPHY

- [63] DAYA BAY collaboration, *Measurement of the Electron Antineutrino Oscillation with 1958 Days of Operation at Daya Bay*, *Phys. Rev. Lett.* **121** (2018) 241805 [[1809.02261](#)]. 53
- [64] NOVA collaboration, *Expanding neutrino oscillation parameter measurements in NOvA using a Bayesian approach*, *Phys. Rev. D* **110** (2024) 012005 [[2311.07835](#)]. 53
- [65] T2K collaboration, *Updated T2K measurements of muon neutrino and antineutrino disappearance using 3.6×10^{21} protons on target*, *Phys. Rev. D* **108** (2023) 072011 [[2305.09916](#)]. 53
- [66] MINOS collaboration, *Combined analysis of ν_μ disappearance and $\nu_\mu \rightarrow \nu_e$ appearance in MINOS using accelerator and atmospheric neutrinos*, *Phys. Rev. Lett.* **112** (2014) 191801 [[1403.0867](#)]. 53
- [67] OPERA collaboration, *Final Results of the OPERA Experiment on ν_τ Appearance in the CNGS Neutrino Beam*, *Phys. Rev. Lett.* **120** (2018) 211801 [[1804.04912](#)]. 53
- [68] K2K collaboration, *Measurement of Neutrino Oscillation by the K2K Experiment*, *Phys. Rev. D* **74** (2006) 072003 [[hep-ex/0606032](#)]. 53
- [69] DUNE collaboration, *Long-baseline neutrino oscillation physics potential of the DUNE experiment*, *Eur. Phys. J. C* **80** (2020) 978 [[2006.16043](#)]. 53, 197
- [70] HYPER-KAMIOKANDE collaboration, *Physics potential of Hyper-Kamiokande for neutrino oscillation measurements*, *PoS NuFact2019* (2019) 040. 53
- [71] P.F. de Salas, D.V. Forero, S. Gariazzo, P. Martínez-Miravé, O. Mena, C.A. Ternes et al., *2020 global reassessment of the neutrino oscillation picture*, *JHEP* **02** (2021) 071 [[2006.11237](#)]. 54, 63

BIBLIOGRAPHY

- [72] T2K collaboration, *Measurements of neutrino oscillation in appearance and disappearance channels by the T2K experiment with 6.6×10^{20} protons on target*, *Phys. Rev. D* **91** (2015) 072010 [[1502.01550](#)]. 54
- [73] NOvA collaboration, *First measurement of muon-neutrino disappearance in NOvA*, *Phys. Rev. D* **93** (2016) 051104 [[1601.05037](#)]. 54
- [74] S. Davidson, E. Nardi and Y. Nir, *Leptogenesis*, *Phys. Rept.* **466** (2008) 105 [[0802.2962](#)]. 55
- [75] SUPERNEMO collaboration, *Probing New Physics Models of Neutrinoless Double Beta Decay with SuperNEMO*, *Eur. Phys. J. C* **70** (2010) 927 [[1005.1241](#)]. 55
- [76] SNO+ collaboration, *Current Status and Future Prospects of the SNO+ Experiment*, *Adv. High Energy Phys.* **2016** (2016) 6194250 [[1508.05759](#)]. 55
- [77] NEXT collaboration, *Sensitivity of a tonne-scale NEXT detector for neutrinoless double beta decay searches*, *JHEP* **2021** (2021) 164 [[2005.06467](#)]. 55
- [78] P. Coloma and P. Huber, *Impact of nuclear effects on the extraction of neutrino oscillation parameters*, *Phys. Rev. Lett.* **111** (2013) 221802 [[1307.1243](#)]. 56
- [79] P. Coloma, P. Huber, C.-M. Jen and C. Mariani, *Neutrino-nucleus interaction models and their impact on oscillation analyses*, *Phys. Rev. D* **89** (2014) 073015 [[1311.4506](#)]. 56
- [80] U. Mosel, *Neutrino Interactions with Nucleons and Nuclei: Importance for Long-Baseline Experiments*, *Ann. Rev. Nucl. Part. Sci.* **66** (2016) 171 [[1602.00696](#)]. 56
- [81] J.A. Formaggio and G.P. Zeller, *From ev to eev: Neutrino cross sections across energy scales*, *Rev. Mod. Phys.* **84** (2012) 1307 [[1305.7513](#)]. 57, 58
- [82] L. Bathe-Peters, S. Gardiner and R. Guenette, *Comparing generator predictions of transverse kinematic imbalance in neutrino-argon scattering*, [2201.04664](#). 58

BIBLIOGRAPHY

- [83] R. Smith and E. Moniz, *Neutrino reactions on nuclear targets*, *Nuclear Physics B* **43** 605. 58
- [84] H.C. Chiang, E. Oset and P. Fernandez de Cordoba, *Muon capture revisited*, *Nucl. Phys. A* **510** (1990) 591. 58, 196
- [85] H. Nakamura and R. Seki, *Quasi-elastic neutrino-nucleus scattering and spectral function*, *Nuclear Physics B - Proceedings Supplements* **112** 197. 58
- [86] A. Nikolakopoulos, R. González-Jiménez, N. Jachowicz, K. Niewczas, F. Sánchez and J.M. Udías, *Benchmarking intranuclear cascade models for neutrino scattering with relativistic optical potentials*, *Phys. Rev. C* **105** (2022) 054603 [2202.01689]. 59
- [87] MINBoNE collaboration, *First Measurement of the Muon Neutrino Charged Current Quasielastic Double Differential Cross Section*, *Phys. Rev. D* **81** (2010) 092005 [1002.2680]. 59
- [88] MINERvA collaboration, *Measurements of the Inclusive Neutrino and Antineutrino Charged Current Cross Sections in MINERvA Using the Low- ν Flux Method*, *Phys. Rev. D* **94** (2016) 112007 [1610.04746]. 59
- [89] MICROBoNE collaboration, *First Measurement of Energy-Dependent Inclusive Muon Neutrino Charged-Current Cross Sections on Argon with the MicroBoNE Detector*, *Phys. Rev. Lett.* **128** (2022) 151801 [2110.14023]. 59
- [90] SBND collaboration, *Neutrino cross-section measurement prospects with SBND*, *PoS NuFact2017* (2018) 067. 59
- [91] NOvA collaboration, *Measurement of the double-differential muon-neutrino charged-current inclusive cross section in the NOvA near detector*, *Phys. Rev. D* **107** (2023) 052011 [2109.12220]. 59

BIBLIOGRAPHY

- [92] T2K collaboration, *Measurement of the ν_μ charged-current cross sections on water, hydrocarbon, iron, and their ratios with the T2K on-axis detectors*, *PTEP* **2019** (2019) 093C02 [[1904.09611](#)]. 59
 - [93] \$\\nu\$PRISM collaboration, *ν PRISM: A new way of probing neutrino interactions*, *PoS NUFAC2014* (2015) 046. 59
 - [94] C. Hasnip, *DUNE-PRISM – A New Method to Measure Neutrino Oscillations*, Ph.D. thesis, Oxford U., 2023. 59, 71
 - [95] DUNE collaboration, *Snowmass Neutrino Frontier: DUNE Physics Summary*, [2203.06100](#). 63, 64
 - [96] DUNE collaboration, *Deep Underground Neutrino Experiment (DUNE), Far Detector Technical Design Report, Volume II: DUNE Physics*, [2002.03005](#). 63, 65, 67, 73, 120, 124, 125, 129, 195, 229, 237
 - [97] SUPER-KAMIOKANDE collaboration, *Search for Proton Decay via $p \rightarrow e^+ \pi_0$ and $p \rightarrow \mu^+ \pi_0$ in a Large Water Cherenkov Detector*, *Phys. Rev. Lett.* **102** (2009) 141801 [[0903.0676](#)]. 64
 - [98] S. Raby, *Grand Unified Theories*, in *2nd World Summit: Physics Beyond the Standard Model*, 8, 2006 [[hep-ph/0608183](#)]. 64
 - [99] KAMIOKANDE-II collaboration, *Observation of a Neutrino Burst from the Supernova SN 1987a*, *Phys. Rev. Lett.* **58** (1987) 1490. 65
 - [100] R.M. Bionta et al., *Observation of a Neutrino Burst in Coincidence with Supernova SN 1987a in the Large Magellanic Cloud*, *Phys. Rev. Lett.* **58** (1987) 1494. 65
 - [101] J. Strait, E. McCluskey, T. Lundin, J. Willhite, T. Hamernik, V. Papadimitriou et al., *Long-Baseline Neutrino Facility (LBNF) and Deep Underground Neutrino Experiment (DUNE) Conceptual Design Report Volume 3: Long-Baseline Neutrino Facility for DUNE*, [1601.05823](#). 65, 66

BIBLIOGRAPHY

- [102] DUNE collaboration, *Deep Underground Neutrino Experiment (DUNE) Near Detector Conceptual Design Report*, *Instruments* **5** (2021) 31 [[2103.13910](#)]. 68, 72, 73, 74, 75, 233, 235, 236
- [103] A. Nehm, *Reconstruction in the DUNE Near Detector Muon Spectrometer*, in *Proceedings of the XXXI International Conference on Neutrino Physics and Astrophysics (Neutrino 2024)*, Zenodo, Oct., 2024, DOI. 70
- [104] J. Asaadi et al., *A New Concept for Kilotonne Scale Liquid Argon Time Projection Chambers*, *Instruments* **4** (2020) 6 [[1908.10956](#)]. 69
- [105] DUNE collaboration, *DUNE Phase II: Scientific Opportunities, Detector Concepts, Technological Solutions*, [2408.12725](#). 71, 74, 77
- [106] DUNE collaboration, *A Gaseous Argon-Based Near Detector to Enhance the Physics Capabilities of DUNE*, [2203.06281](#). 73
- [107] ALICE collaboration, *ALICE: Physics Performance Report, Volume II*, *J. Phys. G: Nucl. Part. Phys.* **32** 1295. 74, 233
- [108] F. Sauli, *GEM: A new concept for electron amplification in gas detectors*, *Nucl. Instrum. Methods Phys. Res. A* **386** 531. 74, 78
- [109] CALICE collaboration, *Construction and Commissioning of the CALICE Analog Hadron Calorimeter Prototype*, *JINST* **5** (2010) P05004 [[1003.2662](#)]. 75
- [110] DUNE collaboration, *SPY: a conceptual design study of a magnet system for a high-pressure gaseous TPC neutrino detector*, *JINST* **19** (2024) P06018 [[2311.16063](#)]. 76
- [111] A. Ritchie-Yates et al., *First operation of an ALICE OROC operated in high pressure Ar-CO₂ and Ar-CH₄*, *Eur. Phys. J. C* **83** (2023) 1139 [[2305.08822](#)]. 77
- [112] ALICE TPC collaboration, *The upgrade of the ALICE TPC with GEMs and continuous readout*, *JINST* **16** (2021) P03022 [[2012.09518](#)]. 77

BIBLIOGRAPHY

- [113] F. Sauli, *The gas electron multiplier (GEM): Operating principles and applications*, *Nucl. Instrum. Methods Phys. Res. A* **805** 2. 78
- [114] C. Lippmann, *A continuous read-out TPC for the ALICE upgrade*, *Nucl. Instrum. Methods Phys. Res. A* **824** 543. 78
- [115] C. Calabria, *Large-size triple GEM detectors for the CMS forward muon upgrade*, *Nuclear and Particle Physics Proceedings* **273–275** 1042. 78
- [116] DUNE collaboration, *Deep Underground Neutrino Experiment (DUNE), Far Detector Technical Design Report, Volume IV: Far Detector Single-phase Technology*, *JINST* **15** (2020) T08010 [2002.03010]. 79, 85
- [117] DUNE collaboration, *The DUNE Far Detector Vertical Drift Technology. Technical Design Report*, *JINST* **19** (2024) T08004 [2312.03130]. 79, 83, 84
- [118] DUNE DAQ Project, “Trigger and Data AcQuisition (TDAQ) System Design.” [EDMS-2826454](#), 2022. 87
- [119] G. Turin, *An introduction to matched filters*, *IEEE Transactions on Information Theory* **6** (1960) 311. 92
- [120] E.D. Church, *Larsoft: A software package for liquid argon time projection drift chambers*, [1311.6774](#). 95, 140
- [121] GEANT4 collaboration, *Geant4—a simulation toolkit*, *Nucl. Instrum. Meth. A* **506** (2003) 250. 96, 140
- [122] J. Allison, K. Amako, J. Apostolakis, H. Araujo, P. Arce Dubois, M. Asai et al., *Geant4 developments and applications*, *IEEE Transactions on Nuclear Science* **53** (2006) 270. 96, 140
- [123] J. Allison, K. Amako, J. Apostolakis, P. Arce, M. Asai, T. Aso et al., *Recent developments in geant4*, *Nuclear Instruments and Methods in Physics Research*

BIBLIOGRAPHY

- Section A: Accelerators, Spectrometers, Detectors and Associated Equipment* **835** (2016) 186. 96, 140
- [124] S.V. Stehman, *Selecting and interpreting measures of thematic classification accuracy*, *Remote Sensing of Environment* **62** (1997) 77. 105
- [125] A.A. Taha and A. Hanbury, *Metrics for evaluating 3d medical image segmentation: analysis, selection, and tool*, *BMC Medical Imaging* **15** (2015) . 106
- [126] J. Silk, K.A. Olive and M. Srednicki, *The Photino, the Sun and High-Energy Neutrinos*, *Phys. Rev. Lett.* **55** (1985) 257. 115
- [127] M. Srednicki, K.A. Olive and J. Silk, *High-Energy Neutrinos from the Sun and Cold Dark Matter*, *Nucl. Phys. B* **279** (1987) 804. 115
- [128] J.S. Hagelin, K.W. Ng and K.A. Olive, *A High-energy Neutrino Signature From Supersymmetric Relics*, *Phys. Lett. B* **180** (1986) 375. 115
- [129] T.K. Gaisser, G. Steigman and S. Tilav, *Limits on Cold Dark Matter Candidates from Deep Underground Detectors*, *Phys. Rev. D* **34** (1986) 2206. 115
- [130] N. Bernal, J. Martín-Albo and S. Palomares-Ruiz, *A novel way of constraining WIMPs annihilations in the Sun: MeV neutrinos*, *JCAP* **08** (2013) 011 [1208.0834]. 115, 116, 117, 251, 254
- [131] C. Rott, J. Siegal-Gaskins and J.F. Beacom, *New Sensitivity to Solar WIMP Annihilation using Low-Energy Neutrinos*, *Phys. Rev. D* **88** (2013) 055005 [1208.0827]. 115, 117
- [132] C. Rott, S. In, J. Kumar and D. Yaylali, *Dark Matter Searches for Monoenergetic Neutrinos Arising from Stopped Meson Decay in the Sun*, *JCAP* **11** (2015) 039 [1510.00170]. 115
- [133] DUNE collaboration, *Searching for solar KDAR with DUNE*, *JCAP* **10** (2021) 065 [2107.09109]. 115, 118, 121, 129, 230, 231, 232, 233

BIBLIOGRAPHY

- [134] G. Busoni, A. De Simone and W.-C. Huang, *On the Minimum Dark Matter Mass Testable by Neutrinos from the Sun*, *JCAP* **07** (2013) 010 [[1305.1817](#)]. 116
- [135] J.N. Bahcall and M.H. Pinsonneault, *Solar models with helium and heavy element diffusion*, *Rev. Mod. Phys.* **67** (1995) 781 [[hep-ph/9505425](#)]. 116
- [136] P. Baratella, M. Cirelli, A. Hektor, J. Pata, M. Piibeleht and A. Strumia, *PPPC 4 DM ν : a Poor Particle Physicist Cookbook for Neutrinos from Dark Matter annihilations in the Sun*, *JCAP* **03** (2014) 053 [[1312.6408](#)]. 117
- [137] T. Golan, J.T. Sobczyk and J. Zmuda, *NuWro: the Wroclaw Monte Carlo Generator of Neutrino Interactions*, *Nucl. Phys. B Proc. Suppl.* **229-232** (2012) 499. 119
- [138] M. Honda, M. Sajjad Athar, T. Kajita, K. Kasahara and S. Midorikawa, *Atmospheric neutrino flux calculation using the NRLMSISE-00 atmospheric model*, *Phys. Rev. D* **92** (2015) 023004 [[1502.03916](#)]. 119, 120
- [139] G. Cowan, K. Cranmer, E. Gross and O. Vitells, *Asymptotic formulae for likelihood-based tests of new physics*, *Eur. Phys. J. C* **71** (2011) 1554 [[1007.1727](#)]. 120
- [140] J. Edsjö, J. Elevant and C. Niblaeus, *WimpSim Neutrino Monte Carlo*. 122, 258
- [141] C. Rott, D. Jeong, J. Kumar and D. Yaylali, *Neutrino Topology Reconstruction at DUNE and Applications to Searches for Dark Matter Annihilation in the Sun*, *JCAP* **07** (2019) 006 [[1903.04175](#)]. 124
- [142] F. Pedregosa, G. Varoquaux, A. Gramfort, V. Michel, B. Thirion, O. Grisel et al., *Scikit-learn: Machine learning in Python*, *Journal of Machine Learning Research* **12** (2011) 2825. 130, 173
- [143] ICECUBE collaboration, *Search for GeV-scale dark matter annihilation in the Sun with IceCube DeepCore*, *Phys. Rev. D* **105** (2022) 062004 [[2111.09970](#)]. 133

BIBLIOGRAPHY

- [144] SUPER-KAMIOKANDE collaboration, *Search for neutrinos from annihilation of captured low-mass dark matter particles in the Sun by Super-Kamiokande*, *Phys. Rev. Lett.* **114** (2015) 141301 [[1503.04858](#)]. 133, 135
- [145] N.F. Bell, M.J. Dolan and S. Robles, *Searching for dark matter in the Sun using Hyper-Kamiokande*, *JCAP* **11** (2021) 004 [[2107.04216](#)]. 133
- [146] E. Behnke et al., *Final Results of the PICASSO Dark Matter Search Experiment*, *Astropart. Phys.* **90** (2017) 85 [[1611.01499](#)]. 133
- [147] PICO collaboration, *Dark Matter Search Results from the Complete Exposure of the PICO-60 C₃F₈ Bubble Chamber*, *Phys. Rev. D* **100** (2019) 022001 [[1902.04031](#)]. 133
- [148] C. Principato, *An Indirect Search for Weakly Interacting Massive Particles in the Sun Using Upward-going Muons in NOvA*, Ph.D. thesis, Virginia U., 2021. 10.18130/x5z2-1466. 135
- [149] G. Wikström and J. Edsjö, *Limits on the WIMP-nucleon scattering cross-section from neutrino telescopes*, *JCAP* **2009** 009 [[0903.2986](#)]. 135
- [150] C. Rott, T. Tanaka and Y. Itow, *Enhanced sensitivity to dark matter self-annihilations in the sun using neutrino spectral information*, [1107.3182](#). 135
- [151] M.M. Boliev, S.V. Demidov, S.P. Mikheyev and O.V. Suvorova, *Search for muon signal from dark matter annihilations in the Sun with the Baksan Underground Scintillator Telescope for 24.12 years*, *JCAP* **09** (2013) 019 [[1301.1138](#)]. 135, 136
- [152] M. Honda, T. Kajita, K. Kasahara, S. Midorikawa and T. Sanuki, *Calculation of atmospheric neutrino flux using the interaction model calibrated with atmospheric muon data*, *Phys. Rev. D* **75** (2007) 043006 [[astro-ph/0611418](#)]. 136
- [153] C. Green, J. Kowalkowski, M. Paterno, M. Fischler, L. Garren and Q. Lu, *The Art Framework*, *J. Phys. Conf. Ser.* **396** (2012) 022020. 140

BIBLIOGRAPHY

- [154] R. Brun and F. Rademakers, *ROOT — An object oriented data analysis framework*, *Nuclear Instruments and Methods in Physics Research Section A: Accelerators, Spectrometers, Detectors and Associated Equipment* **389** 81. 140
- [155] C. Andreopoulos et al., *The GENIE Neutrino Monte Carlo Generator*, *Nucl. Instrum. Meth. A* **614** (2010) 87 [[0905.2517](#)]. 140
- [156] C. Andreopoulos, C. Barry, S. Dytman, H. Gallagher, T. Golan, R. Hatcher et al., *The GENIE Neutrino Monte Carlo Generator: Physics and User Manual*, [1510.05494](#). 140
- [157] C. Hagmann, D. Lange and D. Wright, *Cosmic-ray shower generator (CRY) for Monte Carlo transport codes*, in *2007 IEEE Nuclear Science Symposium Conference Record*, vol. 2, pp. 1143–1146, IEEE, 2007, [DOI](#). 141
- [158] H. Bethe, *Zur theorie des durchgangs schneller korpuskularstrahlen durch materie*, *Annalen der Physik* **397** (1930) 325. 145
- [159] E. Fermi, *The ionization loss of energy in gases and in condensed materials*, *Physical Review* **57** (1940) 485. 146
- [160] R. Sternheimer, M. Berger and S. Seltzer, *Density effect for the ionization loss of charged particles in various substances*, *Atomic Data and Nuclear Data Tables* **30** (1984) 261. 146
- [161] W.W.M. Allison and J.H. Cobb, *Relativistic Charged Particle Identification by Energy Loss*, *Ann. Rev. Nucl. Part. Sci.* **30** (1980) 253. 146
- [162] W. Blum, L. Rolandi and W. Riegler, *Particle detection with drift chambers*, Particle Acceleration and Detection (2008), [10.1007/978-3-540-76684-1](#). 146
- [163] ALICE TPC collaboration, *Particle identification of the ALICE TPC via dE/dx*, *Nucl. Instrum. Meth. A* **706** (2013) 55. 146

BIBLIOGRAPHY

- [164] L. Landau, *On the energy loss of fast particles by ionization*, *J. Phys. (USSR)* **8** (1944) 201. 147, 269
- [165] A.S. Cornell, W. Doorsamy, B. Fuks, G. Harmsen and L. Mason, *Boosted decision trees in the era of new physics: a smuon analysis case study*, [2109.11815](#). 165
- [166] L. Jost, *Entropy and diversity*, *Oikos* **113** (2006) 363. 171, 174
- [167] L.S. Shapley, *Notes on the N-Person Game II: The Value of an N-Person Game*, RAND Corporation, Santa Monica, CA (1951), [10.7249/RM0670](#). 171, 174
- [168] I.T. Jolliffe and J. Cadima, *Principal component analysis: a review and recent developments*, *Philos. Trans. R. Soc. A* **374** 20150202. 172
- [169] G.H. Golub and C. Reinsch, *Singular value decomposition and least squares solutions*, *Numerische Mathematik* **14** 403. 173
- [170] S.M. Lundberg and S.-I. Lee, *A unified approach to interpreting model predictions*, in *Advances in Neural Information Processing Systems 30 (NIPS 2017)*, Curran Associates, Inc., 2017. 175
- [171] D.S. Wilks, *Statistical Methods in the Atmospheric Sciences*, Academic Press. 181
- [172] ALICE collaboration, *Production of pions, kaons and protons in pp collisions at $\sqrt{s} = 900 \text{ gev}$ with alice at the lhc*, [1101.4110](#). 185
- [173] U. Einhaus, *Charged hadron identification with de/dx and time-of-flight at future higgs factories*, [2110.15115](#). 185
- [174] GENIE collaboration, *Neutrino-nucleon cross-section model tuning in GENIE v3*, *Phys. Rev. D* **104** (2021) 072009 [[2104.09179](#)]. 196
- [175] J. Nieves, J.E. Amaro and M. Valverde, *Inclusive quasi-elastic neutrino reactions*, *Phys. Rev. C* **70** (2004) 055503 [[nucl-th/0408005](#)]. 196

BIBLIOGRAPHY

- [176] J. Nieves, I. Ruiz Simo and M.J. Vicente Vacas, *Inclusive Charged-Current Neutrino-Nucleus Reactions*, *Phys. Rev. C* **83** (2011) 045501 [[1102.2777](#)]. 196, 230
- [177] C. Berger and L.M. Sehgal, *Lepton mass effects in single pion production by neutrinos*, *Phys. Rev. D* **76** (2007) 113004 [[0709.4378](#)]. 196, 232
- [178] C. Berger and L.M. Sehgal, *PCAC and coherent pion production by low energy neutrinos*, *Phys. Rev. D* **79** (2009) 053003 [[0812.2653](#)]. 196
- [179] A. Bodek and U.K. Yang, *Modeling deep inelastic cross-sections in the few GeV region*, *Nucl. Phys. B Proc. Suppl.* **112** (2002) 70 [[hep-ex/0203009](#)]. 196, 232
- [180] J.E. Gaiser, *Charmonium Spectroscopy From Radiative Decays of the J/ψ and ψ'* , Ph.D. thesis, Stanford University, 1982. 224, 289
- [181] T. Golan, L. Aliaga and M. Kordosky, *Minerva's flux prediction*, in *Proceedings of the 10th International Workshop on Neutrino-Nucleus Interactions in Few-GeV Region (NuInt15)*, Journal of the Physical Society of Japan, DOI. 229
- [182] A. Bashyal, H. Schellman and L. Fields, *PPFX Implementation In Deep Underground Neutrino Experiment*, . 229
- [183] A. Bodek and J.L. Ritchie, *Fermi Motion Effects in Deep Inelastic Lepton Scattering from Nuclear Targets*, *Phys. Rev. D* **23** (1981) 1070. 230
- [184] C. Wilkinson et al., *Testing charged current quasi-elastic and multinucleon interaction models in the NEUT neutrino interaction generator with published datasets from the MiniBooNE and MINERνA experiments*, *Phys. Rev. D* **93** (2016) 072010 [[1601.05592](#)]. 230
- [185] T2K collaboration, *Search for CP Violation in Neutrino and Antineutrino Oscillations by the T2K Experiment with 2.2×10^{21} Protons on Target*, *Phys. Rev. Lett.* **121** (2018) 171802 [[1807.07891](#)]. 230

BIBLIOGRAPHY

- [186] MINERVA collaboration, *Identification of nuclear effects in neutrino-carbon interactions at low three-momentum transfer*, *Phys. Rev. Lett.* **116** (2016) 071802 [[1511.05944](#)]. 230
- [187] C. Colle, O. Hen, W. Cosyn, I. Korover, E. Piasetzky, J. Ryckebusch et al., *Extracting the mass dependence and quantum numbers of short-range correlated pairs from $a(e, e' p)$ and $a(e, e' pp)$ scattering*, *Phys. Rev. C* **92** (2015) 024604. 232
- [188] D. Rein and L.M. Sehgal, *Neutrino Excitation of Baryon Resonances and Single Pion Production*, *Annals Phys.* **133** (1981) 79. 232
- [189] M. Sanchez, “NOvA Results and Prospects.” June, 2018. 232
- [190] D.H. Stork, *FIRST OPERATION OF THE TPC FACILITY AT PEP*, *Le Journal de Physique Colloques* **43** C3. 234
- [191] H. Aihara, M. Alston-Garnjost, D.H. Badtke, J.A. Bakken, A. Barbaro-Galtieri, A.V. Barnes et al., *Spatial Resolution of the PEP-4 Time Projection Chamber*, *IEEE Transactions on Nuclear Science* **30** 76. 234
- [192] I. Lehraus, *Progress in particle identification by ionization sampling*, *Nucl. Instrum. Meth.* **217** (1983) 43. 234
- [193] J. McClellan and T. Parks, *A personal history of the Parks-McClellan algorithm*, *IEEE Signal Processing Magazine* **22** (2005) 82. 241
- [194] L. Weinberg and P. Slepian, *Takahasi’s results on tchebycheff and butterworth ladder networks*, *IRE Transactions on Circuit Theory* **7** (1960) 88. 241
- [195] J.W. Goodman, *Statistical Optics*, Wiley (1985). 245
- [196] B. Dwork, *Detection of a pulse superimposed on fluctuation noise*, *Proceedings of the IRE* **38** (1950) 771. 246
- [197] L. Wainstein and V. Zubakov, *Extraction of Signals from Noise*, Prentice-Hall (1962). 246

BIBLIOGRAPHY

- [198] R. Garani and S. Palomares-Ruiz, *Dark matter in the Sun: scattering off electrons vs nucleons*, *JCAP* **05** (2017) 007 [[1702.02768](#)]. 251, 252, 254, 255, 256, 262
- [199] V.A. Bednyakov and F. Simkovic, *Nuclear spin structure in dark matter search: The Zero momentum transfer limit*, *Phys. Part. Nucl.* **36** (2005) 131 [[hep-ph/0406218](#)]. 251
- [200] R. Catena and B. Schwabe, *Form factors for dark matter capture by the Sun in effective theories*, *JCAP* **04** (2015) 042 [[1501.03729](#)]. 252
- [201] A. Gould, *WIMP Distribution in and Evaporation From the Sun*, *Astrophys. J.* **321** (1987) 560. 252
- [202] A. Gould, *Resonant Enhancements in WIMP Capture by the Earth*, *Astrophys. J.* **321** (1987) 571. 254
- [203] T. Bringmann, J. Edsjö, P. Gondolo, P. Ullio and L. Bergström, *DarkSUSY 6 : An Advanced Tool to Compute Dark Matter Properties Numerically*, *JCAP* **07** (2018) 033 [[1802.03399](#)]. 255
- [204] J.N. Bahcall, M.H. Pinsonneault and S. Basu, *Solar models: Current epoch and time dependences, neutrinos, and helioseismological properties*, *Astrophys. J.* **555** (2001) 990 [[astro-ph/0010346](#)]. 255
- [205] T. Kaluza, *Zum Unitätsproblem der Physik*, *Sitzungsber. Preuss. Akad. Wiss. Berlin (Math. Phys.)* **1921** (1921) 966 [[1803.08616](#)]. 257
- [206] O. Klein, *Quantum Theory and Five-Dimensional Theory of Relativity. (In German and English)*, *Z. Phys.* **37** (1926) 895. 257
- [207] T. Appelquist, H.-C. Cheng and B.A. Dobrescu, *Bounds on universal extra dimensions*, *Phys. Rev. D* **64** (2001) 035002 [[hep-ph/0012100](#)]. 257
- [208] N. Arkani-Hamed, S. Dimopoulos and G.R. Dvali, *The Hierarchy problem and new dimensions at a millimeter*, *Phys. Lett. B* **429** (1998) 263 [[hep-ph/9803315](#)]. 257

BIBLIOGRAPHY

- [209] L. Randall and R. Sundrum, *A Large mass hierarchy from a small extra dimension*, *Phys. Rev. Lett.* **83** (1999) 3370 [[hep-ph/9905221](#)]. 257
- [210] G. Servant and T.M.P. Tait, *Is the lightest Kaluza-Klein particle a viable dark matter candidate?*, *Nucl. Phys. B* **650** (2003) 391 [[hep-ph/0206071](#)]. 258
- [211] H.-C. Cheng, K.T. Matchev and M. Schmaltz, *Radiative corrections to Kaluza-Klein masses*, *Phys. Rev. D* **66** (2002) 036005 [[hep-ph/0204342](#)]. 258
- [212] M. Blennow, J. Edsjö and T. Ohlsson, *Neutrinos from WIMP annihilations using a full three-flavor Monte Carlo*, *JCAP* **01** (2008) 021 [[0709.3898](#)]. 258
- [213] D. Hooper and S. Profumo, *Dark Matter and Collider Phenomenology of Universal Extra Dimensions*, *Phys. Rept.* **453** (2007) 29 [[hep-ph/0701197](#)]. 258
- [214] M. Colom i Bernadich and C. Pérez de los Heros, *Limits on Kaluza-Klein dark matter annihilation in the Sun from recent IceCube results*, *Eur. Phys. J. C*, **80** 2 (2020) 129 **80** (2019) [[1912.04585](#)]. 260
- [215] ANTARES collaboration, *Search for Dark Matter in the Sun with the ANTARES Neutrino Telescope in the CMSSM and mUED frameworks*, *Nucl. Instrum. Meth. A* **725** (2013) 76 [[1204.5290](#)]. 260
- [216] N. Deutschmann, T. Flacke and J.S. Kim, *Current LHC Constraints on Minimal Universal Extra Dimensions*, *Phys. Lett. B* **771** (2017) 515 [[1702.00410](#)]. 260
- [217] U. Haisch and A. Weiler, *Bound on minimal universal extra dimensions from anti-B → X(s)gamma*, *Phys. Rev. D* **76** (2007) 034014 [[hep-ph/0703064](#)]. 260
- [218] A. Freitas and U. Haisch, *Anti-B → X(s) gamma in two universal extra dimensions*, *Phys. Rev. D* **77** (2008) 093008 [[0801.4346](#)]. 260
- [219] J. Kopp, V. Niro, T. Schwetz and J. Zupan, *DAMA/LIBRA and leptonically interacting Dark Matter*, *Phys. Rev. D* **80** (2009) 083502 [[0907.3159](#)]. 261

BIBLIOGRAPHY

- [220] PARTICLE DATA GROUP collaboration, *Review of Particle Physics*, *PTEP* **2020** (2020) 083C01. 262
- [221] M. Beltran, D. Hooper, E.W. Kolb and Z.C. Krusberg, *Deducing the nature of dark matter from direct and indirect detection experiments in the absence of collider signatures of new physics*, *Phys. Rev. D* **80** (2009) 043509 [[0808.3384](#)]. 263
- [222] PLANCK collaboration, *Planck 2018 results. VI. Cosmological parameters*, *Astron. Astrophys.* **641** (2020) A6 [[1807.06209](#)]. 263
- [223] XENON collaboration, *Light Dark Matter Search with Ionization Signals in XENON1T*, *Phys. Rev. Lett.* **123** (2019) 251801 [[1907.11485](#)]. 264, 265
- [224] DARKSIDE collaboration, *Search for Dark Matter Particle Interactions with Electron Final States with DarkSide-50*, *Phys. Rev. Lett.* **130** (2023) 101002 [[2207.11968](#)]. 264, 265
- [225] PANDAX-II collaboration, *Search for Light Dark Matter-Electron Scatterings in the PandaX-II Experiment*, *Phys. Rev. Lett.* **126** (2021) 211803 [[2101.07479](#)]. 264, 265
- [226] W. Ulmer and E. Matsinos, *Theoretical methods for the calculation of Bragg curves and 3D distributions of proton beams*, *The European Physical Journal Special Topics* **190** (2010) 1. 270
- [227] ARGONeUT collaboration, *A Study of Electron Recombination Using Highly Ionizing Particles in the ArgoNeuT Liquid Argon TPC*, *JINST* **8** (2013) P08005 [[1306.1712](#)]. 272
- [228] E. Aprile, A.E. Bolotnikov, A.L. Bolozdynya and T. Doke, *Noble Gas Detectors*, Wiley (Oct., 2008), [10.1002/9783527610020](#). 272

BIBLIOGRAPHY

- [229] R. Frühwirth, *Application of filter methods to the reconstruction of tracks and vertices in events of experimental high energy physics*, Ph.D. thesis, Technischen Universität Wien, 1988. [277](#)
- [230] P. Astier, A. Cardini, R.D. Cousins, A. Letessier-Selvon, B.A. Popov and T. Vinogradova, *Kalman filter track fits and track breakpoint analysis*, *Nucl. Instrum. Methods Phys. Res. A* **450** (2000) 138. [277](#)
- [231] T2K UK collaboration, *The Electromagnetic Calorimeter for the T2K Near Detector ND280*, *JINST* **8** (2013) P10019 [[1308.3445](#)]. [284](#)